# Design Optimization of Contactless Power Transfer Systems for Electric Vehicles Using Electromagnetic Resonant Coupling


Junlong Duan

Department of Engineering and Design

School of Engineering and Informatics

University of Sussex

United Kingdom

Thesis submitted in partial fulfilment of the requirements for the degree of

*Doctor of Philosophy*

October 2020

*This thesis is dedicated to my mother and father. I also dedicate this thesis and extend my special appreciation to my elder uncle.*

# Declaration

I hereby declare that this thesis, in full or in part, has not been and will not be submitted to any other university for the award of any other degree.

Signature: ……

Date: ……

# Abstract

Contactless power transfer (CPT) systems have been gaining considerable attention and have achieved tremendous technology advancements across a wide variety of utilizations in the past decade. CPT technologies offer promising advantages and open up new avenues for development of numerous real-world applications. Of particular importance is the implementation of CPT systems on the charging of electric vehicles (EV), which are considered as a sustainable alternative that will effectively address global fossil energy scarcity and climate change issues in the future.

The overarching aim of this thesis is to investigate and improve the operation performance of CPT systems for contactless EV charging. Optimized high-performance CPT systems are expected to be the ultimate goal for EV wireless charging in the following century. In the CPT applications, some certain characteristic outputs and parameters such as overall system efficiency, RMS power transfer, air gap and resonant frequency are considered as key performance metrics to be addressed. These crucial metrics and properties have been emphasized throughout this thesis. The electromagnetic resonant coupling technique has been put forward and adopted for most designed prototypes in this thesis in order to optimize the overall performance of CPT systems. The research methodology development, model designs, implementations and results analysis of the thesis are undertaken from the perspective of both power electronics and electromagnetics towards achieving the main objectives of the research.

With focuses on overall system efficiency, real transfer power to load, air gap, frequency, magnetic coupler design, shielding materials, inner shielding distance and misalignment characteristics, a range of studies have been conducted in the thesis based on the proposed methodology, enhanced simulation models and laboratory prototypes.

A number of important contributions have been made by the thesis. The four most significant contributions are: Firstly, the originally developed methodology for the CPT research of the thesis – the research flowchart system based on the preliminary natural resonant frequency probe and anticipation method. This uniquely proposed method for this thesis has been used to effectively probe, track and narrow down the most appropriate

resonant frequency range to be chosen for CPT systems to perform with, towards reaching an optimized status of electromagnetic resonant coupling in terms of CPT technology-based EV charging. Secondly, the magnetic coupler modular-based CPT designs for investigating overall system performance optimization. As a result, in the thesis, a novel small-sized CPT prototype that is based on a geometrically improved H-shaped magnetic coupler, with ferromagnetic cores, passive aluminium shielding, an SS compensation topology and electromagnetic resonant coupling, has been proposed as an optimal design solution. Thirdly, approximating a CPT system to operate in close proximity to its calculated natural resonant frequency point by tuning and controlling system operating frequency could effectively lead to an overall system performance optimization most of the time in practical applications using electromagnetic resonant coupling, whereas setting the system operating frequency exactly at its calculated natural resonant frequency to make the system maximally operate at an extreme state of magnetic resonance may only produce a partial optimization from perspective of the system parameters and outputs. Fourthly, reasonable trade-offs between performance metrics are required to be considered and evaluated in order to achieve a feasible overall CPT system optimization.

Through the detailed analysis of the results, model outcome comparisons, explanations on findings, limitation discussions and holistic system evaluations, this thesis is devoted to report and provide a series of newly proposed solutions and innovatively designed CPT systems. These solutions are supported by empirical findings, conclusions and contributions, which may encourage further pursuits of system performance optimizations for high-power high-frequency CPT charging technologies applied for future EV, despite methodological limitations, experiment restrictions and external uncertainties.

# Acknowledgement

First of all, I would like to express my sincerest thanks to my supervisor, Dr. William Weiji Wang who offered me the opportunity to work towards PhD after my MSc at Sussex University and has consistently supported me from all aspects through these years. His encouragement, guidance, patience, expertise and advice have been most invaluable for me to explore and pursue on my project leading to the completion of this thesis.

My deep gratitude goes to my second supervisor, Dr. Spyros Skarvelis-Kazakos who provided precious suggestions and guidance to me in the past years. I am also grateful to Dr. Chang Wang and Dr. Kun Liang, for their constructive advices, critical but generous comments at each stage of my doctoral research progression. Many thanks to Dr. Martin White, the Director of Doctoral Studies, and Mr. Luke Scott of the School of Engineering and Informatics, for their kind support work.

Special thanks to my colleague as well as one of my best friends, Dr. Auday Al-Mayyahi who worked with me for years at Sussex towards his PhD and now has become a lecturer of Basrah University in Iraq, for his heartfelt help and for treating me like his own brother. We have the solidest friendship due to what we went through together in England. I also wish to thank Ms Catherine Warden and all other fellow colleagues in the Engineering Department community and it is my pleasure to work as an associate tutor with them for my doctorial years at Sussex.

My deepest appreciation going to my parents cannot be put into words. I am always grateful to my mother and father for their countless sacrifices and encouragement over my well-being and education.

Finally, last but not least, I am particularly thankful to my uncles, aunts, grandmother and the whole big family of mine, for their most ceaseless and truthful encouragement and loving care. My two uncles have always been the most shining examples and trusted mentors in my life ever since my childhood. My special gratitude is to my elder uncle and his family for their tremendous support to me during my PhD studies.

# Table of Contents

# List of Figures

# List of Tables

# List of Abbreviations

| | |
|---|---|
| ADC | Analogy-to-digital converter |
| AGVs | Automated guided vehicles |
| CPT | Contactless power transfer |
| CET | Contactless energy transmission |
| DSP | Digital signal processing |
| DFT | Discrete Fourier transform |
| DAQ | Data acquisition |
| EVs | Electric vehicles |
| EMI | Electromagnetic field interference |
| EMF | Electromagnetic field |
| EMC | Electromagnetic compatibility |
| e.m.f. | Electromotive force |
| FEM | Finite element methods |
| FFT | Fast Fourier transform algorithm |
| FPGA | Field-programmable gate array |
| HF | High-frequency |
| HEVs | Hybrid electric vehicles |
| HFCHEVs | Hydrogen fuel cells hybrid electric vehicles |
| ICE | Internal combustion engine |
| ISM | Industrial, scientific and medical band |
| IPT | Inductive power transfer |
| LF | Low-frequency |
| PS | Primary parallel – secondary series compensation topology |
| PP | Primary parallel – secondary parallel compensation topology |

| | |
|---|---|
| PF | Power factor |
| RFID | Radio frequency identification |
| SS | Primary series – secondary series compensation topology |
| SP | Primary series – secondary parallel compensation topology |
| UAVs | Unmanned aerial vehicles |
| VLF | Very low-frequency |
| VNA | Vector network analyser |
| WPT | Wireless power transmitting |

# List of Symbols

| | |
|---|---|
| $\nabla$ | Vector differential operator |
| $\nabla \cdot$ | Divergence of a vector field |
| $\nabla \times$ | Curl of a vector field |

# Chapter 1 Introduction

## 1.1 Motivation and relevance

Research in contactless power transfer technologies based on magnetic induction has been obtaining considerable attention due to the growing dependence on a series of battery-powered applications ranging from low-power medical implants, mobile phones to relatively higher-power electric vehicles (EVs) and unmanned aerial vehicles (UAVs). However, the larger-scale use of battery as a substitute for less frequent plug-in charging manipulations for conventional EVs is eventually not an optimal solution due to accordingly rising operational costs of batteries, lifetime limits of all type of batteries, hardware weight, etc. More generally, power-cords and battery-based devices appear to have some inherent drawbacks for large-scale mobility and utilization due to wire-associated hazards caused by inevitable mechanical abrasions, a waste of fabrication material caused by unstandardized socket-plug protocols worldwide, safety concerns in extreme weather conditions, inconvenience for customer experience, etc.

Therefore, the evidently potential advantages of contactless power transfer (CPT) technologies have been able to motivate investigations in various applications. Specifically, without exposed cords and frictions, CPT methods can be more reliable and durable; with independence and non-contact requirement between subsystems such as the powering front end and vehicle end, the entire system will be able to work with electrical insulations and prevention of sparks, enabling the applications like the EVs charging to be safer, more flexible, reliable, multi-functional, etc.

In terms of further sides of relevance and motivation, CPT technologies could facilitate the development of power electronics with not only the scientific and theoretical significance but also the huge potentials of utilization, resulting in wider power applications such as environmental-friendly transportation, emerging machine manufacturing techniques, biomedical devices, smart-home options, etc. These foreseen scopes of applications will then be advantageous to the economic returns and social benefits to the world in the future.

## 1.2 Research gaps, challenges and objectives of the work

In spite of the promising advantages of CPT technologies compared with conventional plug-in charging methods for EVs, the current CPT technologies per se could pose a number of challenges in practical scenarios and of gaps in research domains, which are identified in this thesis as follows. Firstly, CPT air gap, namely the maximum transfer distance. Secondly, power transfer efficiency of the system. Thirdly, RMS real power output of the system. Fourthly, challenge of tackling coil misalignments, which is also a realistic issue in real-world EV parking for charging scenarios in different displacement directions. Fifthly, total losses, which includes copper winding losses and core losses consisting of eddy current loss and hysteresis loss. Sixthly, potential challenges from safety and security aspects for long-term considerations in the future such as cyber-attacks from external sources and possible human exposure concerns from thermal, high electromagnetic interference (EMI) and electromagnetic compatibility (EMC) aspects.

These challenges and limitations exist in the current CPT research domains as key questions, ranging from low-power near-field RF-level wireless devices, to medium-power applications like wireless phone charging, and to the expected high-power high-frequency CPT utilizations such as the CPT technologies for EV charging. Nevertheless, some limitations mentioned above are currently seen negligible or overlooked in the literature. More detailed discussions based on characteristic results and findings from this thesis are in Chapter 8 for mid-term and long-term considerations and studies in the CPT research domain for the future.

The objectives of this thesis are to maximize CPT system efficiency, RMS power transfer ratings, coupling coil air gaps, tolerance to misalignment, effective utilization of shielding, inner shielding distance, etc., all of which aim to address the key question – fundamentally facilitate the holistic system performance of CPT technologies that are applied for high-power high-frequency stationary EV charging with optimized CPT system designs using electromagnetic resonant coupling.

The major contributions of the studies in this thesis are on the research methodology that is uniquely developed for CPT, including the preliminary natural resonant frequency probe and anticipation method, and on the CPT coupler modular designs for overall

system performance optimization since it is the core part of the magnetic field-based CPT system in terms of inductively producing EMF metrics and generating electric outputs.

With emphases on coupling module enhancements using electromagnetic resonant coupling conditions, groups of specifically designed CPT systems are to be tested and compared based on results analysis from both perspectives of power electronics outputs and electromagnetic field performance metrics, which could be also considered as methodological contributions, along with other findings arising from this thesis, seeing that there are relatively the lacks of studies and reports in the literature so far addressing the practical electromagnetic field flux distributions with real-time EMF parameters that directly and indirectly impose delicate impacts onto the targeted outcomes for CPT-based EV charging applications.

## 1.3 Thesis outline

This thesis is organized as follows:

Chapter 1: states the motivation of implementing this research and sets out the research gaps, challenges and the objectives of this research work.

Chapter 2: introduces the history and development of wireless power transfer concepts over the past century and describes the state of the art of contactless energy transmission technologies for real-world applications especially for electric vehicles. The latest research and application breakthroughs from pioneer institutions and industrial sectors related to all wireless energy transmission approaches worldwide have been reviewed and summarized in this chapter.

Chapter 3: derives analytical expressions of typical stationary contactless power transfer systems with formulations and proposes the methodology structure for this thesis research in order to address the technical obstacles and challenges. This methodology of implementing the simulation model and laboratory prototype tests with the preliminary natural resonant frequency probe and anticipation method originally developed in Chapter 3 has been applied to most experiments throughout the thesis. Since CPT system development highly relies on advancements of magnetic coupling, high-frequency

switching power supply, power electronics, metallic component materials, the specifically proposed research methods and techniques in this thesis are to integrate most of the advantageous aspects of these particularly relevant technologies for pursuing optimizations of CPT applications with feasibility for EVs.

Chapter 4: reports various analytically designed CPT simulation models and comparatively investigates the advantageous potentials of the optimally enhanced models with different emphases of performance metrics pursuits based on simulation results and post-stage computed outputs from both aspects of power electronics and electromagnetics. By focusing on the magnetically inductive coupling module of generic CPT systems, a range of different coupler-predominant models have been put forward for experiment, analysis and comparison in terms of fulfilling optimal system performance criteria from different perspectives. The geometrically enhanced H-shaped coupler-based CPT schematic is designed and proved to be the optimized option through this chapter for the system model establishment towards an overall optimization of CPT performance metrics. Some results-based findings are summarized in each subsection of this chapter.

Chapter 5: focuses on effectiveness of shielding, reporting different shielding materials tests and various inner shielding distance tests. The results throughout this chapter in terms of each significant determinant and emphasis have been quantitatively analysed for further exploring optimization approaches for CPT technologies applied on EV charging based on the H-shaped CPT system. These ranges of investigations are considered to fill the gaps regarding some potentially influential subtopics under CPT system optimizations especially for feasible applications on EV chassis and contactless charging. By following the methodology structured in Chapter 3 and by revising and integrating it with enhancive feedback from implementations throughout Chapter 4, some novel findings and new conclusions based on the series of experiments, result analyses and comparisons have been perceived and drawn with discussions and summaries at end of each section.

Chapter 6: addresses the effects of coupling misalignments, as well as presents groups of simulation-based CPT models with quantitative metrics analysis, from perspectives of both power electronics outputs and electromagnetic field performance. The simulation designs in this chapter accentuates the major challenges, providing some new conclusions and introducing feasibly new coupler-dominated system design ideas towards CPT

technology optimizations, in spite of foreseen limitations and unspecified obstacles regarding EMF in this topic, empirically for the laboratory prototype investigations and practical apparatus in future studies.

Chapter 7: presents a series of implemented lab-based CPT prototypes using experimental measurements and DSP techniques for extensive results analysis and discussion in spite of some inevitably foreseen limits in the lab test implementations. Following the basics of the methodology in Chapter 3, a series of variable-driven laboratory prototypes have been handcrafted for performance tests, by which some characteristic metrics have been revealed and validated for ferromagnetic core-based coupler CPT systems, despite some performance behaviours of the no-core planar circular coil coupler CPT system being not analysed thoroughly due to limitations from the laboratory setup such as data acquisition (DAQ) board sampling limits. Overall, this chapter presents a number of laboratory prototypes that could be equivalent to several optimal designs in simulations in the last chapter, providing practical CPT system performance outcomes as partial verifications for the series of analytically designed CPT system solutions by this thesis.

Chapter 8: summarizes the methodology specifically developed for the thesis, evaluates the studies in this thesis from perspectives of limitations and accentuates the main contributions arising from the thesis by discussing some major key findings based on the studies throughout this thesis.

Chapter 9: concludes this thesis and puts forward some ideas for the future scope of work in this domain.

# Chapter 2 Literature review

## 2.1 Background

Contactless power transfer (CPT) has become a major trend of bringing new possibilities of supplying electrical energy to potential applications covering a wide range of fields by allowing eliminations of exposed or mechanical contacts. The innovative CPT based technologies preliminarily inspired by Nikola Tesla [1], [2] at the late 19$^{th}$ century have been considered as new solutions of increasing reliability, performance and machinery maintenance in a broad and critical set of areas, including energy generation [3], [4], automotive [5]–[9], aerospace [10], [11], energy harvesting [14], biomedicine [13], [14], robotics [15], [16], multi-sensors [17], measurement instrumentations [18], [19] and industrial applications [20]–[29] over the past half century.

A large number of CPT technologies have been proposed with various classifications and established over the on-going research topics in electronic, electrical and telecommunication engineering. In long-distance signal transfer applications via electromagnetic waves, the contactless electrical energy transfer is also prevalently called wireless power transmitting (WPT) [30] and widely applied in radio [31], [32], television and communication systems [33], [34] in the past century. In recent decades, inductive power transfer (IPT)-based CPT methods have been introduced and rapidly developed for the increasing fulfilments of portable electronic equipment such as laptops and smart phones despite the conspicuous limitations regarding transmitting power levels [35], efficiencies [36] and safety issues [37] over the batteries [38]. Loosely coupled IPT technology could be suitable to deliver a wide power range from milliwatts to kilowatts, which determines its prevalence in the emerging small electronic device markets [39].

With considerations of current limitations and realization feasibility of applying CPT technologies to wide ranges of commercial products, the key issues of power transfer rating levels, maximum efficiencies, actual transfer distances and overall system performance at different operation conditions are required to be emphasized and investigated. In order to address the general limitations above, within the low-power CPT applications such as wireless cell phone chargers and some other tens of watts-level small

devices, the expected energy transmission can be achieved by adopting suitable control sub-systems, front-end circuits like ‘tuning’ in the transmitting unit and rear-end power electronic circuits in the receiving unit, which can eventually convert the induced AC signal to DC and regulate the voltage and current levels that can significantly fluctuate depending on the real-time inductive coil alignments in order for the entire WPT system to charge the device battery. However, the realizations to tackle the WPT challenges are difficult to reach when it comes to high-power level contactless energy transfer applications such as wirelessly charging for electric vehicles. From the initial developments of EVs to the recent CPT technologies that are being extensively explored in the literature, the following sections will deliver the fundamental reviews regarding the EVs charging and CPT technologies.

## 2.2 Basics and methods of emerging EVs charging

### 2.2.1 Conventional plug-in charging technologies for EVs

With the tendency of electric vehicles (EVs) being massively investigated as a major direction of the future transportations to reduce greenhouse gas emissions caused by traditional internal combustion engines (ICE) based vehicles [40], [41], EVs have also been identified as an opportunity to integrate renewable energy sources and to reduce dependency of oil imports for most countries. In last decades, the studies and efforts towards electric vehicles charging have been focused on the main obstacles which are long charging time, low power efficiency, low tolerance of misalignment, driving range and charging costs of both customers and hardware infrastructure suppliers.

Conventional plug-in charging electric vehicles are basically categorized into two types: pure electric vehicles (EVs) and hybrid electric vehicles (HEVs). The pure EVs manufacturing technology is the integration of up-to-date automobile engineering, electrical engineering, power electric engineering and chemical engineering, in which the electrical engineering includes the motors, controllers, power electronic converters, energy management systems and batteries. As known that the HEVs are propelled by an electric motor/generator with a series/parallel configuration and an internal combustion engine (ICE), the HEVs gain the added value from the advantages and flexibilities of a collaboration of electric motor propulsion and ICE propulsion, as well as the kinetic

energy recovery during braking. HEVs normally have more electrification components adopted than ICE vehicles [42], such as ultra-capacitors, microcontrollers and multi-sensors. In addition to the potential objectives related to ICE systems, the main challenges of HEVs propulsion systems comprise hybrid control strategies; refined modelling and simulation of the powertrain system; advanced powertrain designs and realizations, such as suitable electric machines, energy storage units and acceptable power electronic converters; power management unit. Currently, the key technique of developing HEV is the control algorithm and its optimization [42].

With the increasing deployment of plug-in charging electric vehicles over the recent decades all around the world, some internationally agreed EVs standards regarding charging plug & socket and hardware infrastructure are being introduced and formed by authoritative organizations like the Institute of Electrical and Electronic Engineers (IEEE), the International Energy Agency (IEA), the Society for Automobile Engineers (SAE), the Deutsches Institute fur Normung (DIN), the International Electromechanical Commission (IEC), the International Standards Organization (ISO) and the Japan Electric Vehicle Association Standards (JEVS). Some pioneering countries with EVs development released their first EVs standardization documents, such as a standard file named 'SAE J-1715: Hybrid electric vehicle (HEV) and electric vehicle (EV) terminology' in USA, April 1994; and a Japanese JEVS standard file named 'G105-1993 Connectors applicable to quick charging system at eco-stations' in 1993, which did represent and facilitate the initial EVs development around the world. In addition to the EVs performance per se, it is also important that the emerging EVs technologies and charging infrastructures could tend to be standardised so that customers will be satisfactory and comfortable with reduced costs of the technology and manufacturing in the near future. Based on some detailed records in the literature, it can be seen that three modes of plug-in charging for EVs and hybrid EVs had already been expected to become standardized to the public EVs charging requirements in some countries despite slight variations of plug-in ratings in amperes and internal battery capacities. For example shown in [43], the power demand and charging options for EVs in Ireland in 2010 are indicated, and it can be noticed that the maximum power rating for fast charging is 44kW with DC voltage source of 400V and peak current of 63A in early 2010s.

Table 2.1: Plug-in charging standard and options in Ireland EVs market 2010 [43].

| Level | Type | Electrical | Resulting Charge | Time | Power Rating |
|---|---|---|---|---|---|
| Mode 1 | Standard (Domestic) | 230V 16A<br>1 or 3 phase | 100% | 6 to 8 hours | 3kW to 10kW |
| Mode 2 | Opportunity | 400V 32A | 50% | 30 minutes | 22kW |
| Mode 2 | Emergency | 400V 32A | 20km | 10 minutes | 22kW |
| Mode 3 | Range Extension | 400V 63A | 80% | 30 minutes | 44kW |

The electric vehicles were firstly invented in 1834. But the rapid development of internal combustion engines (ICE) and the severe battery limitations made the EVs vanished until 1970s. In the last decade of the 20$^{th}$ century, USA, Japan and several European countries restarted the investments in plug-in EVs and hybrid EVs due to concerns caused by the energy crisis, which directly facilitated the EVs industry. By 2010, some EV systems tended to be matured for commercial productions and public use despite the energy storage unit technology limited by present development of chemistry, material science and so on. Nevertheless, the EVs and HEVs industry have been moving forward with some excellent vehicles on road, such as Toyota Prius, Honda Insight, Honda Civic, Ford Escape, Tata EV in Figure 2.1, Saturn Vue, etc. Toyota Prius represented the first commercially produced plug-in hybrid electric vehicle in the world and its 6.5Ah and 21kW nickel-metal battery can be charged by regeneration braking system. The plug-in standard charging technology was able to deliver a several kilowatts-level power output as shown in Table 2.1 by 2010.

Since 2010, higher power ratings and standardisations for plug-in EVs and HEVs were introduced by some emerging EV companies and government-led energy films, such as Tesla in USA and WestTrans projects in England. Tesla charging station could deliver maximum 120kW with its version 2 supercharger in 2017 and maximum 150kW to 200kW with the latest version supercharger technology in 2019 [44]. As shown in Figure 2.2 and Figure 2.3, WestTrans working with Transport for London (TfL) provides the latest plug-in charging facilities including high power charging pumps and EV parking space for charging at main motorway services.

Figure 2.1: On-street plug-in charger for Tata G-Wiz EV, London [44].

Figure 2.2: Parking lot for EV charging at motorway services, UK [45].

Figure 2.3: Four-pin high-power fast charger manufactured by Nissan for general EVs at motorway stations, UK [45].

Figure 2.4: Two socket modes plug-in EVs charger with different power ratings[45].

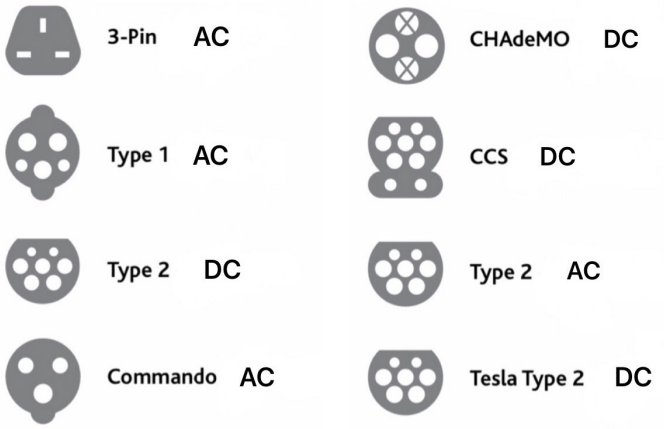


Figure 2.5: Current main plug types for EVs and HEVs [45].

As indicated in Figure 2.4, Figure 2.5 and Table 2.2, there are currently about 8 socket modes for plug-in charging and 3 main charging speeds. Rapid charging units provide 43, 50 and 120kW power to charge EV battery to 80% in half an hour. Slow charging units are normally adopted for charging at home or garage overnight with up to 3kW power and 6 to 8 hours for a full battery charge. Fast charging modes can be popularly used for public charging with 7-22kW power output and a full recharge in 4 hours. Based on WestTrans and TfL documents, there are statistically 5541 socket stations in London and its surrounding areas in the end of 2018 [45].

Table 2.2: Three main EV charging speeds in London by WestTrans 2018.

| **Three EV plug-in charging speeds** | **Rapid** | **Fast** | **Slow** |
|---|---|---|---|
| Compatible plug types | CHAdeMO – 50kW DC | Type 2 – 7-22kW AC | 3-Pin – 3kW AC |
| | CCS – 50kW DC | Type 1 – 7kW AC | Type 1 – 3kW AC |
| | Type 2 – 43kW AC | Commando – 7-22kW AC | Type 2 – 3kW AC |
| | Tesla Type 2 – 120kW DC | | Commando – 3kW AC |

### 2.2.2 Proposed CPT charging versus plug-in charging

In the field of automobile, electric vehicles (EVs) and hybrid electric vehicles (HEVs) have been rapidly gaining popularity in the past decades due to a pursuit of greener and cleaner energy replacements. There have been numerous studies over the CPT solutions and its feasibility in the literature, which unavoidably leads to different naming and abbreviations with ambiguities. The major technology definitions and names based on inductive phenomenon include contactless power transfer or transmitting (CPT), inductive power transfer (IPT) [46]–[48], wireless power transmitting (WPT) [30], [49], contactless energy transmission (CET) [50], unplugged charging, plug-less charging, magnetic resonance, magnetic induction, electromagnetic resonant coupling, etc. In this thesis, the name WPT is more often used to refer to small devices with lower power ratings whilst the names CPT and IPT refer to general induction based contactless charging for all equipment including electric vehicles. CPT can generically include all the different names and classifications mentioned above.

Plug-in EVs and HEVs have inherited weaknesses and drawbacks: charging infrastructures are sensitively vulnerable against extreme weather conditions; charging inconvenience caused by long cord; risk of forgetting that an EV is plugged when the charging is complete; connector compatibility caused by different plug types from different EV manufacture standardizations; risk of electrical shock by high voltage and current; vandalism concerns like connector outlet blocked and cord stolen; etc. [51], [52].

Contactless power transfer (CPT) technologies, by contrast, are supposed to provide more advantages: convenience for customers without hassles of plugging and unplugging

before and after charging; high tolerance to various climate conditions; no risk of cord connection failures or electrocution; no compatibility issues on plug types as long as the parking position is within accepted area for satisfactory mutual induction phenomenon to occur [53]; lower vandalism due to the buried transmitting module into the ground and no outlets exposed; opportunity to build more feasible autonomous parking system as some car manufacturers like Hyundai have launched a CPT automatic valet parking concept which is expected to allow the EV to be automatically moved to customer-pointed locations after a full recharge and wait for pick-up, as indicated in Figure 2.6 to Figure 2.9 [54]; etc.

Figure 2.6: Contactless charging concept proposed by Hyundai 2019 [54].

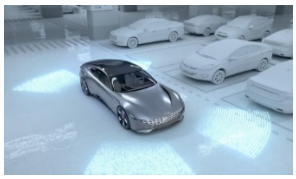

Figure 2.7: Autonomous re-location after a full battery charge [54].

Figure 2.8: Driver calls for the EV [54].

Figure 2.9: EV autonomously returns to the expected location of the driver [54].

### 2.2.3 Development prospects of EVs charging

Although the contactless power transfer (CPT) technologies based electric vehicle charging has several advantages and potentials over the conventional plug-in charging, some limitations of CPT have been objectively pointed out as ongoing study topics: low efficiency issues; heat generation on the coupling coils; more electric energy consumption; high costs of infrastructure and maintenance [55]; challenging establishments on suitably complex circuitry including control units [56], [57] and compensation options; potential concerns on magnetic radiation [58] and electromagnetic compatibility (EMC).

The automobile engineering world has been concentrating on addressing all the drawbacks of both plug-in charging and contactless charging in order to implement a

transformation from fossil fuel dependency to zero carbon emission in this industry. In the meantime, from emission and propulsion power point of views, the hydrogen fuel cells hybrid electric vehicles (HFCHEVs) have been considered to have potential to gradually replace the traditional energy sources [59] in the future. Hydrogen fuel cell is a new type of energy equipment and is different from gasoline and batteries, which could be integrated with other EV technologies and high power density devices like lithium-ion battery and ultra-capacitor to produce maximum energy efficiency, electric propulsion, system reliability, and optimum driving range with reasonable cost and minimum emission for future use [60].

From an aspect of customer experience and convenience, the contactless power transfer based electric vehicles have been categorized into two types: stationary CPT charging and dynamic CPT charging/on-road charging. Stationary charging is relatively more feasible for both realization and commercial use. However, dynamic charging technology has far more technical difficulties and infrastructure challenges. The Hyundai automated parking and charging concept shown in Figure 2.6 to Figure 2.9 could represent one of expectations in the EV future [54]. There are more detailed literature reviews on both stationary and dynamic CPT charging for EVs in the following sections and the research implements in the thesis are focused on stationary CPT investigations.

## 2.3 State of the art of the CPT technologies

### 2.3.1 Theories and main categories towards CPT

Charging electric vehicles is of great importance since the plug-in pure electric vehicles became increasingly accepted by the commercial vehicle markets worldwide during the last decades. Methods of plug-in charging still have drawbacks to be addressed although numerous investigations have been carried out mainly on energy storage system [20], [61] and battery lifetime extension [17], [26], along with the development of advanced semiconductor technologies [62], in order to optimize the holistic electric vehicle performance. Nevertheless, in this thesis, the investigation emphases will be on the actual electromagnetically analytical designs, the relations between electronically theoretical

performance and real-world magnetic field generated performance of the contactless power transfer (CPT) module of the proposed prototypes.

Regarding the main theories and methods, based on power rating levels, energy transmitting range and electromagnetic mechanism, the CPT technologies can be categorized into photoelectric, radio frequency (RF) or radio waves, laser, microwaves, inductive coupling and magnetic resonant coupling in a broad sense [63].

Based on energy transmitting distance, the contactless power transfer (CPT) could be categorized into two types: far field and near field methods. In radio frequency identification (RFID), the two coils based CPT system is considered as an electromagnetic field antenna due to its capability of responding to both magnetic and electric fields within it [31], [32], [64]. Generally, if energy transmission distance is longer than the wavelength of the electromagnetic wave, the CPT system is considered as an approach of the far field, such as RF, microwave, laser and photoelectric [12]. Whilst induction-based loose coupling and magnetic resonant coupling can be categorized into near field methods. Typically, frequency ranges of near field methods are between kHz to MHz levels while far field applications have much higher range of frequency corresponding to GHz levels, lower power ratings and transmission distance of couple of kilometres [23], [65]. Different from the ideal transformers with high coupling coefficient at 50 Hz, the actual CPT system for EVs charging should be working at kHz to MHz levels with loosely coupled induction [66]–[69] and tens of kilowatts level power requirements, which determines different theories, methodologies, numerical analysis, prototyping methods and model verifications.

Thus, CPT systems for EVs are more like an overlapping topic in between high-frequency (HF) antennas with low signal energy transmission [70] and low-frequency (LF) transformers [71], [72] with high power transfer from electrical and electronic point of views [73], [74]. From electromagnetics point of view, CPT systems for EVs tends to be a case of loosely coupled induction with centre meter level air gaps, requiring more studies related to electromagnetic field characteristics and parameters like magnetic flux density, magnetic field strength, real-time flux line distributions, actual flux linkages, etc [75]. Therefore, the CPT for EVs is supposed to be discussed from aspects of both the power electronics and electromagnetics with respects to theories and methods, which

could be also regarded as one of the innovative methodologies leading the investigations of this thesis.

### 2.3.2 Applications of contactless power transfer technologies

Contactless power transfer technology have shown its wide range of advantages in real world applications until present, especially in low-powered equipment as the flexibility, controllability and convenience could be maximized without electrical connections and with expected distance or medium, contributing to many advanced engineering applications such as consumer electronics, factory automations, medical implants, lightings, defence systems, instrumentation test systems, electric vehicle public transportations [15], [76]–[79] and dynamic automotive battery systems as one of the long-term ultimate aims [80], [81].

***(a) Biomedical implant applications***

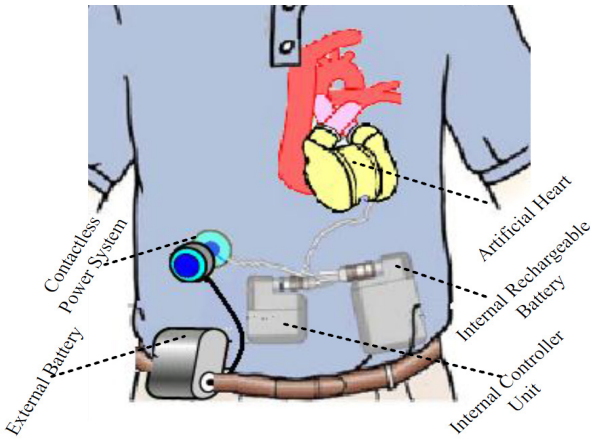


Figure 2.10: A CPT based artificial heart [82].

With resonant coupling based CPT approaches, the biomedical equipment with low power of hundreds of millwatts has been applied into patient's body as implants to reach some medical purposes like neural monitoring, pressure monitoring [83], heart rate regulatory scheme [84], temperature measurement [85], human intestine diagnosis [86], etc. As depicted in Figure 2.10, an inductive coupling based configuration for an artificial heart prototype was introduced in 2007 with a distance of 3 cm between the internal coil under the skin and the external coil mounted outside the human body. In tests of a wireless energy transfer medical implant in Figure 2.11, the implantable load received about 102 mW power at 13.56 MHz with control units and communication setup.

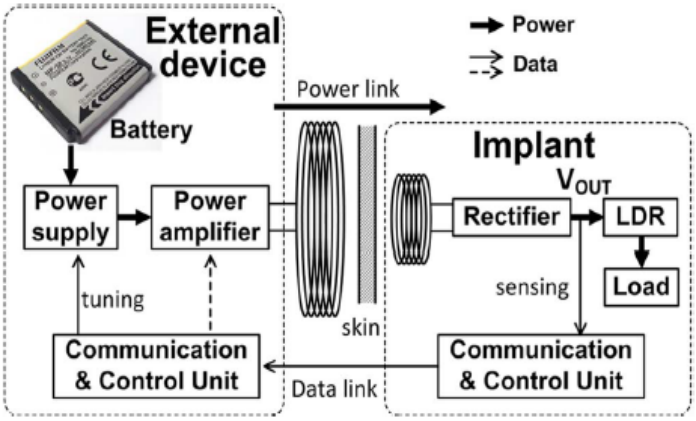


Figure 2.11: CPT scheme for medical implants [87].

***(b) Rotating equipment***

In rotation based industrial applications such as wind turbine based energy industry, the traditional contactless electrical power transmitting methods have been implemented for a few decades [88]. Also, some electrical machines like drill machines and magnetic micro-machines need to power rotary loads with avoiding physical and electrical connections due to impossibility of deploying wires and cables in continuous rotation operations.

***(c) Low-power devices***

With the popularity of portable equipment in the past years especially since the 21$^{st}$ century due to electrochemistry, smart device and microprocessor advancements, some battery based personal devices for instant communication and complex computing purposes have shown their advantages [38]. CPT based contactless charging for mobile phones have recently been becoming favourable by customers worldwide despite some challenging issues like over-current, temperature excess and some other difficulties which could be neglected and tolerated within low-power watts-level CPT applications. Nevertheless, contactless charging or wireless charging is preferred in mobile phone industry due to its main pros: no charging wires between the phone and the charger pad; no risk of electric shock caused by wet surroundings; possibly able to charge multiple low-power required devices at the same time. For instance, some pioneers like Huawei have announced that their latest product named supercharger is able to deliver up to 15 W for European market based models [89] in Figure 2.12 and 27 W for Chinese market-based models in Figure 2.13.

Figure 2.12: Wireless charging pad by Huawei and Qi standard - European market version 2019 [89].

Figure 2.13: Huawei supercharger model - Chinese market version 2019 [89].

Some inherited limitations and challenges are still required to be addressed even in low-power CPT devices, which are over-voltage, under-voltage, over-current and overheating problems. Technically, these issues are caused by inductive coupling level and largely dependent on how the secondary coil in the receiving device is positioned onto the charging pad with the primary coil in it every time. As how to perfectly put the phone onto the charging pad at the exact centre point by customers is uncontrollable, in order to overcome these issues from the manufacturer side, Huawei is trying to insert a mini radiator fan and control circuits into its product illustrated in Figure 2.14 to provide temperature protection once the coupling coefficient is really low causing the high current on the primary side namely the charging pad overheating harzard. This technique which theoretically seems to work is just proposed but still waiting for the actual feedbacks regarding heating issues from the customers by time as the proof of effectiveness. Also, to definitely avoid overheating and over current risks, the wireless charger cannot produce high-level power ratings over tens of watts at the present, which is corresponding to the power rating challenge in the investigations of the entire CPT technologies.

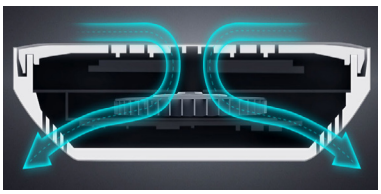

Figure 2.14: Radiator fan to avoid overheating [89].

***(d) Medium-power household devices***

Household applications as daily appliances are also related to contactless power transfer methods with low-power or medium-power level transmission requirements. Charging without wires shows the attractiveness and flexibility of CPT technologies in addition to a better and compact appliance appearance. Mainstream examples of the household CPT applications can include laptop charging, portable power bank charging, coffee machine,

inductive toothbrush, heating system, shaving machine, lighting [90], movable LED TV monitor [91], etc.

***(e) Public transportation systems***

Since the first electric vehicle as public transportation was invented in 1834, a series of electric trams and trains were massively produced in USA, UK and mainland Europe in the last decades of 19$^{th}$ century. Unfortunately, the electric vehicles vanished for about half a century since 1920s as the internal combustion engines were rapidly developed and electrochemistry regarding battery had not gained optimistic advancements. Since 1970s, the electric vehicles was re-emerged as some countries started suffering from energy crisis, after which the electric vehicles had been developed dramatically and some countries like USA and United Kingdom launched national research and legislated development laws over EVs. Gradually, in public transportation systems of some pioneering countries, the electric brush trams, trains and buses were adopted widely. Figure 2.15 shows a traditional tram in Europe.

Figure 2.15: A conventional electric tram in Portugal in 1990s [91].

Since the beginning of 21$^{st}$ century, the pure electric vehicles and hybrid electric vehicles have been developed rapidly due to the advancement of large-scale high energy density battery. Some electric buses have gradually replaced traditional brush trams in urban areas of some countries. As shown in Figure 2.16 and Figure 2.17, pure battery electric buses, hybrid electric buses and new generation charging infrastructures have been adopted for public transportation systems in some countries and districts such as in China, Switzerland and California of USA.

Figure 2.16: A battery electric bus at a charging point [93].

Figure 2.17: A hybrid electric bus being charged via stretching conductors [94].

Due to the potential advantages of contactless power transfer (CPT) applied in public transportation systems, such as economic aspect, reliability, no needs of brushes and conductive cables, the CPT technologies based transportation approaches have acquired a lot of attractiveness. For instance, the high speed train Maglev in Switzerland has been conceptualized with CPT technologies and numerically modelled [20], [94], as illustrated in Figure 2.18.

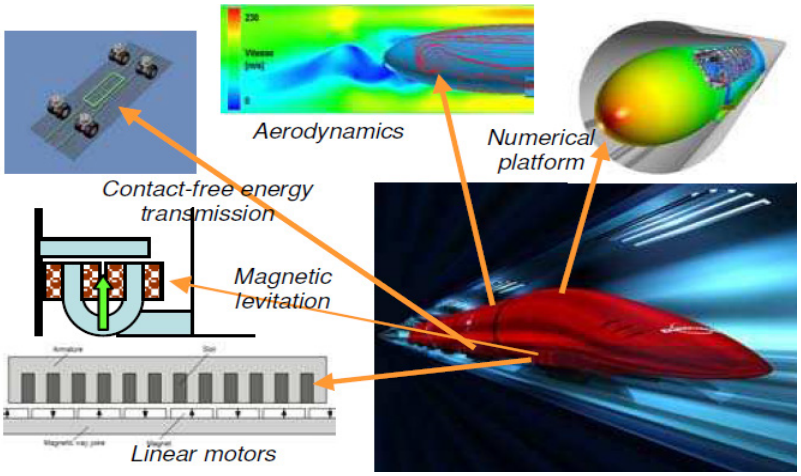


Figure 2.18 The proposed Swissmetro Maglev high speed train project [20].

### *(f) Electric vehicles with CPT realizations*

In the recent decade, the driving range of pure EVs with zero emission target has become a popular topic as the massive battery requirement for longer distance travels means higher vehicle cost and longer time of recharging periods. If the CPT technologies could be applied into wider public charging infrastructure coverage, either stationary or on-road CPT charging solutions could be an alternative to reduce EVs weight, size and energy storage unit costs in the long term. Fortunately, with progressive success of low-power CPT charging applications proposed to be commercially produced in the past decade, hundreds of kilowatts level high-power CPT charging techniques for EVs are more and more anticipated to be an optimally suitable solution for recharging EV batteries [95],

providing higher propulsion and delivering continuously longer driving range in the next generations of the EVs. The idea of deploying inductive coupling for EVs has acquired a lot of attentions in the last decade due to the contributions and advancements of power electronics, switching power supply, semiconductors, microprocessors, electrochemistry, material sciences, control technologies, electromagnetics and so on, despite many challenges to be addressed including EV manufacturing integration with CPT system under the chassis [96], infrastructure difficulties [97], system maintenance on both vehicle and transmitting ground sides, actual CPT performance with real-time coupling on real-world road [98], etc.

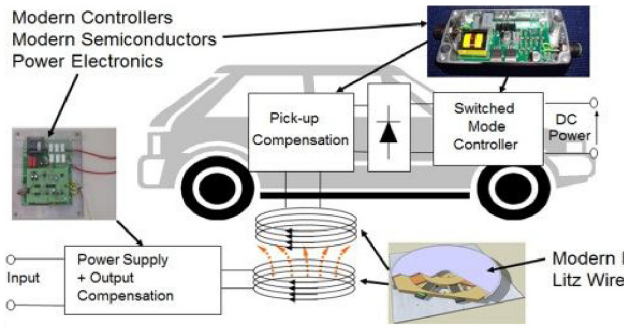


Figure 2.19: An IPT based CPT system for stationary EVs charging [52].

In order to ensure the realization and enhance the sustainability in transportation sector with the emerging CPT ideas, the potential knowledge gaps and optimal solutions can be explored and proposed as leading attentions from both short term and long term perspectives. From short and middle term aspects, contemporarily the stationary CPT charging solution based on inductive power transfer (IPT) has been developed at laboratory level which are expected to be a first step for the tests of commercial realizations in the short-to-mid-term future. The stationary IPT Charging technology was firstly developed in transportation areas in 1990 [55]. Due to the high costs limitations of automotive side and infrastructure side, the Stationary IPT charging application has just been revisited in the recent decade. Figure 2.19 is a brief system illustration of IPT based stationary charging method [52]. From the long term perspective, the idea of dynamic EV charging was proposed and is now under development at the same time. A pilot proposition and test related to dynamic charging and road vehicle automation have been found in 1980s and 1990s in California [99]. Further detailed investigations upon stationary and dynamic charging methods, theories and implementations are to be presented in the following sections of the thesis.

### 2.3.3 Stationary CPT for EVs

As briefly summarized in the previous subsections above, the mainly significant performance parameters and objectives of a satisfied CPT system are power transfer rating level, maximum charging distance, maximum system efficiency, charging tolerance to misalignments, system size and weight. The power level can refer to how long one full battery recharge would take for a full driving range of EV. The maximum charging distance determines the vehicle chassis structure for achieving contactless charging. The system efficiency is the overall comprehensive parameter of the entire system, which illustrates how electrically efficiently the CPT phenomenon operates from AC power supply end to DC battery end for the EV. Charging tolerance could reveal how the horizontal and longitudinal misalignments caused by EV drivers' parking habits impact the actual coupling charging and power delivered between primary coil and secondary coil, which also indicates how the flexibility and advantages of CPT systems are when compared with conventional plug-in charging methods. The system size and weight could be subject to the actual energy density of the battery products utilized and could present the convenience of the CPT deployment when mounted on EVs, which is not quite a topic and priority for the investigations in this thesis compared with other main objectives.

As introduced before in Section 2.2.3, it is more convenient to categorize the CPT technologies into two major types: stationary and dynamic CPT charging, when it comes to the actual applications in real-world. The stationary CPT technologies could comprise of loosely inductive coupling and electromagnetic resonant coupling depending upon different operating frequency range levels and capacitive compensation adoptions, which are both based on inductive coupling phenomenon and most of the time are collectively called inductive power transfer (IPT) in the literature [75], [100].

***(a) Principles***

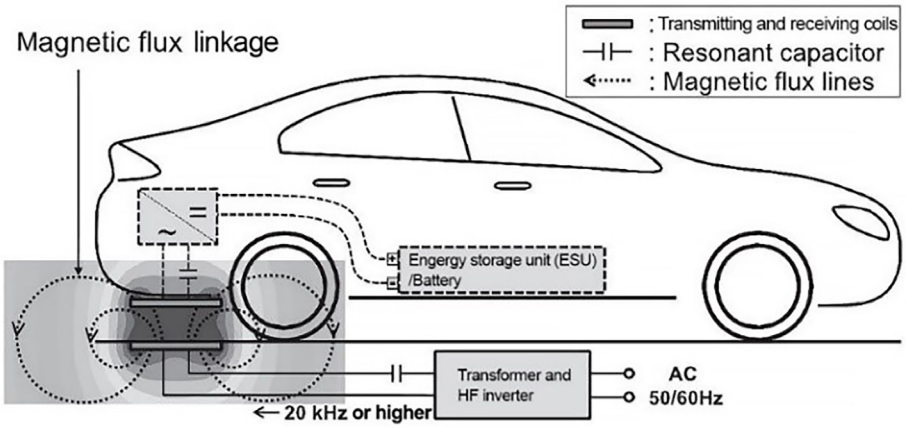


Figure 2.20: A loosely inductive coupling and magnetic flux linkage based CPT system for stationary EV charging.

For the technical background and fundamental principles of contactless power transfer systems, the Figure 2.20 and Figure 2.21, along with Figure 2.19, illustrate the typical systematic diagram and basics of IPT based stationary CPT systems.

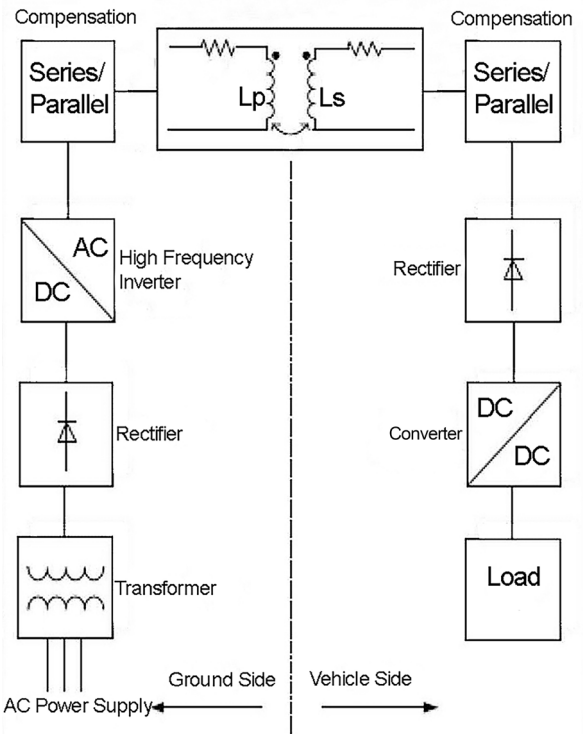


Figure 2.21: Schematic of a typical CPT system.

When the IPT charging system is activated by the signal from EVs reaching over the particular charging platform, the power supply under pavement will provide 230V AC mains to a transformer converter which could convert and rectify the high voltage power

to required range of DC voltage. Then, a high frequency (HF) inverter converts the low frequency AC power to HF AC power. Before being sent to transmitting pad, the HF AC power is supposed to go through the compensation module [66] which is considered to optimize the transformer loss factor. Contactless power transfer coupler transmits the power to the vehicle side via effects of magnetic flux linkage namely inductive phenomenon. After receiving the induced AC power, the compensation circuit and rectifier or AC-DC converter would operate on the power then the DC to DC converter of direct conversion method converts the energy to a required voltage for battery energy storage in the end of the whole CPT system. Regarding the power supply at the very front end of an entire CPT system, the further design or re-enhancement of a switching power supply functionality is not quite a focused part for the investigations in the thesis but still worth being mentioned here for a consistency of the whole system introduction. At a basic level of a real-world CPT system, a power supply requirement before the coupling module as depicted in Figure 2.21 is supposed to include an input rectifier and filtering section, an H bridge inverter section and current controller if necessary. Besides, compensation topologies are a subtopic in the theories and methodology chapter later in the thesis.

***(b) History of CPT for EV***

In 1887, Nikola Tesla invented induction machine that converts electrical power to mechanical power from a stator to a rotor, which inspired Tesla again to come up with the idea of wirelessly transmitting energy via large air gaps based on the principle of electromagnetic induction machine that was just technically and commercially proved by himself. In 1901, the concept of wireless power transmitting (WPT) was firstly proposed and was believed by Nikola Tesla that it can be used to transfer electricity even far from America to Europe with an electromagnetics based giant tower named Wardenclyffe tower in USA, which was terminated by US government in 1917 and proved that the actual coupling distance is a huge obstacle to WPT efficiency and effectiveness. Since then, some experiments were implemented in order to wirelessly transfer power to a moving train with coupled energy but still went unsuccessful, which on the other hand proved that only low-power signal could be transmitted over large distances such as radio frequency (RF) signals, microwaves, etc. A conclusion was made at that time that electrical power wirelessly transmitted is practically impossible from a power point of view throughout the rest of 19$^{th}$ century [101]. Whilst on the ‘signals’ side, the sciences

over communication systems, non-contacted current sensors and inductive antennas had been significantly developed based on Maxwell equations, laws of Ampere's and Faraday's and attempts of Nikola Tesla's WPT.

With the attempts of powering EVs inductively since 1970s, stationary CPT topics were re-proposed at the same time. In 1986, Kelly and Owens [102] designed a wireless power transfer method for a low-power level aircraft entertainment system with 38 kHz currents going through wires under the carpet successfully coupling and delivering 8 W power for each passenger entertainment platform despite very low transfer efficiency. In 1990, this wireless aircraft entertainment system powering innovation named 'regulator for inductively coupled power distribution system' was enhanced with a voltage controller and was patented by Turner and Roth for Boeing aircrafts in the US [103].

In the beginning of 1990s, as academic pioneers, Boys and Green developed a systematic stationary CPT technology and patented it in the US [104] with the first definitional names in this area: inductive power transfer (IPT) or inductively coupled power transmission (ICPT) system, which includes an elongate inductor, parallel capacitive compensation, paralleled pickup coils, decoupling and voltage controllers [105]. This complete IPT system was modified and improved with enhanced control circuits by Boys, Covic and Green in 2000, which resulted in an output of up to 600W with a maximum voltage of 600V at 10 kHz by the system power supply [106] and, thereby from the power point of view, it was apparently unable to sufficiently power tens of kilowatts level EVs or to accomplish hundreds of kilowatts level required fast high-power battery charging cycles of EVs.

Over the past 20 years, the performances of different stationary CPT approaches were significantly improved. However, most of the research development were achieved in laboratory rather than industrial level applications. In 2007, MIT WiTricity project group made a demonstration and claimed that their wireless power transmission system can lighten a 60 W bulb over 1 to 2 meters at 9.9 MHz with a transfer efficiency of between 30% and 90%. This demonstration itself was convincing but the measured results were unavoidably doubtful when analysed according to previous studies and experiments over the past decades in the literature. Nevertheless, the development of stationary CPT technologies has been facilitated dramatically by the academic interests and the

commercial market requirement of EVs towards pursuits of zero emission transportation era in the 21st century.

***(c) Current status of inductive coupling-based CPT technologies***

Among the various previous studies and reports in the literature, it can be noticed that numerous subtopics have been covered and many breakthroughs have been made towards the CPT system performance optimization and the commercially productive realization for EVs. A variety of applications based on inductive power transfer principle have diversified as briefly introduced before in Section 2.3.2, the actual technical challenges have been becoming more noticeable at the same time, especially for the stationary and dynamic high-power required contactless charging for practical EVs. Nonetheless, the inductive coupling based CPT technologies and the derived techniques are promising. This subsection briefly reviews the development of stationary charging for EVs over the past decade as well as presents state of the art of stationary CPT method.

More recently, some research institutes, university research groups and industrial manufacturers have been playing pioneering roles in this field and making new knowledge contributions from different aspects.

Oak Ridge National Laboratory (ORNL), as a bullet research institute sponsored by the US Department of Energy in the CPT area, has carried out some practical experiments empirically resulting in some analyses and conclusive methods in the national research centre lab in Tennessee. ORNL focuses on grid-tied high frequency power inverter, grid side regulation converter, control system and loosely coupled coil design. Based on the new ultra-thin silicon IGBT technology, an experimental power inverter and a grid-tied power converter were designed and tested by ORNL in 2012 [107], which aims to minimize the mass and size of the coil, rectifier, filtering, wires, and other components mounted on the secondary side of vehicle chassis [108].

A 5 kW output inductive stationary CPT system was designed by a group of the Utah State University, in which an external 37W power required field-programmable gate array (FPGA) sensors or controller was added to the CPT system for the dual-side control. Circular coils and LCL converter were used in this system. Practical experiments in this study were used to validate the effectiveness of the proposed schematic, by which the

researchers claimed that the system can maintain a very optimistic efficiency from the grid side to the load despite of too many ideally assumed conditions that were made in the derivative analyses and post-data processing [109]. Nonetheless, a dual-side control method in this report was proposed to the inductive coupling system as an innovative way.

A researcher of the University of British Columbia deployed a set of magnetic gears as transmitting and receiving magnets, an electric motor on the ground side and a generator on a car chassis to realize a wireless power transmitting, which is implemented and accomplished via coupling magnetic gears and driving the generator on the car to power the vehicle motor. It was claimed that this system could reach a maximum transmission part efficiency of 81% with a transferred power of 1.6 kW at a very low frequency of 150 Hz [110]. Regarding the feasibility and realization by gear coupling and re-generating electricity in a real-world EV charging application, the proposed system seems to be doubtful in this study as the additional process of driving the secondary generator via the magnetic field stored energy for inductively producing the electricity itself would unavoidably introduce more power losses eventually contributing to a further reduction of overall system efficiency ratio.

Two researchers of the Setsunan university in Japan conducted investigations on several different coil dimensions, in which it was found that three-dimensional horn-shaped antennas as transmitting and receiving coils could lead to higher power transfer efficiency than patch and array antennas whilst the patch antennas in a nature of planar could be more practical and suitable for EVs chassis CPT system installation. Thus, the size and operation performance are to be a trade-off when considering the entire stationary CPT system from design to actual fabrication onto EVs. In this study [111] of the University of Setsunan, the system operating frequency is between 1.2 Ghz and 2.45 GHz, which is in a range of HF. Besides, it is claimed that the array antennas performs with lower transmission loss than patch antennas at 2.45 GHz and with a transmission efficiency of over 20% despite of unknown actual power transferred through the entire system.

A team of Tokyo University contributed numbers of reports to the field of CPT technologies in the past ten years. Based on the method conceptualized and named with electromagnetic resonant coupling by MIT WiTricity in 2007, the research group of Tokyo University started studying the feasibility and technical performance of this

method with theoretical and practical depth since 2009. Different from the previous inductive power transfer (IPT) methods and concepts, the proposed electromagnetic resonant coupling technology emphasizes on impedance matching [112] in order for the whole system to approximate to magnetic resonance, by which predictably the energy transfer efficiency of the CPT system could be optimized and theoretically the actual power rating to the load could be very satisfactory. This group of researchers considered the CPT technology as small-sized helical antenna transmission topics and pure electrical equivalence problems [64], [113], which led to a convenience of investigating the system with the antenna scattering parameter (S-parameter) analysis and the direct experimental methods of using a vector network analyser (VNA) [114] to measure the outputs at a usable frequency of the industrial, scientific and medical (ISM) band – 13.56 MHz [115]. Significantly, the impedance matching theory contributes to the theoretical structure construction of CPT technologies, especially for the magnetic resonance accomplishment in this case. Whilst, the over-idealized impedance matching circuits used in this case neglects the non-linear magnetic circuit part in the coupling module, which determines a lot regarding how the actual electromagnetic flux distribution contributes to the real-time coupling phenomenon over the air or core based distance with non-linear magnetic characteristics in nature such as B-H curves and hysteresis effects in the electromagnetic field. Thus, the absolutely equivalent circuit method in the case of this research group may be not sufficiently appropriate and suitable for a CPT system scenario. Besides, working at megahertz level operating frequency and considering the system as a pure antenna problem especially with traditional scattering parameter analysis may be not proper as firstly the real-world CPT systems are not milliwatts level ‘signal transmission’ topics from power point of view, and secondly the VNA measurement with a two-port network S-parameter method may not be adequately applicable any more when it comes to kilowatts level electrical power issues despite of resonance status. Nevertheless, the University of Tokyo team did make contributions towards the knowledge gaps at that time in the last years of the first decade of 2000s. With the same methodology, a battery hybrid energy storage system was also studied by this research group, by which it is claimed that both the transmission side power control configuration and the receiving antenna side controller were designed to achieve satisfactory power charging without communication units between transmitting and receiving antennas [30].

However, the Tokyo University research team has turned to study the CPT systems in a loosely coupled frequency range in the order of kilohertz [116] rather than megahertz any more since 2014. More practically in laboratory and realistically in applications, the researchers started to mainly investigate the circuit topologies, transmission coil types, control methods and capacitor compensations in depth, pointing out that the effectiveness of magnetic resonance to the wireless power transfer coupling purpose and proving that the new methodology contributes more to the system efficiency and power transfer rating issues [117] with results of 40-90% and 60 W, respectively. Some of the major coil designs are to be further studied in the next subsection 2.3.3(d), in addition to the main investigation topics of the thesis.

Nonetheless, several technology driven companies and manufacturers in industry have also been making contributions to the field of emerging wireless power transfer technologies for stationary charging from multiple levels and more aspects over the past twenty years, such as WiTricity Corporation, Bombardier, HEVO Power, Qualcomm Group, Conductix-Wampfler etc.

As mentioned before in the last subsection, WiTricity as a corporation was founded by a group of MIT researchers to investigate and invent wireless energy transmission terminals for commercial purposes since the first demonstration in 2006. With the proposed resonant coupling method, WiTricity team designed a CPT system with tuned coils to wirelessly transfer power which was claimed with 60 W to 3.3 kW over one meter at 145kHz operating frequency [118]–[121]. Afterwards in 2011, some other researchers in East Asia carried out resonant coupling simulations based on WiTricity designs and studies the position tolerance of the method, by which it was claimed that the simulated WiTricity model showed a maximum performance at 2.34 MHz with a coil distance of 50 mm [39]. However, in this report [39], a real power rating and effectively convincing system efficiency were not derived and discussed in details although the peak values of output voltage magnitudes corresponding to various coil distances and frequencies were recorded and compared.

Bombardier Transportation company, a leading technology and solution supplier in Germany, tested their wireless static charging system called PRIMOVE for buses in 2013. As part of the pure electric public buses, the PRIMOVE system has been integrated with

improved EV system via this project. Bombardier designed their own control unit named ‘vehicle detection and segment control’ (VDSC) and interface called ‘supervisory control and data acquisition’ (SCADA) subsystems at industrial levels [122], which seems to be feasible and successful in the real-world application in spite of insufficient technical reports or data released and published yet.

HEVO Power is another technology provider in the US which aims to innovate a wireless charging system for public transportations. This company proposed a stationary system requiring a fixed operating frequency of 85 kHz and targeting at transferring up to 10kW power over an air gap of about 30 cm. It was claimed in 2014 that the receiving side prototype mounted on the vehicle weighs 11 to 23 kg and that the heating problems on both the vehicle and ground charging sides can be prevented by their parking zone design and mobile phone app monitoring [123].

Qualcomm, a pioneering company dedicated in communication technologies, informatics and lately emerging wireless power transmission, has also been implementing research programs towards an optimal wireless charging equipment for both low-power electronic devices and high-power charging applications. Qualcomm Halo is a specific project regarding achieving CPT charging for EVs. Qualcomm aims to realize three options of charging power ratings for future customers in their report in 2013, which are 3.3 kW, 6.6 kW and 20 kW and targets at very high and stable efficiency rate of over 90%. With IPT method, proposed BiPolar and DD coil designs, Qualcomm claimed that their Halo IPT system used 20 kHz operating frequency in the simulations and trial runs of this prototype would be implemented in East London in 2011. It can be noticed that, from the research report [124] in collaboration with Auckland University, Qualcomm Halo project is very practically profound and technically convincing with strong simulation supports and mathematically theoretical representations by themselves and other researchers [125]. Besides, the double D method has been patented by Qualcomm years ago from commercial point of view.

Furthermore, Conductix-Wampfler, another technology company in CPT research, is very dedicated in investigating inductive power transfer (IPT) techniques and already patented their own IPT trademark in the US. This company focuses on developing IPT system for automated guided vehicles (AGV) in warehouse applications with robotics

[93], [126]. According to their reports until 2018, Conductix-Wampfler aims to produce the power supply module, charging mat and power pickup with charging manager unit. Technically, the power supply AC voltage can be one-phase 100-240 V or three-phase 380-480 V at 50 or 60 Hz, the output power and current can be 1.5 kW and 5 A, respectively. Their power pickup namely receiving coil module with charging manager subsystem aims to inductively receive about 55 V induced voltage and 10 A current to send to charge a 24 V DC battery with 12 A and 144 W after the power regulation, DC to DC converter and current monitoring of the charging manager subsystem. The dimensions of power pickup pad and charging mat are H 80.3 mm × W 222 mm × D 216 mm and H 7 mm × W 435 mm × D 180 mm, respectively. The aim of the charging distance is 10 mm. It can be seen that Conductix-Wampfler shows not only respectful ambitions but also technical skills in the industrial applications for AGV in warehouse systems.

***(d) Proposed designs of coupling coils***

The coupling module design especially the coil geometry design, as the most important part of contactless power transfer systems with regards to the overall system outputs and performances, plays a significant role in order for any types of CPT architectures from both the power electronics and electromagnetics perspectives to eventually address the three main objectives: electrical power transfer ratings of the system; efficiencies including overall system efficiency to the load end and coupling part efficiency; CPT air gaps namely charging distances. Therefore, it is very worthwhile proposing, analysing and evaluating various coil designs to comprehensively implement the investigations upon CPT technologies. In this subsection, the proposed coil designs in the literature until present are to be enumerated and briefly analysed.

◆ Circular coils

Until present, the circular coil designs have become the most common and acceptable approach for various power-lever devices such as wireless charging pads for smart phones and many other portable electronic products. Also, as for the initial feasibility for high-power level EVs contactless charging, circular coil with its derivative topologies has been focused and developed towards the optimizations and some of them are originally derived

from traditional pot cores, according to the reports in the literature [127]–[129]. Within the current studies and even commercial level applications, most of the circular coil designs are coreless especially for low-power applications [130]–[132].

As known in transformer theories and applications, the ferromagnetic cores like ferrite cores are deployed to prevent excessive energy loss into surrounding air and materials due to existence of magnetic leakage. And with the fairly tiny air gap design crossing the core structure instead of completely enclosed core loop, the core windings can have minimum disadvantages when effects of proximity occur due to hysteresis loss and eddy current loss. Similarly and theoretically, deploying ferromagnetic cores like ferrite in CPT coil designs is able to constrain magnetic flux lines to expected paths and to shape the actual electromagnetic field in order to enhance the effectiveness of coupling, which consequently improves the wireless energy transfer system performance.

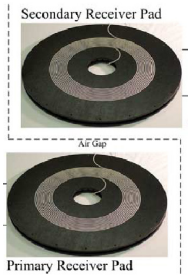


Figure 2.22: Circular coil design with ferrite pads [109].

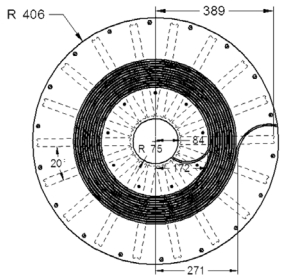


Figure 2.23: Dimension of a circular coil with ferrite pads [109].

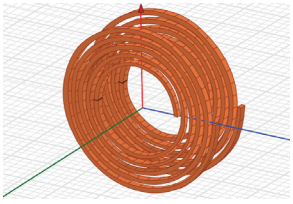

Figure 2.24: Simplified planar circular coreless coils [133].

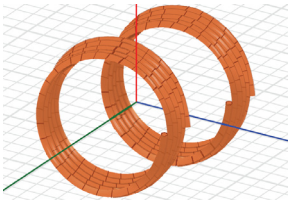

Figure 2.25: Simplified coreless solenoid coils [133].

In most small-scale low-power CPT systems for portable electronic devices like cell phones, wireless charging pads with coreless coils can acquire more popularity due to pursuits of relatively thin and lighter design from real-world customers, certainly under acceptable conditions such as charging power rating and basic efficiency to be at least satisfied by manufacturers' efforts on advanced electronic circuitry and control unit designs. However, high-power CPT applications are more supposed to need cores to

assure the satisfactions of the overall system performance [75], [134], for instance, the circular coil couplers with solid ferrite pads could form the flux distribution much better. A design of circular coil with ferrite pad is shown in Figure 2.22 and Figure 2.23 [109], in which the dimension is in mm. And two coreless circular coil designs are illustrated in Figure 2.24 and Figure 2.25 for comparisons.

In addition, the derivatives of circular design have also been depicted here in Figure 2.24 and Figure 2.25 [133]. In this thesis, the former design could be called a design of simplified planar circular coreless coils and the latter one could be called a design of simplified coreless solenoid coils, with a categorization nomenclature based on the characteristics and natures introduced above. The model in Figure 2.26 could be named a design of circular ring coreless coils, which illustrates expected magnetic flux lines and distributions in 3D magnetic simulation. It can be seen that with no ferrite pads or cores, the flux lines flow through the coils showing more naturally and smoothly curved paths in air, which can be different from the circular coils with shaping effects by ferromagnetic materials such as ferrite pads used on the external sides.

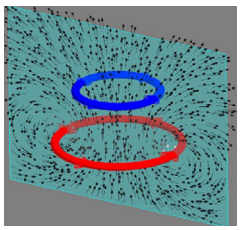

Figure 2.26: Circular ring coreless coils with expected magnetic flux distributions [82].

◆ Planar square coils

Geometrically, square windings can take better advantage of the space under the chassis of vehicles for system installation. Some reports also have already presented the designs regarding square coils and the derivatives and practically tested. The Oak Ridge National Laboratory (ORNL) in the US proposed the detailed designs of their square coupler shown in Figure 2.27 and Figure 2.28 [98], [107], [108], for which a category name of ‘planar square coil without a cavity’ can be applied based on the reviewed designs and categorization nomenclature in this thesis. The square coils of ORNL are single-layered with multiple circles of windings as illustrated and the winding wires are made of copper. No ferromagnetic materials are used in this design.

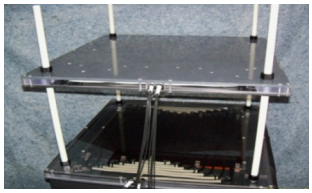

Figure 2.27: Planar square coupler without coil cavity prototype [108].

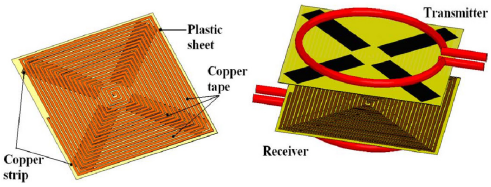


Figure 2.28: Simulation design of a planar square coupler [108].

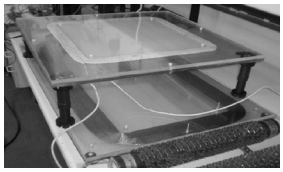

Figure 2.29: Planar square coil with cavity [95].

Figure 2.30: Simplified simulation design of a planar square coil with cavity [95].

Considering different magnetic flux lines generated and formed by whether or not a cavity exists in the planar coils, another derivative design can be categorized into 'planar square coils' here. Compared with the planar square coil without a cavity prototype, the model that can be named the 'planar square coil with a cavity' has been presented in [95], which is nearly based on the same dimensional parameters except the empty cavity design existence within the coils as shown in Figure 2.29 and Figure 2.30.

- Solenoidal square coils

When the installation space under a vehicle chassis is not a major issue, for instance for small-sized automated guided electric vehicles (AGEV) in warehouse rather than on public traffic road, a combination design of solenoid coils and square coils can be proposed, which here is named 'solenoidal square coil' despite a different name in the original report [135].

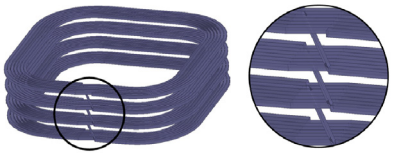

Figure 2.31: Simulation model of a solenoidal square coil [135].

By a comparison analysis in this thesis, it can be explained that, the huge dimensional size of this kind of design can take advantage of the intracavity space of the AGEV and theoretically present the optimal performance of both planar square coil and solenoidal

coil due to a larger internal magnetic flux area and path length as shown in Figure 2.31. Expectedly, this solenoidal square coil design can improve the magnetic flux density and eventually enhance the power transfer efficiency and power rating, which however still needs to be tested and proved with actual system output performance and feasibility yet.

◆ Helical solenoid coils

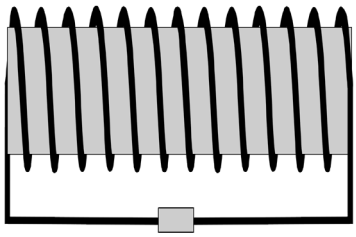

Figure 2.32: A traditional solenoid coil - side view [136].


Figure 2.33: A cross section of single-layered solenoid coil [136].

Similar to conventional solenoid structure, the helical solenoid coil categorized here can be one of the applicable CPT coupler designs. As shown in Figure 2.32 and Figure 2.33 [136], the helical solenoid coil design ideally has two coaxial solenoids with horizontal flux central lines in parallel. With one solenoid as transmitting coil on the primary side and another solenoid as receiving coil on the secondary mounted on the vehicle chassis. Figure 2.33 shows a cross section of a helical solenoid coil with single-layered windings. This coil structure theoretically has satisfactory mutual inductance when two coils have zero misalignment in parallel and short coupling distance, especially for small electronic devices. However, this design may have low tolerance to misalignments which could be a challenge from the EV customer end in real-world high power applications if installed on vehicle chassis. Ferrite cores can be inserted into the cylindrical centre in helical solenoid coil design for coupling enhancement.

◆ Multilayer helical coils

A novel design called ‘multi-layered helical coil’ is illustrated in Figure 2.34 and Figure 2.35. Theoretically, with numbers of winding turns and layers, the coil coupling and mutual inductance will be increased, consequently enhancing the CPT system performance.

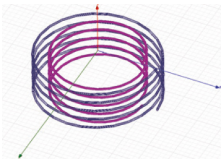

Figure 2.34: A multilayer helical coil structure [63].

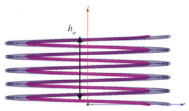

Figure 2.35: Front view of a multilayer coil design with two-layered shell [63].

When it comes to high frequency applications like CPT charging for EVs, the total effects of proximity losses will be significant if the distance of each turn and layer separation are too close, which lowers the system efficiency [63]. Thus, this design is not suitable for high frequency, space tightened and high power required applications. Further investigations and experimental results from practical prototypes rather than ideal simulation models are still required to study this multi-layered helical coil design for the feasibility and realization of CPT charging of EVs in the future.

◆ Mixed-type coils design

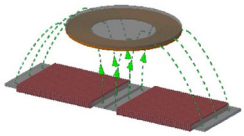

Figure 2.36: A mixed-type coil design [116].

An innovative structure design shown in Figure 2.36 was proposed by a team in Japan in 2015. This mixed-typed coil design [116] is supposed to allow higher tolerance to misalignments, smaller size and more compact installation for energy receiving side on EVs as two coaxial square solenoid coils on the transmitting side are anticipated to generate stronger magnetic field in order for the circular receiving coil to capture more amount of magnetic flux lines. Expectedly, the overall coil magnetic flux distribution of the CPT system could be boosted when compared with a pure circular coil design for the same size of chassis of EVs. However, this design still needs to be further theoretically studied, practically tested and comprehensively analysed from modelling to experiment due to few reports in the literature until present.

◆ Double D coils

A structure of double D shaped coils was proposed by Qualcomm Halo program as illustrated in Figure 2.37.

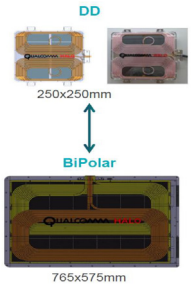


Figure 2.37: Double D and BiPolar Design [47].

Two coils of the ideal D shape winded with one long copper wire are on the ground side as a transmitter, and a polarized receiving coil with two partially overlapping windings is on the EV chassis side [47]. This DD design was reported to produce higher coupling than a same-sized circular coil structure [137], [138]. However, further developments about DD coil design and its derivatives are required by more numerical results and effective system performance.

- Asymmetric coils

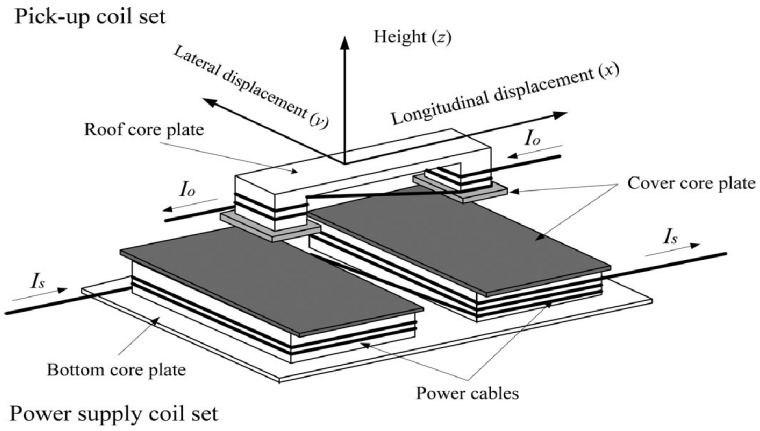


Figure 2.38: Asymmetric coil design [139].

The asymmetric coil structured in Figure 2.38 was proposed in 2014 in order to investigate the impact of tolerance to the stationary CPT system performance. The receiving coil is smaller than the energy transiting coil set with a purpose of improving the tolerance of misalignments when parking a vehicle [139]. This structurally innovative coupler design with a transmitting bottom set size of 200 cm x 100 cm each and a pickup set size of 16 cm x 16 cm each is claimed to output 15 kW at 20 kHz and the maximum misalignments can be 40 cm and 20 cm for lateral and longitudinal axes. This coil design contains ferrite cores to facilitate the field. The power supply is a current source of maximum 100 A in the simulation models. Nevertheless, further studies about the

feasibility for real-world EVs contactless charging with this type of design are required in the future, addressing the other major objectives of CPT systems.

Regarding more novel coupler designs proposed and investigated throughout the doctorate study, Chapters 3 and 4 of this thesis will present and describe them further in details from different aspects of knowledges, as parts of the contributions via the thesis.

***(e) Magnetic resonance in inductive CPT systems for EVs charging***

As introduced before, a basic inductive power transfer (IPT) system consists of a front-end power supply, a coupling coil structure, a load and other essential power electronic units such as high-frequency inverter, rectifier, and voltage regulator. If necessary for high RMS real power rating requirement, a suitable compensation topology can be added into the CPT system. Over relatively large charging distance, a loosely coupled induction can realize the basic wireless energy transmitting purposes for low-power applications, which have been tremendously studied before 2010 as the initial investigations implemented during 1990s and 2000s are mostly about the basic realization of wireless power transfer. Since around 2010, institutional researchers and industrial R&D sectors started to focus on the major challenges and objectives: the CPT system efficiency for electricity usage consideration, the system power transfer ratings for fast charging requirement of EVs customers, the large air gap pursuit for higher charging flexibility and safety, etc. Therefore, as a new branch of CPT technologies, magnetic resonance based CPT technology was proposed by MIT WiTricity and later structured by researchers in this field within the last decade.

Electromagnetic resonant coupling, so-called magnetic resonance inductive coupling, has currently been proposed as an approach to reach higher CPT system performance, which is not only based on IPT techniques but also deployed with theories of electronic circuit and magnetic resonance under necessary conditions specifically built for a CPT system. Normally, basic IPT systems works at VLF up to kilohertz range of operating frequency to achieve loosely coupled wireless energy transmission. Whilst magnetic field resonance based CPT systems operate at tens of kilohertz level frequencies due to resonance conditions and impedance matching applying to compensation capacitors and actual inductance values of inductive coils. When the compensation capacitors can optimally minimize the magnitudes of reactance in the system, the magnetic resonance can be

theoretically reached in order to maximize CPT system capacity via the magnetically coupled coils under the condition.

With the rapid development of semiconductors, material sciences and power electronics such as switching power supply [140], power amplifier [141], active rectifiers [142] and high-frequency inverters, the electromagnetic field resonance for high frequency high-power stationary CPT systems with large charging distance tends to be achievable in the near future.

### 2.3.4 Dynamic CPT for EVs as a scope of the future

From the long-term perspective, CPT systems with online charging techniques will be more pragmatic and convenient for long or even unlimited range of EVs, which will enable drivers to charge EVs continuously while in motion. However, the actual real-time electrical energy received via dynamic CPT is theoretically and practically reliant on power transfer ratings of the system, time duration of the EV travelling within the dynamic charging zone, vehicle speed, and actual coupling efficiency and so on. Accordingly, besides of the major challenges of stationary CPT charging, achieving dynamic CPT charging of EVs has much more difficulties and complexities in real-world applications. This subsection describes the fundamental principles of dynamic CPT system and addresses the main challenges to be tackled as a scope of future dynamic CPT technologies for EVs.

***(a) Principles***

Dynamic CPT can be regarded as a derivative stemmed from stationary CPT as its receiving coil side on the EV chassis fundamentally has similar mechanism and subsystem structure with the secondary receiving side of a stationary CPT system. Therefore, dynamic CPT charging approaches can be categorized into two methods according to transmitting side coupler designs. The first method is segmented coil track design and the second method is single transmitting track design [63], [81]. Theoretically, the former one has multiple ground-side segmented coil arrays connected to high frequency voltage power sources as shown in Figure 2.39 and these coil arrays have similar dimensional size with the receiving coils on the vehicle chassis. The latter type of design consists of one single substantially long transmitting track connected to one

single power source [143], in which the dimension of single track is much longer and larger than the receiving coupler coil on vehicle chassis.

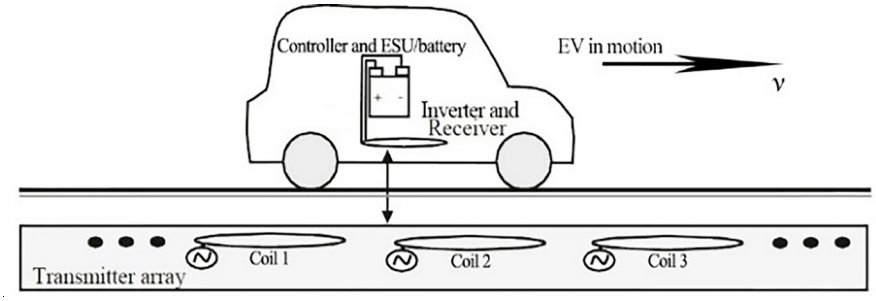


Figure 2.39: A proposed segmented coil track for EVs dynamic CPT [63].

The mechanism of a segmented coil array type of dynamic CPT system can be depicted by Figure 2.39 and Figure 2.40 [63]. When the EV travels along the online charging enabled lane and through the air space under which the coil array is activated, accordingly the power source and HF inverter corresponding to this coil turns to be switched by the system control and immediately then the inductive coupling occurs. The EV passes over this array zone to the next segmented array then the previous inductive coupling transfer will be cut by system switch and the next array will be supplied with power to start another inductive energy cycle. The foreseen challenges of dynamic CPT approaches are more about control system complexity, switching power supply module complexity, extremely high construction cost and coupling effectiveness determined by displacement, vehicle speed, weather conditions, etc.

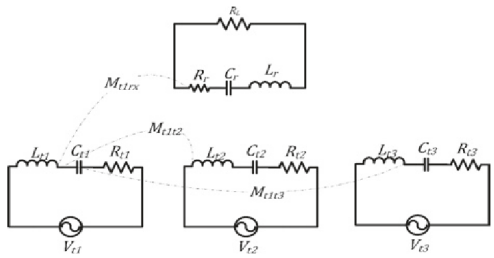

Figure 2.40: The proposed dynamic CPT system illustrating a method of using multiple segmented coils based transmitting array [63].

***(b) Analytical comparisons between two categories of transmitting coil arrays***

The segmented coil array design could eliminate the issues of electromagnetic field exposure and solve the complexed distributed compensation requirement. Unavoidably, some challenges will exist in this array design as every coin has two sides. Sensor detection units are required on the ground array side to track and locate the real-time

position of the vehicle and appropriately switch on the power sources of the arrays covered by the moving receiving coil as illustrated in Figure 2.39. Thus, the power transfer efficiency could be feasibly remained high as the array electromagnetic fields only get switched on instantly when the vehicle is travelling over them. Besides, the separation distance between arrays may determine the continuity and efficiency of online charging due to the issues caused by the negative mutual inductance between adjacent transmitter arrays generating negative currents and by the high complexity of too many power source converters connected to each coil to realize effective control of system power flows.

Comparatively, the single transmitting track CPT system is powered from a single source, which could give advantages of easier control and nearly constant coupling coefficient along the track. However, this type may also suffer from: the inevitable electromagnetic field emission and exposure; large inductance that is required to be compensated with one distributed compensation capacitor; coupling coefficient would be fairly low causing low efficiency due to very small effective coupling area between transmitting track and receiving coil on vehicle side in the real-world scenarios.

***(c) History, current status and future potential of dynamic CPT***

Based on studies, reports, patents and other documents in terms of the development of dynamic contactless charging for EVs in the literature, it can be found that probably the first real attempt to wirelessly inductively transfer electrical energy was implemented by Hutin and LeBlang in 1894, which can be seen from the US patent [144] describing a method of transmitting electricity to an electric rail vehicle using an AC generator at 3 kHz without outlet exposed contact. In 1972, Nikolaus Otto used a 10 kHz generator with a sinusoidal silicon controller rectifier inverter to couple circular coils for moving an EV, in which two copper winding coils were buried 20 cm under the pavement, each carrying 2 kA current. Since 1980s, the project called the Partner for Advanced Transit and Highways (PATH) was launched towards realizing inductive power transfer road for EVs in California. This project deployed a 400 Hz generator to inductively transmit energy for a bus with capacitive tuning control. However few details were released and later this project was terminated. There were insufficiently academic studies and industrial reports about practically realizing satisfactory dynamic contactless power transfer for high-power

required EVs until late 1990s. At the same time in industry, the plug-in EVs and hybrid EVs were emerging and becoming popular during these decades.

More recently within the last two decades, both the academic and industrial fields have presented a series of development regarding dynamic CPT technologies for EVs. As a leading academic institution in the world, the Korean Advanced Institute of Science and Technology (KAIST) has been carrying out a research project called 'online electric vehicles (OLEV)', by which about 3 kW output power has been claimed to transfer wirelessly for an EV over a dynamic charging enabled road with a distance of 10 mm in 2013 [51]. A SUV type of EV and an electric train were able to receive 15 kW power on a rail with 120 to 170-mm air gap [145], [146].

The researchers of Auckland University and Conductix-Wampfler developed a dynamic IPT system with circular segmented coils under a monorail surface to transfer approximately 1.5 kW at 40 mm charging distance for EVs [97], [137], which seems convincing and feasible for monorail based CPT but the long track costs and system efficiency would be still big challenges for real-world transportation application.

Utah State University and Tokohu University also paid efforts on investigating electric bus for campus use and actual coupling factor issues regarding large air gaps and circuit designs. The former university targets at 25 kW power transfer and battery weight reduction for buses [147], [148].

On the other hand in industry, some technology companies are also investing into development on dynamic charging for EVs. For instances, Momentum Dynamics claimed that they tested a prototype system in 2012 that could supply 240 V for commercial EVs with distance of maximum 60 cm and kilowatts level power to fully charge a Chevy Volt within 1 hour [118]. Qualcomm Halo, Bombardier and Conductix-Wampfler also have been implementing investigations on dynamic charging along with feasible stationary technologies in their R&D sectors since about 2010.

Overall, most of the methods of dynamic CPT have been pervasively acknowledged the feasibility of segmented coil array design. A derivative improved dynamic CPT coupling schematic has been proposed towards higher coupling effectiveness shown in Figure 2.41, which deploys multiple switches, multiple transmitting coils and multiple receiving coils

to magnetically couple and capture the flux [149]. Nevertheless, this innovative type of derivative was tested at several watts level and may still require further simulation and practical experiments to verify its electronic and magnetic complexity against the real-world performance from high-power point of view for EVs applications.

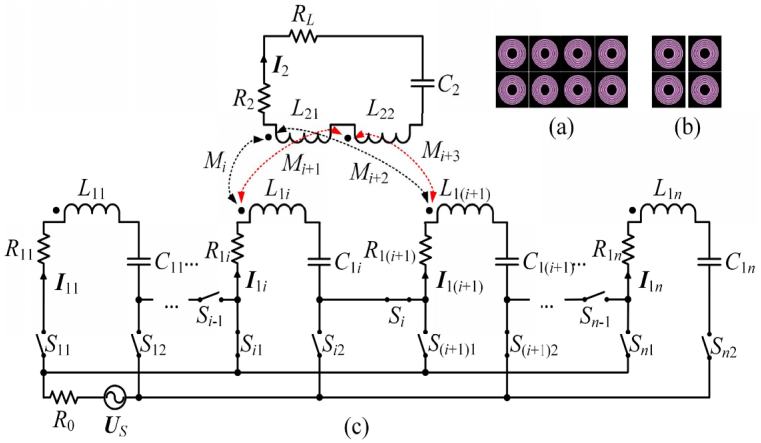


Figure 2.41: An improved derivative dynamic CPT coupling topology [149].

For the future, dynamic CPT charging technologies will still undoubtedly be an academic research mainstream and development direction as an unlimited long range of EVs is an ultimate objective from any perspectives. Some other difficulties are to be solved, such as high costs of the entire CPT system including roadway infrastructure, control modules, fragile and expensive ferromagnetic materials, long service life purposes, electromagnetic field interference (EMI) considerations, etc. Nonetheless, it can be believed that the dynamic CPT systems will be realizable and feasible based on the mature stationary CPT technologies in the short future and further technical supports from other scientific areas.

## 2.4 Chapter conclusions

The history and basics of CPT systems mainly based on magnetically inductive coupling power transfer phenomenon have been introduced in Chapter 2. A number of leading research institutes and pioneer industrial companies who have been attempting to apply CPT techniques for their EVs mostly operating in warehouse scenarios have been listed and discussed in terms of the development directions, proposed methods and concepts over contactless energy transmission realization. In addition, the currently proposed mainstream coil coupler designs from both stationary and dynamic aspects in the literature have been described and reviewed towards the main performance output

objectives of CPT systems and towards developing the methodology of this thesis, in spite of immature technical realizations and foreseen huge challenges such as reliability, suitability, accuracy, construction costs, etc., especially from the long-term CPT application perspective. This thesis is to report the investigations regarding stationary CPT system performance optimization with an emphasis on coupler module design.

# Chapter 3 Theories, methodology and analytical model designs

This chapter presents and describes theories, numerical representations and methodologies of CPT modelling in depth despite basic principles briefly introduced in Chapter 2. In order to achieve the main objectives of CPT technologies for EVs charging, new systematics and design methodologies of CPT systems have been investigated from simulations to practical experiments. As the significantly major part of CPT systems, the optimization of the coupler coil with its determinations of geometric and electromagnetic parameters on both the electrical energy transfer characteristics and the magnetic coupling performance has been considered as a core topic over CPT studies. Apart from the power electronic aspect to enhance system performance, the research emphasis in this thesis will be on the design and methodology optimizations of CPT coupler modular including a variation of innovatively proposed coil structure designs, coupler geometries, shielding methods, ferromagnetic materials, tolerance to misalignments, etc., mainly against groups of air gaps, ranges of operating frequencies and so on.

## 3.1 Introduction

As mentioned before in Section 2.1, based on the basics of inductive power transfer that were discovered, proposed and developed by Michael Faraday, Hans Oersted, John Henry Poynting, James Maxwell and Nikola Tesla, the CPT technologies have been under investigations for over one century [150], [151]. By a time-varying magnetic field instead of wires, it was proved and described in Faraday's law of inductance that electrical energy can be transferred wirelessly and inductively via electromagnetic field (EMF) [152], [153]. New applications with low-power and high-power CPT technologies have become commonly developed and gradually realized over the past two decades due to constant contributions of fast switching power electronics [154]–[156], signal communication systems [157], [158] and new magnetic materials [159].

In order to address the challenges of CPT system performance optimization, the transferred real power, system efficiency, maximum power transfer air gap and tolerance

to misalignments, it is significantly necessary to study the methodologies of modelling, to implement the newly proposed coupler designs and to analyse the outcomes by comparisons from aspects of power electronics and electromagnetics, by which the CPT system structures can be optimized especially for high-power applications like EVs wireless charging considerations.

The following subsections of this chapter will describe the principles of inductively coupled CPT, compare the differences of theories between the industrial transformer, the RF antenna and the IPT systems with magnetic resonant couplings and compensation topologies. Then theoretical representations and numerical calculations towards CPT system optimization based on power electronics will be discussed. Besides, formulations and investigations based on integration of electromagnetic theories, EMF metrics and 3D FEM-based analytical modelling are to be discussed for implementations of the subsequent chapters of the thesis.

## 3.2 Theoretical analysis of CPT

### 3.2.1 Analysis methodology of inductively coupled CPT systems

Conventional plug-in EVs have been accepted very rapidly worldwide in the automobile industry, which can be anticipated to be indirectly beneficial to development of CPT technologies to enhance EV performance and widen commercial markets of CPT-based EVs in return.

Compared with conventional plug-in EVs charging system, CPT systems tends to result in much more complex architecture in nature from front power supply end to rear load end. Every single different system performance requirement corresponds to different technical efforts in designing and manufacturing the CPT systems. In order to ensure highly satisfied system performance characteristics, the entire CPT system is required to be systematically designed and redesigned before practically producing satisfactory system outputs. Therefore, a reliably, effectively, feasibly and systematically analytical CPT design methodology needs to be established and proposed.

Theoretically and practically, the magnetic coil coupler designed and power electronics adopted crucially determine the system outputs including the aspects that are emphasized in this thesis, which are maximum real power transfer, system efficiency, optimum charging distance, etc. As the most significant and determinant component of high-performance CPT systems, the magnetic coil coupler, the so-called coupling modular, will be focused on in the range of investigations of this thesis.

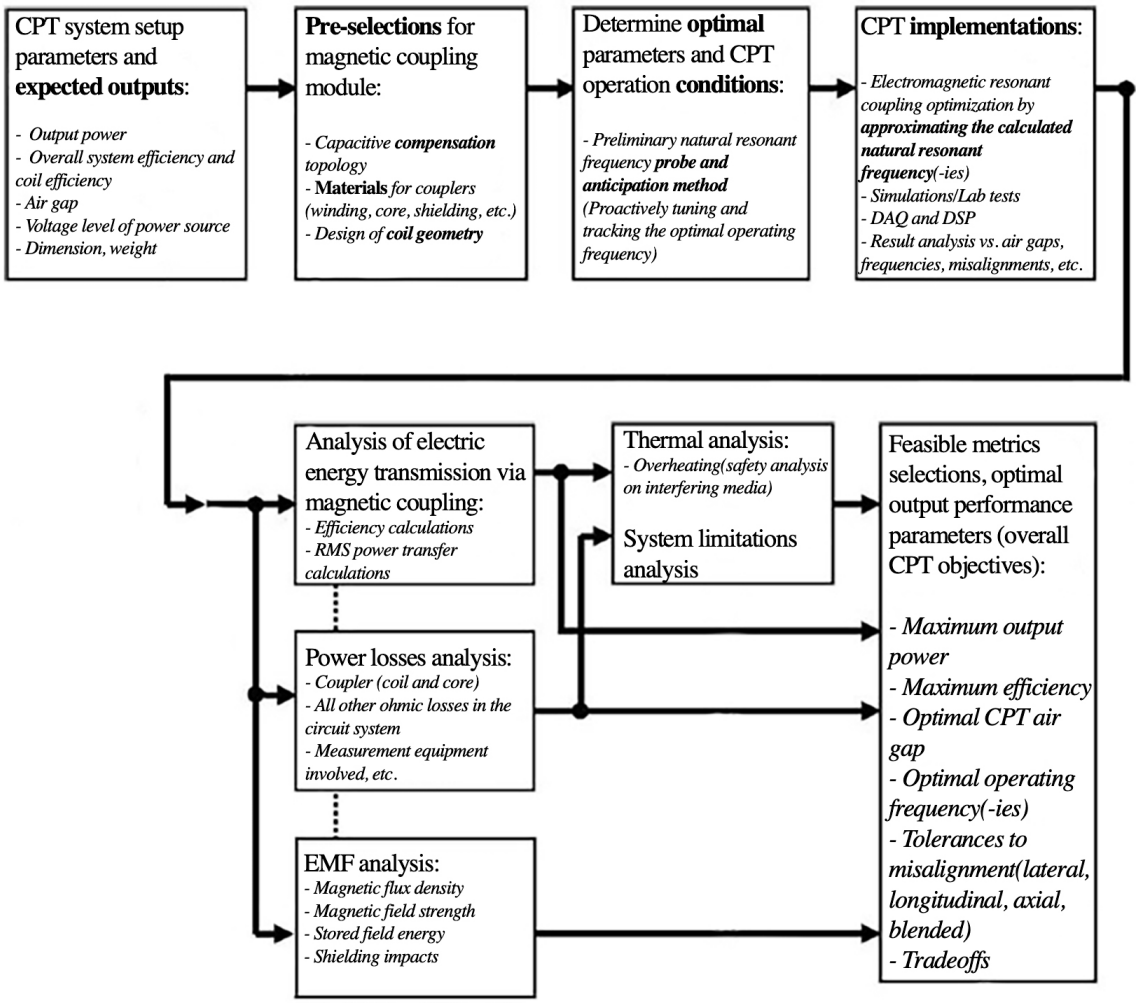


Figure 3.1: The methodology for structuring and analysing CPT systems of the thesis.

A proposed methodology of designing and analysing CPT systems is depicted and summarized in Figure 3.1. The preliminary natural resonant frequency probe and anticipation method for effective tracking and tuning purposes towards reaching an optimal electromagnetic resonant coupling state of the system is developed in this methodological flowchart above. From the system structure to the output analysis, this methodology can be deployed to develop CPT systems with comprehensive analyses and

constructive considerations for both theoretical designs and practical implementations. From the design point of view, the design variations of coil type, coupler geometry and coupler material properties need to be initially taken into account as the starting point of all the parameter determinations. In addition to magnetic coil design for better magnetic field coupling reasons, the capacitor compensation topologies also need to be suitably added into the system in order to cancel out reactive powers and leakage inductance for higher values of power factor (PF) and system efficiency.

By setting coil coupling distance, load and operating frequency as main variables, along with configuring voltage power supply at the system input, inverters and converters, the designed small-sized CPT prototype can be implemented and analysed. When the entire system tends to be operating at the anticipated steady status, the required output data of both electronics and magnetic field can be acquired for analysis of the transient contactless electrical energy transfer behaviour and then for evaluation on the overall system performance. In order to reach higher transferred power rating and efficiency, it is necessary to calculate and analyse every aspects of results and electromagnetic field's characteristic parameters for redesigns and further improvements on each modules of the system. Iteratively, along with the calculated theoretical results by electronic circuit and EMF equations, the comparison, verification and analysis addressing major objectives towards approximating an optimized CPT system can be carried out. Detailed designs and implementations for the investigations in the thesis regarding utilizing this innovatively proposed methodology will be presented and reported in Chapters 4 to Chapter 7.

### 3.2.2 Comparisons with conventional energy transmitting applications

***(a) Discussion and comparison between CPT couplers and industrial transformers***

As known, ideal transformers in theory are fairly different from real-world transformers in industrial applications when analysing actual performances. For examples, in ideal transformers, magnetic coupling is considered perfect and coils dissipate zero energy. The transformer core is considered to perfectly trap all the magnetic flux with all the flux lines passing through any cross-section of the core without any leakage. Numerically, the induced electromotive force (e.m.f.) is equal to alternating source voltage by applying Faraday's law. All the power from source on the primary coil is considered to be

transferred to the secondary circuit due to assumption of zero losses. Importantly, power factors in both coils are considered to be the same in ideal transformer theory. The relations between voltages and currents are seen proportional and linear.

However, the characteristics of ideal transformers cannot be realized for practical power transformers. The perfectness of magnetic coupling between coils cannot be achieved. There exists ferromagnetic saturation in high magnetic fields. Significantly, power losses in coil windings, core and power electronic elements are definitely unavoidable and not simply proportional any more.

By contrast, the CPT systems investigated in the thesis have more different parameters and nonlinear characteristics than ideal transformers and conventional transformers in real-world applications. Due to additional requirements toward charging distance, coil misalignment tolerance, magnetic leakage and so on, the system performance characteristics tend to be relevant to more variables and factors which can also affect each other in practice. Particularly, system input voltage, geometry of coils, capacitor compensation circuit, winding ratio, operating frequency, charging air gap and coupling misalignment can be determinant to the main objectives among the system outputs – output power level, maximum system efficiency, actual power losses, effectiveness of charging distance, tolerance rate to lateral and longitudinal misalignment, etc.

Thus, it is required to investigate CPT systems from aspects of both power electronics and electromagnetics with theoretical modelling, numerical computation and practical test. When the CPT system operating frequency is in range of kilohertz level or above, the system performance characteristics need to be analysed based on the systematic methodology illustrated in Figure 3.1 instead of using formulations of ideal transformers with ideal assumptions to analyse the real-world industrial electrical energy transformers.

***(b) Discussion and comparison of CPT systems with antenna applications in signal transfer systems via high frequency microwaves***

As known that loosely coupled inductive method and magnetic resonant coupling are generally regarded as near-field CPT techniques, while RF and microwave are regarded as far-field CPT approaches with energy transmission range of a couple of kilometres and low efficiency rate in signal communication areas. In order to heighten the frequency

range from LF of Hz-kHz to VHF of GHz for realizing longer energy transfer distances like RF and microwave applications, it can be found that some academic reports [3], [70], [113], [160]–[162] at the initial stages and years of CPT study in the literature suggested to consider the general CPT issues as far-field HF low-powered antenna and RF microwave topics, which was to be found methodologically easier for analysing but insufficiently suitable and practically unconvincing for real-world high-power CPT scenarios in nature especially for EVs.

At low-power levels using the definitions of two-port network theory and measurement of scattering parameters (S-parameter) matrix, it was believed, in an initial series of reports [64], [73], [111], [112], [115], [163] before about 2013, that designing and estimating the system performance characteristics of a CPT prototype using S-parameter based analysis was recommended. In these studies, the prototyped low-powered wireless energy transmission antenna setup was measured with a vector network analyser (VNA) to directly acquire the S-parameters $S_{21}$ and $S_{11}$, and then simply work out the transmission ratio $\eta_{21} = |S_{21}|^2 \times 100\%$ and reflection ratio $\eta_{11} = |S_{11}|^2 \times 100\%$ of the system in order for experimental verification based on definition equation in [64]. With two-port network theory and VNA method, $\eta_{21}$ is supposed to represent the coupling coil efficiency of the WPT system.

In the main papers [64], [111], [112], [115] regarding this two port network using VNA measurement and S-parameter theory, the output system power was low with range of 5 W to 100 W. This signal-level antenna based small circular coil setup at 15.9 MHz and with a 200 mm coil distance was claimed to produce an efficiency of up to 95 %, which seems too high and is almost the same as a real-world coaxial high-quality transformer. It can be noticed that there were too many idealistic assumptions and unconvincing method used in this case considering CPT issues as pure antenna far-field RF scenarios. Conclusively, the real-world CPT charging for high-power EVs should be analysed from power electronics and electromagnetic field point of views instead of simply using low-power setup VNA measurement to evaluate a practical CPT system model. Thus, the electromagnetic field analysis and power electronics based CPT design is to be studied and presented in the following sections of the thesis, addressing the major systematic

parameters such as coil geometry design, resonant frequency, output RMS power rating, air gap variation, coupling misalignment, etc.

## 3.3 Design basics of electromagnetic resonant coupling CPT systems

As briefly introduced in Section 2.3.3(c), researchers of MIT WiTricity firstly proposed and demonstrated a prototype named ‘magnetic resonance’ wireless energy transmission in 2006, after which the magnetic resonance coupling has been increasingly considered in many studies while the loosely coupled inductive power transfer (IPT) is still a main stream among all ranges of contactless power transfer applications. However, magnetic resonance coupling had not been defined and differentiated from electromagnetic induction based loosely coupled IPT until a leading team of Tokyo University technically compared these two methods and recognized the former as a specific type of the latter in between 2009 and 2017 [112], [113], [117], [162]. Under certain conditions being satisfied by system circuit setup parameters, an electromagnetic resonance coupling CPT can be categorized as a distinct branch method of typical electromagnetic induction based loosely coupled IPT approaches.

In electric circuit theory, a circuit system tends to operate at resonant state when the RLC circuit impedance matching is met and then the corresponding power factor ideally tends to be maximized and approximated to 1. Theoretically the maximum RMS real power transfer can be achieved. For coupling coils, the transferred power and system efficiency are supposed to be at peak values via mechanism of magnetic resonance while the specific conditions to reach resonant status are varied relying on corresponding actual electric circuit and generated magnetic circuit. Based on the concept of electromagnetic resonant coupling, the established theoretical CPT system methodology and analytical design can be undertaken and presented in this section.

### 3.3.1 Architectures and structures

Similarly, the main mechanism of magnetic resonant coupling CPT systems is based on magnetic induction phenomenon. Other electric circuit elements are similar to previously

introduced loosely coupled IPT, establishing a full range of energy conversion processes from AC supply front end to load rear end. The basics of typical IPT and principles of CPT systems have been described and introduced in previous chapters above. The major difference between the electromagnetic resonant coupling and IPT from electric circuit point of view is the emphasis on structuring the capacitance compensation topology for each customized CPT system. In an electromagnetic resonant coupling system, as the focus is on 'resonant', the impedance matching and the natural resonance frequency tracking based on RLC theory [164] are mainly needed to achieve magnetic resonance under specifically required conditions as there exists various factors in actual operations [75], [165]. Figure 3.2 is a simplified schematic of an electromagnetic resonant coupling based CPT system selected from a prototype of Chapter 4, illustrating a transient optimal electromagnetic resonance status taking place for a series of satisfactory system outputs and performance characteristics [166], with a uniquely designed coupler modular and specific compensation circuit.

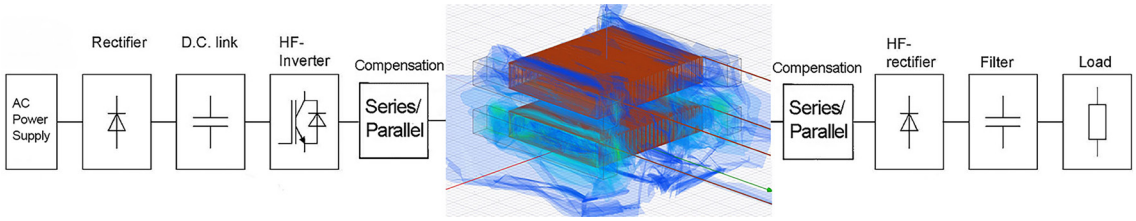


Figure 3.2: A simplified architecture of a resonant coupling CPT system.

### 3.3.2 Compensation topologies

In order to accomplish the main goals of maximizing power transfer rating and transfer efficiency across large air gaps, capacitance compensation circuits can be introduced when designing a CPT system. By improving magnetic coupling to its peak states and reducing all losses, it is worthwhile pointing out that cancelling out reactive powers to increase power factors (PF) can increase RMS real power transfer ratings in actual applications. In loosely coupled IPT systems, the magnetic performance is weak due to high flux leaking as reactive power effects for establishing electromagnetic field or as pure wastes that cannot be captured during magnetic induction phenomenon. In other words, a loosely coupled IPT system cannot be as highly efficient as an ideal transformer or an industrial transformer. In industrial transformers, the flux lines can nearly hundred percent fully pass through the coaxial coils and its core which results in coupling

coefficient of almost 1 as no flux lines are considered as leakage. However, in CPT system considerations, flux lines in the field and reactive power lead to different magnetic coupling strength.

Therefore, an optimal compensation can be used to tune out or cancel out the high leakage inductance in the circuit and reactive power in the field. Ideally, the maximized PF values on both primary and secondary sides of CPT system should be close to 1 which means no phase angles between voltage and current when coupling. But the actual scenarios could not never be approximated or designed to reach that ideal status. Nonetheless, it is still possible to design an approximate magnetic coupling reachable model for CPT systems using compensation capacitors matching with actual inductance values in operations in order to practically maximize transferred power levels and efficiencies, which is also implemented and concluded in the following chapter. In other words, the power rating of the primary source side can be decreased by the primary compensation capacitor and the actual power transfer capacity of the designed system can be facilitated by the appropriate secondary compensation capacitor, which is comprehensively expected to ensure the unity power factor for the CPT system.

Figure 3.3 depicts a practical structure of primary series - secondary series (SS) compensation for experimental CPT tests, in which the SS capacitors can also be substituted with SP, PS, PP and other derivative topologies. In this subsection here, major compensation topologies with simplified circuits are to be described and compared for understanding and preliminary explanations of using a specific topology in implementations in Chapters 4 to 7.

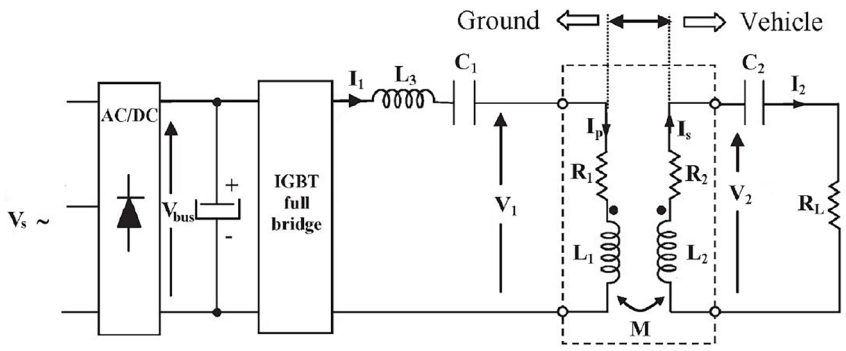


Figure 3.3: A schematic of SS compensation topology for experimental tests.

***(a) SS***

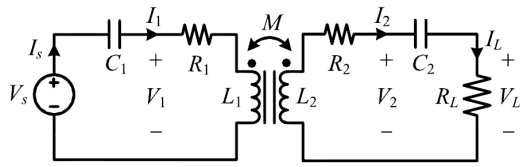


Figure 3.4: Primary series-secondary series (SS) compensation topology.

In a couple of reports, the voltage source type of SS compensation circuit was found to appear a characteristic of load-independent output on current and was also tested to be independent of magnetic coupling coefficient in terms of unity power factor [167]–[169]. Additionally, SS compensation was found to be suitable for low power supply voltage requirement and its circuit equivalent impedance at resonance conditions tends to be minimum. Importantly, SS topology shows high tolerance of PF to operating frequency variation, which is more suitable for real-world EV parking scenarios from different parking pattern point of view. In [16], it was found that $C_1$and $C_2$ in SS compensation do not depend on mutual inductance. However, SS topology was tested and found to be unsafe for inverter and power supply end if the coupling coefficient is 0 [170]. In other words, the power supply and inverter modules of a CPT system can be damaged if no CPT based EV is parked over the CPT charging pad but while circuit system is activated, which shows a high-level requirement of the switching power supply control system within the primary side for safety reasons of the system. Nonetheless, it can be noticed the SS topology is popularly adopted in research solutions and application tests in the literature due to its advantages of load-independent characteristic, insensitivity to mutual inductance changes and generally high peak efficiency output [171].

***(b) SP***

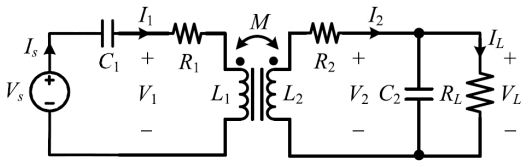


Figure 3.5: Primary series-secondary parallel (SP) compensation topology.

The voltage source type of primary series - secondary parallel (SP) compensation topology was found to have a load-independent characteristic on output voltage [172] and have advantage of reducing power supply voltage rating requirement [173]. In [174] reported in 1998, it was thought that a voltage source type of SP circuit could maintain a

higher unity PF than SS circuit. Similarly with one of the disadvantages of SS topology, PS compensation was also tested unsafe enough for protection on its power supply and inverter when coupling coefficient is 0.

***(c) PS***

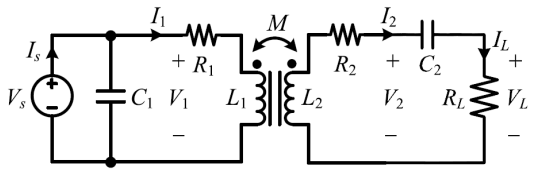


Figure 3.6: Primary parallel-secondary series (PS) compensation topology.

It was found that PS topology is load-dependent and has low tolerance of efficiency to frequency variation. However, with current power supply, PS circuit shows higher peak efficiency and higher tolerance of PF against frequency variation than PP topology with current source. Beside, PS has high circuit impedance and the actual power transferred to secondary circuit appears to be less constant than SS, SP and PP. PS was found to be adequate for reducing the inverter current rating [100], [173].

***(d) PP***

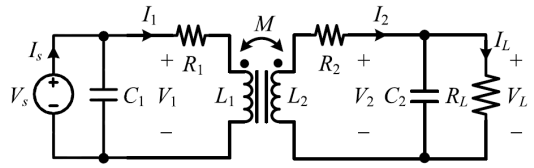


Figure 3.7: Primary parallel-secondary parallel (PP) compensation topology.

PP topology was found to have characteristics of load-dependent, high impedance at resonance and low tolerance of PF against variable operating frequency. Although, several advantages were found such as higher power transferred to load from constant current power source and higher tolerance of efficiency versus variable operating frequency than PS [100], [175]. In the literature, PP compensation topology so far has rarely been selected for CPT technologies.

***(e) Summary on compensation topology selection***

In terms of choosing the most suitable compensation topology based on the system constrains of each type of CPT prototype, it can be found from a couple of studies [16], [35], [171], [176], [177] to summarize a basic series of guidelines in order to provide

reliable rules for improving the electrical quantities and maximize the CPT system power transfer capability and overall system efficiency. If the load and the magnetic coupling status are variable, it is suggested to deploy SS compensation as two compensation capacitors in SS are independent of the resistance of load and the mutual inductance; If the load is fixed, it is the best method to select SS compensation circuit according to actual produced value of secondary inductance by tests; If a high-power CPT system has ineligible parasitic parallel capacitance from the windings or the equivalent impedance at the input is varied by winding resistances, it is suggested to choose SP or PP topologies to compensate for the system [173].

There is one significant characteristic for consideration of topology selections, which can be found from [170] that PS and PP are able to be safe for the power source when secondary coil is absent but unable to couple for expected rated power if misalignments exist in between the two coil. However, SS and SP compensations can perform with higher tolerance to misalignments simultaneously transferring rated values of real power to the load despite less safety for the source.

Based on the literature until present, there are even more types of complex compensation circuits such as the primary nonresonant-secondary nonresonant (NN), the primary nonresonant-secondary parallel (NP), the primary nonresonant-secondary series (NS), the primary series-secondary nonresonant (SN), the primary parallel-secondary nonresonant (PN), the primary series plus parallel-secondary series (SP-S), the primary series plus parallel-secondary parallel (SP-P), etc., despite insufficiently applicable analysis of options for real-world high power level CPT charging towards EVs. In this thesis and also in most research papers that has contributed to this field, the major four compensation topologies above are selected for CPT technology investigations although it is still unclear about which type within these four is the most appropriate solution for CPT design [178], which also reflects that the CPT technologies for EVs still require more further comparative results and insights against a series of variables and factors that may affect the actual magnetic coupling effects in real world.

### 3.3.3 Frequency and resonance

As is well known, operating frequency plays an important role in normal power transfer systems. In magnetic resonance based CPT systems, a high frequency (HF) of power supply is a vital factor potentially causing a high overall system efficiency. Whilst limited by advancement and restriction of semiconductor and material sciences, generating a HF power signal tends to be technically difficult. Electromagnetically, flux leakage, magnetizing current and radiation loss are also related to high frequency operation. It can be seen that appropriate capacitors deployed as compensation in CPT system are able to establish a resonance circuit with the effects of generated winding inductances[179].

Resonance occurs as a phenomenon in many types of patterns in nature. Generally, energy oscillation between two modes tends to be involved in resonance. The establishment of a resonance tends to take place when the rate of energy injection into the system is much greater than the rate of energy loss from the system. Different from the energy oscillation between kinetic and potential forms in mechanics, in the electromagnetic resonance circuit, electric energy and magnetic field energy can operate with an oscillation state at the resonant frequencies between the resonator capacitors in which electric energy stores and the inductor or coupler storing magnetic field energy, and at the same time, resistors dissipate heat loss in nature.

Conventionally, film capacitors are suitable to be used as compensation resonant capacitors due to the property of high breakdown voltage while the drawback of film capacitors are high losses at high frequency [116]. Thus, the consideration and trade-off between HF operation, capacitors and other elements need to be taken into account when initially designing a magnetic resonant coupling CPT prototype.

A magnetic resonance coupler system consists of at least two resonance circuits, exchanging energy at resonance frequency but not affecting other non-resonant elements based on circuit theory. The operating frequency for the compensation capacitors is a significant parameter to be determined, which may be limited by the property of converter's maximum operating frequency point [100] or by maximum of HF inverter. Nonetheless, there is no frequency peak limit in general simulation platforms while there does exist limit in real-world experimental setups and equipment. In CPT scenarios, coils

with physical gaps are utilized to build resonance phenomenon via electromagnetic field [119]. With operation at resonance conditions, proper magnetic field establishment and electric circuit including compensation capacitors on primary and secondary sides of CPT systems can maximize the power factors generated on both sides of system and improve system efficiency by reducing the magnetizing current. In this thesis, electromagnetic resonance coupling based CPT prototypes are to be analytically designed and implemented for analysis.

### 3.3.4 Core with material characteristics and shape of coupling modular

In order to design optimal magnetic resonance coupling CPT system, in addition to electric circuit considerations, the coil core is also a factor determining how effectively a magnetic field performs for CPT coupling. Therefore, utilizing ferromagnetic cores could be of help in facilitating electromagnetic field flux distribution by taking advantages of ferromagnetic material characteristic, which is the effectiveness of high magnetic permeability in power transfer applications. As shown in Figure 3.8, general ferromagnets has much higher permeability $\mu_f$ than paramagnets, diamagnets and free space represented by $\mu_p$, $\mu_d$ and $\mu_0$, respectively.

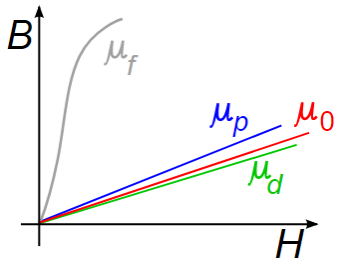


Figure 3.8: A simplified B-H curve comparison of permeabilities for ferromagnets, paramagnets, diamagnets and free space.

The relation of **H** to **B** for ferromagnetic substances is generally nonlinear as depicted in Figure 3.9. If impressed electromotive forces are applied to coils of CPT coupler, the magnetic field is to be built up gradually from unmagnetized status with zero value for vectors **B** and **H** at the beginning point. Then the function $\mathbf{B} = \mathbf{B}(\mathbf{H})$ will apply to the magnetization of the ferromagnetic material following a curve relation illustrated in Figure 3.9. However, the ferromagnetic materials show a characteristic in nature, which is called hysteresis in material science. As indicated in Figure 3.10, it can be seen that the

absolute value of **B** is greater than its initial value on the dotted curve for the same value of **H** at all points along the segments $\mathbf{B_1B_2}$ and the change of **B** lags behind that of **H**. The net work done per unit volume and per cycle throughout the entire field can be represented by equations (3.1) and (3.2) [153].

$$w = -\oint \mathbf{B} \cdot d\mathbf{H}, \tag{3.1}$$

$$Q = -\int dv \oint \mathbf{B} \cdot d\mathbf{H}, \tag{3.2}$$

where Q is the hysteresis loss, an irretrievable fraction of the field energy dissipated in heat, contributing to the total losses of a CPT system. Regarding the hysteresis loss as one of the core losses, there will be further discussion about field energy and losses later in the following chapters of the thesis.

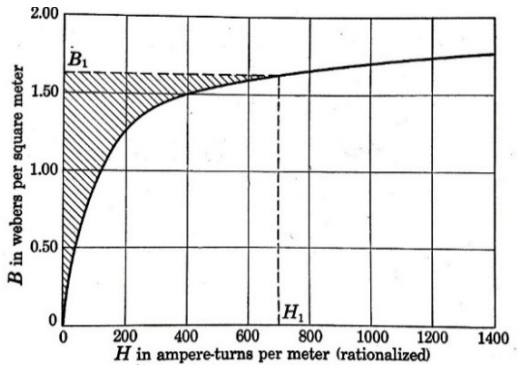


Figure 3.9: A typical magnetization B-H curve for annealed sheet steel [159].

In most of the designed CPT couplers in this thesis, ferromagnetc materials are deployed as cores or for shielding tests, such as ferrite, steel1010 type, etc. The outstanding property of ferromagnetc materials is their relatively high electrical resistivity when compared with other metals, which makes them suitable for many applications. The specific resistivity of ferromagnets ranges from $10^2$ to $10^{10}$ Ω cm, which is up to 15 orders of magnitude higher than that of iron. For example, ferrites are mixed oxides general chemical composition MeOFe2O3, in which Me stands for a divalent metal iron such as Ni, Mn or Zn. Besides, in most high frequency applications, eddy currents of ferrites are absent or negligibly small [159], which reflects the usefulness of ferromagnetc materials as cores in CPT coupling module at resonance frequencies with minimum eddy current losses counted into core losses.

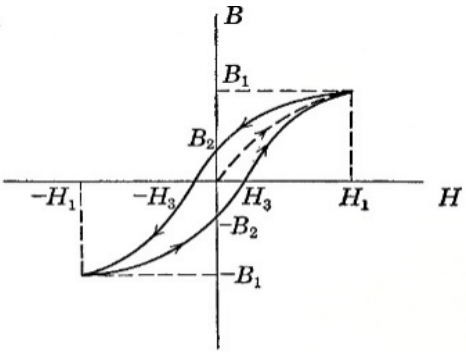


Figure 3.10: Hysteresis loop [159].

At the same time, the geometrically designed cores could be of significant help on facilitating magnetic strengths in the formed inductive electromagnetic field by shaping the flux line trajectories, which, from the perspective of electromagnetics, utilizes the most of the stored magnetic field energy leading to higher induced currents and magnetic fluxes through the secondary coil. Thereby, ferromagnetic core utilization and specially shaped coupler are expected to contribute to total improvements on addressing major objectives of high-quality CPT system designs.

## 3.4 Theoretical CPT system representations and optimizations

In order to output a highest power transferred to the load end, the first step for designing an electromagnetic resonant coupling CPT system is to select an appropriate geometric structure of coupler modular, with which then self-inductance $L_1$ and $L_2$, as well as mutual inductance $M$, can be theoretically calculated. Then the next step is to approximately determine other essential electrical parameters for the designed system. The highest value of power transferred to secondary load end in a magnetic resonant coupling CPT system is given by equation (3.3) [105],

$$\mathrm{P_L} = \frac{\omega_0 \mathrm{M^2 Q_s I_p^2}}{\mathrm{L_2}}, \tag{3.3}$$

where $Q_S$ is the quality factor of the secondary coil voltage and current after circuit tuning, $Q_S = \frac{\omega L_2}{R_L}$ for SS and PS compensation topologies and $Q_S = \frac{R_L}{\omega L_2}$ for SP and PP compensation topologies. The relation $\frac{M^2}{L_2}$ in equation (3.3) reflects the necessity of using ferromagnetic core in CPT coupler, which is for enhancing the coupling coefficient in

between the coils and the actual power transfer rating onto the load [180]–[182]. On the other hand, the relation $\frac{M^2}{L_2}$ represents the nonlinear characteristic of the magnetic coupling system and the unavoidable generation of magnetic losses [183], [184].

The following subsections will mainly focus on equations and derivations for rectangular coil based models with SS compensation topology and electromagnetic resonant coupling as most of the designs in implementations of the thesis studies are based on rectangular windings, whilst in some parts of this chapter comprehensive equations will still necessarily be given for reasons of explanations towards general CPT model designs and for overall representations.

### 3.4.1 Self-inductance and mutual inductance

Numerically and theoretically, based on Neumann's equations (3.4a) and (3.4b) [95], [185]–[187], the calculations of $L_1$, $L_2$ and $M$ can be approximated with $\mathrm{i} = 1$ for primary and $\mathrm{i} = 2$ for secondary,

$$\mathrm{L_i} = \frac{\mu_0}{4\pi} \mathrm{N_i^2} \oint\oint \frac{\mathrm{dl_1 \cdot dl_2}}{\mathrm{r_i}}, \tag{3.4a}$$

$$M = \frac{\mu_0}{4\pi} N_1 N_2 \oint\oint \frac{\mathrm{dl_1 \cdot dl_2}}{\mathrm{D}}. \tag{3.4b}$$

The equation (3.9) as a general expression of mutual inductance for two coils with dimensional difference and coupling misalignment can be applied to the designed CPT couplers for EV charging prototypes in the implementations and investigation of this thesis.

Due to actual winding structures and field flux distributions in real-world cases, calculated results according to these two equations are supposed to be slightly inaccurate only using a first approximation. Thus, in the simulation based computation method in section 3.6, more precise results can be worked out by 3D finite element method and its iterative process in order to more accurately approximate the resulted performance parameters of a CPT model. From electromagnetics point of view later, there will be different methods of calculating self-inductance and mutual inductance according to

actual magnetic field vectors and values, which will be more often used for design and analysis later in the thesis.

### 3.4.2 Total impedance

The total current absorbed by the compensated system from the front end power source can be defined as $I_s$, and $Z_T$ is the load impedance seen by the power supply. The total impedance of the compensation topology deployed for CPT system can be expressed by equations (3.5a) to (3.5d) corresponding to each of the major four compensation topologies indicated in Figure 3.4 to Figure 3.7.

$$Z_{T-SS} = \left(R_1 + j\left(L_1\omega - \frac{1}{C_1\omega}\right)\right) + \frac{\omega^2 M^2}{(R_2+R_L+j(L_2\omega-\frac{1}{C_2\omega}))}, \tag{3.5a}$$

$$Z_{T-SP} = \left(R_1 + j\left(L_1\omega - \frac{1}{C_1\omega}\right)\right) + \frac{\omega^2 M^2}{(R_2+jL_2\omega+\frac{R_L}{1+jR_LC_2\omega})}, \tag{3.5b}$$

$$Z_{T-PS} = \frac{1}{(R_1+jL_1\omega)+\frac{\omega^2 M^2}{(R_2+R_L+j(L_2\omega-\frac{1}{C_2\omega})}+jC_1\omega}, \tag{3.5c}$$

$$Z_{T-PP} = \frac{1}{\frac{1}{(R_1+jL_1\omega)+\frac{\omega^2 M^2(1+jR_LC_2\omega)}{R_L+(R_2+\mathrm{j}L_2\omega)(1+jR_L\mathrm{C}_2\omega)}}+jC_1\omega}. \tag{3.5d}$$

Regarding the power $P_L$ transferred to the load $R_L$, there must be a series of preliminary adoptions for the design parameters to achieve optimal system performance. The defined resistance of the load can be equivalent with $R_L = \frac{V_L^2}{P_L}$.

### 3.4.3 Power transferred to load end

In realistic scenarios, depending on the selected compensation topology and power source generator, the expression of output power on load is not uniquely fixed with formulations. The actual power generator would introduce a series impedance $Z_S$ accounting for addition losses to the overall system. As SS compensation topology will be mainly selected for the designed CPT prototypes in the implementations due to a number of

advantages described in Section 3.3.2. The SS circuit based schematic in Figure 3.4 can be further realistically equivalent with the system in Figure 3.11 for analysis.

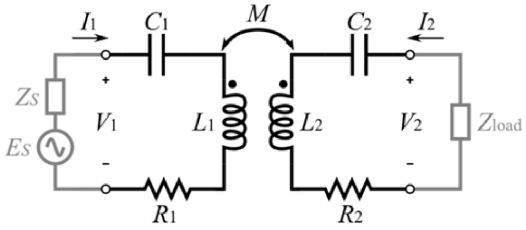


Figure 3.11: Equivalent magnetic resonant coupling CPT schematic with SS compensation in realist cases.

The maximum power transferred to the load with SS compensation circuit can be expressed by equation (3.6a),

$$P_L = -\frac{1}{2} Re[\boldsymbol{V}_2 \boldsymbol{I}_2], \tag{3.6a}$$

i.e.

$$P_L = \frac{R_L}{2} \frac{{E_S}^2}{\left(\frac{(Z_S+Z_1)(Z_2+Z_L)}{\omega M}+\omega M\right)^2}. \tag{3.6b}$$

In a real-world application, in order to optimize the power transfer capacity and achieve maximum output power on the load, with SS compensation, the load end and power source impedance can be considered as pure resistive loads meaning $X_L = X_S = 0\,\Omega$. When the electromagnetic resonance is achieved at $\omega = \omega_0 = \frac{1}{\sqrt{L_1 C_1}} = \frac{1}{\sqrt{L_2 C_2}}$ with $Z_1 = Z_1 = 0\,\Omega$, equation (3.6) turns into equation (3.7),

$$P_L = \frac{R_L}{2} \frac{{E_S}^2}{\left(\frac{R_S R_L}{\omega_0 M}+\omega_0 M\right)^2}. \tag{3.7}$$

By differentiating the second term of equation (3.7) [178] in terms of $R_L$, the maximum capacity of power transferred to load can be discussed with consideration of the load.

### 3.4.4 System efficiency

The system power transfer efficiency with SS compensation network can also be derived from basic efficiency formula and expressed as in equation (3.8a) [178], with $X_2 = \omega L_2 - \frac{1}{\omega C_2}$ and $Z_L = R_L + jX_L$.

$$\eta = \frac{P_L}{P_1} = -\frac{Re[\boldsymbol{V}_2\boldsymbol{I}_2]}{Re[\boldsymbol{V}_1\boldsymbol{I}_1]}, \tag{3.8a}$$

it can be written as

$$\eta = \frac{R_L}{R_1\frac{(X_2+X_L)^2+(R_2+R_L)^2}{\omega^2M^2}+(R_2+R_L)}. \tag{3.8b}$$

It can be found in equation (3.8b) that the nonlinear relation is between efficiency and coupling effectiveness represented by $M$. Also, the efficiency and two resistance values of windings reflect a nonlinear relationship. Significantly, it can be seen that the primary compensation capacitor is not a determinant to the system efficiency and mathematically the efficiency could be enhanced by reducing wire resistance $R_1$ and escalating coupling resonance expressed by mutual inductance $M$ here. Nonetheless, in addition to the numerically theoretical derivations, the practical calculation methods will be widely deployed in the implementations based on actual generated output waveforms for comprehensive comparisons and analyses.

### 3.4.5 Electrical parameters of the system using four compensation topologies

Based on design methodology and numerical representations, the other remaining preliminary electrical parameters derived from basic magnetic resonant coupling conditions and variables set in the beginning are given in Table 3.1 [95] for evaluations and verifications in chapters later.

Table 3.1: Electrical parameters with four compensation topologies for magnetic resonant coupling CPT model.

| | SS | SP | PS | PP |
|---|---|---|---|---|
| $I_p$ | $I_1$ | $I_1$ | $I_1 - j\omega C_1 V_1$ | $I_1 - j\omega C_1 V_1$ |
| $I_{C1}$ | $I_p$ | $I_p$ | $V_1 j\omega C_1$ | $V_1 j\omega C_1$ |
| $V_{C1}$ | $\frac{I_1}{j\omega C_1}$ | $\frac{I_1}{j\omega C_1}$ | $V_1$ | $V_1$ |
| $I_S$ | $\frac{j\omega M I_p}{R_2 + R_L + j(L_2\omega - \frac{1}{C_2\omega})}$ | $\frac{j\omega M(1 + jR_L C_2\omega) I_p}{R_L + (R_2 + j\omega L_2)(1 + j\omega R_L C_2)}$ | $\frac{j\omega M I_p}{R_2 + R_L + j(L_2\omega - \frac{1}{C_2\omega})}$ | $\frac{j\omega M(1 + jR_L C_2\omega) I_p}{R_L + (R_2 + j\omega L_2)(1 + j\omega R_L C_2)}$ |
| $I_2$ | $I_S$ | $\frac{1}{1 + jR_L C_2\omega} I_S$ | $I_S$ | $\frac{1}{1 + jR_L C_2\omega} I_S$ |
| $I_{C2}$ | $I_S$ | $jR_L C_2\omega I_2$ | $I_S$ | $jR_L C_2\omega I_2$ |
| $V_{C2}$ | $\frac{I_S}{j\omega C_2}$ | $\frac{I_{C2}}{j\omega C_2}$ | $\frac{I_S}{j\omega C_2}$ | $\frac{I_{C2}}{j\omega C_2}$ |
| $V_L$ | $R_L I_2$ | $V_{C2}$ | $R_L I_2$ | $V_{C2}$ |

## 3.5 Electromagnetic field formulations and theorems

Considering most of the designed CPT coupling modules are structured based on solenoid-type of geometry, the fundamental formulations derived from basic solenoid considerations in this section can apply to the real-situation windings later in the implementations. Some theoretical formulas defined for principle understanding and concept structuring may differ from practical computation methods for measurements and actual calculations in analytical designs and implementations.

### 3.5.1 Self-inductance and mutual inductance for solenoid-type of coils

According to Faraday's law, there will be an induced electromotive force (e.m.f.) generated when the current *I* in the solenoid changes in the coil, which is in physics supposed to oppose the change of current:

$$\mathrm{V} = -\frac{d\Phi}{dt} = -u_0 N^2 \pi r^2 l \frac{dI}{dt} = -\mathrm{L}\frac{dI}{dt}. \tag{3.9}$$

When the relation between total flux Φ and current $I$ is nonlinear or the total flux generation is activated by an alternating current, the total flux has an unproportionate relation with self-inductance and current through the coil, which is expressed as below [151],

$$\mathrm{L} = \frac{d\Phi}{dI}. \tag{3.10}$$

If the solenoid is an asymmetric and long one with the total flux proportional to the current, the self-inductance of the coil can be defined as equation (3.12):

$$\mathrm{L} = u_0 N^2 \pi r^2 l, \tag{3.11}$$

$$\mathrm{L} = \frac{\Phi}{I}. \tag{3.12}$$

In terms of mutual inductance, similarly based on two solenoids, an e.m.f. $V_2$ can be induced in the secondary coil when the total flux $\Phi_2$ changes caused by varying primary current $I_1$:

$$V_2 = \oint_{S2} E \cdot dl = -\frac{d\Phi_2}{dt}. \tag{3.13a}$$

The induced voltage $V_2$ can be expressed as below if the total flux $\Phi_2$ via a mutual inductance is not proportional to the primary current $\mathrm{I}_1$,

$$V_2 = -\frac{d\Phi_2}{d\mathrm{I}_1} \cdot \frac{d\mathrm{I}_1}{dt} = -\mathrm{M}\frac{d\mathrm{I}_1}{dt}. \tag{3.13b}$$

The incremental mutual inductance defined by $\mathrm{M} = \frac{d\Phi_2}{d\mathrm{I}_1}$ for CPT system coils with cores depends upon the B-H curve for the specific core material [150]. Besides, the actual value of mutual inductance in CPT systems is generally smaller than that in industrial transformers and ideal transformers due to a variable existence of coupling coefficient k in real world coupling applications. In practical tests, equation (3.14) is more often to be used for analysing performance of CPT systems,

$$\mathrm{M} = \mathrm{k}\sqrt{L_1 L_2}. \tag{3.14}$$

In magnetic coupling phenomena, the total flux in each coil is a sum of the flux of self-inductance and the flux of mutual inductance. Each flux linkage will be varying depending on whether a varying current exists in each winding-made inductor. For better theoretical understanding, there are constitutive relations for a pair of magnetic coupling coils between induced voltages $u_1, u_2$ and currents $i_1, i_2$ as expressed below,

$$\begin{cases} u_1 = L_1 \frac{di_1}{dt} \pm M \frac{di_2}{dt} \\ u_2 = L_2 \frac{di_2}{dt} \pm M \frac{di_1}{dt} \end{cases}. \tag{3.15}$$

It is necessary to mention that, in most of the implementation cases in the studies in this thesis, the total flux has nonlinear relation with current due to the deployment of ferromagnetic materials in the coupler and the changing current during initial periods of waveform establishments before steady status. Therefore, depending on magnitude of alternating current and its angular frequency $\omega$, the incremental self-inductance needs to be defined by $\mathrm{L} = \frac{d\Phi}{dI}$. In order to work out the values of self-inductance of real-world coils, a mathematical integration needs to be undertaken over the current filaments constituting the current in the winding wire. Nonetheless, after the designed CPT system tends to be stabilized, which can be illustrated by periodic waveform generations of electrical parameters and magnetic field parameters, the values of self-inductance on both coils can be calculated with equation (3.12). Further computations and analyses will be implemented in following chapters.

### 3.5.2 Energy storage in magnetic field

***(a) Energy density***

Considering nonlinear materials from electromagnetic field point of view, the field terms can be expressed as derivatives of energy density functions in terms of electric energy density $W_e$ and magnetic energy density $W_m$. The power energy supplied to the unit volume can be written as $W_e(D)$, a time derivative of electric flux density vector D. Then the electric energy density and magnetic energy density can be defined and illustrated in Figure 3.12.

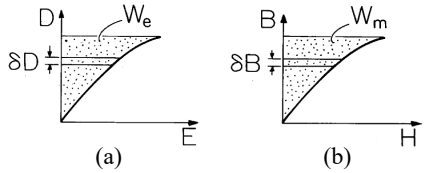


Figure 3.12: Single-valued constitutive laws indicating (a) electric energy density and (b) magnetic energy density [150].

By the integral, the function of the electric energy stored per unit volume can be expressed as:

$$W_e(D) = \int_0^D E\delta D = \int_{-\infty}^t dtE\,\frac{\partial D}{\partial t}. \tag{3.16}$$

If the magnetic field intensity vector **H** has a single-valued relation with the magnetic flux density vector **B**, then $W_m$ can be formularized [188]:

$$\frac{\partial W_m}{\partial t} = \boldsymbol{H} \cdot \frac{\partial \mathbf{B}}{\partial t}, \tag{3.17}$$

$$W_m = W_m(B) = \int_0^B H\delta B. \tag{3.18}$$

By definition and constitutive laws, the total of the electric energy and magnetic energy densities represents the total energy density of the nonlinear material-based field as equation below despite its different integral expressions in terms of Maxwell equations later.

$$\mathrm{W} = W_e + W_m. \tag{3.19}$$

***(b) Energy conservation of a coupled-coil system***

As for more realistic two coupled coils based system, relations of flux linkages and self-inductances for a linear system can be simply expressed as:

$$\begin{bmatrix}\lambda_1\\ \lambda_2\end{bmatrix} = \begin{bmatrix}L_{11} & L_{12}\\ L_{21} & L_{22}\end{bmatrix}\begin{bmatrix}i_1\\ i_2\end{bmatrix}, \tag{3.20}$$

$$\mathrm{d}\omega_m = i_1 d\lambda_1 + i_2 d\lambda_2. \tag{3.21}$$

If the roles of $i_1$ and $i_2$ are reversed along a path for all the integrations, then it is known that $L_{12} = L_{21} = M$, and equation (3.20) turns into:

$$\begin{bmatrix}\lambda_1\\ \lambda_2\end{bmatrix} = \begin{bmatrix}L_1 & \mathrm{M}\\ \mathrm{M} & L_2\end{bmatrix}. \tag{3.22}$$

For nonlinear systems, the co-energy conservation in a two-coil system in terms of flux linkages is defined as [188], [189]:

$$\mathrm{d}\omega_m = d(i_1\lambda_1 + i_2\lambda_2) - \lambda_1 di_1 - \lambda_2 di_2, \tag{3.23a}$$

$$\mathrm{d}\omega'_m = \lambda_1 di_1 + \lambda_2 di_2, \tag{3.23b}$$

therefore

$$\omega'_m = (i_1\lambda_1 + i_2\lambda_2) - \omega_m. \tag{3.23c}$$

Substitution for equation (3.20) can now give the total energy conservation of the system by equation (3.24) [136] when energy transfer coupler has the energy stored in a unity-coupled system, meaning $\omega'_m = \omega_m$:

$$\mathrm{W} = \frac{1}{2}L_1 i_1^2 + M i_1 i_2 + \frac{1}{2}L_2 i_2^2. \tag{3.24}$$

It is necessary to mention that the CPT prototypes in the thesis studies may comply with the nonlinear material based formulations and derivatives as two-coils coupling systems for analytical modelling and understanding.

### 3.5.3 Maxwell equations

It is worth introducing Maxwell equations and field fundamentals since any electromagnetic field must be governed by relations between field vectors **E**, **D**, **B** and **H** in electromagnetics, in which **E** represents the electric field intensity vector, **D** represents the electric flux density vector, **B** stands for a magnetic flux density vector and **H** represents the magnetic field intensity vector. The constitutive equations [152], [153]:

$$\nabla \cdot \mathbf{D} = \rho_{\mathrm{f}}, \tag{3.25a}$$

$$\nabla \cdot \mathbf{B} = 0, \tag{3.25b}$$

$$\nabla \times \mathbf{E} = -\frac{\partial \mathbf{B}}{\partial t}, \tag{3.25c}$$

$$\nabla \times \mathbf{H} = \mathbf{J}_f + \frac{\partial \mathbf{D}}{\partial t}. \tag{3.25d}$$

There is a constitutive relation between **B** and **H** shown as below for saturable materials like ferromagnetic cores in the magnetic field describing the behaviour of electromagnetic materials, as a supplement for the above field equations:

$$\mathbf{B} = \mu\mu_0\mathbf{H} \tag{3.26}$$

where μ is magnetic relative permeability and $\mu_0$ is permeability of free space.

While the constitutive relations for the related electric fields are [151], [190]:

$$\mathbf{J} = \sigma\mathbf{E}, \tag{3.27}$$

$$\mathbf{D} = \varepsilon\varepsilon_0\mathbf{E}, \tag{3.28}$$

where, $\nabla \times$ is curl operator; $\nabla \cdot$ is divergence operator; $\boldsymbol{J}_f$ = conduction current density; $\rho_f$ = free charge density; **J** = total current density vector; ε = relative permittivity; $\varepsilon_0$ = permittivity of free space; σ = electric conductivity. Additionally, definitions and introductions of the divergence and curl of a vector field can be found in Appendix A [191].

There are a number of other representations regarding the problem of entire domain Ω in addition to the original Maxwell equations above, which however will be introduced along with other detailed magnetic theorems in the following subsections in terms of 3D electromagnetic field magnetic vector potential methods when implementing computations for the investigations over the designed CPT prototypes in the thesis.

## 3.6 Simulations and field calculations based on 3D FEM

In order to analytically develop and assess the output performance of the designed CPT systems, the sophisticated modelling in fields is required to be undertaken using finite-element method (FEM) based electromagnetic simulation tools in the frequency domain or using finite-difference time-domain (FDTD) [192] method. FEM based platforms have been utilized for the electromagnetic simulations in the implementations of the thesis as

well as in numbers of studies in the literature due to main advantages of FEM [193]–[196] such as numerical stability, computational efficiency, ability of obtaining solution uniqueness, EMF analysis robustness, etc.

As two leading high-performance iterative software packages using FEM to solve electric and electromagnetic problems, the MagNet platform developed by Infolytica corporation and the ANSYS 3D Maxwell platform have been deployed for modelling and simulation implementations in the CPT technology investigations in this thesis.

With 2D FEM in MagNet environment, in order to solve the magnetic potentials, regions of problems are divided into a mesh of triangular elements, which are approximated by a coordinate function numerically and iteratively. For 3D problems in MagNet, the Newton-Raphson method or successive substitution were chosen to calculate and update the element permeability values when considering the method of permeability calculation and models containing nonlinear magnetic materials.

With assistance of ANSYS Maxwell software package, the electromagnetic field problems are worked out by solving Maxwell equations in a finite region of space enclosing a fundamental unit of finite unit which is known as a tetrahedron, with specific initial conditions and appropriate boundary conditions based on the solver chosen from magnetic transient, magnetostatic, electrostatic and eddy current solvers. By breaking an arbitrary geometry into simple pieces of tetrahedron as finite elements, the solution is numerically obtained with FEM. In general, a desired field in each element in 3D ANSYS Maxwell is approximated with a 2nd order quadratic polynomial function expressed as:

$$H_x(x,y,z) = a_0 + a_1x + a_2y + a_3z + a_4xy + a_5yz + a_6xz + a_7x^2 + a_8y^2 + a_9z^2. \quad (3.29)$$

In order to obtain the basis functions, the field quantities are calculated for 10 points of vertices and edges in each tetrahedron element in 3D simulation. Two matrix solution techniques are normally used as Maxwell solution methods such as the direct solver and the ICCG iterative solver, in which the former one is a default solver meaning a method of sparse Gaussian elimination and the latter one is a method of incomplete Choleski conjugate gradient for special cases.

Generally, the accuracy [197] of the solution in FEM based software packages relies on three factors: the nature of the field itself, the size of the elements defined and the element order. Higher accuracy requires smaller elements or higher element orders since the direction and magnitude of the field is changing or alternating rapidly in the regions [198]. Iterative method is the basic but powerful technique for solving EMF constitutive equations numerically.

### 3.6.1 Field equations

To investigate and analyse the CPT system outputs with its expected electromagnetic coupling performance, the electric current density **J** induced on the secondary side of the coupler model is required to be determined. Hence, the Maxwell equations constitutively expressed by Ampere's law in equation (3.30a), Gauss' law in equation (3.30b), Faraday's law in equation (3.30c) and the B-H curve relation in equation (3.30d) are required to be solved:

$$\nabla \times \mathbf{H} = \mathbf{J}, \tag{3.30a}$$

$$\nabla \cdot \mathbf{B} = 0, \tag{3.30b}$$

$$\nabla \times \mathbf{E} = -\frac{\partial \mathbf{B}}{\partial \mathrm{t}}, \tag{3.30c}$$

$$\mathbf{B} = \mu \mathbf{H}, \tag{3.30d}$$

where **H** is the magnetic field strength in ampere per meter (A/m), **B** is the magnetic flux density in tesla (T), **E** is the electric field strength in volt per meter (V/m), and μ is the permeability non-linearly depending on local value of **B** in $\mathbf{B} = \mathrm{f}(\mathbf{H})$. The electric current density **J** is in ampere per square meter ($\mathrm{A/m^2}$).

To determine the magnetic flux density **B** in electromagnetic field, according to Maxwell equations and electromagnetic theory, the expression of the flux density B in terms of vector **A** can be given as:

$$\mathbf{B} = \nabla \times \mathbf{A}, \tag{3.31}$$

where **A** is the magnetic vector potential. Note that $\nabla \times \mathbf{A}$ is a vector, also written as Curl **A** equal to $\boldsymbol{a_x}\left(\frac{\partial A_z}{\partial y} - \frac{\partial A_y}{\partial z}\right) + \boldsymbol{a_y}\left(\frac{\partial A_x}{\partial z} - \frac{\partial A_z}{\partial x}\right) + \boldsymbol{a_z}\left(\frac{\partial A_y}{\partial x} - \frac{\partial A_x}{\partial y}\right)$ in Cartesian coordinates. Curl **A** is often called the rotation of **A**. $\nabla \times \mathbf{A}$ is read as 'del cross **A**'.

Simultaneously with Ohm's law in electromagnetics by equation (3.32) and material equations of Pouillet's law by equation (3.33), the 3D finite-element method (FEM) is adopted to numerically solve Maxwell equations above and the relative material equations, using the methods of discretizing the modelled 3D space by tetrahedrons, translating the differential equations into algebraic equations [186]. The methods of semi-iterative conjugate gradient for each magnetic vector potential **A** [197], based on the initial B-H curve, constant values of μ can be selected for each finite element depending on local nonlinear value of **B** for the beginning. The flux density **B** values afterwards can be computed according to the calculated magnetic vector potential **A** by equation (3.31) derived from Gauss' law of equation (3.30b). Repeatedly, the numerical computations can be completed until the convergence of the element permeability. It is known that:

$$\mathbf{J} = \boldsymbol{\sigma}\mathbf{E}, \tag{3.32}$$

$$\mathbf{R} = \boldsymbol{\rho}\frac{\mathbf{l}}{\mathbf{C}}, \tag{3.33}$$

where $\boldsymbol{\sigma}$ is the material-dependent parameter conductivity. $\boldsymbol{\rho}$ is the resistivity of the windings. **R** is known as electric resistance of the wire material. $\boldsymbol{l}$ is the total length of the wire. **C** is the cross-sectional area of the wire.

### 3.6.2 FEM with numerical solution

FEM is a powerful numerical technique for dealing with complex geometries-based problems such the targeted topics of electromagnetics in the thesis although FEM has an origin in the field of structural analysis. The systematic generality of this FEM analysis provides with a possible method to construct general-purpose computer programs for solving a wide variety of problems. The basic FEM includes discretizing the targeted solution region into finite number of subregions or elements; deriving governing equations for a typical element; assembling of all elements in the solution region and solving the system of equations obtained [199].

As known, many real-life situations have no symmetry that simply allows a description to be made in terms of two, instead of three, independent space coordinates. These practical arrangements need to be specified with three independent coordinates with a full 3D consideration, which inevitably requires the methods of analysis involving the division of three-dimensional space into finite elements. Of course, the discretization with a specified accuracy in 3D case requires correspondingly quite large amount of central storage and processing time in computer manipulation.

In the general electromagnetics scenarios with time variation, as well as based on the differential form of Ampere's law, the fact of the enclosed curves of magnetic flux lines and all the equations above, the full set of variables represented by equations (3.30a) and (3.31) turns into equations (3.34) and (3.35), respectively, and equation (3.35) allows time-varying problems.

$$\nabla \times \left(\frac{1}{\mu}\nabla \times \mathbf{A}\right) = \mathbf{J}, \tag{3.34}$$

$$\nabla \times \mathbf{A} = -\mu\varepsilon\frac{\partial \nabla}{\partial t}. \tag{3.35}$$

Together with Faraday's law and Lorenz gauge vector potential by equation below [200],

$$\mathbf{E} = -\nabla\phi - \frac{\partial \mathbf{A}}{\partial \mathrm{t}}, \tag{3.36}$$

by using 3D FEM computations, the magnetic flux density **B**, the electric field strength **E** and the magnetic field with values of magnetic flux $\phi$ in weber can be numerically solved and determined.

Regarding the numerical solution in terms of non-linear materials in numerical technique-based simulation software, equation (3.34) is essential to be solved to specify the magnetic vector potential **A**, for which the numerical solver developed in the simulation software is required. To work out the field parameters, firstly, constant values of permeability $\mu$ are selected for each element based on the initial slope of the B-H curve of the non-linear magnetic material. Secondly, by using the semi-iterative conjugate gradient method, the magnetic vector potential **A** can be solved numerically with the resulting linear equations. Thirdly, the flux density **B** can be calculated from values of

magnetic vector potential **A** with equation (3.31), which then are used to calculate new values for the permeability of each element. Repeatedly, the numerical technique and process are to be executed until the element permeability values have converged.

### 3.6.3 Inductance calculation and flux linkage

In magnetic fields, inductance matrices can be normally expressed in terms of flux linkage and current. Values of inductance are given in henry. For nonlinear materials, the definition of inductance requires additional details when compared to linear cases. There are commonly three inductance values and concepts used for applications, which are illustrated in Figure 3.13 [201], [202].

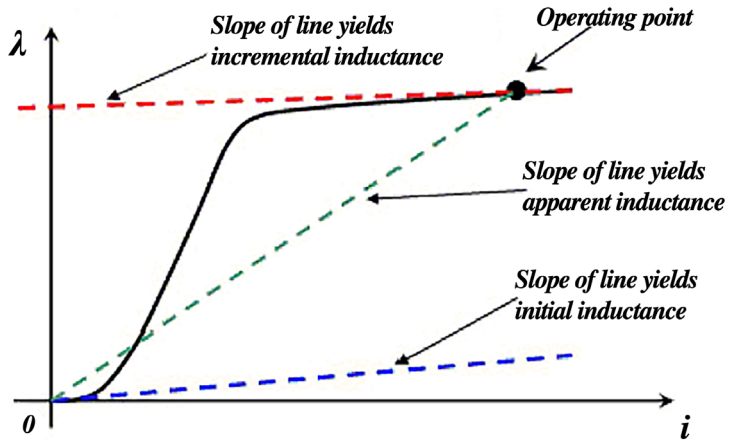


Figure 3.13: Current i vs flux linkage λ for nonlinear inductance.

In ANSYS Maxwell used in the thesis, apparent inductance is used to calculate flux linkage as a function of the independent variables as it will vary with current values due to the material properties varying. The slope of any line in Figure 3.13 has unit in henry and any enclosed area on the plot represents unit of energy in joule when the magnetic flux is in weber and current in ampere.

From a perspective of the nonlinear inductance graph, the three inductances have different definitions. Initial inductance $L_{init}$ applies to magnetic materials with a 'toe' in the magnetization curve, which in value is the tangent to the curve at the origin; Incremental (differential) inductance $L_{inc} = \frac{d\lambda}{di}$, a line tangent to the curve at the operating point, is evaluated using an operating point determined from a DC solution and is used in time domain system simulations. Incremental inductance relates to differential permeability

defined as $\frac{dB}{dH}$; Importantly in ANSYS Maxwell, apparent inductance is well-suited for the state equation or basis function approach to the time domain simulations as due to the total flux linkage in terms of current from the origin to the operating point. Although apparent inductance can be used to calculate energy, the calculated results cannot perfectly represent the stored energy since the actual path of the nonlinear curve is ignored by defined calculation of apparent inductance. In time domain simulations, apparent inductance varies with varying current shown in Figure 3.13, which can be able to track the characteristic nonlinear curve of the material by varying resulted value [136], [201].

From the practical magnetic coupling field point of view, in order to determine the self-inductance values of L in henry produced by the electromagnetic field on the both sides of the CPT system, the relations between the coil current values of $i$ and the flux linkage λ satisfy:

$$\lambda_1 = \mathrm{N}_1\phi_1 = \mathrm{L}_1 i_1, \tag{3.37a}$$

$$\lambda_2 = \mathrm{N}_2\phi_2 = \mathrm{L}_2 i_2, \tag{3.37b}$$

$$\mathrm{L} = \frac{\lambda}{i}. \tag{3.37c}$$

### 3.6.4 Magnetic field energy storage in terms of fields B and H

It is necessary to introduce and explain the transformed forms of expressions of magnetic field energy in terms of magnetic fields **B** and **H**, despite of the formularized expressions of magnetic field energy in terms of current $i$ and flux linkage λ that are described before in last subsections.

For a single long solenoid-type of winding coil, the total energy stored in the magnetic field is:

$$W_{total} = \frac{1}{2}LI^2 = \frac{1}{2}u_0N^2\pi r^2 lI^2, \tag{3.38}$$

where the $N$ is the turns per unit length, each of radius $r$ has a current $I$ flowing and the winding is $l$ long in the field. $\boldsymbol{B} = u_0NI$ and $\boldsymbol{H} = NI$ are field magnetic density and field

strength intensity inside the solenoid-type of winding [150]. Thus, equation (3.38) turns into the form:

$$W_{total} = \frac{1}{2} BH\mathcal{V} = \frac{1}{2} \int \boldsymbol{B} \cdot \boldsymbol{H}\, dv, \tag{3.39}$$

where $\mathcal{V}$ is the volume of the solenoid, the integral is taken over all space. The energy stored in a magnetic field may be considered to be distributed with an energy density $\frac{1}{2}\boldsymbol{B} \cdot \boldsymbol{H}$ and the total energy is stored in the whole field.

In 3D FEM field solutions for cases of linear material properties, the integrals of magnetic energy of a system are expressed simply. In linear materials, permeability $u$ is constant so that values of the magnetic energy and co-energy are identically equal, namely $W = W_c$, as shown in Figure 3.14(a). The field energy and co-energy is given:

$$W = W_c = \frac{1}{2} \int \boldsymbol{B} \cdot \boldsymbol{H}\, dv. \tag{3.40}$$

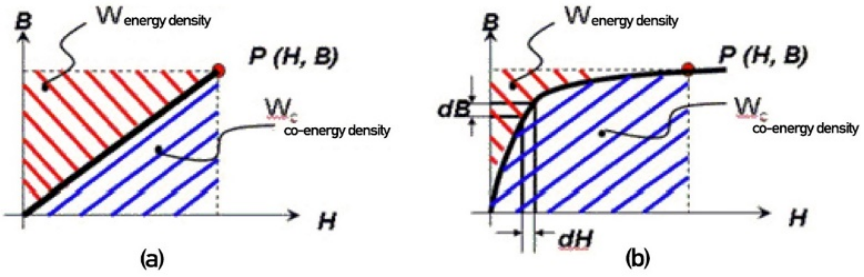


Figure 3.14: Energy and co-energy. (a) Linear materials; (b) Nonlinear materials.

However, in nonlinear materials-based fields like the proposed CPT system in this thesis, the field energy stored is given by equation (3.41) and the co-energy is mathematically expressed by equation (3.42).

$$W = \int w \cdot dv = \int (\int_0^B \boldsymbol{H} \cdot d\boldsymbol{B}) dv, \tag{3.41}$$

$$W_c = \int w_c \cdot dv = \int (\int_0^H \boldsymbol{B} \cdot d\boldsymbol{H}) dv. \tag{3.42}$$

### 3.6.5 RMS real powers and efficiencies

In addition, based on RLC circuit theories [136], [203] and circuit resonance conditions [204], [205], the approximate natural resonant frequency for the designed coupling

system in this paper can be determined in order to specify power source operating frequencies, which then is for analysis and optimization of the actual system performance.

To study the actual inductive magnetic coupling outcomes and electromagnetic field performance represented and reflected by the numerical vectors and scalars above, the actual RMS power generations given by equation (3.43) and the efficiencies given by equation (3.44) and (3.45) from the front end to the load end of the CPT system are required to be calculated, compared and analysed. cos φ is the power factor (PF) caused by phase difference $\varphi$ between the induced voltage and current waveforms.

$$\mathrm{P}_{RMS} = \mathrm{V}_{RMS}\,\mathrm{I}_{RMS}\left|\cos\varphi\right|, \tag{3.43}$$

$$\eta_{Coupler} = \frac{\mathrm{P_{RMS}}_{Secondary\ coil}}{\mathrm{P_{RMS}}_{Primary\ coil}}, \tag{3.44}$$

$$\eta_{Overal\ system} = \frac{\mathrm{P}_{Load}}{\mathrm{P_{RMS}}_{Power\ supply}}. \tag{3.45}$$

$$f_{natural\ resonant} = \frac{\omega_0}{2\pi} = \frac{1}{2\pi\sqrt{LC}}. \tag{3.46}$$

## 3.7 Chapter conclusions

This chapter describes the fundamental computation methods by setting forth the main electromagnetic theories and formulas that are to be essentially deployed in the thesis.

In the main simulation-based studies in the thesis, the designed coupling models and computations are solved by 3D FEM, in which the series of integral equations mentioned above in this chapter are adopted. Nonetheless, the practical experiments by laboratory setup prototypes in the thesis are investigated and calculated using actual output data acquisition, data processing and theoretical calculations based on real-world waveform generated in terms of magnitudes and angular phases, which will be further studied in the following four chapters of design implementations, result analysis and laboratory experiments.

# Chapter 4 Implementations for optimizing the basic designs of CPT coupler

## 4.1 Coupler design improvements with ferrite cores for CPT of EVs

As mentioned in Chapters 2 to 3, the comparatively up to date CPT technologies for EVs charging and the project methodology need to be investigated from the aspects of maximizing the charging system efficiency, power transfer rating levels and air gaps of charging coupling coils. Until present, the different coil designs, ferrite core deployments, operating frequencies and airgaps are acting as the main investigation factors regarding producing transfer efficiencies and power ratings on the load side.

In section 4.1, by modelling and simulating the electromagnetic field couplings with the simplified inductive transmitting system in 3D finite-element methods based environment, an Axis-to-Axis (Coaxial) rectangular coil CPT system and an Axis-Parallel (Non-coaxial) rectangular coil system have been modelled and quantitatively compared. Besides, an axis-parallel coil system and a C-Type rectangular coil system deploying ferrite cores with a 50 mm air gap have been analysed, resulting in output system efficiencies of over 85% and 74%, respectively. In addition, the effectiveness of using a ferrite core to improve the flux linkage and magnetic flux density can be noticed. From the perspective of electromagnetic field, the contributions of evaluating and deploying natural resonant frequencies of transmitting ground side and vehicle chassis receiving side in terms of system efficiency, magnetic field strength generated and RMS actual power transfer rating have been described and discussed.

### 4.1.1 Background

Greenhouse gases caused by more than 100 years of gasoline engine vehicles and the rapidly increasing scarcity of fossil energy in the past decades have driven the research progress in the field of electric vehicles (EV), hybrid electric vehicles (HEV) and hydrogen fuel cell vehicles (FCV) to target at environmental friendly transportation. Although the plug-in and battery electric vehicles (PEV) have been proposed and become

more pervasive worldwide, the inherited drawbacks of plug-in charging system such as safety issues, inconvenience, inflexibility in some particular situations would be the obstacle in the development of EVs. Therefore, the imaginational idea of Nikola Tesla — Wireless Power Transfer (WPT) technology has been proposed to contribute to the contactless charging solutions for EVs, which is remarkable for the future transportations, based on the formulation of Maxwell's equations in which Maxwell described radio wave phenomena in 1862 [33], and Poynting theorem in which Henry Poynting illustrated electromagnetic waves as an energy flow in 1884.

CPT technologies have been believed to become a feasible alternative to deliver power for battery charging ranging from small low-powered devices to high-powered applications over the past decades due to the foreseen reliance and many other advantages as described in previous chapters. However, some issues and challenges of current CPT prototypes have not yet been adequately addressed and comprehensively resolved from theoretical levels to practical applications despite some immature contactless energy transmission techniques that have been applied to small devices nowadays.

Reportedly in various technical publications, the stationary electromagnetic resonance coupling WPT operating at MHz range was proposed by WiTricity (MIT) theoretically in 2006 [120]. An IPT system (2009) in [206] is presented with a 5 kW power transfer rating operating at 38.4 kHz over an air gap of 150 mm. The authors in [207] focused on a system with a 10 mm air gap and 20 kHz operating frequency, which transfers 3 kW at 80% efficiency. ORNL Laboratory tested with high-frequency inverter, misalignment effects, coil-to-coil efficiency and insertion loss of ground surface materials in the air gap were discussed in [107]. A 2 kW prototype with use of inductively coupled power transfer (ICPT) in Sallan's research group [95] was deployed to check different compensation topologies and an efficiency of 82% with 15 cm charging distance was achieved in 2009. By 2012, Sallan and Villa's team, using the same 2 kW prototype, found that a series-parallel-series (SPS) combination compensation topology showed a suitable performance for the CPT system [170]. Misalignment conditions and charging gap variations were discussed in [208], a loosely coupled transformer (LCT) IPT system was tested when the air gap varies from 6 to 20 mm and the misalignment varies from 0 to 50 mm, in resulting an efficiency deviation of 3.5% for a proposed asymmetrical LCP prototype. Investigators

in [47] proposed a polarized coupler topology called double D couplers, using a flux pipe winding structure. A 1.5 kW CPT system with a core called H-shaped in paper [209] was developed to be more robust to misalignment conditions and more efficient, achieving an efficiency of over 90% with a charging distance of 70 mm. In addition, the H-shaped core winding previously mentioned was proved, by the same research group, that the H-shaped coil appears to have lower iron loss and copper loss than traditional solenoid coils in reference [210] in 2011. In [211], a DD pad design with Bi-polar was measured to have the same performance as a circular pad design via a series of the technical tests and comparisons between circular, solenoid and DD-DDQ/bi-polar coil architectures.

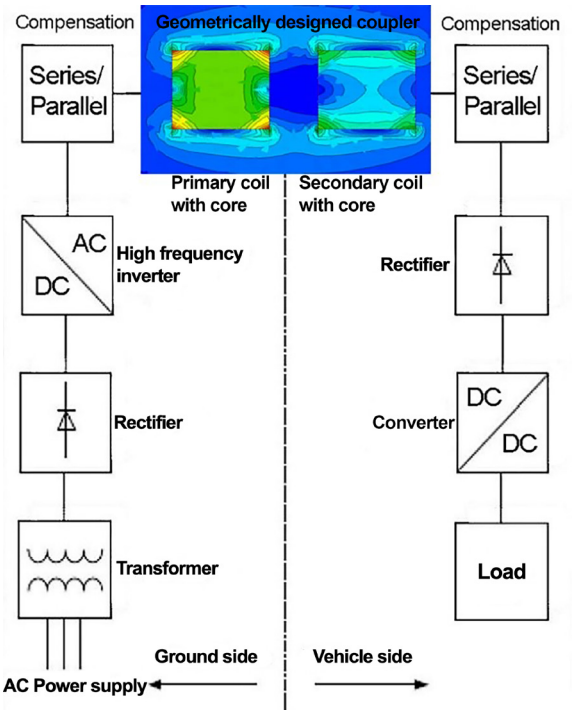


Figure 4.1: A typical stationary CPT system with a geometric coupler design.

### 4.1.2 Designs and results of proposed CPT systems with inductive coupling

Based on methodology and formulations described in detail above in the previous chapter, stationary CPT systems can be analytically established and modelled for investigations from each aspect that are required to be focused on. With field equations, inductance calculation methods and advantages of using ferromagnetic cores introduced before, three types of models with ferrite cores (axis-to-axis, axis-parallel and C-type) are structured and operated in this Section 4.1 for investigations.

Figure 4.1 illustrates the typical comprehensive CPT system layout for stationary cases, which could also be equivalent to the schematic circuit with a selected S-S compensation shown in Figure 4.2. In most cases including the designs in this Section 4.1, S-S topology is supposed to optimally perform for CPT outputs based on the introduction in Section 3.3 and 3.4.

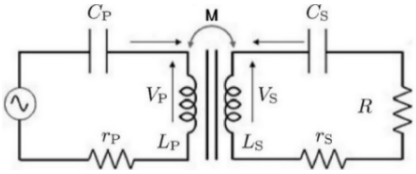


Figure 4.2: The equivalent circuit of a stationary CPT system with S-S compensation.

***(a) Axis-to-axis coils with ferrite cores***

In order to achieve high overall system efficiency, satisfactory power level delivered and larger air gap, the coil design can take a lead role to the objectives as it determines the electromagnetic field in between the primary coil and secondary coil. Considering the normal use of ferrite core in conventional transformers, the effectiveness of shaping the magnetic flux of deploying ferrite cores can also work for contactless power transfer applications to facilitate the inductive coupling performance.

The basic design parameters: the air gap is 50 mm and voltage power source supplies sinusoidal AC 10 kV rms in the electromagnetic environment of MagNet 7.6, the series for primary side and series for secondary side 150 uF capacitors (S-S compensation method) are adopted as compensation topology. The coil turns are 1500 on both sides, the load is a 50 Ohm resistor.

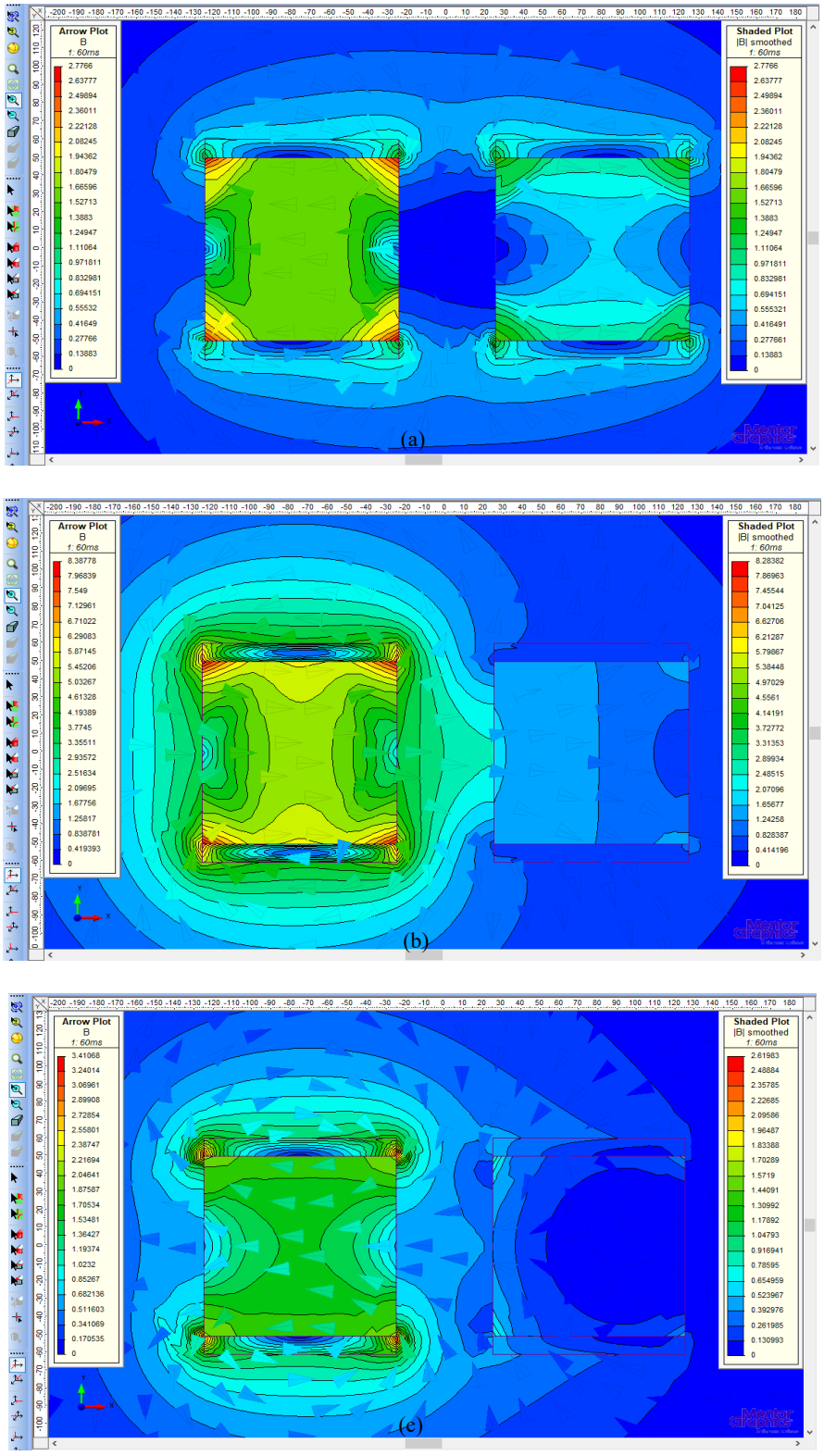


Figure 4.3: Axis-to-axis coil models with 50 mm air gap at selected frequencies. (a) At 75 Hz. (b) At 2 kHz. (c) At 50 kHz.

Therefore, the designed small-scale coils with ferrite cores of different shape and size have been undertaken and simulated in 3D finite-element method software. Figure 4.3(a)

to Figure 4.3(c) selectively show the electromagnetic field statuses of the conventional axis-to-axis (coaxial) coils with square soft ferrite at 75 Hz, 2 kHz and 50 kHz.

Table 4.1: Calculated main results for axis-to-axis coils system vs operating frequency range of 75 Hz-50 kHz.

| Operating frequency (Hz) | Calculated inductance L1 (H) | Calculated inductance L2 (H) | Power transferred to load (W) |
|---|---|---|---|
| 75 | 0.298168 | 0.1268340 | 21083.6 |
| 150 | 0.296989 | 0.0620210 | 4446.0 |
| 300 | 0.296735 | 0.0307398 | 1058.2 |
| 800 | 0.296673 | 0.0112169 | 139.4 |
| 2000 | 0.296702 | 0.0039281 | 16.9 |
| 10000 | 0.296805 | 0.000304339 | 8.583e-2 |
| 50000 | 0.296820 | 0.000027416 | 1.504e-4 |

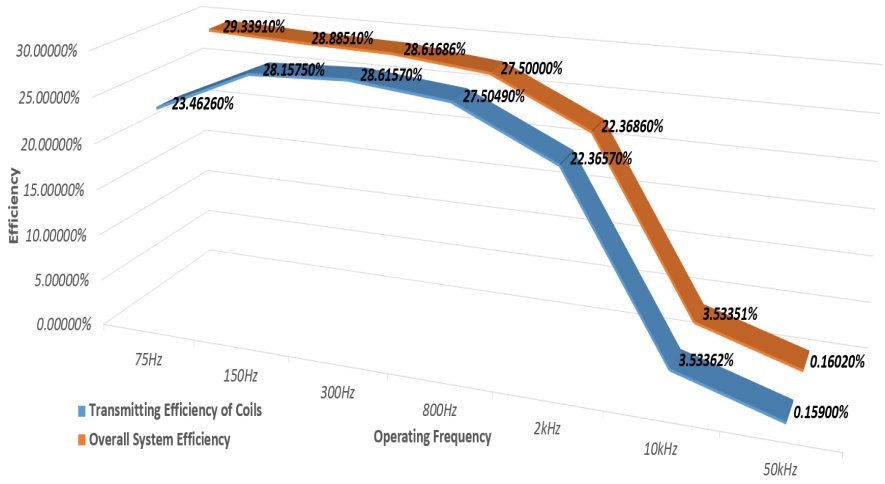


Figure 4.4: Efficiencies of axis-to-axis (coaxial) coils with ferrite cores vs operating frequencies (model with 50 mm air gap).

By simulating MagNet prototypes with axis-to-axis coupler designs across the frequency range of 75 Hz to 50 kHz with 50 Ohm load and series-series compensation capacitance (S-S method), the computed field results can be output by using 3D finite-element method, as presented in Figure 4.3, Figure 4.4 and Table 4.1, which illustrate the system efficiency of about 29.34% and power transfer of about 21.08 kW. It can be observed that the magnetic flux density B when electromagnetically coupling is up to 2.78 teslas at the power supply operating frequency of 75 Hz. The effectiveness of using ferrite cores to

the CPT inductive coupling could be shown by the differences of fields the power transferred to the load side.

To investigate the system performance from electromagnetic field point of view, three typical frequencies are selected to compare the actual fields and outputs via simulation raw RMS scalar results shown in Table 4.2 and also via vector results depicted in Figure 4.3(a) to Figure 4.3(c). It can be noticed that the CPT system is able to deliver high ratio of secondary coil flux linkage and primary coil one, which reflects relatively satisfactory coil energy transmission efficiency. The magnetic field density can show a high value of over 8 teslas at an operating frequency of 2 kHz, however a low ratio between secondary and primary flux linkage can be seen. A higher and stronger magnetic energy generation and storage in field can be noticed at 2 kHz than 75 Hz and 50 kHz, while the highest power transferred to load is produced at 75 Hz, which also reflects sometimes higher field energy storage may not lead to higher transmission efficiency from the front end to the rear load end. There is supposed to be a comprehensive comparison and balance over choosing relatively accepted operation conditions towards overall targets from both electric and magnetic aspects.

Table 4.2: Major outcomes of fields at selected frequencies at transient 60 ms.

| Operating frequency (Hz) | Flux linkage primary (webers) | Flux linkage secondary (webers) | Magnetic energy (joules) | Magnetic coenergy (joules) | RMS field B maximum (teslas) |
|---|---|---|---|---|---|
| 75 | 10.1488 | 8.4151 | 367.6821 | 372.9431 | 2.7766 |
| 2000 | 83.7845 | 19.4138 | 14167.48 | 18760.74 | 8.2838 |
| 50000 | 19.7121 | 0.3512 | 648.6949 | 648.7873 | 2.6198 |

***(b) Axis-parallel coils with ferrite cores***

To further compare the different dimensions, coils positions and coupling performance with the flux shape effect of ferrite cores, the transmitting coil and receiving coil are adjusted to be in axis-parallel (non-coaxial), other geometric parameters are set the same as the previous axis-to-axis (coaxial) coils prototype. Then the simulation results appear to be changed and the maximum power transfer efficiencies are improved by at least 3% at 75 Hz, 150 Hz and 300 Hz as shown in Table 4.3 and Figure 4.6. It can be noticed, from Figure 4.5, that the maximum value of the field magnetic flux density in the 75 Hz

electromagnetic coupling is increased to about 5.76 teslas, which is significantly higher than 2.78 teslas in the axis-to-axis coils model in Section 4.1.2(a). This may also reflect the noteworthy effectiveness of this geometric improvement of the transmitting part of the CPT system when compared with the traditional axis-to-axis (coaxial) coil design. Also, the new axis-parallel (non-coaxial) coils with the ferrite cores model shows better capability to produce more optimistic actual power transfer to the load side, which is of help on the charging time for electric vehicles in service.

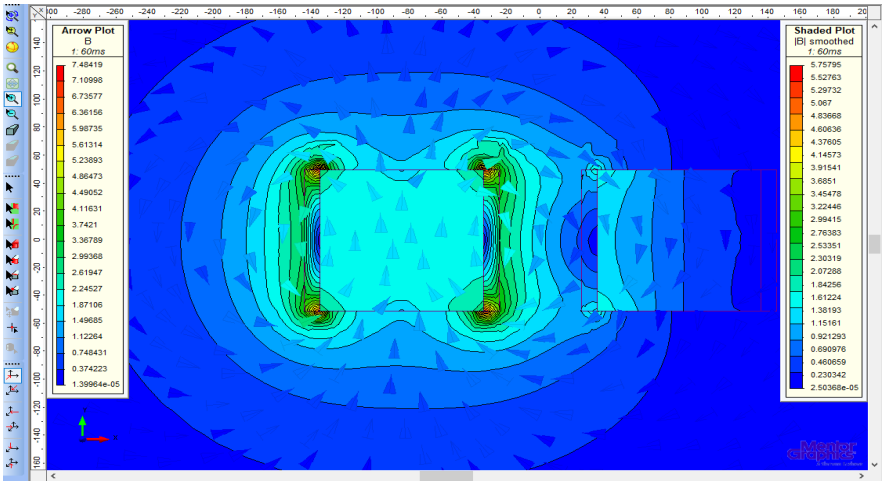


Figure 4.5: Axis-parallel coils CPT prototype with its optimal efficiency performance at 75Hz, 50mm air gap.

Table 4.3: Calculated main results for axis-parallel coils system vs operating frequency range of 24 Hz-50 kHz.

| Operating frequency (Hz) | Calculated inductance L1 (H) | Calculated inductance L2 (H) | Power transferred to load (W) |
|---|---|---|---|
| 24 | 0.320270 | 0.48407 | 1941160.0 |
| 35 | 0.307560 | 0.29793 | 246085.9 |
| 75 | 0.298100 | 0.12683 | 24259.0 |
| 150 | 0.296750 | 0.06202 | 5120.902 |
| 300 | 0.296464 | 0.030740 | 1218.9675 |
| 800 | 0.296393 | 0.112340 | 160.563 |
| 2000 | 0.296430 | 0.003928 | 19.4744 |
| 10000 | 0.296546 | 0.003043 | 9.8870e-2 |
| 50000 | 0.296563 | 0.000027415 | 1.7325e-4 |

It also could be found that the calculated natural resonant frequency of primary side slightly changes, based on $f_c = \frac{1}{2\pi\sqrt{LC}}$, as calculated inductance L1 insignificantly changes. The calculated natural frequency of primary side keeps at about 23.9Hz. However, another finding is that the natural resonant frequency of secondary side can be influenced notably, as illustrated in Table 4.3, by changing the power source operating frequency. The natural resonant frequency of secondary side can nonlinearly vary from 18.67 Hz to 2.48 kHz, depending on the different inductive coupling situations driven by different system operating frequencies.

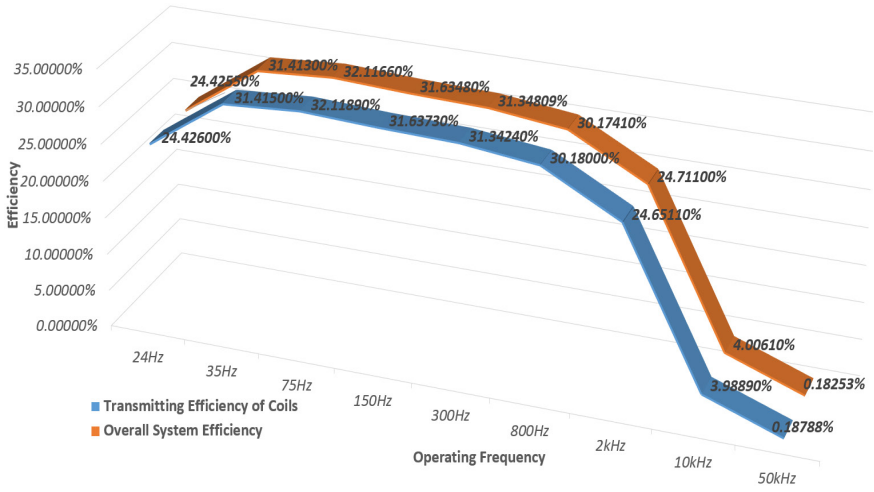


Figure 4.6: Efficiencies of axis-parallel (non-coaxial) coils with ferrite cores vs operating frequencies (model with 50 mm air gap).

***(c) Axis-parallel coils with ferrite cores and increased natural resonant frequencies as operating frequency***

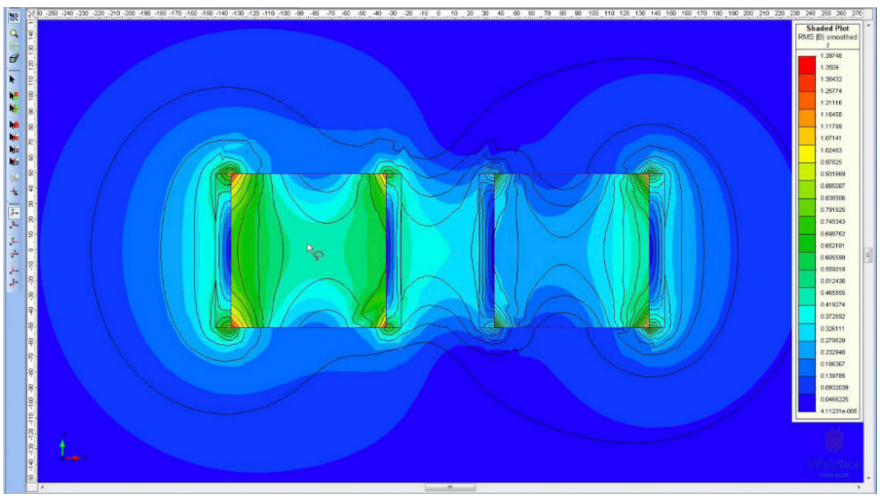

Figure 4.7: Axis-parallel 150 nF S-S compensation CPT system with 10 kV rms at 930 Hz.

In order to increase the natural resonant frequencies of primary and secondary circuits to observe the CPT system performance and results, according to $f_c = \frac{1}{2\pi\sqrt{LC}}$, the series-series compensation capacitors C1 and C2 have been decreased to 150 nF. In this set of simulation experiments, the natural resonant frequency of primary side is supposed to be escalated from previous 24 Hz to approximate 1.5 kHz for contrast analysis. The electromagnetic field simulation and calculated results can be presented in Figure 4.7, Figure 4.8 and Table 4.4.

Table 4.4: Calculated main results for axis-parallel coils system with smaller C1, C2 vs operating frequency range of 300 Hz-10 kHz.

| Operating frequency (Hz) | Calculated inductance L1 (H) | Calculated inductance L2 (H) | Power transferred to load (W) |
|---|---|---|---|
| 300 | 0.32599 | 1.879040 | 1.8350 |
| 750 | 0.19368 | 0.302800 | 29.3019 |
| 930 | 0.25790 | 0.197765 | 17087 |
| 1500 | 0.28890 | 0.077270 | 129976.9 |
| 10000 | 0.29642 | 0.001929 | 1.0115e-2 |

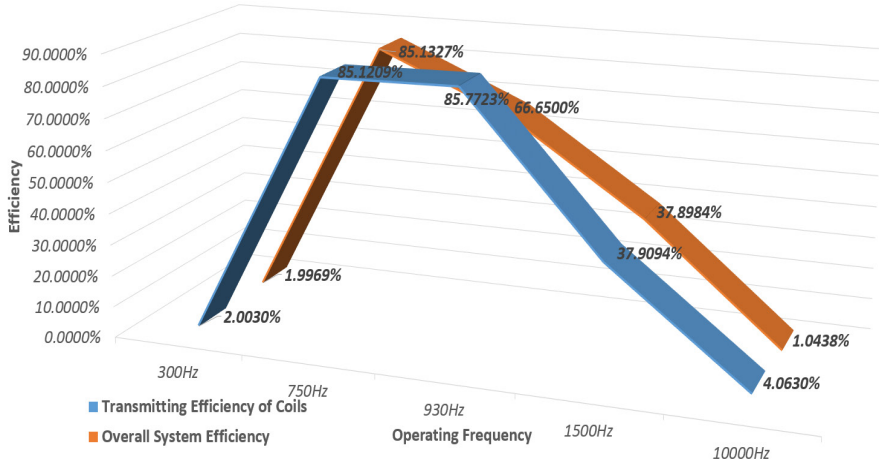


Figure 4.8: Efficiencies of axis-parallel (non-coaxial) coils with ferrite cores and smaller C1, C2 vs operating frequencies (model with 50 mm air gap).

It can be seen that, when the operating frequency is set between 750 Hz and 930 Hz, the system efficiency can be over 85% with 29.3 W power transferred to the load. While the power level on the load is able to reach the highest, 129.9 kW, at 1500 Hz power source operating frequency as shown in Table 4.4, which is slightly outside of the natural resonant frequency range of primary transmitting side. From Figure 4.8, it also can be

found that the system efficiency reaches the maximum at around the natural resonant frequency of primary coil side although the power transferred to the load does not achieve its optimal value at the frequency. Therefore, the maximum value of power transferred to the load tends to occur when operating frequency is set around the resonant frequency range, which could mean faster charging for electric vehicles, but the energy losses would be a trade-off leading to the system efficiency of about 38%.

From the aspect of magnetic field, the field performance of this axis-parallel model with higher natural resonant frequency appears to be fairly satisfactory due to optimistic results of its instantaneous magnetic energy, coenergy, primary flux linkage, secondary flux linkage and B field, with values of 3419.59 joules, 3422.65 joules, 46.70 webers, 9.20 webers and 5.76 teslas, respectively. This may reflect the usefulness of escalating the natural resonant frequency of the same geometric model despite of the manufacturing challenges over the desired capacitors due to current material engineering limitations which would probably be tackled in a decade.

***(d) C-type coils with ferrite cores***

To achieve a higher secondary flux linkage as presented in equation (3.37b), (3.37c), and a stronger magnetic flux density as in equation (3.31), the ferrite cores could be designed like C-shape style as it is more capable to produce more flux lines through both coils and cores with better inductive coupling or even resonant performance. The transmitting coil and receiving coil are adjusted to be in axis-parallel (non-coaxial) again but the inner side surfaces of ferrite cores are shaped like in Figure 4.9, other geometric parameters are set the same as the axis-parallel (non-coaxial) coils prototype in Section 4.1.2(c) above. The air gap is 50 mm and the voltage power source supplies a sinusoidal AC of 10 kV rms, Series for primary side and series for secondary side 150 nF capacitors (S-S compensation method) are adapted as compensation topology. The windings are 1500 turns on both side, and the load is a 50 ohm resistor.

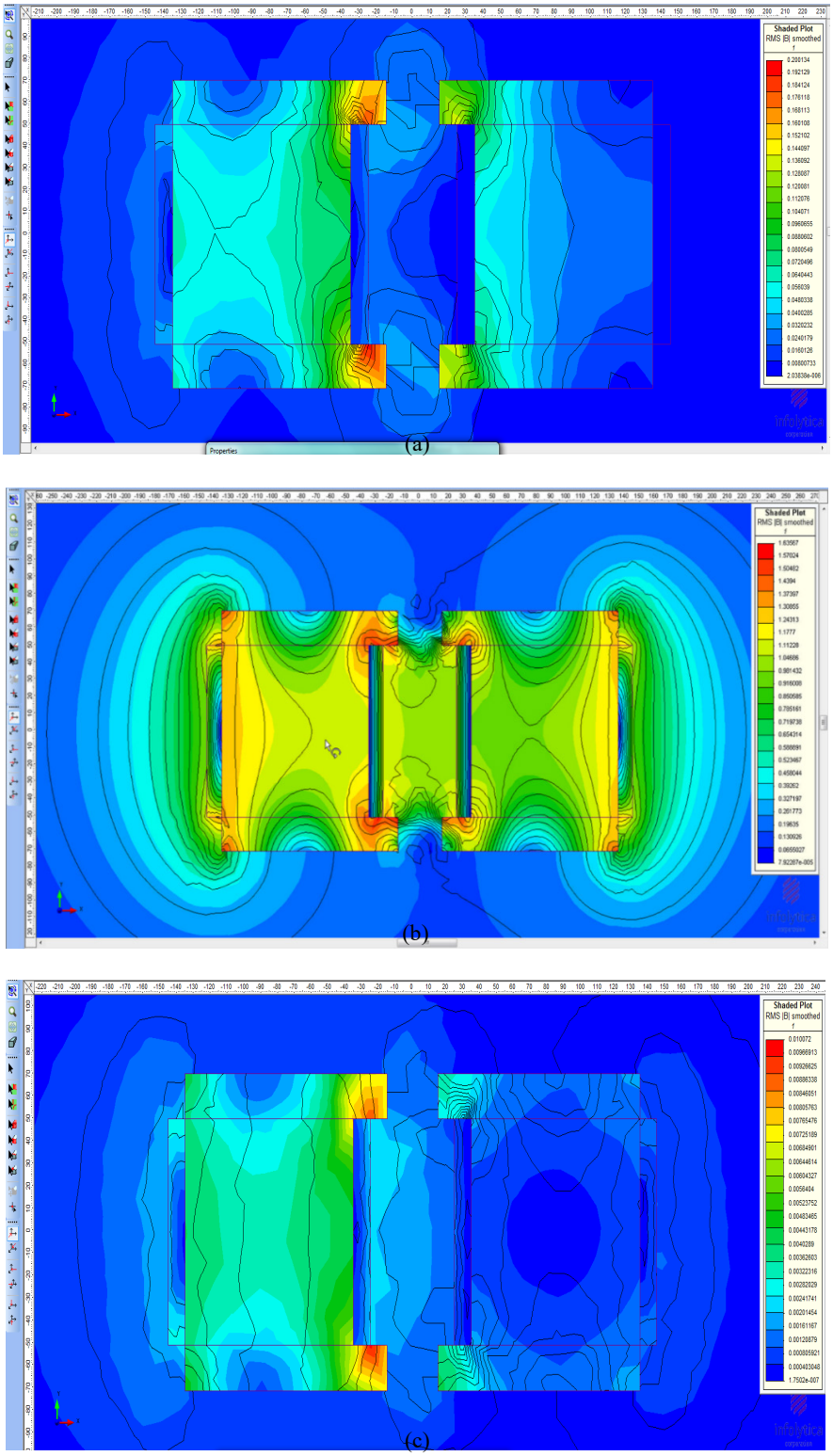


Figure 4.9: Electromagnetic fields of C-type cores at a variety of operating frequencies. (a) at 150 Hz. (b) at 800 Hz. (c) at 30 kHz.

Table 4.5: Calculated main results for C-type axis-parallel coils system vs operating frequencies.

| Operating frequency (Hz) | Calculated inductance L1 (H) | Calculated inductance L2 (H) | Power transferred to load (W) |
|---|---|---|---|
| 60 | 0.58899 | 46.91279 | 0.64368e-3 |
| 150 | 0.59960 | 7.50527 | 0.20788 |
| 300 | 0.65382 | 1.87657 | 47.73737 |
| 400 | 0.77028 | 1.05557 | 3723.97592 |
| 800 | 0.32165 | 0.26411 | 46234.20821 |
| 1000 | 0.38168 | 0.16912 | 1345.19544 |
| 1200 | 0.40419 | 0.11752 | 407.52901 |
| 1500 | 0.41924 | 0.075300 | 152.62980 |
| 1700 | 0.42451 | 0.058680 | 98.54954 |
| 2000 | 0.42934 | 0.042470 | 59.94127 |
| 2500 | 0.43362 | 0.027263 | 32.91586 |
| 3000 | 0.43584 | 0.019010 | 21.09762 |
| 7000 | 0.43981 | 0.36880e-2 | 3.35692 |
| 10000 | 0.44024 | 1.92297e-3 | 1.61871 |
| 30000 | 0.44063 | 0.35952e-3 | 0.17741 |
| 50000 | 0.44065 | 1.95996e-4 | 0.63798e-1 |
| 100000 | 0.44067 | 9.35266e-5 | 0.15942e-1 |
| 150000 | 0.44068 | 6.17841e-5 | 7.08514e-3 |

It can be noticed, from Figure 4.9(b) and Table 4.5, that the new geometrically designed coil with a ferrite core generates up to 1.84 teslas of magnetic flux density B and 46.23 kW system power when electromagnetically coupling at about the natural resonant frequency of 800 Hz. The maximum value of magnetic flux density and the system power rating to the load in the C-type inductive coupling model are much higher than those of axis-parallel models before, which is now along with the efficiency of 74%, in Figure 4.10, could reflect that the improved C-type model can be able to produce better inductive coupling performance for contactless power transfer on electric vehicles. In addition, the stable and sustainably satisfactory system efficiencies can be achieved by a longer range of power source operating frequency.

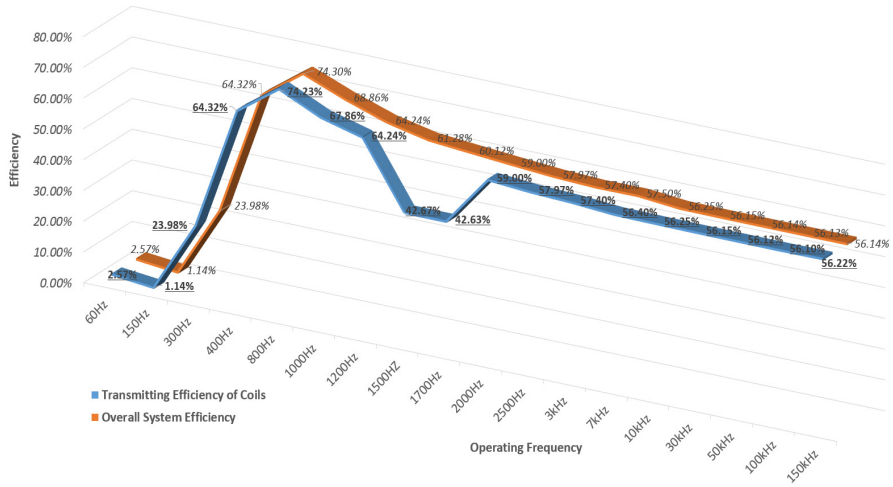


Figure 4.10: Efficiencies of C-type axis-parallel (non-coaxial) coils with ferrite cores vs the operating frequencies (model with 50 mm air gap).

Moreover, in this C-type coupler system, at the same transient time point, the instantaneous magnetic energy is 1471.36 joules. Its instantaneous coenergy is 1742.96 joules. Its primary and secondary flux linkages are 37.66 webers and 6.97 webers, respectively. The RMS value of the magnetic field density B is 3.88 teslas. It can be seen, by comparison with the previous axis-parallel model at resonant coupling condition or at maximum power output condition, that the peak power output and field performance of the C-type one when resonating at 800 Hz seem smaller than those of axis-parallel model at its resonant frequency of 1500 Hz, while the corresponding system efficiency of C-type model with value of 74.30% is evidently far higher than 37.89% of axis-parallel model when at their own resonant condition, 800 Hz and 1500 Hz, respectively. This could indicate that satisfactory electromagnetic field generation may not determine better power electrical output when analytically comparing two different geometric coupler-based CPT systems. Considering constant and sustainable outputs of power transfer ratings and overall system efficiency, the relatively longer range of frequency versus efficiency and output power by the C-type model shows more compatibility and capability for real-world CPT charging applications. Nonetheless, other flaws of the C-type coupler model can be compromised by other less significant factors.

### 4.1.3 Limitations and evaluations

Conducting 3D FEM based simulations for coils with ferrite core materials is numerically complicated and computationally intensive, hence solving the simultaneous equations would not reduce computational inaccuracies which can depend on the mesh element size,

the characteristics of materials, the conjugate gradient tolerance, the polynomial order adopted, boundary conditions, etc.

When considering the overall losses, the iron losses including hysteresis losses and eddy-current losses are not taken into account in this Section 4.1, which depend on the hysteresis characteristics of materials, the specific resistance and frequency. In addition, the copper losses count on the total losses. The winding copper losses on both side have been taken into account while the loss of the system circuits has not, which may reduce the overall system efficiency.

In real world application, the misalignment affects the electromagnetic coupling. The coils of the models in this section are ideally set towards each other. Whereas in reality, the misalignment degree could increase the reduction of power transfer efficiency depending on how the primary coil and secondary coil inductively couple by the actual flux linkage generated. Also, the different dimensions of the coil design on ground side and vehicle side would produce uncertainties regarding the effective distance of inductance.

### 4.1.4 Summary

The analytical CPT models deploying ferrite cores with 50 mm air gap have been proposed for charging EVs. An axis-to-axis (coaxial) rectangular coil CPT prototype, an axis-parallel (non-coaxial) rectangular coil CPT prototype and a C-type prototype have been built and analysed. Evidently, the effect of dimensions of coils with ferrite cores plays a significant role in a CPT system, determining the flux linkage and magnetic flux density in an electromagnetic field system generated by inductive coupling, which indirectly affects the maximum system efficiency, power transfer rating level to the load end. A couple of CPT models in electromagnetic field have been studied with 3D FEM techniques and series-series capacitance compensation configuration in this Section 4.1.

Comparing the axis-to-axis (coaxial) coil CPT system with axis-parallel (non-coaxial) coil CPT system, the maximum power transfer efficiencies are improved by at least 3% at 75 Hz, 150 Hz and 300 Hz. The maximum value of the field magnetic flux density in the 75 Hz electromagnetic coupling is increased to 5.76 teslas, which can reflect the

noteworthy effectiveness of the newer geometric improvement of a coil-ferrite core to a CPT system. It has been seen that the inductance of primary coil could not be affected significantly by using different operating frequencies while the inductance value of secondary (vehicle) side can be noticeably influenced by varying power source frequencies.

Setting higher natural resonant frequency by using smaller compensation capacitors and offering the system with an operating frequency that is in close proximity to the natural resonant frequency of primary side can contribute a high efficiency to the system and can boost the magnetic field density. The new geometrically designed C-type coils with ferrite cores can generates up to 1.84 teslas of the magnetic flux density and 46.23 kW of system power when operating at about the natural resonant frequency, maximizing the system efficiency and sustaining it between 56% to 74% within a fairly wide range of power source operating frequency. The results of C-type coil model with a ferrite core indicates the electromagnetic effectiveness of shaping the flux lines and strengthening the flux linkage by using the C-shaped ferrite core, which would be an optimal geometric option for the transmitting part of a CPT system for EVs in real applications. Also, in a real-world application, some unavoidable compromises need to be considered, such as the trade-off between the maximum power transfer rating to the load end and the optimized overall system energy efficiency.

From the perspective of electromagnetic field and inductive coupling, an axis-to-axis (coaxial) rectangular coil CPT, an axis-parallel (non-coaxial) rectangular coil CPT and an optimized C-type CPT system with ferrite cores have also been investigated and evaluated with electromagnetic field performance outputs. The limitations of the design optimization methods are discussed. Further investigations would remain on improving the power transfer rating, charging air gap and effective system efficiency in terms of iron losses, ohmic losses, energy stored in the electromagnetic field, misalignments and generated phase angles of induced currents and voltages on both sides of the actual CPT systems.

## 4.2 A novel H-shaped CPT system with soft ferromagnetic material cores and electromagnetic resonant coupling for EVs

Section 4.2 describes a novel contactless power transfer (CPT) system with geometrically improved H-shape ferromagnetic cores and electromagnetically prospective modelling analysis methods for wireless power transmitting (WPT) applications of electric vehicles (EVs). A CPT prototype, using optimized H-shaped magnetic couplers and series-to-series (SS) compensation, is proposed to address and ensure the maximization of system efficiency, power transfer ratings, and air gaps of coupling coils.

By focusing on the main factors such as various system operating frequencies, different geometric designs of coils, changeable inductive coupling distances, electromagnetic field performances and actual phase angle deviations when the inductive coupling system tends to be stable with its waveforms, this small-sized H-shape CPT system has been analytically modelled in a finite-element method (FEM) environment, resulting in a maximum system efficiency of 59.5%, a coil transmitting efficiency of 83.8% and a maximum power output of 42.81 kW on the load end when the resonant coupling of CPT system tends to occur within a range of calculated resonant frequencies, with an air gap of 10 mm. Moreover, the system efficiency and coil transmitting efficiency can reach 47.75% and 77.22%, respectively, and the highest RMS real power to load can achieve 31.95 kW with an air gap of 20 mm. Besides, with an air gap of 30 mm, this H-shape CPT system is measured to output 20.39 kW RMS power, along with the maximum system efficiency and coil efficiency of 41.78% and 63.23%, respectively.

Furthermore, the improvements of flux linkage, magnetic flux density regarding the actual electromagnetic performance produced and the issues on the calculated natural resonant frequencies have been studied by result analysis and comparison of electromagnetic field parameters generated. In addition, the current limitations and further design considerations have also been discussed in this section.

### 4.2.1 Background

Based on the wireless power transmitting (WPT) proposed by Nikola Tesla, the fundamental principles of Faraday's law of induction and Maxwell's equations [150],

[151] in the 19th century, the contactless power transfer (CPT) using loosely coupled inductive energy transfer or electromagnetic resonant coupling could show the main advantages such as wireless charging convenience and charging implementation safety especially in dusty or humid conditions. Numerous studies and industrial applications worldwide have been carried out in the past two decades. A 2 kW circular pads based inductive power transmitting (IPT) model with 700 mm diameter windings and 200 mm charging air gap was constructed and tested in 3D FEM software in [58], which examined that this circular pad modular can result in satisfactory outputs and that the result difference between the simulation and experiment tests was claimed within 10% despite no detailed discussions about RMS real power ratings.

In order to cancel out the reactive power generation from inductive coupling system to increase the RMS real power to the load end, four basic capacitor compensation topologies have been introduced and studied, which are primary series to secondary series (SS), primary series to secondary parallel (SP), primary parallel to secondary series (PS) and primary parallel to secondary parallel (PP) circuits. In [212], a current source based SP compensation IPT system was built, resulting in an output of 200 W at 100 kHz with up to 88% excluding inverters. An innovative primary series-parallel to secondary series (SPS) combination compensation topology was proposed in a large sized IPT system with 15 cm air gap [170] and was claimed to show a high tolerance to misalignment degree. To allow voltage source based inverters to produce constant AC current from the primary side of a CPT system, an inductor-capacitor-inductor (LCL) network was embedded with an SP compensation, which was reported to achieve a constant current waveform independent of the load end value variations [213] and to minimize the reactive currents in the pickup coil [46]. A larger dimension stationary CPT system model in laboratory was designed in [139] with width of 200 cm and length of 100 cm, which was reported to acquire an output power of 15 kW with an air gap of 15 cm and a lateral displacement tolerance of 40 cm. The study in [95] compared the four compensation performances with a 2 kW model and suggested that the SS compensation method has lower copper loss than the other three methods, which also attempted to identify an optimal system configuration for the designed CPT application and obtained an efficiency of about 80% using the rectangular coil based inductive battery charging system. To improve power transfer capability and efficiency, a dual side control IPT scheme was proposed in [109] based on

decoupling and primary track current control [214], validating a 7% efficiency improvement with 813 mm diameter circular power transmitting pads and each winding of 1300 strands.

To improve inductive power transfer performance and produce higher coupling misalignment tolerance, conventional flat circular coils were adopted for the energy pickup CPT system designed in [130], [183]. The experiments in [212] verified a coreless spiral coil IPT system using current-source-supply series-to-series (I-SS) and series-to-parallel (I-SP) compensation schemes, by which the 200 W IPT model achieved an efficiency of up to 88% excluding its inverter at a non-magnetic coupling frequency, 100 kHz, as reported. Generally, the larger the effective coupling area is, the higher mutual inductance value is, a large circular coupler IPT system was built with a coil diameter of 700 mm and a coupling charging distance of 200 mm, which was reported to yield a transfer power of 2 kW [47], [215].

In this Section 4.2, the H-Shaped magnetic couplers with a series-to-series (SS) compensation has been fabricated and implemented in order to address the main challenges of maximizations of the system efficiency, power transfer ratings, and air gaps of coupling coils. By analysis and comparison on the experimental results and system performance, firstly, the improvements of the flux linkage, magnetic flux density and flux line distribution can be noticed due to the contributions of using soft magnetic material core Steel1010 and the effectiveness of its high permeability for the overall system electromagnetic performance enhancement. Secondly, the specifically designed H-shaped cores could be of significant help on facilitating magnetic strengths at critical points in the formed inductive electromagnetic field by shaping the flux line trajectories, which, from the perspective of electromagnetics, utilizes the most of the stored magnetic field energy leading to higher induced currents and magnetic fluxes through the secondary coil. Thirdly, it can be found that the maximum system efficiency and power transfer to load could be reached when the system operating frequency is set close to, but not exactly to, the calculated resonant frequency of the primary coil. Nevertheless, in some cases of near-field coupling such as the models with 10 mm and 20 mm coupling distances in this section, the maximum system efficiency and power rating can be achieved twice at two peaks, respectively, which could be caused by the combined effects of the superposed

fields from two coils and by the actual real-time power factors (PF) resulting in various RMS real powers. Furthermore, as the secondary coil resonant frequency is increasing in terms of higher strengthened coupling, approximating the system operating frequency to the calculated secondary coil resonant frequency may contribute to the second peak values of efficiency and power.

### 4.2.2 System overview

***(a) System structure***

Regarding the actual overall performance of a CPT system and the electromagnetic field characteristics generated in real world applications, the inductive coupling modular could play a significant role whilst the wireless energy transmitting phenomenon occur due to the contributions of the continual magnetic flux generations and the effectiveness of inductive coupling within the non-linear ferromagnetic core materials and in between the coupler coils.

By optimally shaping the flux line trajectories and forming the flux distributions using H-shape soft magnetic cores, the actual flux linkages and induced currents can be indices to enhance the inductive coupling performance in real-world CPT scenarios. Specifically, the high permeability and low core loss of soft ferromagnetic materials could contribute to flux linkage and magnetic flux density in order for the CPT system to produce an optimized electromagnetic field performance especially when the electromagnetic resonant coupling tends to occur at specific conditions [75]. A stationary CPT system layout using the designed H-shape coupler with four compensation topologies (series-to-series, series-to-parallel, parallel-to-series and parallel-to-parallel) has been shown in Figure 4.11. A series-to-series (SS) compensation has been selectively adopted to implement the investigations in the study through this section.

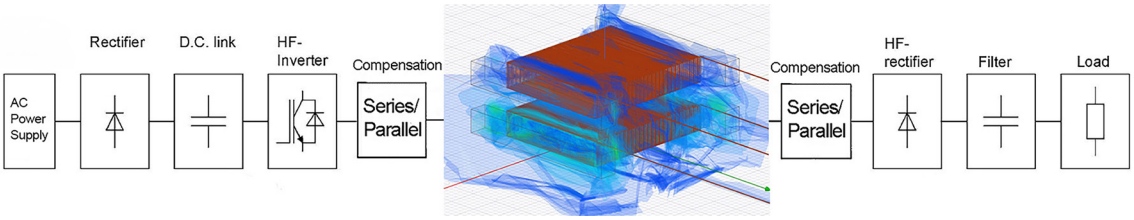


Figure 4.11: The system structure for the CPT prototype using an H-shaped coupler.

To analyze the inductive coupling performance of the proposed CPT system, based on the RLC circuit theories, the impedance matching principle and the initial system tests with calculations for conditions of approaching electromagnetic resonant coupling, the designed system circuit parameters have been configured with both the compensation capacitors set as 150 nF. The load is set with a resistor of 50 ohm and a voltage source with an RMS value of 5 kV has been adopted as the system power supply.

***(b) Geometric design for couplers***

As mentioned above, the particularly shaped soft ferromagnetic core with analytical geometry design and characteristics of high permeability and low core loss can be able to form the magnetic flux paths as expected in order to facilitate the generations of flux linkage, magnetic flux density and field strength. Therefore, the Steel1010 with a relative permeability μ of 1000 is employed as the ferromagnetic core material in this coupling modular built in the software package ANSYS 3D Maxwell as shown in Figure 4.12.

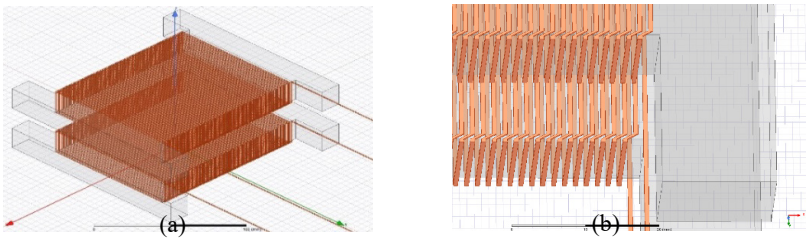


Figure 4.12: The H-shape coupler prototyped in 3D FEM environment. (a) An overview of the coupler. (b) Details of windings.

Besides, considering the benefits of proximity effects mitigation, skin effects reduction and high frequency application capability, Litz wire is adopted for the windings in this prototype. The geometric model design parameters of the small sized magnetic coupler have been specified in Table 4.6 below.

Table 4.6: The geometric specifications of the designed H-shape couplers for the CPT system.

| Parameters | Values |
|---|---|
| Winding size | 100 mm x 100 mm x 20 mm |
| Soft magnetic core size | 150 mm x 150 mm x 20 mm |
| H-shaped core bar size of each side | 150 mm x 15 mm x 20 mm |
| Primary winding number of turns | 80 turns |
| Secondary winding number of turns | 80 turns |
| Air gaps of the CPT charging system | 10 mm, 20 mm and 30 mm |

### 4.2.3 Results and analyses

It is well-known that the charging distance affects the inductive coupling performance in applications by flux line distributions and effects in between the intermediates. In this Section 4.2.3, in order to investigate the actual resulted relation between the air gap change and the overall system outputs, a 30 mm, a 20 mm and a 10 mm air gap CPT model have been built and implemented for analysis.

***(a) EMF performances with analytical comparisons***

◆ Field of 30 mm air gap H-shape model based on electromagnetic metrics

By shaping the magnetic flux lines enclosed through the both coils and air space in between the transmitter side and receiver side with particularly shaped ferromagnetic material cores, the magnetic resonant coupling status of the coupler tends to occur when the system is supplied with operating frequencies being approximated to the calculated natural resonant frequency. With the electric circuit parameters predefined and an initial set of tests for tracking the approximate value of self-inductance $\boldsymbol{L_1}$ [75] in order to manually approximate the derivation of the natural resonant frequency of the primary coil side [134], [166], thereby the formal simulations versus a range of operating frequencies can be carried out and statistically recorded.

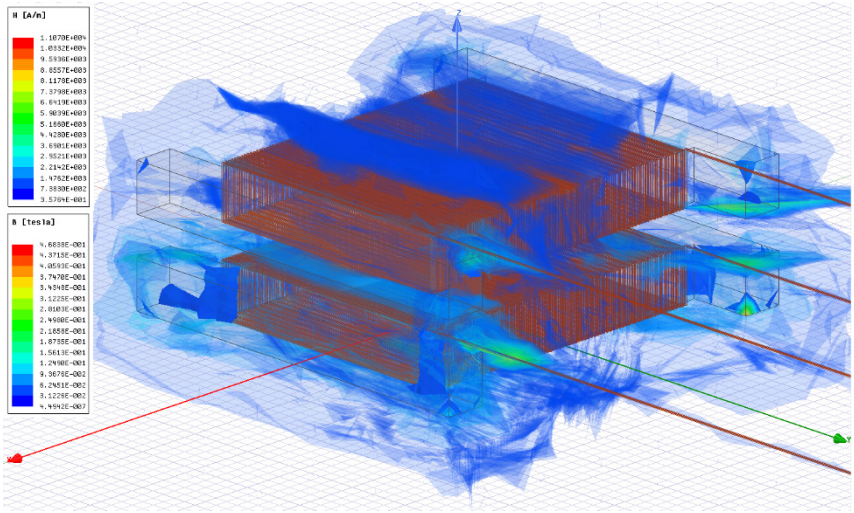


Figure 4.13: The electromagnetic field overlays for the designed H-shape couplers for the CPT system at the operating frequency of 8000 Hz, with an air gap of 30 mm.

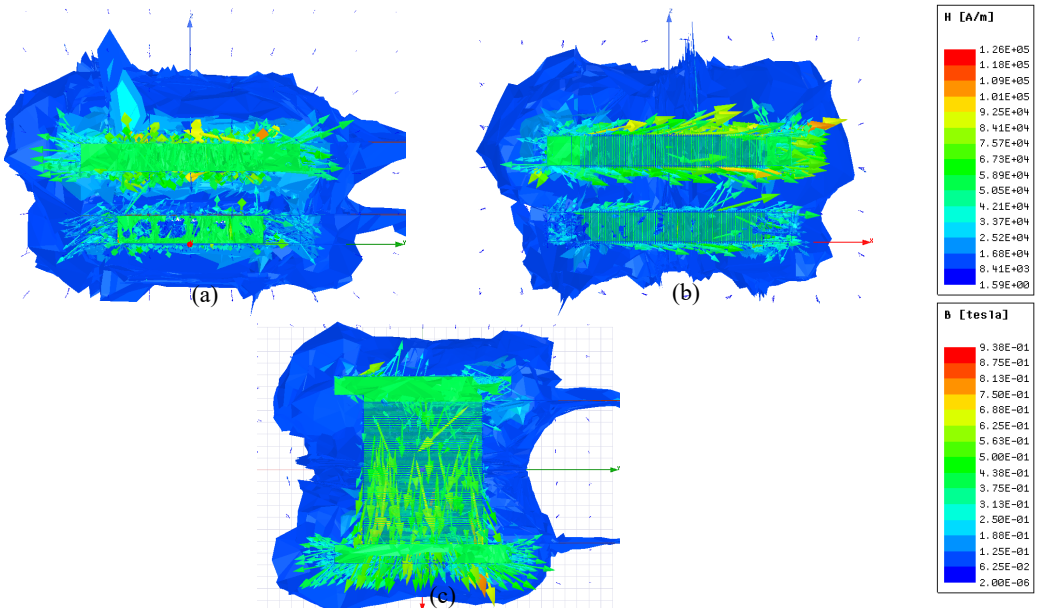


Figure 4.14: The front (a), left (b) and top (c) views of the field for the designed H-shape couplers for the CPT system at the operating frequency of 8000 Hz, with an air gap of 30 mm.

At about the calculated resonant frequency of 8 kHz, the CPT system appears to operate at a very high degree of proximity to its magnetic resonant coupling status as the generated electromagnetic field strongly tends to be producing peak RMS values of each alternating output parameters. As can be seen in Figure 4.13 and Figure 4.14, the 30 mm air gap CPT coupler shows satisfactory EMF outputs at this condition, with a magnetic flux density **B** of 0.47 teslas and a magnetic field strength **H** of 10.07 kA/m at some specific positions in the field space, by which highly reshaped and contoured EMF flux distributions throughout the air region and both the windings are to be established. It can be seen that the H shape cores form the flux line trajectories and field vectors as significantly expected, which witnesses the effectiveness of the geometrically enhanced design and utilization of the ferromagnetic material.

◆ Field of 20 mm air gap H-shape model based on electromagnetic metrics

It can been noticed that the actual electromagnetic field performance has been significantly promoted in terms of the magnetic field strength **H** and the magnetic flux density **B** in Figure 4.15 and Figure 4.16.

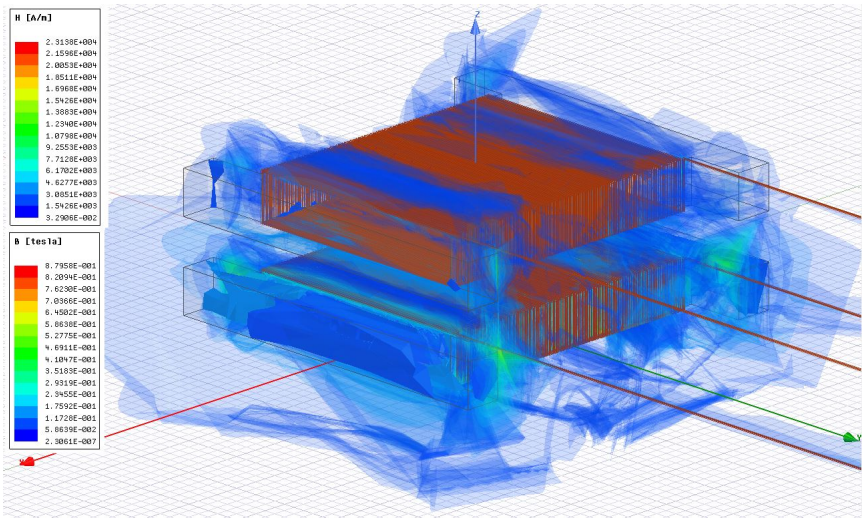


Figure 4.15: The electromagnetic field overlays for the designed H-shape couplers for the CPT system at the operating frequency of 7000 Hz, with an air gap of 20 mm.

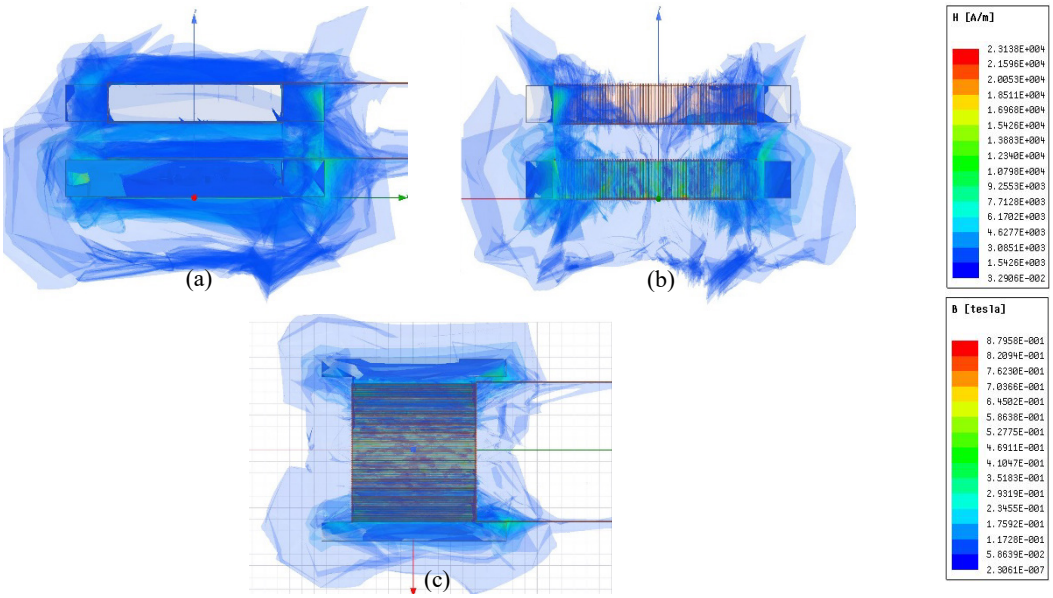


Figure 4.16: The front (a), left (b) and top (c) views of the field for the designed H-shape couplers for the CPT system at the operating frequency of 7000 Hz, with an air gap of 20 mm.

Compared with the generated values in Figure 4.13 of the 30 mm air gap model, similarly when the entire modular magnetic field with its output waves tend to be stable after a few transient periodic times of operation, the maximum magnetic flux density **B** has risen to a peak value of 0.88 teslas at the H-shape edge sides in Figure 4.16(a)-(c) at about the natural resonant frequency of 7000 Hz, which is much higher than 0.47 tesla in the 30 mm distance model shown in Figure 4.13. Moreover, the maximum value of the magnetic field strength **H** in the 20 mm distance model is also markedly improved to 23.14 kA/m, which is more than a double of the peak value of the 30 mm air gap model.

◆ Field of 10 mm air gap H-shape model based on electromagnetic metrics

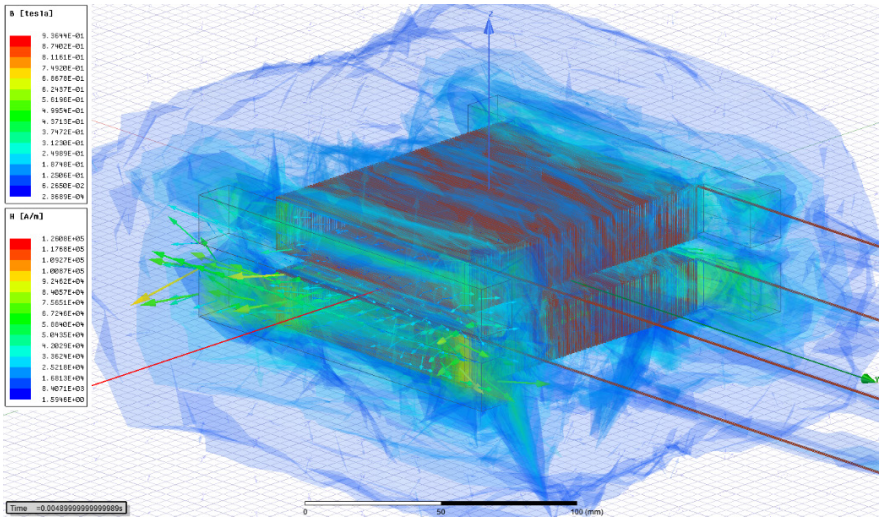

Figure 4.17: Electromagnetic field overlays of the CPT coupler with an air gap of 10 mm, at 8000 Hz.

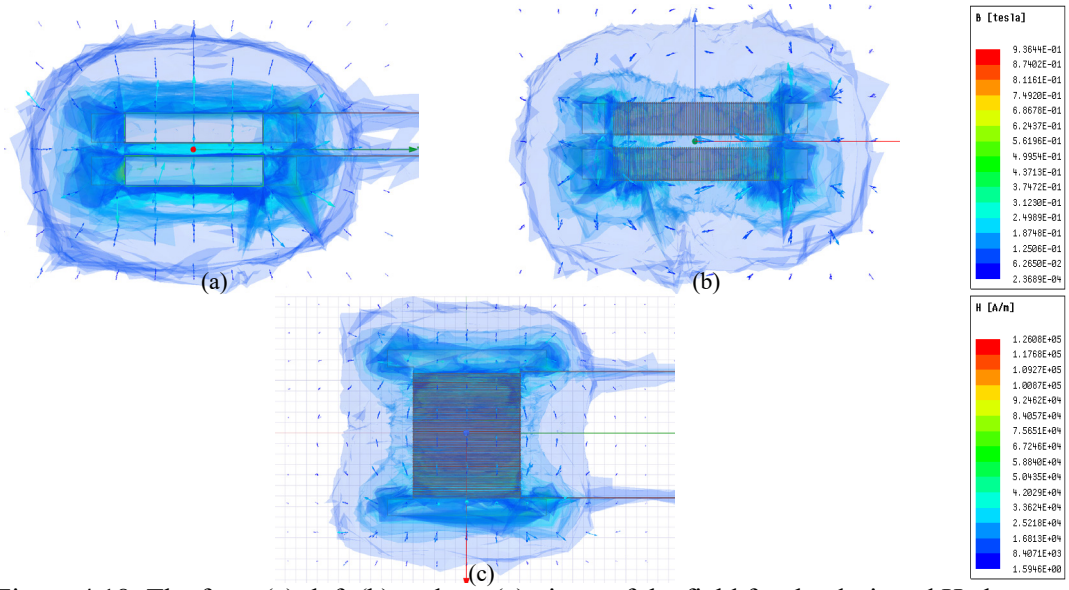


Figure 4.18: The front (a), left (b) and top (c) views of the field for the designed H-shape couplers for the CPT system at the operating frequency of 8000 Hz, with an air gap of 10 mm.

As presented in Figure 4.18, by the effects of flux line forming of the H-shape cores, both the vector arrows of magnetic flux density **B** and magnetic field strength **H** tend to be able to reach their peak magnitude values at the edged corner of the very end points of the H-shape cores, with maximum scalar values of 0.94 teslas and 126.08 kA/m, respectively, at about the natural resonant frequency of 8000 Hz.

Along with the 10 mm air gap field overlay views presented in Figure 4.8 (a) to (c), it can be found that the magnetic flux density **B** in the primary core and winding seems much

higher than those in Figure 4.13 of 30 mm one and Figure 4.15 of 20 mm one. Furthermore, the magnetic field strength **H** values shown from Fig. 8 (b) and (c) in both primary and secondary windings appear to be very strong especially at the bar sides of the H-shape cores towards each other. This effect reflects the effectiveness of using H-shape ferrite cores, in addition to manipulating a closer charging distance and approximating the calculated resonant frequency of the system towards improving the magnetic field outputs, both of which indirectly facilitates the electric power generations and efficiencies.

◆ Optimized flux linkage and currents – 10 mm air gap

To investigate the optimally actual electromagnetic field system performance of the CPT coupler proposed, the flux linkage λ and coil current $i$ are required to be addressed. Based on Faraday's law of induction in electromagnetics and equation (3.37a)-(3.37c), the changing magnetic flux ϕ that causes electromotive force (e.m.f.) and flux linkage λ is determined by the electric field strength **E** and the magnetic field density **B**. Thus, analyzing the actual changing status of the system in electromagnetic field in Figure 4.17 and observing the flux linkage waveforms in Figure 4.19, with reference to the induced current waveforms in Figure 4.20, can be proper methods to evaluate an optimal CPT system's characteristics with a 10 mm air gap at about the natural resonant frequency, 8000 Hz, of this specific prototype.

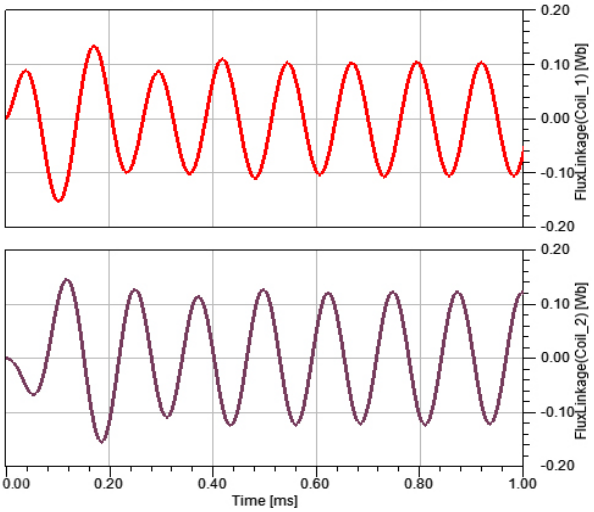


Figure 4.19: Flux linkage waveforms of the 10 mm air gap CPT system at 8000 Hz.

From Figure 4.19, it can be found that both the alternating flux linkage waveforms of two coils tend to be stable sinusoidal AC waveforms since about 0.5 ms onwards, which means the CPT system electromagnetic stability is able to be immediately established after only 4 periods. Once the outputs tend to be AC stable, the amplitudes of the flux linkages have been measured to be 0.10 Wb and 0.12 Wb for the primary coil and secondary coil, respectively, which are corresponding to RMS values of 0.07 Wb and 0.08 Wb.

From the current waveforms presented in Figure 4.20, similarly, both the primary coil and secondary coil currents tend to be AC stable after 4 periodical waveforms, reaching amplitudes of 34.57 A and 41.73 A, corresponding to RMS values of 24.44 A and 29.5103 A, respectively.

Based on the Figure 4.19 and Figure 4.20, compared to the long-time need of a full charging cycle for the EV batteries, 0.5 ms is time transient and can be negligible. In other words, this 10 mm air gap H-shape CPT system could accomplish a fast inductive coupling matching towards constant stable AC power transfer for EVs once the vehicle receiving side is started for CPT charging.

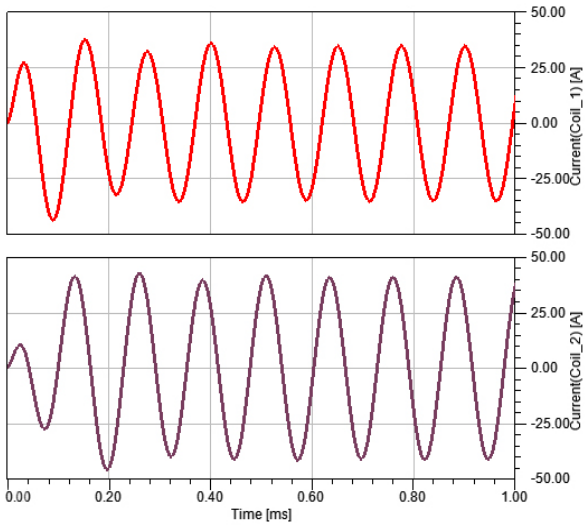


Figure 4.20: Current waveforms of the 10 mm air gap CPT system at 8000 Hz.

Besides, it can be noticed that the RMS flux linkage of the secondary coil is higher than the primary coil by 0.01 Wb and the RMS current of the secondary coil is 5.07 A higher than the primary coil as well, which could be mainly due to the contributions of SS compensation capacitors and the alternating field energy stored in the space since the

initial coupling of about 0.3 ms. Nevertheless, when considering the phase differences of actual real-time voltages and currents on both sides, the calculated RMS power of the secondary side is lower than the primary side due to the power factor (PF) $\cos\varphi$ corresponding to the reactive power's $\sin\varphi$ that is for the continually establishing and sustaining the optimistic electromagnetic field of the CPT system.

***(b) Analysis on flux linkages and currents for different air gaps versus various operating frequencies***

In this investigation, the H-shape coupler CPT prototypes with 10, 20 and 30 mm air gaps, across various ranges of operating frequency, have been implemented and analyzed. The system performances at electromagnetic resonant coupling conditions have also been emphasized in each model by peak values and characteristic trends.

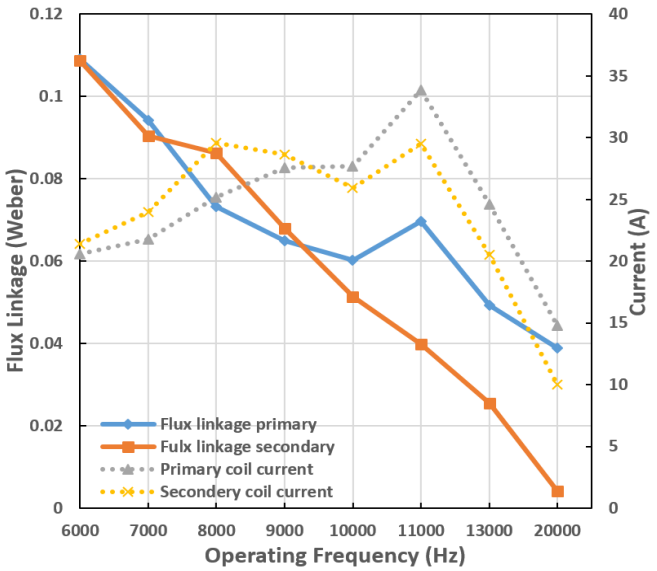


Figure 4.21: Flux linkages, currents vs operating frequencies for the 10 mm air gap model.

From Figure 4.21, it could be seen that the secondary coil current could have two peak values at 8 kHz and 11 kHz, which are 29.57 A and 29.52 A, respectively. The primary coil current reaches its maximum value of 33.84 A at the operating frequency of 11 kHz. However, both the primary and secondary flux linkages show decreasing tendencies when the operating frequency supply increases although there is one salient point with value of 0.07 Wb for the primary linkage at 11 kHz.

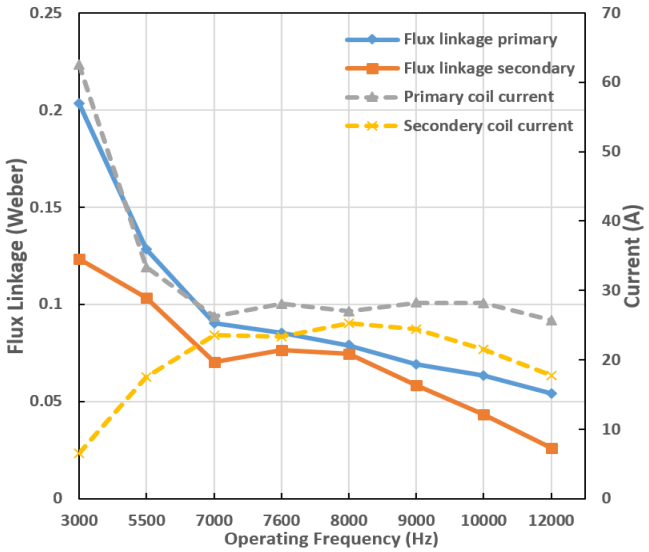


Figure 4.22: Flux linkages, currents vs operating frequencies for the 20 mm air gap model.

For the 20 mm air gap CPT model, in Figure 4.22, both the primary and secondary coil currents tend to have stably high values between 7 to 10 kHz while the secondary coil current shows its maximum value of 25.23 A at 8 kHz and the primary coil current reaches its maximum of 28.24 at 9 kHz. It can be seen from Figure 4.22 that the values of secondary flux linkage could stay optimistic when the operating frequency is between 7 to 8 kHz.

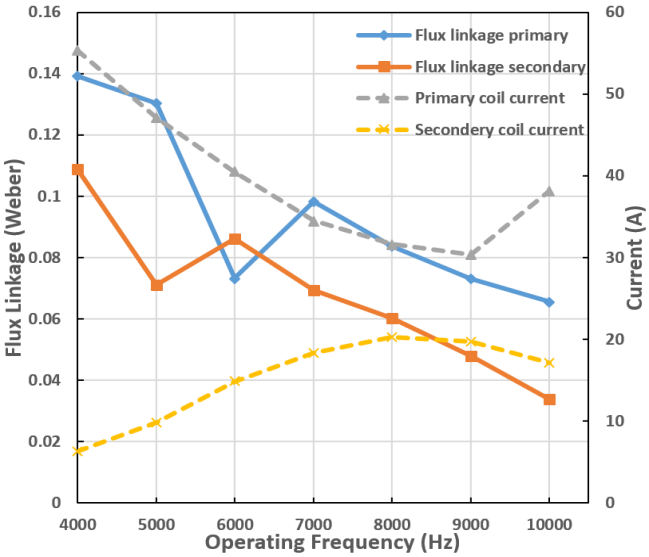


Figure 4.23: Flux linkages, currents vs operating frequencies for the 30 mm air gap model.

In Figure 4.23, it could be seen that the secondary coil current reaches its maximum of 20.29 A at 8 kHz where the primary coil current almost drops to its bottom value. There

is a maximum salient point at 6 kHz for the secondary flux linkage however the primary flux linkage shows two sharp knee points at 6 and 7 kHz.

### *(c) Real powers and efficiencies*

Due to the different power factors (PF) and various electromagnetic field parameters in the CPT models with changeable air gaps, the RMS real power generations on each modular of the system could be different, which can lead to different efficiency on every two circuitry elements selected for analysis. In the 10, 20 and 30 mm air gap CPT models, the coil transmitting efficiency, the overall system efficiency from the power source front end to the load rear end have been analyzed and compared in Figure 4.24 to Figure 4.26. In each figure, the system input power, primary coil power, the secondary coil power and the system output power against the operating frequency have also been presented.

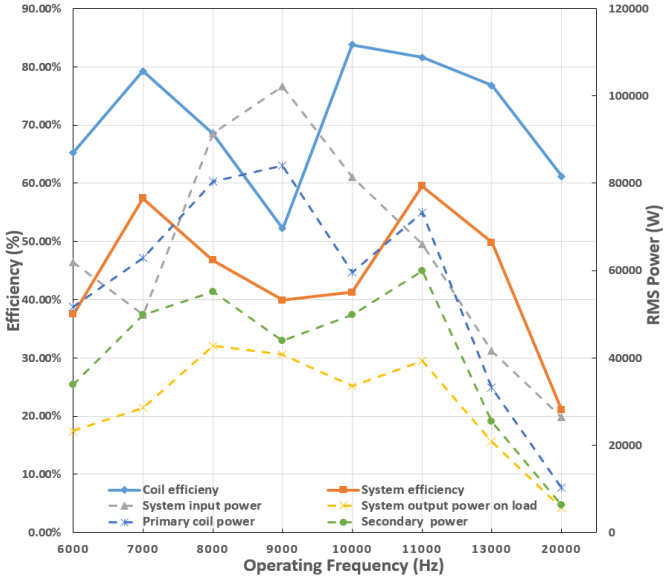


Figure 4.24: Efficiencies, RMS real powers vs operating frequencies for the 10 mm air gap model.

As can be seen from Figure 4.24, both the system efficiency and the coil efficiency show the two peak values at two operating frequency points. The system efficiency reaches 57.41% at 7 kHz and 59.53% at 11 kHz. The coil efficiency reaches 79.28% at 7 kHz as well and 83.81% at 10 kHz. The overall system output power RMS values on load could stay satisfactory from 8 kHz to 11 kHz, with a maximum value of 42.81 kW at 8 kHz.

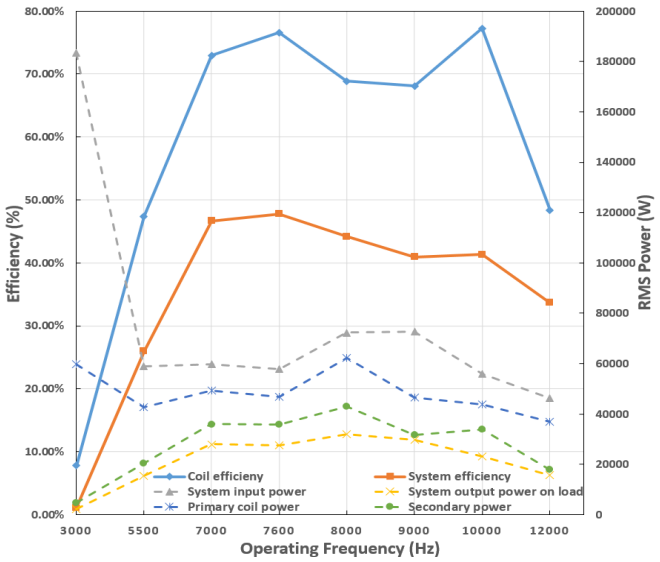


Figure 4.25: Efficiencies, RMS real powers vs operating frequencies for the 20 mm air gap model.

As shown in Figure 4.25, the 20 mm air gap system can produce stably high coil efficiency over 68% across the operating frequency range of 7 kHz to 10 kHz, with a maximum point of 77.22% at 10 kHz. The system overall efficiency shows a wide range of high efficiency over 40% across the operating frequency of 7 kHz to 10 kHz, with a peak value of 47.75% at 7.6 kHz. It also can be seen that the system output power to the load achieve its maximum of 31.95 kW at 8 kHz. The secondary coil and the system load could show stable real power generations within a wide range of operating frequency in Figure 4.25.

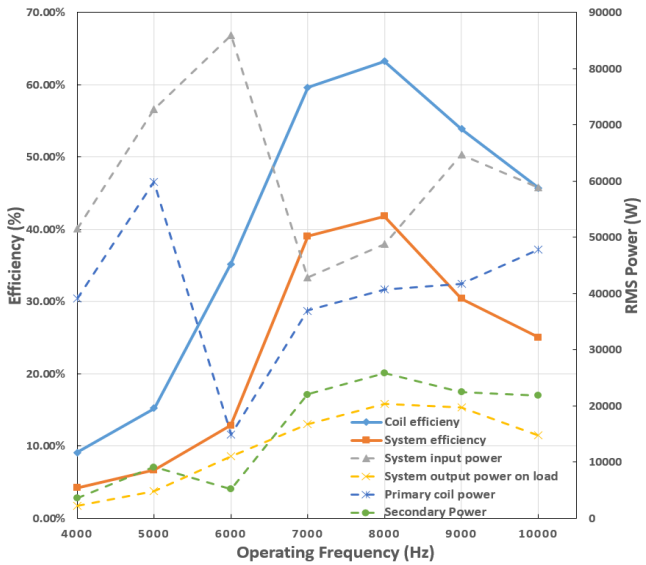


Figure 4.26: Efficiencies, RMS real powers vs operating frequencies for the 30 mm air gap model.

It can be found, from Figure 4.26, that the system efficiency and coil efficiency share almost the same trend against the operating frequency. The coil efficiency reaches its peak value of 63.23% at 8 kHz, at which the system efficiency reaches its maximum of 41.78%. Similarly, both the secondary coil power and the output power on load achieve their maximum values of 25.75 kW and 20.39 kW, respectively, at the operating frequency of 8 kHz.

***(d) Calculated natural resonant frequencies and calculated inductances***

As found and concluded in [75], the natural resonant frequencies of primary side and secondary side of the CPT system could be varied directly depending on the generated inductance L, based on $f_{resonant} = \frac{1}{2\pi\sqrt{LC}}$. Fundamentally, the magnetic flux ϕ and flux linkage λ in equations (3.36) and equation (3.37) are subject to the actual coupler's geometric design, which then determines the inductances on both coils.

Therefore, it is necessarily required to investigate and analyze the relations between the increasing operating frequencies and the changeable resonant frequencies of primary and secondary sides by tracking and approximating the natural resonant frequency using various operating frequencies, in addition to the different air gaps against the system performance parameters in sections above.

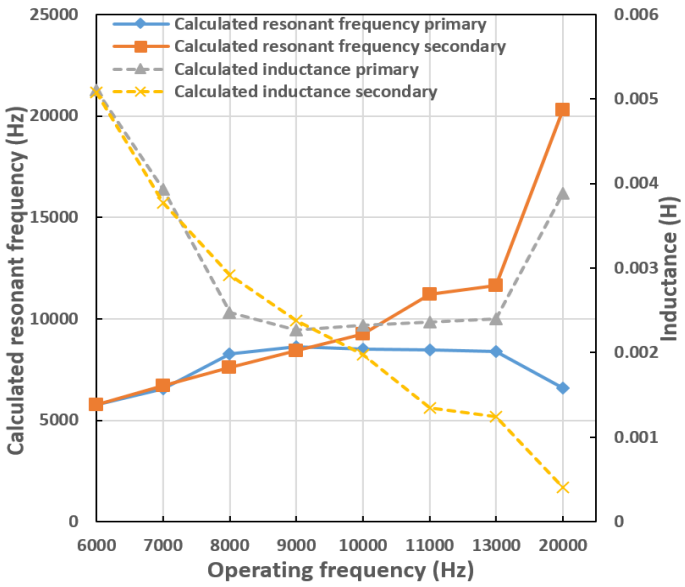


Figure 4.27: Calculated resonant frequencies, calculated inductances vs operating frequencies for the 10 mm air gap CPT prototype.

From Figure 4.27, it can be noticed that the primary side's calculated natural resonant frequency tends to fall within a range of 8.2 to 8.5 kHz, which means the natural resonant frequency of the primary side could be independent of increase of the operating frequency supply when the CPT system air gap is 10 mm. This could be due to the stably flat values of calculated inductance of the primary side at about 0.0024 H, across the operating frequency of 8 to 13 kHz. On the other hand, the electromagnetic resonant coupling for optimized CPT system outputs could be approximated by feeding the operating frequency of 8.2 to 8.5 kHz, which has also been observed by the flux linkage, induced current, RMS power and system efficiency values in previous subsections.

However, compared with the primary side, the calculated natural resonant frequency of the secondary side keeps increasing versus the operating frequency, with nearly a proportional relation of a gradient of 1, which could be mainly caused by the constantly decreasing inductance of the secondary side, based on Figure 4.27.

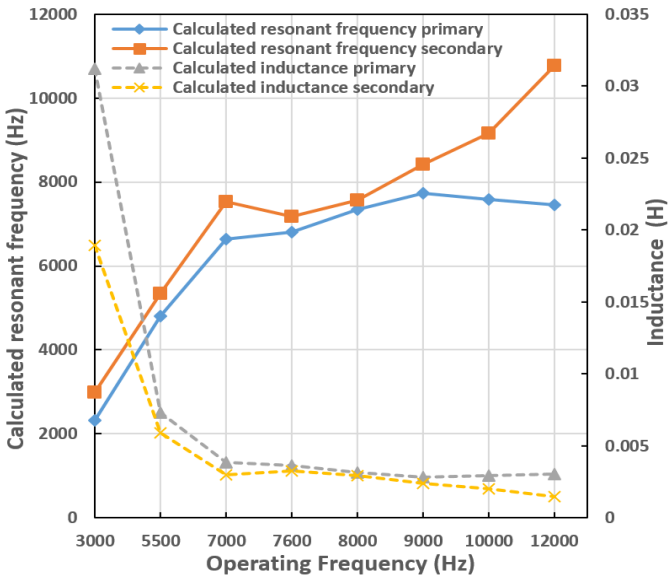


Figure 4.28: Calculated resonant frequencies, calculated inductances vs operating frequencies for the 20 mm air gap CPT prototype.

It can be found from Figure 4.28 that the calculated resonant frequency of the primary side tends to achieve stable values of around 7.5 kHz. Whereas, the calculated resonant frequency of the secondary side keeps rising, in terms of feeding higher operating frequency. Regarding the calculated inductance values of two sides, the primary side's calculated inductance tends to be stable at about 0.0028 H whilst the secondary side's

calculated inductance keeps gradually decreasing when the system operating frequency is set growing over 12 kHz.

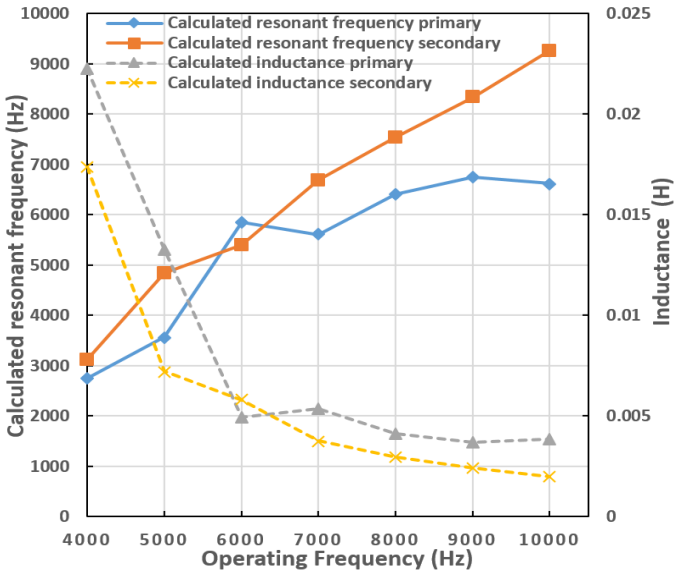


Figure 4.29: Calculated resonant frequencies, calculated inductances vs operating frequencies for the 30 mm air gap CPT prototype.

In Figure 4.29, it can be seen that there exists a knee point at 6 kHz for the curve of calculated resonant frequency of primary side, which could be caused by the dramatic dropped value of primary coil flux linkage shown in Figure 4.23. And the calculated resonant frequency of primary side tends to stabilize at 6.7 kHz. Similar to the trend in Figure 4.28, the secondary side's calculated resonant frequency keeps increasing due to constantly descending inductance.

### 4.2.4 Discussion

From the perspectives of electromagnetics, due to the positive contributions of employing ferrite material with high permeability and H-shape effects, the designed CPT model has shown the improvements on the flux linkage, magnetic flux density, magnetic field strength and flux line distribution based on the analyses in the previous sections. Especially, the specifically designed H-shape soft ferromagnetic cores have demonstrated its significance on facilitating the magnetic strength and flux density at critical points and positions of the couplers such as the external edges and corners of the H-shape cores with expected maximum scalar values and vector directions representing the optimally formed flux distributions and trajectories.

Importantly, the maximum system efficiencies and maximum power transfer ratings of each model coupling scenario can be achieved by approximating the operating frequency to the range of calculated natural resonant frequencies of the primary side. In other words, all the CPT models tend to have an approximate resonant frequency range for the primary side rather than the secondary, as shown in Figure 4.27 to Figure 4.29, the optimal system performance including the maximum system efficiencies and maximum power transfer ratings can be reached when the system tends to perform at magnetic resonant coupling although there would be necessary trade-offs between the optimal efficiency and the optimal power ratings within the corresponding frequency range for electromagnetic resonance in each model as these two optimal values may not occur at the same time. After comparing the proposed three models, obviously the 10 mm air gap CPT system demonstrates the best coupling performance with the strongest magnetic strength and flux density. In the meantime, the 10 mm air gap system shows two optimal system efficiency points not only at its original calculated natural resonant frequency of about 7 kHz of the primary side, but also at 11 kHz, which may be a consequence caused by the combined effects of the superposed fields induced from both coils, especially the highly strong resonant coupling from the secondary side. Besides, the positive effect from compensation capacitor and the lowest reactive power on the secondary side may occur at 11 kHz to lead to highest system efficiency and RMS power to load for the secondary time during the wide range of frequency.

In terms of the RMS real powers, the phase differences between AC voltages and currents play a vital role in working out not only the real power for energy transfer to the load but also the reactive power for establishing and sustaining the electromagnetic field with stored field energy. Thus, the actual phase difference produced in real-time couplings is essentially to be studied and tuned when necessary by adjusting compensation capacitors to an optimal condition at the fixed optimal range of operating frequency. This would be a good topic for further investigations since the stored field energy contributes to the overall system performance and efficiency calculations.

In order to further improve and optimize the flux distributions, the electromagnetic field shielding could be considered in the future research. By using different shielding materials and shapes, the optimal designs towards electromagnetic field performance

could be investigated. Furthermore, more potentially optimal core shapes could also be proposed and studied in the future research.

### 4.2.5 Limitations

In the 3D FEM model built in 3D ANSYS Maxwell, regarding the boundary conditions, an open boundary is supposed to be established as a satisfactory approximation in order to be equivalent to real world CPT applications. However, there must be existing traces of flux escaping from the investigated model in real scenarios, for which about 15 times the coupler model has been implemented in this section to sufficiently simulate the CPT charging cases. Besides, due to the flux line imperfection and element meshing limits of finite element methods, the boundary conditions for this designed prototype from an electromagnetic point of view could not be hundred percent flawless, which may affect the final computed results to some extent in this investigation.

In terms of materials, the air region employed in this model has a relative permeability of 1.0000004. The ferrite core material is a steel1010 type with a nonlinear relative permeability and B-H curve. As for the losses, the core loss, eddy-current loss and iron hysteresis losses are not considered in this model due to the computationally intensive and numerical complications in the specific CPT system. Moreover, the main losses are contributed by the winding Litz wires with a copper relative permeability of 0.999991.

In addition, the misalignment tests and considerations have not been taken into account in this section study. The misalignment degree in the experiments in Section 4.2 has been ideally set up and misalignment tolerance has not been undertaken and evaluated. In real application, depending on how the vehicle users park the cars, the actual lateral and longitudinal displacements would significantly affect the inductive coupling performance due to more imperfect electromagnetic field generations. The misalignment experiments will be looked into in the following Section 4.5.

Importantly, the copper losses from the circuit and winding as the main energy loss in the entire CPT system are also required to be profoundly considered as a tradeoff criterion when the maximum RMS power transferred to the load is required. Besides, the actual phase differences and delays in the waves generated would be difficult to control for a

very satisfactory power factor (PF) of every single module of the CPT system, which could be another subtopic and challenge towards overall system enhancement purposes.

Moreover, the model size in this section's simulations is not sufficiently large to be equivalent to a real application for a vehicle chassis due to the considerations on computational complexity and accuracy in the selected 3D FEM environment. In the future investigations, all limitations mentioned above will be supposed to be addressed, along with an industrially scaled-up larger coupler for the CPT system. It is believed that more accurate and profound results could be gained and larger air gap charging distance can be guaranteed once the coupler size is exactly suitable and compatible to be mounted on a real-world vehicle chassis.

### 4.2.6 Summary

To address and achieve the maximizations of the system efficiency, the power transfer ratings, and the air gaps of coupling coils, a novel small sized CPT prototype using a geometrically optimized H-shaped magnetic coupler and a series-to-series (SS) compensation has been analytically modelled and investigated in terms of operating frequency, varying air gaps, electromagnetics metrics, RMS powers and efficiencies.

The methodology on studying CPT topics in this section has been presented with emphasis from perspective of electromagnetics. The actual electromagnetic indices and magnetic coupling parameters generated have been evaluated, which could provide some different insights into the integrated system analysis methods for both electronic and magnetic field criteria towards inductive coupling based CPT questions.

Three CPT models with 10, 20 and 30 mm air gaps have been investigated in this Section 4.2. It can be found that the 10 mm air gap H-shape soft ferromagnetic coupler CPT system, as an optimal prototype, could produce a maximum system efficiency of 59.5%, a coil transmitting efficiency of 83.8% and a maximum power output of 42.81 kW on the load end when the resonant coupling of CPT system tends to occur within a range of calculated resonant frequencies of the primary side. The enhancements of RMS flux linkage, magnetic flux density and magnetic field strength in terms of the actual electromagnetic performance produced have been demonstrated. In addition, the resonant

couplings for the designed CPT systems relating to the calculated inductance and natural resonant frequency have been studied by result analyses and comparisons.

## 4.3 Chapter conclusions

This chapter analytically proposed a series of CPT models with specifically designed groups of comparisons to address the overall system performance metrics for paths of optimizing using electromagnetic resonant coupling, from aspects of both power electronics outputs and electromagnetics.

Section 4.1 reports an axis-to-axis rectangular core-based model, an axis-parallel rectangular core-based model and an enhanced C-type coupler model, with design emphases on geometric structure of coupling modular and on effectiveness of using ferrite material as cores in order to form the EMF flux distributions more advantageously. Configuring appropriate natural resonant frequencies for coils on each model has also been proved to be one of approaches to resonant coupling optimization. By comparison between all the performance outputs of these models, the newly geometrically designed C-type coupler with ferrite cores appears to be an optimal solution from a perspective of most metrics despite limitations of design method and simulation condition remaining in this set of study.

A novel small-sized H-shaped coupler CPT system has been systematically built and assessed in Section 4.2 considering the main influential factors such as coil geometric design, changeable air gaps, actual system operating frequencies, phase angles of electronic outputs in real-time electromagnetic field scenarios. Different coupling distances as main variables with resulting in divergent system outputs such as flux linkages, B-field, H-field, induced currents, calculated natural resonant frequencies, maximum efficiencies and RMS real powers have been analysed in the section in details. Besides, Section 4.2 provides an insight into the flawless outcomes of the 3D FEM-based models from many perspectives like ferromagnetic material characteristics, winding types, misalignment impacts, energy loss, etc.

# Chapter 5 Implementations and investigations on shielding designs

## 5.1 Design and analysis with tests of different shielding materials

In Section 5.1, a CPT system using a novel geometrically enhanced energy transfer coupler with three different shielding materials has been built and analysed, along with the evaluations from aspects of electromagnetics and RMS power transmission based on electromagnetic resonant coupling. A CPT system design improvement with the proposed H-shape ferromagnetic cores and the combined semi-enclosed passive electromagnetic shielding methods have been investigated in terms of generated electromagnetic field characteristics, system power transfer ratings, system efficiency optimization and performances of shielding materials. The results have shown that, across the range of operating frequency of the CPT system, aluminium shielding as a metallic material method could deliver better overall CPT system performance than other two ferromagnetic materials, steel1010 and ferrite. In addition, coupler prototype design limitations, misalignment tolerance and passive shielding design considerations including distance between windings and inner surfaces of shielding shells have been discussed.

### 5.1.1 Background

A conventional flat circular coils based contactless energy transmitting design was proposed for electric vehicles (EV) battery charging in [7], with introduction to inductively coupled technology. The compensation topologies have been evaluated in [170], which concluded that the series-series (SS) topology could perform the best. Among the proposed wireless energy transfer technologies, most of the studies regarded the CPT system issues as near-field transformer problems and analysed their models from equivalent circuits and electronics points of view. However, the CPT inductive coupling via air space or cores could be nonlinear scenarios due to permeability μ and B-H relations of the specific materials used within the coupling module, which causes that the mutual inductive coupling unit cannot be equivalent to a fixed electronic circuit like that of conventional ideal transformers.

In this section, considering the changeable flux linkage and variable magnetic coupling against different operating frequencies, shielding materials and other factors in real CPT situations, the modelling and analysis based on electromagnetic field and 3D FEM have been implemented in order to evaluate the three different shielding methods using ferromagnetic materials and conductive metallic materials. From aspects of both the electromagnetics and power electronics, the flux linkage, magnetic flux density, magnetic field strength and flux line distribution in real-time field have been investigated, along with power electronics indices which are induced currents, system output RMS real power, and system power transfer efficiency and so on. By comparisons of using steel1010, ferrite and aluminium as shielding materials for the designed small-sized CPT system, the aluminium shielding appears to yield the highest overall system performance within these three shielding methods.

### 5.1.2 CPT system design

***(a) System overview***

An electromagnetic resonant coupling based CPT system consists of AC power supply, rectifier, high frequency inverter, capacitance compensation topology, magnetic coupler, high frequency rectifier, voltage regulator and load end. In order to optimize the RMS real power transfer and efficiency of the CPT system, the design of the magnetic coupling coil modular called coupler acts as a highly significant part in the overall system when the effectiveness of a constantly satisfactory magnetic flux generation and inductive coupling tend to occur at resonant conditions in between the space of coupler coils and ferromagnetic cores as studied in Section 4.2. In addition to the important role of the coupler, an efficient power electronic circuit including soft switching and active rectifier devices could also highly contribute to the CPT system performance [140], [142], [216].

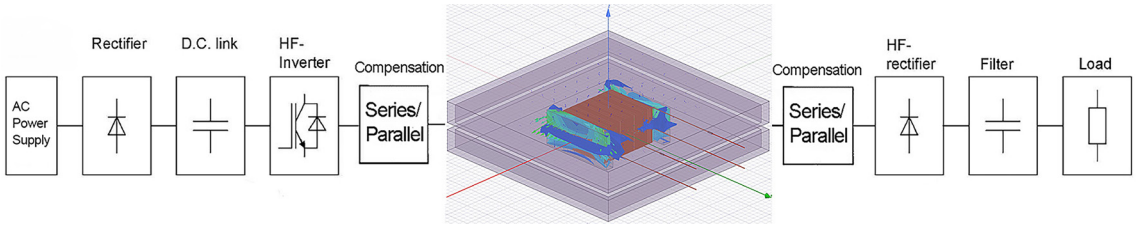


Figure 5.1: The H-shape coupler CPT system configuration with combined semi-enclosed shielding.

Within the space of inductive coupling, optimally shaping the flux line trajectories and forming the flux distributions using H-shape ferrite cores could expectedly improve the actual flux linkages and induced currents in real-world CPT scenarios which have been proved and studied in previous sections. Practically, the high permeability and low core loss of ferrite materials could contribute to flux linkage and magnetic flux density in order for the CPT system to produce an optimized electromagnetic field performance especially when the electromagnetic resonant coupling tends to occur at specific conditions [75].

A stationary CPT system layout using the designed H-shape coupler with four compensation topologies (series-to-series, series-to-parallel, parallel-to-series and parallel-to-parallel) has been shown in Figure 5.1. To achieve the magnetic resonance when the proposed CPT system tends to be stably operating, an appropriate capacitance compensation topology could be utilized to maximize energy transmitting capability between inductively coupled coils mounted on the designed H-shaped ferrite cores and as well as to minimize the magnitude of the real time values of reactance in the coupler.

In order to analyse the inductive coupling performance of the proposed CPT system, based on RLC circuit theories, impedance matching principle and initial system tests with calculations for conditions of approaching electromagnetic resonant coupling, the designed system circuit parameters have been configured, in which both the SS compensation capacitors are set with 150 nF, the load is set with a resistor of 50 ohm and a voltage source with an RMS value of 5 kV has been adopted as the system power supply.

***(b) Geometric modelling for CPT coupler with semi-enclosed shielding***

Since the physical and geometric implementation of the coupling modular for the CPT system can definitively determine a maximum efficiency and highest transferred real

power, the actual coupler design is important in the system configuration as well as considering the coupler size as one of the criteria.

To promote the magnetic flux density, flux linkage, mutual inductance and field strength, the specifically proposed H-shape core using steel1010 as ferromagnetic core material is designed to guide the magnetic flux along the expected paths. On the other hand, preventing energy loss in surrounding air [217] and conductive materials on the chassis of vehicle and reducing the magnetic field flux leakage can be also contributive to overall CPT system performance, which could be achieved by using passive magnetic shielding.

Due to the effects of high permeability and relative low eddy current loss of using ferromagnetic or conductive materials, the magnetic flux could be guided and formed by passive magnetic shielding methods [159]. Therefore, steel1010, ferrite and aluminium have been utilized as the shielding materials in the ANSYS 3D Maxwell platform based experiments in this section. The Steel1010, as a ferromagnetic material, has nonlinear B-H curve. The ferrite adopted in this study has a relative permeability μ of 1000. The aluminium has a relative permeability μ of 1.000021.

Table 5.1: The geometric characteristics of the H-shape coupler with passive shielding.

| Parameters | Values |
|---|---|
| Winding size | 100 mm x 100 mm x 20 mm |
| Core size | 150 mm x 150 mm x 20 mm |
| H-shaped core bar size of each side | 150 mm x 15 mm x 20 mm |
| Primary winding number of turns | 80 turns |
| Secondary winding number of turns | 80 turns |
| Air gaps of the CPT charging system | 10 mm |
| Shielding size | 400 mm x 400 x 30 mm |
| Shielding thickness | 10 mm |
| Inner distance between shielding and coil | 5 mm |
| Passive magnetic shielding materials | Steel1010, Ferrite and Aluminium |

In this section, the H-shape coupler and the combined semi-enclosed passive shielding have been prototyped as presented in Figure 5.2. The three different shielding materials are utilized to the CPT system coupler to output the performance results, respectively.

Litz wire is selected for the windings in this model due to its skin effects reduction, proximity effects mitigation and capability for high frequency application. The small-sized magnetic coupler is designed as the geometric parameters given in Table 5.1.

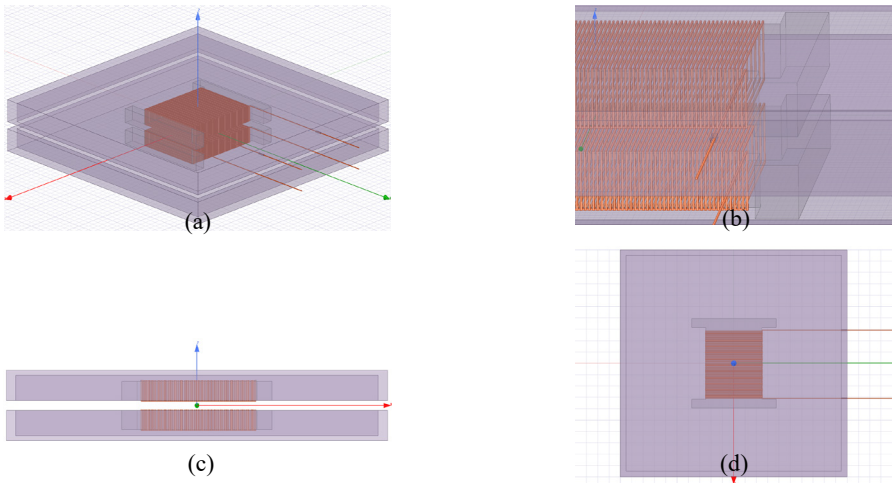


Figure 5.2: The H-shape coupler with the combined semi-enclosed shielding built in 3D FEM platform. (a) The CPT system coupler overview. (b) Detailed view of the windings and cores. (c) Left view of the system. (d) Top view of the system.

### 5.1.3 Results and analyses

***(a) Flux linkage and currents with different shielding materials***

In this investigation in terms of different ferromagnetic and conductive metallic shielding materials, the proposed H-shape coupler CPT system performance has been investigated across the major significant range of operating frequency and has been emphasized on the characteristic trends, from both the electromagnetics and electronics points of view. Theoretically, the flux linkage in electromagnetics and the induced current in power electronics have relatively reflective relations to the system performance based on Maxwell equations and induction principles.

From Figures 5.3(a), (b) and (c), it can be seen that both the primary and secondary values of flux linkage for three shielding materials tend to decrease against the increase of system's operating frequency. Similarly, the primary and secondary coil currents for steel1010 and ferrite in Figure 5.3(a) and (b) show the decreasing trends. However, the values of primary and secondary coil currents tend to increase after 6000 Hz in Figure 5.2(c), which may reflect better inductive capability of aluminium to produce satisfactory coupling for the system than steel1010 and ferrite as passive shielding material.

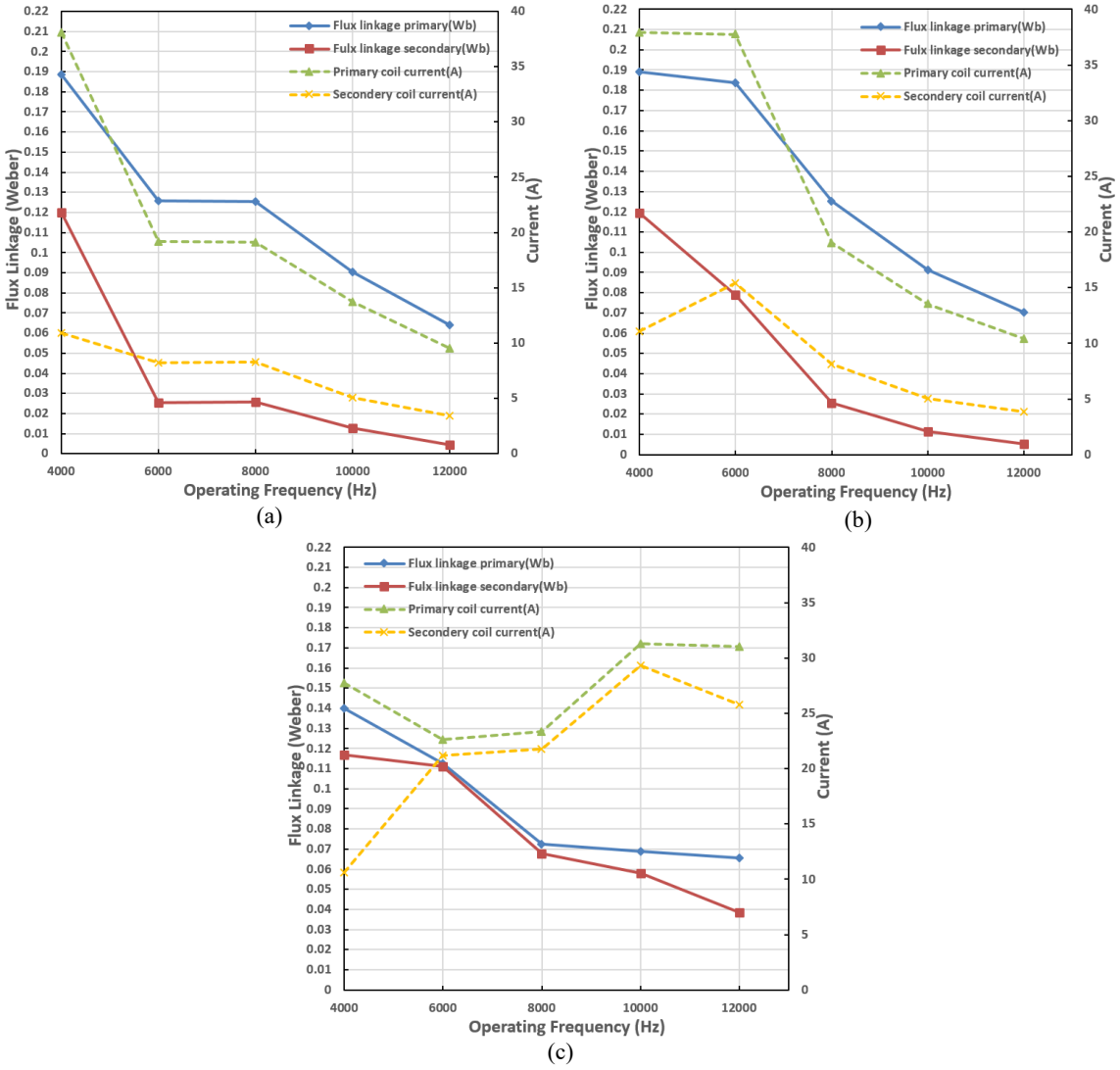


Figure 5.3: The flux linkage and current values of the designed CPT system versus system operating frequency. (a) Steel1010 as shielding material. (b) Ferrite as shielding material. (c) Aluminium as shielding material.

In terms of the characteristic values, the flux linkage of primary and secondary coils for steel1010 have shown relatively stable values of about 0.1257 Wb and 0.0258 Wb, respectively, corresponding to frequency range of 6000 to 8000 Hz in Figure 5.3(a), after which these two values gradually tend to decrease. In the meantime, the induced currents of primary and secondary coils have the similar tendency like the corresponding flux linkages. It could be noticed that the values of primary and secondary currents tend to stabilize at about 19.13 A and 8.25 A, respectively, when the system operating frequency is supplied between 6000 Hz to 8000 Hz, in Figure 5.3(a).

Regarding the flux linkage and current values for ferrite shielding in Figure 5.3(b), both the values of the flux linkage of primary and secondary sides have a gradually moderating trend from 0.1890 Wb and 0.1195 Wb at 4000 Hz, respectively, down to 0.0703 Wb and 0.0054 Wb at 12000 Hz. While the primary coil current shows stable trend before 6000 Hz, after which a sharp drop can be seen against the operating frequency. However, the secondary coil current shows a peak value of 15.39 A at 6000 Hz, which is also the calculated optimal resonant coupling point for ferrite as shielding material.

With regard to shielding using conductive metallic material, aluminium shielding for the designed CPT system can be initially seen as a proper shielding method according to Figure 5.3(c). The overall values of primary and secondary flux linkage are higher than steel1010 and ferrite despite the similar downward tendency. It could be seen that, after 8000 Hz, flux linkage values of primary and secondary sides show gradually decreasing change until 0.0581 Wb and 0.0384 Wb, respectively, at 12000 Hz, which is higher than the final and lowest values of steel1010 and ferrite.

***(b) RMS real powers and efficiencies with different shielding materials***

As indispensable indices for evaluating the CPT system performance, the RMS real power and efficiency across a range of system operating frequency could reflect the design effectiveness for the energy transmitting purpose of a system in real-world applications. In this section regarding the three different shielding materials, the actual values of real transferred power and efficiency on both coil sides of the designed coupler are compared and analyzed.

The actual electromagnetic field parameters generated are variable and the real-time phase angle differences are changeable in terms of various system operating frequencies [75], as well as the different shielding materials proposed in this paper, which determines the RMS real power and efficiency. Based on the actual power factor (PF) generated and original waveforms acquired after the CPT system outcomes stabilize at each testing operating frequency, the resulted values of RMS real power and efficiency can be worked out and analyzed.

From Figure 5.4(a), it can be seen that the coil energy transfer efficiency could reach a peak value of 74.76% at 8000 Hz, at which point the system efficiency also reaches a

maximum of 6.67%. The system input power significantly drops from 138.62 kW to 32.51 kW while the system output power on the load also reduces by about 10 times from 5.92 kW to 0.59 kW. It is noticeable that the primary coil power decreases to a lowest value of 7.51 kW at 8000 Hz whilst the secondary coil power could produce a second highest value on its curve, which causes the peak values 74.76% and 6.67%, respectively, for the coil efficiency and system efficiency.

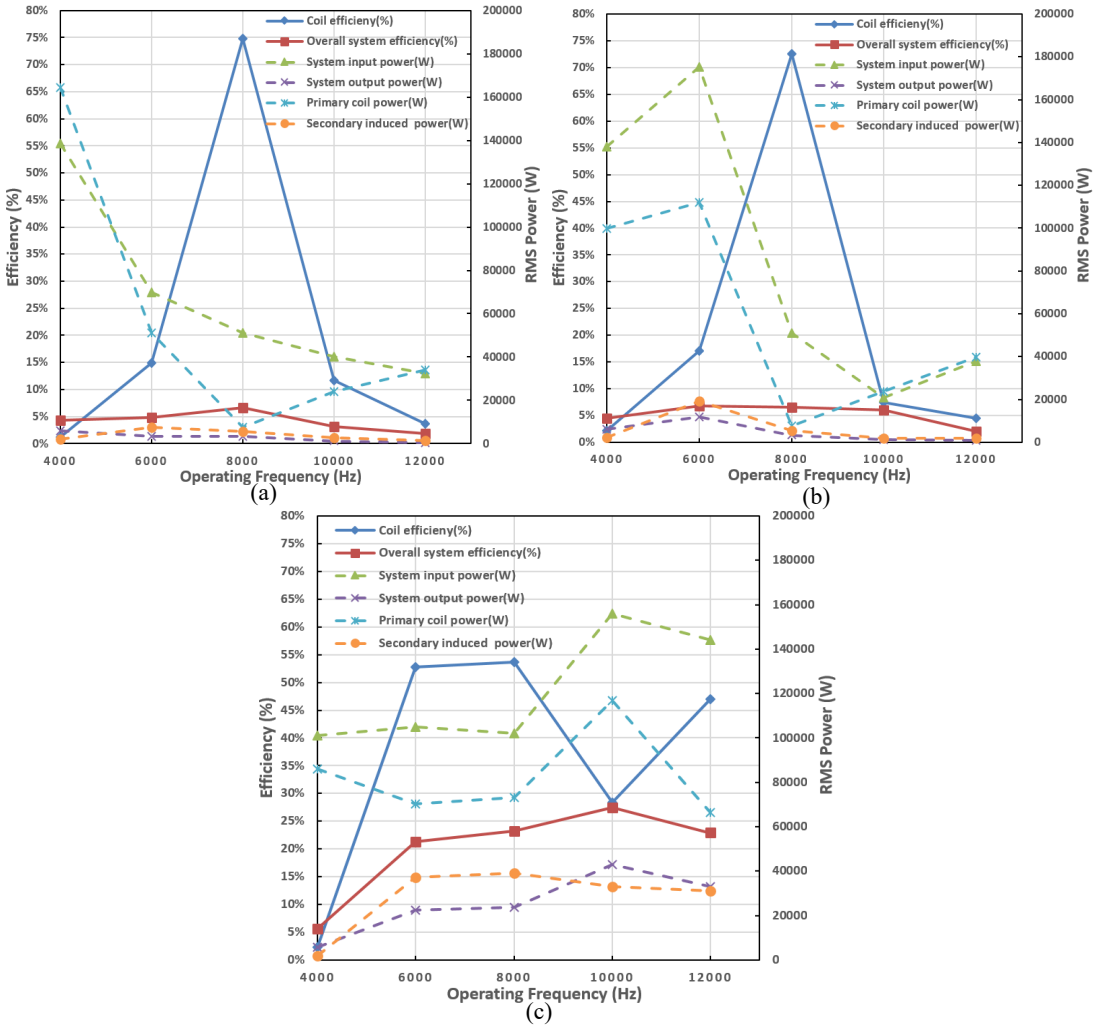


Figure 5.4: The RMS real powers and efficiencies of the designed CPT system versus system operating frequency. (a) Steel1010 as shielding material. (b) Ferrite as shielding material. (c) Aluminium as shielding material.

Figure 5.4(b) depicts almost the same trend for the coil efficiency like in Figure 5.4(a), whilst the overall system efficiency show a stably higher range of values over 6% across the operating frequency range between 6000 Hz to 10000 Hz. The overall system efficiency reaches its maximum of 6.77% at 6000 Hz. Importantly, it can be noticeably seen that the system input power, system output power on load, primary coil power and

secondary coil achieve their maximum values of 175.19 kW, 11.85 kW, 112.11 kW and 19.11 kW, respectively, at the calculated magnetic resonant coupling frequency of about 6000 Hz.

Regarding the performance of aluminium shielding, it can be noticed that almost all the results of the system could show improvements in Figure 5.4(c). Significantly, the overall system efficiency could reach a peak value of 27.48% at 10000 Hz and could also stay at stably satisfactory values of over 20% when the operating frequency is supplied with 6000 Hz and above. The system output power on load end achieves a maximum of 42.90 kW at 10000 Hz.

Therefore, the aluminium shielding performs with the highest results of criteria within the three shielding materials, which indicates satisfactory power transfer rating, efficiency in addition to acceptable electromagnetic field flux distributions and coupling performance.

***(c) Analysis on main results with different shielding materials based on EV charging***

In addition to graphic trend analysis for each model with different shielding methods above, Table 5.2 below could indicate the major critical results for comparing and evaluating the CPT system outcomes and performance. As known, the load current could firstly reflect the effectiveness of inductive coupling phenomena, by which it can been seen that the CPT system with aluminium could produce highly effective inductive coupling for electric vehicle contactless charging applications than systems with steel1010 and ferrite shielding according to numerical comparisons in Table 5.2.

Generally, electric vehicles (EV) could gain faster charging depending on higher CPT system output real power rating. From Table 5.2, the system output power of steel1010 shielding is unable to deliver a rating value of over 1 kW, while the ferrite shielding CPT system can produce 11.85 kW system output power on load at its resonant coupling status with the calculated natural resonant frequency of about 6000 Hz. Noticeably, the CPT system with aluminium shielding could generate relatively high system output real power across a wider range of operating frequency, which contributes to a maximum value of 42.90 kW when the CPT system performs to stabilize, at the resonant coupling frequency of about 10000 Hz. When considering the energy use efficiency from the power supply,

the overall system efficiency could be of reference. By comparison, the aluminium shielding CPT system is able to produce relatively high system efficiency especially at 10000 Hz as presented in Table 5.2.

Table 5.2: Main numerical results of the H-shape coupler CPT system with threes passive shielding materials.

| **Oper. Freq. (Hz)** | **CPT system with Steel1010 Shielding** | | | **CPT system with Ferrite Shielding** | | | **CPT system with Aluminium Shielding** | | |
|---|---|---|---|---|---|---|---|---|---|
| | Load Current (A) | System Output Power (W) | Overall System η | Load Current (A) | System Output Power(W) | Overall System η | Load Current (A) | System Output Power (W) | Overall System η |
| 4000 | 10.88 | 5921.64 | 4.27% | 11.08 | 6140.19 | 4.45% | 10.64 | 5659.80 | 5.60% |
| 6000 | 8.25 | 3406.86 | 4.88% | 15.39 | 11852.41 | 6.77% | 21.16 | 22389.69 | 21.34% |
| 8000 | 8.26 | 3411.47 | 6.67% | 8.13 | 3303.67 | 6.49% | 21.77 | 23704.41 | 23.21% |
| 10000 | 5.08 | 1244.71 | 3.09% | 5.03 | 1262.48 | 6.05% | 29.29 | 42899.59 | 27.48% |
| 12000 | 3.44 | 593.27 | 1.82% | 3.88 | 752.37 | 1.99% | 25.81 | 33008.59 | 22.91% |

### *(d) Analysis on a selected CPT system model with aluminium shielding method based on electromagnetic field*

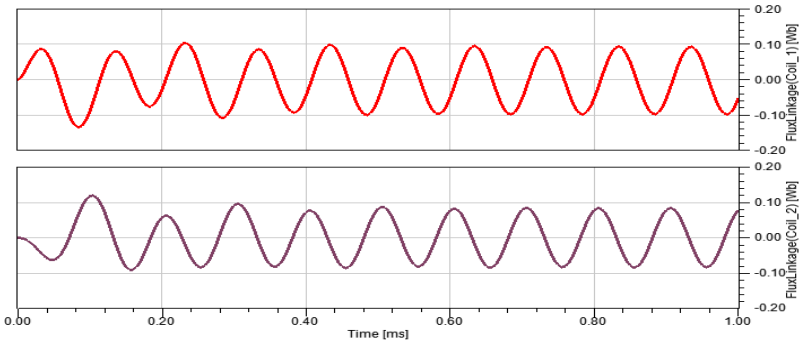


Figure 5.5: The flux linkage waveforms of the designed H-shape coupler CPT system with aluminium passive shielding, at the operating frequency of 10000 Hz.

Based on comparisons and analysis in previous sections, it can be found that the H-shape coupler CPT system with aluminium shielding could provide highest power electronic performance in the three shielding methods. Thus, the CPT system with aluminium shielding, at its optimal performance frequency of 10000 Hz, has been selected to be analysed from aspects of the electromagnetics.

As can be seen from Figure 5.5, the alternating flux linkage waveforms of the primary and secondary coils are able to be sinusoidally stable since the sixth period, which means the CPT system could tend to perform immediately with electromagnetic coupling

stability within 1 *m*s after the system is activated to be magnetically coupled. Once the electromagnetic stability is established, the RMS values of the primary and secondary flux linkage could be 0.0689 Wb and 0.0581 Wb, corresponding to the measured amplitude values of 0.0974 Wb and 0.0822 Wb, respectively. Besides, it also could be computed that the phase difference between the two AC flux linkages tends to be about 108 degrees when the system reaches an AC stable and magnetic resonant coupling.

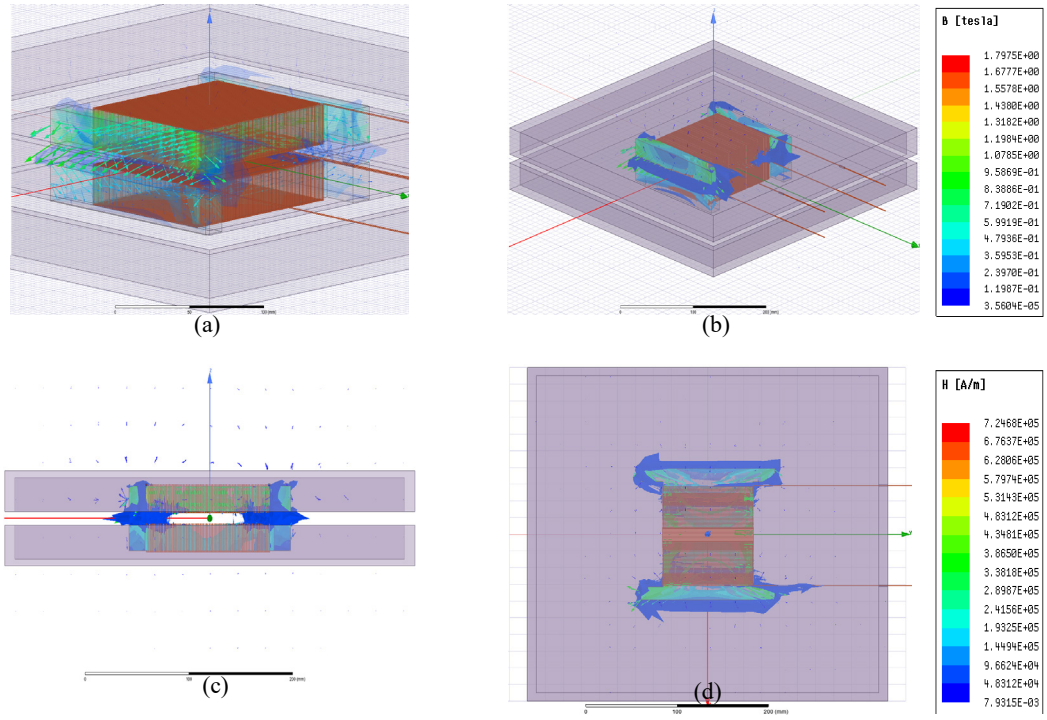


Figure 5.6: The electromagnetic field of the designed H-shape coupler CPT system with aluminium passive shielding at 1 ms, *indicating the magnetic field strength* ***H*** *and the magnetic flux density* ***B****,* at 10000 Hz. (a) ***B*** vector in the field. (b) Dimitric view of the field. (c) Left view of the field. (d) Top view of the field.

In terms of the electromagnetic field parameters and performance, the CPT system with aluminium shielding at the operating frequency of 10000 Hz has been selected to be investigated as a typical magnetic resonant coupling scenario. As shown in Figure 5.6(a), the vector arrows of the magnetic flux density **B** show the expected directions, mostly concentrating at the external edges and corners of the designed H-shaped core, along with maximum scalar magnitude of 1.7975 teslas, In the meantime, the magnetic field strength **H** reaches its peak value of 7.2468 x $10^5$ A/m at the ending point of the external corners of the core, which also indicates the effectiveness of the geometric H-shape design for shaping and guiding the flux lines.

According to Figures 5.6(b), (c) and (d), the vector field **B** and **H** are established to be alternatively varying within the combined semi-enclosed air space by the effects of aluminium passive magnetic shielding, which can prove that the shielding does prevent the magnetic field flux distributions from spreading and leaking to the remote surrounding space. In real-world applications, this effect may consequently reduce energy losses to the air, to the surrounding conductive elements of electric vehicle chassis or even to the human driver as a potential EMI issue when in a high frequency range.

### 5.1.4 Discussion

As demonstrated and illustrated in the electromagnetic field of the designed H-shape coupler CPT system, the ferromagnetic material as the core with high permeability and H-shape can produce and form the magnetic flux distribution as expected, especially facilitating the magnetic flux density and magnitude field strength at the external corners and edges of the H-shape core. The optimally guided and formed flux vector trajectories and field distribution can be utilized and has been proved to promote the CPT system coupling performance from perspectives of electromagnetics.

By comparing the obtained power transfer ratings and system efficiency values of three shielding methods using different ferromagnetic and conductive materials, it can be found that deploying aluminium as shielding material could output relatively more satisfactory CPT system performance. The H-shape coupler CPT system using aluminium shielding enables to deliver a maximum overall system output RMS real power of 42.90 kW and to produce a peak system efficiency of 27.48% at about the natural resonant frequency of 10000 Hz. Besides, at higher range of operating frequencies, the CPT system with aluminium shielding appears to generate sustainable satisfactory system efficiency, transfer power rating on load and flux linkage, which could be of advantage for real-world electric vehicle contactless charging applications.

With regard to limitations, the distance between the windings and inner shielding surfaces in this prototype may be too small, which would probably have caused distribution of the ultimately optimal magnetic field flux to be restricted and optimum flux linkage values to be achieved, to some degree. In future investigations in this field, the distance between the windings and inner shielding surfaces is supposed to be enlarged from 5 mm to 15

mm under the preconditions of expected shielding functions and limited space usage, to find out the optimized inner shielding distance for the CPT system.

In real-world applications, the actual electromagnetic field performance and inductive coupling quality can be significantly affected by how the electric vehicle is parked over the ground side power transmitting module with longitudinal and lateral misalignments, which should be counted as system tolerance to parking misalignment. In addition, the module size of CPT system will have to be optimized to be completely suitable to real-world vehicle chassis for installation and application.

# 5.2 Various inner shielding distance tests for a CPT system using electromagnetic resonant coupling and aluminium shielding

## 5.2.1 Methods and focuses

Section 5.2 focuses on passive magnetic shielding, which acts as one of the major factors mainly determining the overall CPT system performance when discussing electromagnetic field flux distribution and its real-time effects on magnetic resonant coupling. As a well-performance conductive metallic material, aluminium has been adopted to be a passive shielding material in the designed novel H-shape coupler CPT system in this section, in order to evaluate and find out the optimal inner shielding distance in between the coil and the inner shielding shell. Three inner shielding distances are applied and analyzed across a critical range of system operating frequency, by which the actual CPT system performance differences from perspectives of electromagnetics and power electronics have been illustrated and compared.

As a result, it can be noticed that the 15 mm inner shielding gap CPT model is able to yield an optimal system performance with a maximum system efficiency, peak system output RMS power of over 36% and 22 kW, respectively, which also shows an optimal capability to address major concerns over electric vehicle contactless charging. Besides, along with the electromagnetic field parameters generated in the model, such as actual real-time values of flux linkage, magnetic flux density and field strength, it can be found that the 15 mm inner shielding gap prototype is able to achieve better overall magnetic field performance than 5 mm and 25 mm inner shielding distance CPT models.

In this section, considering inductive coupling via air space or cores could be nonlinear scenarios due to permeability μ and B-H relations of the specific materials used within the coupling module, a proposed H-shape coupler CPT system with aluminium shielding method is then introduced to analyze and evaluate the system performance differences in terms of inner shielding distance changes, based on electromagnetics and 3D FEM. Thus, the induced currents, system output RMS real power, and system power transfer efficiency as power electronics indices, along with the flux linkage, magnetic flux density, magnetic field strength and flux line distribution have been investigated in this section.

The overall system performances of 5 mm, 15 mm and 25 mm inner shielding gap CPT models have been analyzed and compared.

### 5.2.2 CPT system design

Based on the effectiveness of high permeability and low core loss of soft ferromagnetic materials mentioned before, the geometrically improved H-shape soft magnetic core coupler is proposed to form magnetic flux line trajectories and enhance flux distributions within the inductive coupling space in and between the cores and coils, which can lead to optimal CPT system coupling performance especially at electromagnetic resonant coupling status [75]. Figure 5.7 presents a stationary contactless power transfer system deploying H-shape ferromagnetic cores with a relative permeability μ of 1000, semi-enclosed combined alumininium shielding and four compensation topologies connecting to both sides of the coupling modular. Due to contributions of minimizing reactance magnitude, the S-S compensation topology has been adopted again in the designed CPT system in this section.

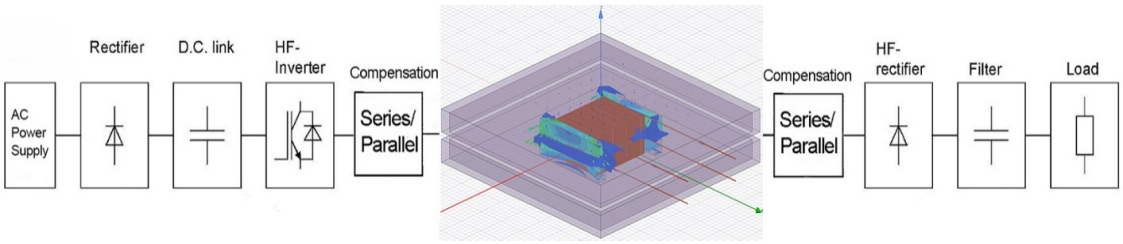


Figure 5.7: The CPT system configuration with H-shape coupler and combined semi-enclosed shielding.

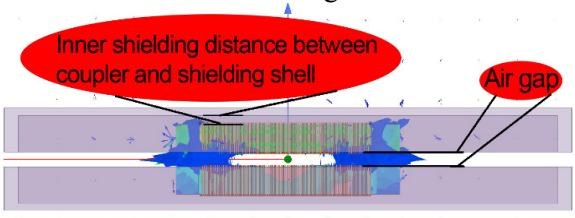


Figure 5.8: The designed coupler indicating the CPT air gap and the inner shielding distance.

In order to properly produce constantly satisfactory magnetic flux generation with electromagnetic resonant coupling occurring at specific conditions, the innovatively proposed semi-enclosed combined alumininium shielding method has been utilized to further guide and form the actual magnetic flux due to its effects of preventing energy loss in surrounding air [217] and reducing magnetic field flux leakage to the infinite air

space [159]. Moreover, different system outcomes of the proposed CPT system with various inner shielding distances, 5 mm, 15 mm and 25 mm, have been delivered and analyzed from both the electromagnetics and power electronics points of view. The designed coupler modular with inner shielding gap and air gap is presented in Figure 5.8. And the detailed design characteristics of the small-sized H-shape coupler CPT system with aluminium passive shielding are given in Table 5.3.

It is necessary to mention that, in order to simulate better scenarios for more accurate and convincing analysis, the power supply here in this set of CPT models has been reduced to RMS 5 kV, which is half the RMS 10 kV in previous prototypes and is more equivalent to common real-world medium power distribution levels [218] after stepping down from power network lines but before final substation for domestic consumptions of 230 V [219], [220]. Objectively, both the EMF and electronic outputs in this section study would be relatively lower than those in Section 4.1 to 5.1, which is nonetheless more feasible and realistic for real-world CPT charging of EVs.

Table 5.3: The specifications of the designed CPT system for inner shielding tests.

| Parameters | Values |
|---|---|
| Winding size | 100 mm x 100 mm x 20 mm |
| Core size | 150 mm x 150 mm x 20 mm |
| H-shaped core bar size of each side | 150 mm x 15 mm x 20 mm |
| Primary winding number of turns | 80 turns |
| Secondary winding number of turns | 80 turns |
| Air gaps of the CPT charging system | 10 mm |
| Winding material | Litz wire |
| Shielding size | 400 mm x 400 x 30 mm |
| Shielding thickness | 10 mm |
| Passive magnetic shielding materials | Alumimium |
| Relative permeability μ of core material | 1000 |
| Relative permeability μ of shielding material | 1.000021 |
| S-S compensation capacitors | 150 nF |
| Load resistor | 50 ohm |
| Voltage power supply | RMS 5 kV |
| Inner shielding distance between coil and shell | 5 mm, 15 mm and 25 mm |

### 5.2.3 Results and analyses

***(a) Flux linkage and currents with different inner shielding gaps***

In Section 5.2, the proposed H-shape coupler CPT systems with aluminium shielding method and three different inner shielding gaps have been investigated across the major significant range of system operating frequency. By emphasizing on the flux linkage in electromagnetics and the induced current in power electronics, it can be seen that the 5 mm, 15 mm and 25 mm inner shielding gap based prototypes produce different characteristic trends against operating frequency.

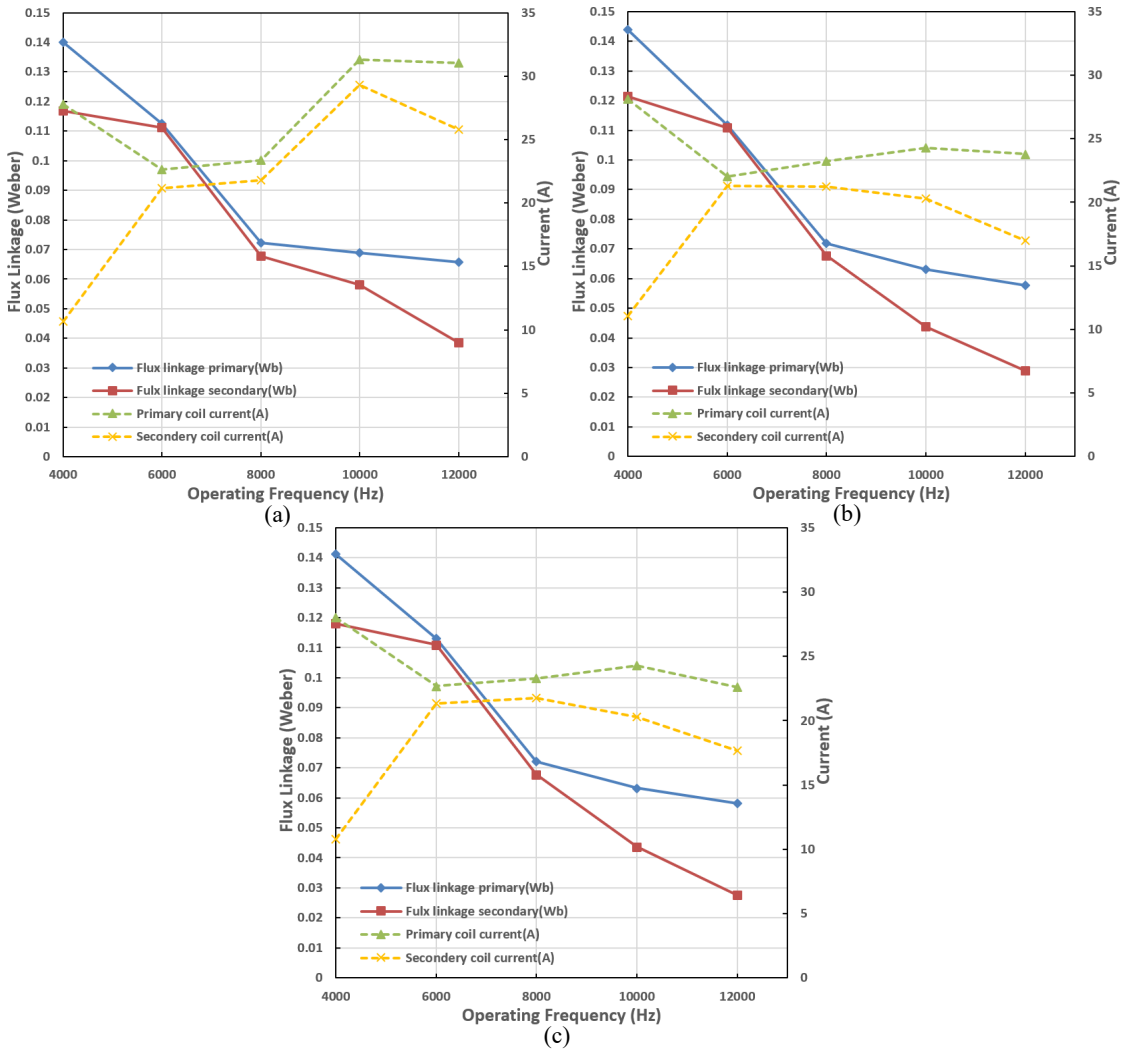


Figure 5.9: The flux linkage and current values of the designed CPT system with aluminium shielding versus system operating frequency. (a) 5 mm inner shielding gap. (b) 15 mm inner shielding gap. (c) 25 mm inner shielding gap.

The results in terms of flux linkage and current have been depicted in Figure 5.9. It can be seen, from Figure 5.9(a), that both the flux linkages of primary and secondary coils

tend to drop down against operating frequency despite a more gradual decrease after the frequency point of 8 kHz. In the meantime, the primary coil current shows a slight decrease before 6 kHz and then tends to rise up to a peak value of 31.28 A at 10 kHz. The secondary coil current shows an increasing tendency before 10 kHz as well, reaching its maximum of 29.29 A. However, the secondary coil current appears to drop down after 10 kHz point, which could be corresponding to the maximum system performance point along with the calculated resonant frequency for the 5 mm inner shielding gap model.

By comparing Figure 5.9(b) and (c), it can be noticed that both the 15 mm and 25 mm inner shielding gap models show very similar tendencies upon flux linkages and coil currents, which may reflect that 15 mm for inner shielding distance could be a critical point due to no further significant differences regarding flux linkage and current against operating frequency with other parameters kept the same in the designed CPT system. Nevertheless, the primary coil currents of both 15 mm and 25 mm inner shielding gap models appear to show maximum values of 24.28 A and 24.30 A at 10 kHz. While, the secondary coil currents of both the 15 mm and 25 mm inner shielding gap models tend to achieve optimal values between 6 kHz to 8 kHz, which can reflect that inductive couplings with satisfactory induced currents to secondary side of the system could be reached during this frequency range in order to produce higher real power on the load end.

***(b) Efficiencies and RMS real powers with different inner shielding gaps***

The actual real-time phase angles of induced currents and voltages are changeable in both sides of the system, which determines different real-time power factors (PF) and generates variable RMS real power results [75], [165]. After each CPT system model tends to produce AC stabilized output waveforms, the results of RMS power and efficiency can be computed based on equation (3.43)-(3.45) in order to be analyzed.

As indispensable indices to evaluate and reflect the CPT system performance, as shown in Figure 5.10, three different inner shielding gaps based models yield different RMS powers and efficiencies. From Figure 5.10(a), it can be seen that the overall system efficiency shows an increasing tendency to reach a maximum value of 27.48% at 10 kHz. At the same operating frequency, the system output power achieves its peak value of 42.90 kW, which indicates the magnetic resonant coupling status tends to occur at its approximate calculated natural resonant frequency of 10 kHz.

Regarding the 15 mm inner shielding gap CPT model, it can be noticed, from Figure 5.10(b), that the overall system efficiency shows a sharp peak point at operating frequency of 8 kHz, which indicates a maximum value of 36.26%. Nevertheless, the peak value of the system output power is produced at 6 kHz, which is 22.63 kW. Significantly, it can be found that, across a wide range of operating frequency after 6 kHz, the system output power is able to stay highly satisfactory and sustainable with values of over 20 kW, which reflects that the acceptable electromagnetic field flux distributions and resonant coupling performance in this 15 mm inner shielding gap model enable stable and satisfactory power transfer ratings and overall system efficiencies for CPT applications to electric vehicles.

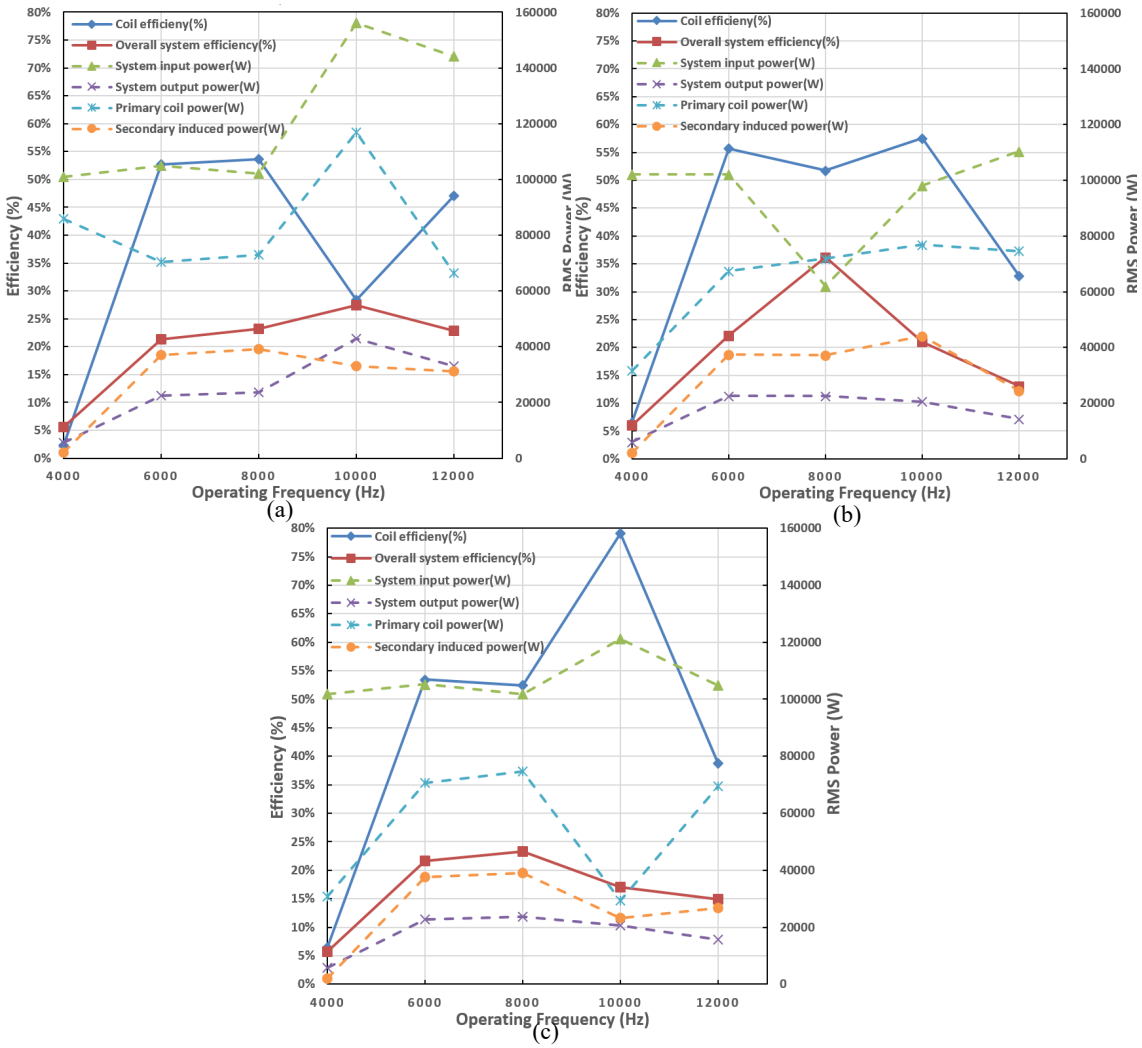


Figure 5.10: The RMS real powers and efficiencies of the designed CPT system with aluminium shielding versus system operating frequency. (a) 5 mm inner shielding gap. (b) 15 mm inner shielding gap. (c) 25 mm inner shielding gap.

In terms of the outcomes of the 25 mm inner shielding gap CPT prototype depicted in Figure 5.10(c), the overall system efficiency tends to be achieved at 8 kHz with a resulted value of 23.25%. In the meantime, the system output power reaches its peak value of 23.68 kW at 8 kHz. By comparison, it can be also found that the average values of overall system efficiency against each operating frequency are almost slightly lower than those of the 5 mm inner shielding gap CPT prototype. Significantly the maximum system efficiency of the third model is much lower than the performance of the 15 mm inner shielding gap CPT prototype, by about 13%, which can reflect and prove that the 15 mm inner shielding gap between coil and inner shell surface can be the optimization for an aluminium passive shielding method.

***(c) Analysis on main results and field performance with different inner shielding gaps***

In addition to graphic tendency comparison and analysis, the detailed major numerical results computed based on theories and equations in previous sections have been illustrated in Table 5.4 for comprehensive evaluations.

Table 5.4: Main numerical results of the CPT system with three inner shielding distances.

| **Oper. Freq. (Hz)** | **System with 5 mm inner shielding gap** | | | **System with 15 mm inner shielding gap** | | | **System with 25 mm inner shielding gap** | | |
|---|---|---|---|---|---|---|---|---|---|
| | System Output Power (W) | Coil η | Overall System η | System Output Power (W) | Coil η | Overall System η | System Output Power (W) | Coil η | Overall System η |
| 4000 | 5659.80 | 2.26% | 5.60% | 6093.50 | 6.64% | 5.96% | 5802.16 | 6.46% | 5.70% |
| 6000 | 22389.69 | 52.74% | 21.34% | 22626.49 | 55.68% | 22.16% | 22734.28 | 53.42% | 21.61% |
| 8000 | 23704.41 | 53.62% | 23.21% | 22526.44 | 51.81% | 36.26% | 23676.08 | 52.38% | 23.24% |
| 10000 | 42899.59 | 28.34% | 27.48% | 20566.49 | 57.51% | 20.99% | 20612.58 | 79.14% | 17.00% |
| 12000 | 33008.59 | 47.01% | 22.91% | 14401.91 | 32.94% | 13.06% | 15617.56 | 38.69% | 14.91% |

As can be seen, the overall system efficiency of 15 mm inner shielding gap model shows the best outcomes within these three different inner shielding gap models although the maximum system output power of the 15 mm inner shielding gap model is about 20.27 kW lower than the 5 mm inner shielding gap model, which could illustrate and reflect that the latter model can deliver faster charging due to its higher output real power on load. Nevertheless, the 15 mm inner shielding gap model seems more able to produce better efficiency of energy utilization with 36.26% as a peak point. On the other hand, the 25 mm inner shielding gap model tends to generate slightly weaker performance than the

15 mm one, which could also mean that 15 mm can be the optimal inner shielding gap for the designed CPT system from system efficiency point of view.

From the perspective of electromagnetics, the magnetic field strength **H** in A/m and the magnetic flux density **B** in tesla can reflect the field performance of a system based on Maxwell's equations. As can be seen from Figure 5.10 to Figure 5.13, different field flux distributions and parameters are shown to be analyzed. The 5 mm inner shielding gap system can produce maximum **H** and **B** values of 7.25 x $10^5$ A/m and 1.80 teslas, respectively, at some crucial surface edges and corners of the coupling modular when the system efficiency reaches its maximum of 27.48%. The 15 mm inner shielding gap system can generate maximum **H** and **B** values of 3.93 x $10^5$ A/m and 1.4026 teslas, respectively, when the system tends to be magnetically resonant coupled at 8 kHz as presented in Figure 5.12 and Table 5.4. From Figure 5.13, it can be seen that the peaks of **H** and **B** field can be 3.45 x $10^5$ A/m and 1.40 teslas, respectively. Comprehensively, the overall vector values throughout the entire coupling space of the 15 mm inner shielding gap CPT system can be found to be optimized although its **H** and **B** maximum points are slightly weaker than those of the 25 mm inner gap model. Therefore, the 15 mm inner shielding gap can be an optimization from perspective of electromagnetics.

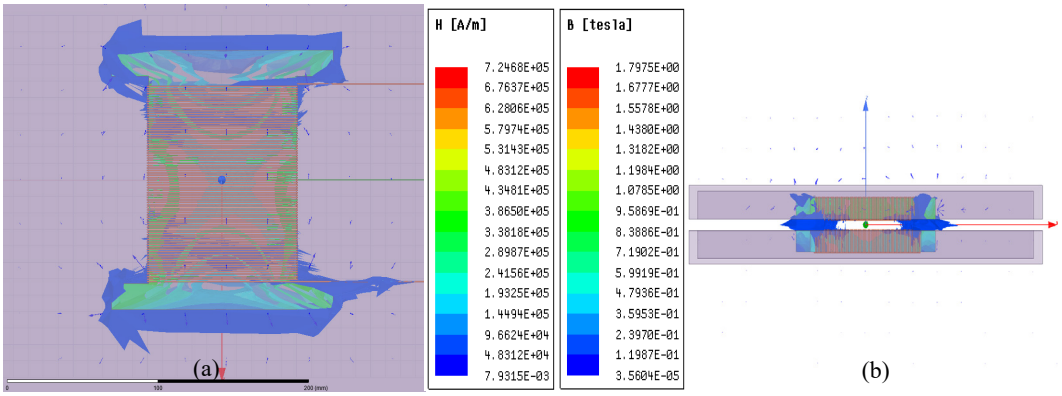


Figure 5.11: The EMF distributions of the H-shape coupler CPT system with 5 mm inner shielding gap and aluminium passive shielding at approximate resonant coupling status as an optimization, at 1 ms,. (a) Top view. (b) Left view.

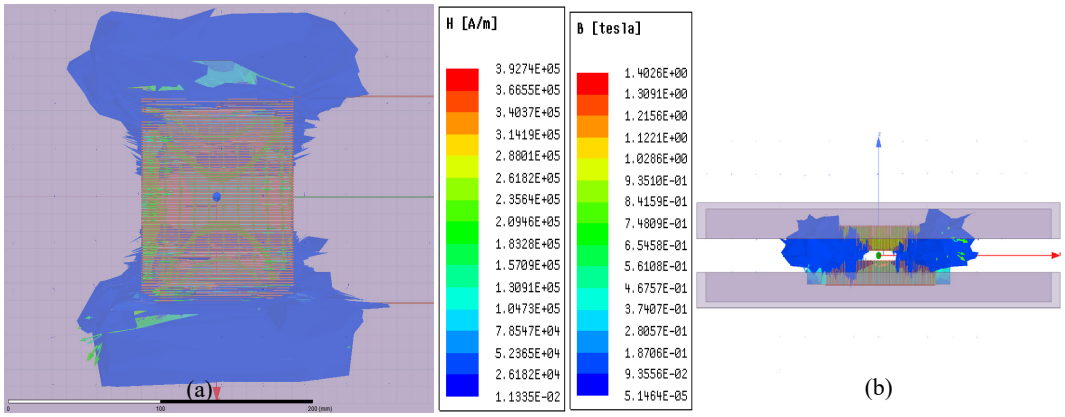


Figure 5.12: The EMF distributions of the H-shape coupler CPT system with 15 mm inner shielding gap and aluminium passive shielding at approximate resonant coupling status as an optimization, at 1 ms,. (a) Top view. (b) Left view.

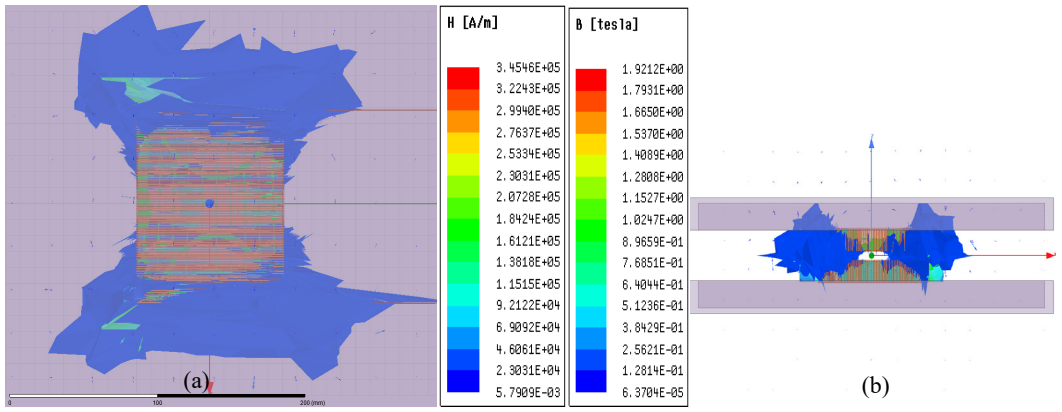


Figure 5.13: The EMF distributions of the H-shape coupler CPT system with 25 mm inner shielding gap and aluminium passive shielding at approximate resonant coupling status as an optimization, at 1 ms,. (a) Top view. (b) Left view.

### 5.2.4 Analysis and discussion from the aspect of waveform characteristics

In order to investigate both the EMF performance and electronic outputs, analysing waveforms seems to have certain reference values when some subtle differences and variations exist between control groups. In this study, waveforms generated and captured can show some delicate characteristics such as angular phases in terms of resulted RMS values and ratios between coils or elements.

In real-world applications, tiny positioning misalignments, supply offsets or frequency deviations may determine large variations in system outcomes like field distributions and output signals. Hence, it is necessary and meaningful to conduct insights into the actual real-time waveforms produced during the initial coupling establishment before a

stabilization tends to occur at some certain time point for the CPT system operation maximization.

Selectively, the 15 mm inner shielding gap CPT modular with semi-enclosed shells has been emphasized for flux wave and circuitry wave investigations despite inner shielding gap-based control groups of RMS flux linkage values versus frequencies graphed statistically before in section 5.2.3(a), which preliminarily, along with section 5.2.3(b) and (c), tends to conclude that the 15 mm inner shielding gap model can be the optimal one within these three groups. Therefore, it has a point in studying the 15 mm inner shielding gap model further from waveform characteristics point of view in section 5.2.4, in which all the raw data and results are based on ANSYS Maxwell outputs and then plotted with MATLAB for numerical statistics in Table 5.5.

***(a) Sinusoidal flux linkage waveforms***

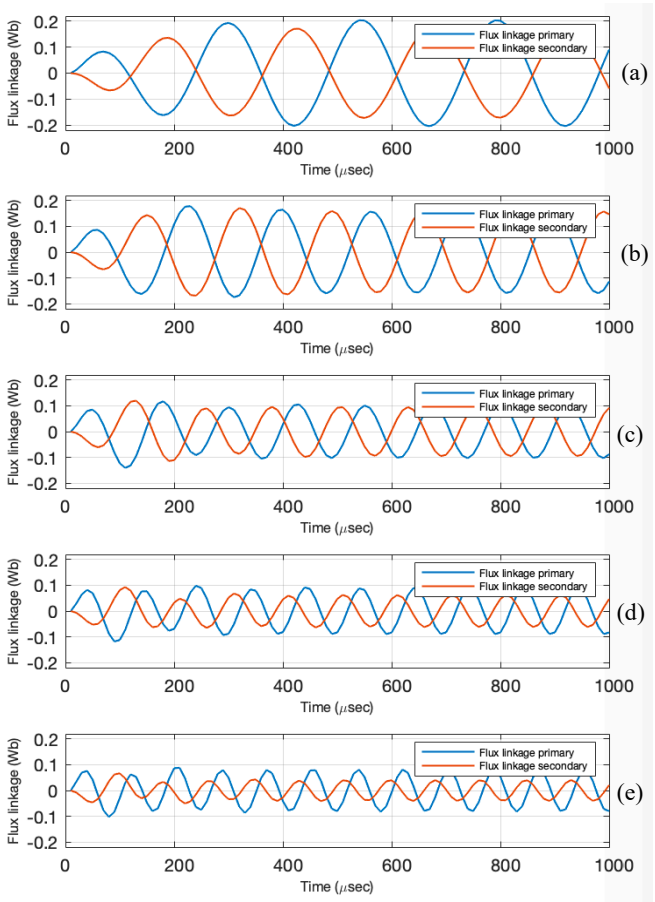


Figure 5.14: Flux linkage waveforms of primary and secondary coils, with 15 mm inner shielding gap at a variety of operating frequencies. (a) At 4 kHz. (b) At 6 kHz. (c) At 8 kHz. (d) At 10 kHz. (e) At 12 kHz.

From Figure 5.14, it can be found that most of the sinusoidal flux linkage waves tends to stabilize after their third or fourth period at frequency range of 4 kHz to 12 kHz, with angular phases and peaks tending to show stabilizations, which means the coupling system has fast response ability to achieve stable inductions for energy transmission within several hundreds of microseconds since initiating the power supply and also means possible capability of achieving fast and resilient CPT charging for EVs since the initial stages.

It can be probed from Figure 5.14(a) and noticed that the secondary induced flux tends to stabilize with a magnitude of 0.1721 Wb while the primary flux tends to have a peak value of about 0.2035 Wb when the 4 kHz inductive system approaches the stable coupling status after 600 microsecond. By calculating the phase angle difference using $\Delta\varphi = \frac{(t_2 - t_1)\times 10^{-6}}{\frac{1}{f}} \times 360°$, the phase difference $\Delta\varphi$ between the primary and secondary coils is 172.8°, with a phase lead by the secondary side.

In the same way of observing and calculating, in the 6 kHz system in Figure 5.14(b), it can be found that the magnitudes of both two flux waves become slightly lower with secondary and primary values of 0.1558 Wb and 0.1591 Wb, respectively, than those of 4 kHz one. The secondary flux waveform has a phase lead of 151.2° in terms of phase angle of primary flux.

Similarly, the 8 kHz model shows peak values of 0.0940 Wb and 0.1021 Wb for the secondary flux wave and the primary, with phase difference of 144° of the secondary leading the primary flux. The 10 kHz system appears to have a lower magnitudes of flux waveforms with values 0.0620 Wb and 0.0891 Wb corresponding to the secondary and primary flux linkages, and has a phase difference of 108° of the primary wave lagging the secondary again. In the 12 kHz flux waves, it can be seen that the secondary flux wave and the primary tend towards stability with magnitudes of 0.0404 Wb and 0.0775 Wb, respectively. A phase difference of 129.6 is computed in the 12 kHz 15 mm model in Figure 5.14(e) indicating the secondary flux AC leading the primary as well.

By comparing the results and tendencies in Figure 5.14, it can be noticed that both the two sides of flux linkages tend to have decreasing magnitudes in terms of increasing

operating frequencies and the secondary flux has a phase lead when compared to the primary flux wave at each operating frequency. In addition, the phase angle difference tends to be decreased by performances of flux waves although the phase difference shows a slightly upward value in the 12 kHz model. The phase angle status per se may not directly reflect the entire EMF strength but may indirectly determine the induced current on the secondary coil by induced magnetic field varying with phase varying.

***(b) Main sinusoidal quantities of the circuit system outputs***

Major sinusoidal quantities of the system include real-time flux linkage waves, voltages and currents on main elements. By comparisons over waveforms in terms of a variation of operating frequency, some subtle differences can be observed to draw conclusions such as angular phases. The signal waveforms of 15 mm inner shielding model are studied in terms of operating frequency range of 4 kHz to 12 kHz within 1000 microseconds, according to Figure 5.15 to Figure 5.19 and Table 5.5.

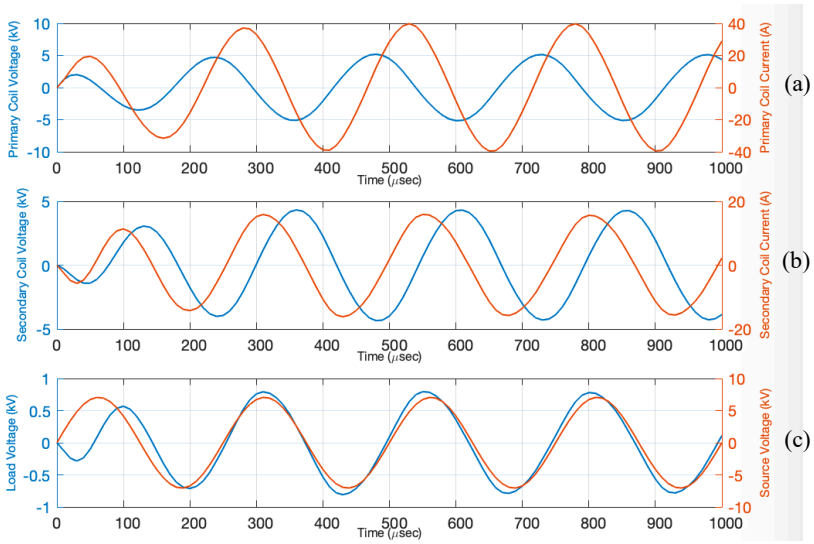


Figure 5.15: Acquired waveforms of the 15 mm inner shielding gap coupler at 4 kHz. (a) Waves of primary coil voltage and currents. (b) Waves of secondary coil induced voltage and currents. (c) Rear-end load voltage and front-end source voltage.

From Figure 5.15(a)-(c), it can be found that the magnitudes of primary voltage Vp, primary current Ip, secondary induced voltage Vs, and secondary induced current Is are 39.80 A, 5.19 kV, 15.89 A and 4.13 kV, respectively, when all the 4 kHz waves tend to be sinusoidally stable. The peak values of source voltage Vsource and load end voltage Vload acquired are 7.06 kV and 0.79 kV, respectively. Besides, by analysing angular

phases in each graph of Figure 5.15, it can be noticed that the primary voltage has a phase lead $\Delta\varphi_p$ of 72° when compared with primary current wave, which contributes to a PF of 0.3090 in Table 5.5. The secondary induced current leads the secondary voltage by 86.4°, resulting in a PF of 0.0628. The power supply voltage wave has a phase lag of 14.4°.

Furthermore, by comparing three pairs of graphs in terms of time axis in Figure 5.15 rather than analysing each pair separately, a finding can be recognized about the phase differences, which is that the Ip leads Is and Vs by 28.8° and 115.2°, respectively. This finding makes sense from perspectives of Faraday's law, which verifies that the power source voltage produces current Ip through the primary coil winding, generating EMF flux linkages and making coupling effects on the secondary coil which induces current Is and Vs. The order here obeys the induction principle and Faraday's law.

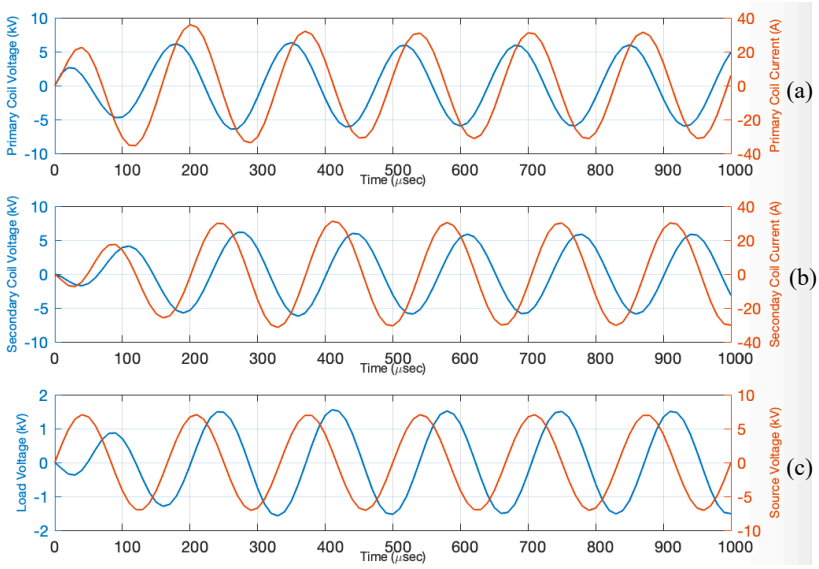


Figure 5.16: Acquired waveforms of the 15 mm inner shielding gap coupler at 6 kHz. (a) Waves of primary coil voltage and currents. (b) Waves of secondary coil induced voltage and currents. (c) Rear-end load voltage and front-end source voltage.

As can be calculated with curves for 6 kHz in Figure 5.16(a)-(c) and Table 5.5, the Ip with a peak of 31.13 A has a phase lag of 43.2° than Vp with a peak of 5.94 kV, resulting in a PF of 0.7289; the Ip with a magnitude of 30.08 A has a phase lead of 64.8° than Vp with a peak of 5.86 kV, contributing to a PF of 0.4258; the Vload with a peak value of 7.06 kV has a phase lag $\Delta\varphi'$ of 86.4° than Vsource with a peak of 1.504 kV. Again, it can be found that the Ip has phase leads than Is and Vs by 108° and 172.8°, which proves the effects and rules of Faraday's law and inductive coupling.

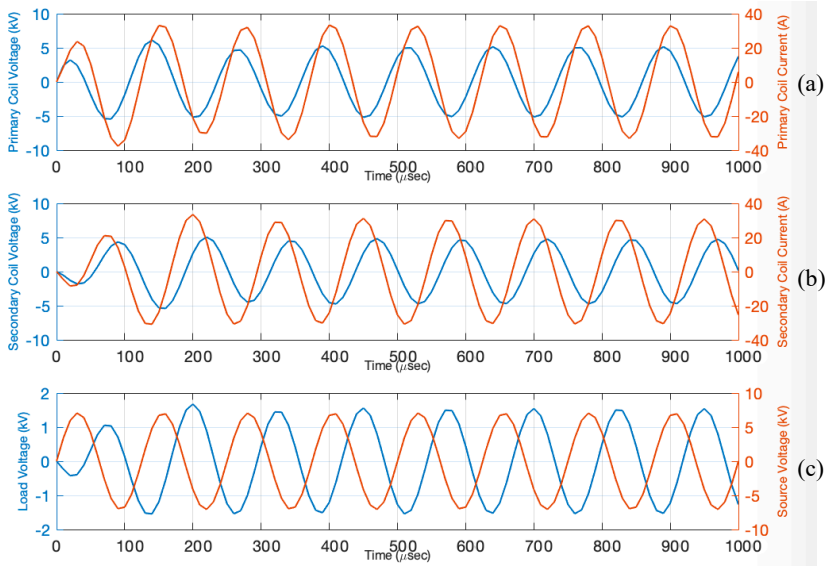


Figure 5.17: Acquired waveforms of the 15 mm inner shielding gap coupler at 8 kHz. (a) Waves of primary coil voltage and currents. (b) Waves of secondary coil induced voltage and currents. (c) Rear-end load voltage and front-end source voltage.

In Figure 5.17, the primary coil current Ip with a magnitude of 32.66 A has a phase lead $\Delta\varphi_p$ of 28.8° than the primary coil voltage Vp with a peak of 4.989 kV, resulting in a PF of 0.8763. The secondary coil current Is with a magnitude of 30.85 A leads the secondary voltage with a peak of 4.76 kV by 57.6°, which determines a PF of 0.5359, as calculated and shown in Table 5.5. The wave of voltage source leads the load voltage by 115.2°.

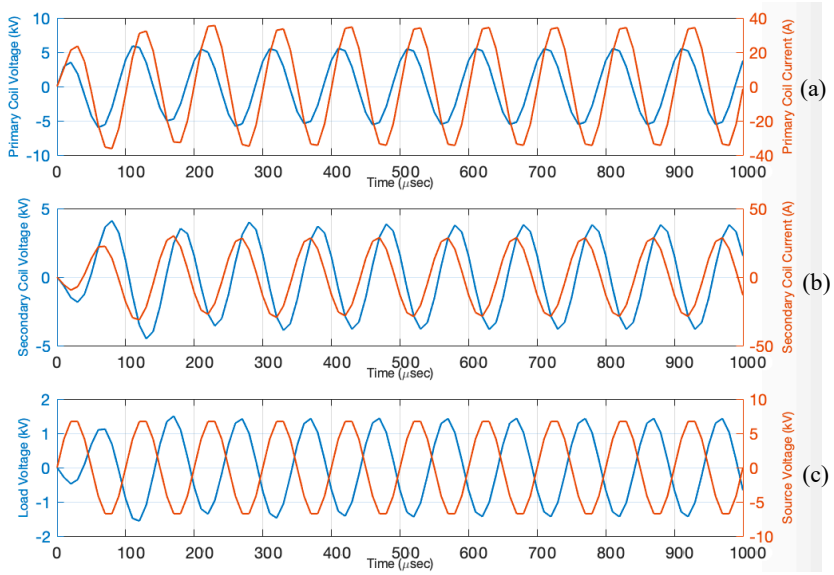


Figure 5.18: Acquired waveforms of the 15 mm inner shielding gap coupler at 10 kHz. (a) Waves of primary coil voltage and currents. (b) Waves of secondary coil induced voltage and currents. (c) Rear-end load voltage and front-end source voltage.

At 10 kHz in Figure 5.18, the waveform characteristics of all signals seem to have similar angular phase relations between each pair of them like at 6 kHz to 10 kHz. It can found that the Ip and Vp have peaks of 34.17 A and 5.50 kV, respectively, with Ip lagging Vp by 72°, which leads to a PF of 0.3090. On the secondary side, the magnitudes of Is and Vs are 28.57 A and 3.79 kV with Is phase-leading Vs by 36°, resulting in a PF of 0.8090. As for the waves of Vsource and Vload, it can be noticed that Vload with a peak value of 1.43 A has 180° opposite phase difference and lag to Vsource with 6.73 kV this time.

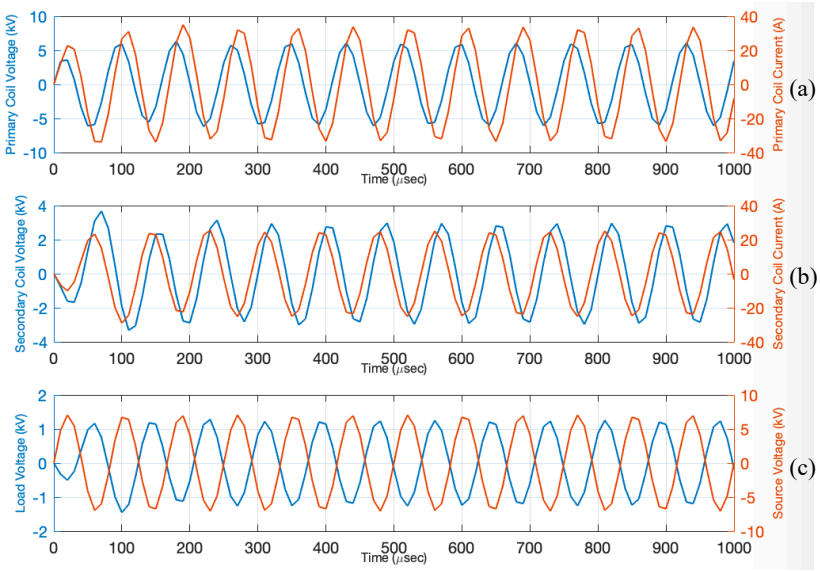


Figure 5.19: Acquired waveforms of the 15 mm inner shielding gap coupler at 12 kHz. (a) Waves of primary coil voltage and currents. (b) Waves of secondary coil induced voltage and currents. (c) Rear-end load voltage and front-end source voltage.

In the same way analyzing the waveforms for the 12 kHz operation within 0.1 ms, it can be seen that the Ip with a stable peak value of 33.06 A has a phase lag than Vp with a peak of 5.86 kV by 43.2°, according to Figure 5.19(a). Since the third period, it can be seen that the secondary coil current Is and voltage Vs have a phase difference of 43.2° with Is leading Vs again. Is shows a peak of 25.01 A and Vs shows a 2.95 kV. For the two ends of the circuit, the Vload presents a stable peak value of 1.25 kV lagging the Vsource of 7.06 kV by 172.8°. The phase difference $\Delta\varphi'$ between Vload and Vsource again tends to have a completely opposite angular relation, which can be found much larger than 14.4° at 4 kHz and the $\Delta\varphi'$ keeps increasing against the increase of operating frequency.

Table 5.5: Waveform characteristics of the 15 mm inner shielding distance model.

| Oper. Freq. (Hz) | $I_p$ (A) | $V_p$ (kV) | $\Delta\varphi_p$ | $PF_p$ | $I_s$ (A) | $V_s$ (kV) | $\Delta\varphi_s$ | $PF_s$ | $V_{source}$ (kV) | $V_{Load}$ (kV) | $\Delta\varphi'$ |
|---|---|---|---|---|---|---|---|---|---|---|---|
| 4000 | 39.81 | 5.19 | 72.1 ˚ | 0.31 | 15.89 | 4.31 | 86.4 ˚ | 0.06 | 7.06 | 0.79 | 14.4 ˚ |
| 6000 | 31.13 | 5.94 | 43.2 ˚ | 0.73 | 30.08 | 5.86 | 64.8 ˚ | 0.43 | 7.06 | 1.51 | 86.4 ˚ |
| 8000 | 32.66 | 4.99 | 28.8 ˚ | 0.88 | 30.85 | 4.76 | 57.6 ˚ | 0.54 | 6.95 | 1.54 | 115.2 ˚ |
| 10000 | 34.17 | 5.51 | 72.1 ˚ | 0.31 | 28.57 | 3.79 | 36.1 ˚ | 0.81 | 6.73 | 1.43 | 180 ˚ |
| 12000 | 33.06 | 5.86 | 43.2 ˚ | 0.73 | 25.01 | 2.95 | 43.2 ˚ | 0.73 | 7.06 | 1.25 | 172.8 ˚ |

Overall, by statistically comparing major data-acquired and calculated results in Table 5.5, there are several findings to be addressed. Firstly, as mentioned in analysis according to Figure 5.15, all other graphs from Figure 5.16 to Figure 5.19 also witness that the primary voltage has a phase lead than primary current, then the primary current leads the secondary induced current, secondary induced voltage and finally the load by phase differences in order. This phenomenon applying to all pairs of signal quantities reflects the effectiveness of electromagnetic coupling corresponding to Faraday's law and induction when it comes to relations between generating electromagnetic fields and inducing electricity via changing current. Secondly, it can be noticed that, at 8000 Hz, the system produces the optimal phase difference $\Delta\varphi_p$ on the primary coil, meaning high coil energy available for transmission; on the secondary side, the induced current appears to be the highest with 30.85 A and also the voltage on the load reaches its highest with 1.54 kV, which together means an optimal power level transferred to load can be achieved at 8000 Hz when the CPT system tends to resonate for the optimized induced current and voltage at its resonant condition approximated to 8000 Hz. Although the coil efficiency at 8000 Hz is seen not the highest with 51.81%, the overall system efficiency can be seen to reach its highest with 36.26% when compared with those at other operating frequencies, according to Table 5.4. Thirdly, it is apparent that the received coil RMS power approximates to its highest when the resonant coupling phenomena tends to occur around the calculated resonant frequency, which in this model scenario is about the range from 6000 Hz to 10000 Hz especially at about 8000 Hz, according to results in Table 5.4 and Table 5.5. This is of help when it comes to considering secondary coil power received as a metric of testing a CPT charging dock system in practical applications for EVs.

These findings regarding field metrics, power outputs and angular phase performance that are all considered as conclusions also prove that the optimization of the H- shape coupler CPT system with 15 mm inner shielding distance and 10 mm air gap at 8000 Hz can be significantly achieved.

## 5.3 Chapter conclusions

In Section 5.1, a small-sized geometrically improved H-shape coupler CPT system and the basic principles of electromagnetic resonant coupling model have been presented, along with the analysis and discussion on RMS power transfers, CPT system efficiencies, generated electromagnetic field characteristics and performances of using three passive shielding materials. It can be found that the magnetic field flux distributions have been optimally formed by the designed ferromagnetic H-shape core. By using aluminium passive shielding to facilitate the field flux paths, the CPT system could output a maximum overall system efficiency of 27.48% and a peak RMS real power of 42.90 kW on the system load end, at about 10000-Hz operating frequency when the CPT system tends to perform with magnetic resonant coupling status.

Section 5.2 presented a small-sized geometrically improved H-shape coupler CPT system and analyzed performances of using three different inner shielding distances. By focusing on RMS power transfers, CPT system efficiencies, generated electromagnetic field characteristics, it can be found that the 15 mm inner shielding gap can be an optimal shielding method with maximum outputs when considering system power transfer, system efficiency and electromagnetic coupling performance. The 15 mm inner shielding gap CPT system can produce a maximum system efficiency of 36.26%, a peak system output power of 22.63 kW, satisfactory values of magnetic field strength and flux density throughout the coupling modular at about the magnetic resonant frequency. Analyses and comparisons regarding angular phase relations have also been proposed and discussed as another support for this optimization of the specifically designed model from a waveform characteristics point of view.

# Chapter 6 Misalignment tests for prototype with inner shielding distance

Chapter 6 focuses on investigating a range of lateral and longitudinal misalignment variations of the transmitting modular and receiving modular, with corresponding actual effects and impacts on system performance of a specific CPT model proposed and optimized by previous sections, from a series of research perspectives such as power electronics outcomes and EMF performance. Besides, a proactively optimal frequency tracking method is proposed to address the shortcomings caused by coupling misalignment behaviours of an imperfectly aligned and coupled CPT system.

## 6.1 Background

One of the most challenging difficulties and shortcomings that need to be highlighted even from a long-term perspective, as briefly introduced and discussed before, is coupling misalignment issue. CPT coil misalignments are normally caused by improper parking position of the EV from the customer side, which would result in displacements in lateral, longitudinal directions and also angular deviations for transmitting and receiving coil modules. Any degree or amount of misalignments will lead to a degraded magnetic coupling performance due to the nature of electromagnetic field alternating and varying which are fairly dependent upon the real-time operating frequency actually required by an optimal CPT system [221], [222]. As a result, the imperfectly aligned and coupled CPT system may appear to operate with much lower energy efficiency, reduced power transmission rating and unexpected longer battery charging time of a full cycle. On the other side, misalignment of coupled coils could lead to an increase of heat dissipation in switching losses from the front-end switching circuit, which largely impacts the system efficiency and operation performance [223].

Therefore, investigating the misalignment tolerance of a prototyped CPT system in order to keep the transferred power, efficiency and field performance within acceptable limits or even at optimally constant rates has also become a challenging sub-divisional topic in Chapter 6 of this thesis.

## 6.2 System design and control groups

As emphasized a lot in previous sections, an optimal CPT system is fairly dependent upon its coupler module designs and specifications as how the produced electromagnetic field distribution in between the coils inductively determines the actual power electronics outcomes and EMF results, which therefore addresses the significance of coupling modular design and real-time operation when implementing performance variations in terms of other main factors.

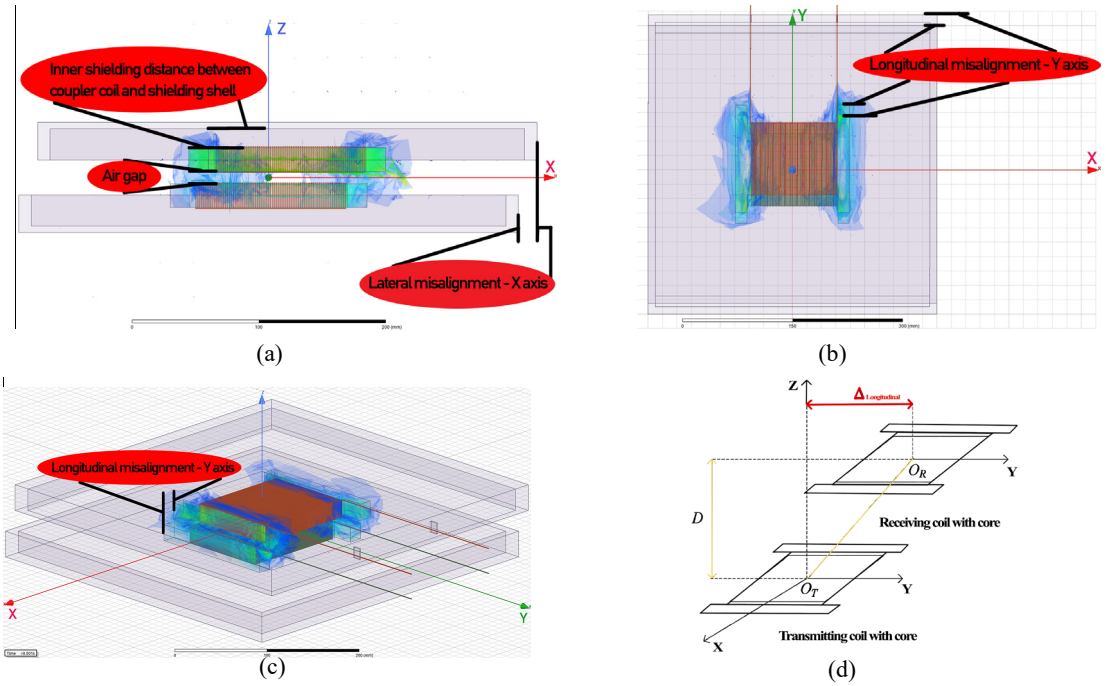


Figure 6.1: Illustrations of designed coupler with misalignments. (a) Lateral misalignment left view. (b) Longitudinal misalignment top view. (c) Dimetric view. (d) A sketch to illustrate longitudinal displacement.

Based on taking advantages of ferromagnetic materials as cores and semi-enclosed shielding design as studied before, the specific CPT coupler prototyped in Section 5.2 has been utilized to build control groups in this section in order to investigate the misalignment topic. As illustrated in Figure 6.1, the upper receiver side corresponding to the secondary coil module may not be properly aligned with the primary coil module in lateral and longitudinal directions, which simulates the actual microscopic scenarios in real-world vehicle parking manoeuvres. In this section, the displacement on X axis is called lateral misalignment while the displacement on Y axis is called longitudinal misalignment as indicated in Figure 6.1(a)-(d). The passive shielding ferromagnetic material adopted and the inner shielding distance between coil and shell in this section

are set up according to the optimization studies conducted in Section 5.1 and 5.2. The specifications of the entire CPT coupling module have been presented in Table 6.1 for the establishment of control groups in terms of various misalignments and supplied operating frequencies. The inner shielding shell-to-coil distance is specifically set as 15 mm in the studies of Chapter 6 based on optimization tests and evaluations from previous chapter.

Table 6.1: The specifications of the designed CPT system for misalignment tests.

| Parameters | Values |
|---|---|
| Winding size | 100 mm x 100 mm x 20 mm |
| Core size | 150 mm x 150 mm x 20 mm |
| H-shaped core bar size of each side | 150 mm x 15 mm x 20 mm |
| Primary winding number of turns | 80 turns |
| Secondary winding number of turns | 80 turns |
| Air gaps of the CPT charging system | 10 mm |
| Inner shielding distance between coil and shell | 15 mm |
| Winding material | Litz wire |
| Shielding size | 400 mm x 400 x 30 mm |
| Shielding thickness | 10 mm |
| Passive magnetic shielding materials | Alumimium |
| Relative permeability μ of core material | 1000 |
| Relative permeability μ of shielding material | 1.000021 |
| S-S compensation capacitors | 150 nF |
| Load resistor | 50 ohm |
| Voltage power supply | RMS 5 kV |
| Range of operating frequency | 4000 to 14000 Hz |
| Lateral misalignment variations | 5 mm, 10 mm and 15 mm |
| Longitudinal misalignment variations | 5 mm, 10 mm and 15 mm |

Without a perfect alignment between coils in real-world applications, the knowledge and methods built to achieve a high misalignment tolerance are needed as a compensation on the other hand in order for a CPT system to operate at an acceptable proximity to a resonant optimum state. It seems necessary to make a very precise control on resonant frequency supply for the system, while the perfectly exact operating frequency of each CPT operation scenario cannot be tracked and provided at all times as every coupling

scenario can be different depending upon the varying magnetic field and its RMS real values that are generated over time at the initial stage before reaching a stability when inductively coupling.

Nevertheless, by preliminarily studying the misalignment behaviours for a specific CPT system in terms of main ranges of operating frequency and main scopes of directional displacements, it is more likely to know how a degree of misalignment requires an accordingly approximate interval of optimal operating frequency as an alternative solution addressing low coupling coefficients, mutual inductances and unacceptable magnetic field outcomes, which can be called an optimum frequency retuning or proactively optimal frequency tracking method in this section. In this way, three lateral displacements and three longitudinal displacements against an operating frequency range of 4 kHz to 14 kHz have been tested for a small-sized laboratory-scale CPT coupling modular in ANSYS 3D Maxwell to explore the misalignment behaviours.

## 6.3 Results and analyses for various lateral misalignments

### 6.3.1 RMS Flux linkages and currents

As two raw matrices used to measure how a magnetic field system performs, flux linkage and current with the nature of their nonlinear relation also reflect the misalignment behaviours in Section 6.3. Based on equations (3.37a) to (3.37c), simulating and tracking the characteristic nonlinear relationships of RMS flux linkage versus operating frequency and of RMS current versus operating frequency are essential for a CPT system to be assessed.

From Figure 6.2(a), it can be seen that the primary flux linkage of the 5 mm lateral misalignment CPT system shows a steady value of 0.0723 Wb at 6000 and 8000 Hz, after which the curve gradually decreases. In the meantime, the secondary flux linkage appears to have a similar trend and also stabilizes at 6000 to 8000 Hz with a value of 0.0677 Wb. Regarding the primary coil current, an upward peak can be seen at 10000 Hz with a value of 24.4860 A. On the other hand, the secondary coil current increases from 10.6561 A at 4000 Hz to its peak at 8000 Hz with a value of 21.7627 A.

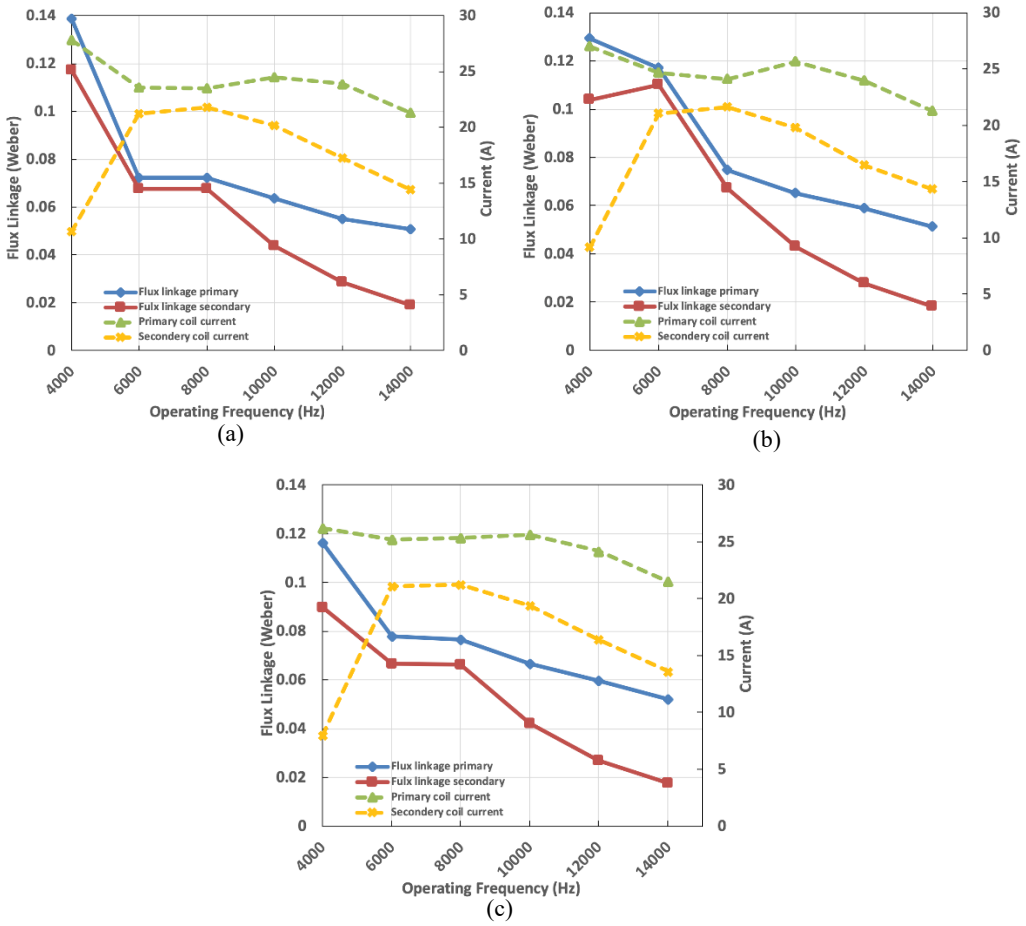


Figure 6.2: RMS flux linkages and currents versus operating frequencies for lateral misalignment tests. (a) 5 mm lateral misalignment. (b) 10 mm lateral misalignment. (c) 15 mm lateral misalignment.

As for the 10 mm lateral misalignment behaviours on flux linkage shown in Figure 6.2(b), the primary flux linkage shows a continuously decreasing curve against operating frequency from 0.1294 Wb at 4000 Hz to 0.0513 Wb at 14000 Hz, which is different from the trend observed in Figure 6.2(a). The secondary flux linkage shows a sharp upward peak of 0.1103 Wb at 6000 Hz and then turns to descend until the lowest at 14000 Hz. However, both the primary and secondary currents can be noticed to have fairly similar tendencies as those in Figure 6.2(a) with peak values of 25.6855 A and 21.2811 A at 10000 Hz and 8000 Hz, respectively.

From Figure 6.2(c), it is apparent that all the flux linkages and currents appear to have similar trends as those four curves in Figure 6.2(a). The flux linkages of primary and secondary coils show steady results between 6000 and 8000 Hz with values of about 0.0779 Wb and 0.0668 Wb, respectively. The primary current stabilized across a long

frequency, which shows a good tolerance to lateral misalignment. The secondary current has relatively steady results between 6000 and 8000 Hz with values of around 21.1132 A.

By comparing these three misalignment behaviours, it can be found that the operating frequency range between 6000 and 8000 Hz is more able to ensure acceptable and stable flux linkage outputs, which could be the relatively optimal and narrow frequency tuning range for lateral misalignment scenarios for CPT applications. On the other side, the primary and secondary coil currents appear to produce satisfactory RMS values over the operating frequency range of 6000 to 10000 Hz for all the three lateral misalignment tests.

### 6.3.2 Efficiencies and RMS real powers

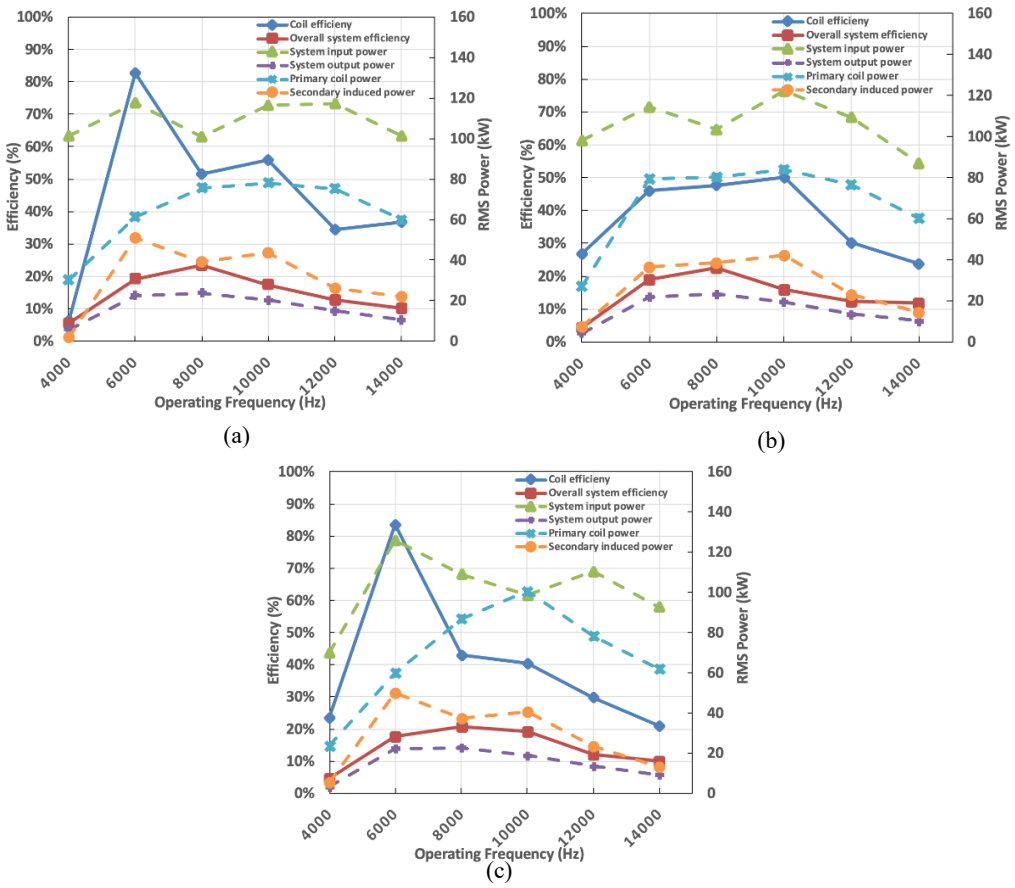


Figure 6.3: Efficiencies and RMS real powers versus operating frequencies. (a) 5 mm lateral misalignment. (b) 10 mm lateral misalignment. (c) 15 mm lateral misalignment.

Based on equations (3.44) and (3.45), the coil efficiency and overall system efficiency can be calculated to analyse and compare the impacts of lateral misalignment variations on a CPT coupling system. According to equation (3.43) and the angular phase

differences observed from raw waveforms, the RMS values of real power on every two circuit elements of the CPT system have been worked out and plotted in the three subgraphs of Figure 6.3 for analysis.

Comparing the three graphs of Figure 6.3 in terms of efficiency, it can be observed that the 5 mm lateral misalignment system has the highest value of overall system efficiency of 23.433%, while the 10 mm and 15 mm lateral misalignment systems present 22.453% and 20.741%, respectively. All these three peaks occur at around 8000 Hz for each test, indicating the resonant frequency effectiveness applies to similarly designed CPT system despite some variations of displacement on X axis and reflecting the optimal operating frequency tolerance to lateral misalignments. On the other hand, it can be found from Figure 6.3(a) to (c) that an optimal overall system efficiency state may not mean the most satisfactory coil efficiency between transmitting side and receiving side.

In terms of coil power ratings in the three lateral misalignment tests according to Figure 6.3(a) to (c), it can be seen that every test appears to show RMS peak value of primary coil power at 10000 Hz, with 78.116 kW, 83.977 kW and 100.550 kW, respectively for 5 mm, 10 mm and 15 mm lateral tests. In the meantime, both the secondary induced powers of 5 mm and 15 mm lateral tests appear to reach their peaks at 6000 Hz with 50.790 kW and 50.129 kW, respectively. However, the 10 mm lateral misalignment test shows its highest secondary coil power at 10000 Hz with 42.147 kW, which is similar to the values of other two tests at 10000 Hz point.

As for the system output power ratings on load, it can be found that all the highest RMS output powers tend to present at the calculated natural resonant frequency point of 8000 Hz of the specifically designed model, with values of 23.681 kW, 23.287 kW and 22.623 kW, respectively. From electric vehicle charging point of view, the highest power rating achieved at load end means fastest and optimal energy transmission for battery charging. Therefore, based on the study on lateral misalignment, when the priority about EV charging is about fast charging or high energy efficiency, the 8000 Hz operating frequency as supply condition with an unavoidable and smallest misalignment is supposed to be reached for a resonant coupling charging.

### 6.3.3 Calculated resonant frequency and calculated inductance

Based on natural resonant frequency equation (3.46) and equation (3.37c) about flux linkage and current, it is necessary to analyse the variable trend of operating frequency supply versus variable calculated resonant frequency at each coupling condition and to observe the relation between the stability of calculated resonant frequency variation and the operating frequency that is fed to the system as a frequency probe for tuning purpose towards an optimal electromagnetic resonant coupling state of the entire CPT system for a contactless energy transmission optimization.

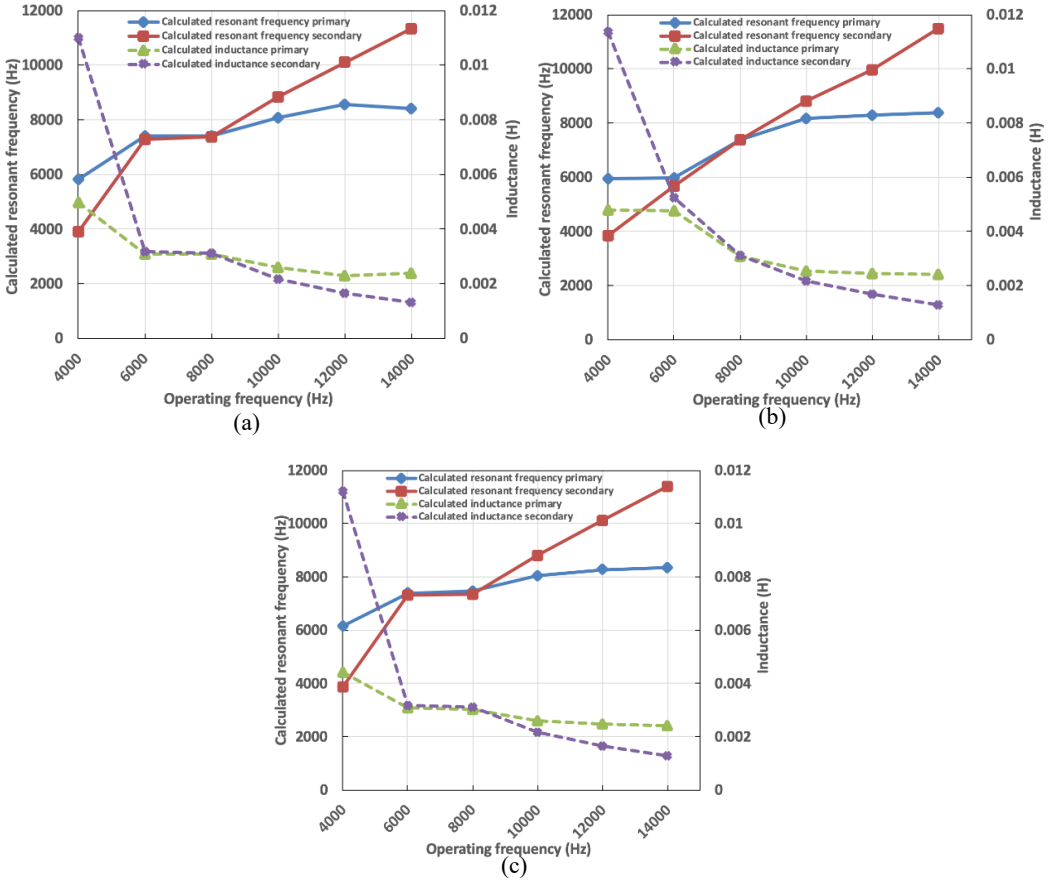


Figure 6.4: Calculated resonant frequencies, inductances versus operating frequencies. (a) 5 mm lateral misalignment. (b) 10 mm lateral misalignment. (c) 15 mm lateral misalignment.

Numerical results that are accurate to four decimal places have also been gathered in Table 6.2 for more detailed and subtler comparisons in addition to the visual graphs depicting approximate tendencies and relations in Figure 6.4(a) to (c).

Table 6.2: Calculated inductances and resonant frequencies versus operating frequency for lateral misalignments.

| Operating frequency (Hz) | ◆ *5 mm lateral misalignment* | | | |
|---|---|---|---|---|
| | Calculated inductance – primary (mH) | Calculated inductance – secondary (mH) | Calculated resonant freq. – primary (Hz) | Calculated resonant freq. – secondary (Hz) |
| 4000 | 4.9850 | 10.9890 | 5820.2778 | 3920.0824 |
| 6000 | 3.0722 | 3.1851 | 7413.9953 | 7281.3473 |
| 8000 | 3.0791 | 3.1108 | 7405.5948 | 7367.7784 |
| 10000 | 2.5933 | 2.1685 | 8069.4988 | 8824.6216 |
| 12000 | 2.2987 | 1.6547 | 8571.1149 | 10102.2623 |
| 14000 | 2.3899 | 1.3122 | 8405.8563 | 11344.1403 |
| | ◆ *10 mm lateral misalignment* | | | |
| | Calculated inductance – primary (mH) | Calculated inductance – secondary (mH) | Calculated resonant freq. – primary (Hz) | Calculated resonant freq. – secondary (Hz) |
| 4000 | 4.7869 | 11.3579 | 5939.4201 | 3855.8956 |
| 6000 | 4.7456 | 5.2458 | 5965.2519 | 5673.7101 |
| 8000 | 3.0958 | 3.1138 | 7385.6748 | 7364.2183 |
| 10000 | 2.5345 | 2.1723 | 8162.5970 | 8816.9507 |
| 12000 | 2.4528 | 1.6972 | 8297.3745 | 9974.9659 |
| 14000 | 2.4122 | 1.2776 | 8367.0036 | 11496.5885 |
| | ◆ *15 mm lateral misalignment* | | | |
| | Calculated inductance – primary (mH) | Calculated inductance – secondary (mH) | Calculated resonant freq. – primary (Hz) | Calculated resonant freq. – secondary (Hz) |
| 4000 | 4.4377 | 11.2028 | 6168.7068 | 3882.4912 |
| 6000 | 3.0891 | 3.1639 | 7393.6142 | 7305.7247 |
| 8000 | 3.0186 | 3.1215 | 7479.4449 | 7355.1159 |
| 10000 | 2.6052 | 2.1730 | 8051.0703 | 8815.3722 |
| 12000 | 2.4655 | 1.6535 | 8276.0296 | 10105.9084 |
| 14000 | 2.4136 | 1.3006 | 8364.4815 | 11394.6496 |

By analysing and comparing numerical results in Table 6.2 and the three graphs of Figure 6.4, it can be found that the secondary calculated resonant frequency of each test model tends to be linearly increasing after 8000 Hz tuning test. Nevertheless, both the secondary calculated resonant frequencies of 5 mm and 15 mm lateral tests show a stable range

across 6000 Hz to 8000 Hz, which may reflect a relatively constant resonant coupling state over feeding operating frequency and power input. As for the primary calculated resonant frequency, all the three tests basically show upward tendencies over the tested operating frequency range, while the 5 mm and 15 mm lateral tests tend to present a slow increasing since 6000 Hz point, which is relatively earlier than that of 10 mm lateral test.

Comparing all the primary and secondary calculated resonant frequency curves, a significant finding is that the primary calculated resonant frequency of each test seems able to reach a relatively constant stability after about 10000 Hz, which means the CPT system can show a satisfactory tolerance to lateral misalignment effects as a long range of frequency supply can be utilized to resonate the secondary receiving coil transmitting energy to the load. However, the secondary side shows a more linear relation when retuning and tracking its natural resonant frequency, which reflects a difficulty in pursuing a satisfactory resonant state for the secondary coil to enhance wireless energy transmission performance from the front coupling side.

From the calculated inductance point of view, it also can be seen that the stabilization state of resonant coupling in terms of frequency is able to occur over the frequency range between 6000 Hz to 8000 Hz according to all the three groups of results from Table 6.2. Furthermore, the relatively constant stability of both coils' calculated inductance values after 6000 Hz is of help when monitoring and predicting the actual winding-produced inductance value in mH level based on stabilized proximity in order for the lateral misalignment behaviours of this kind of designed coupler to be further evaluated.

### 6.3.4 Analysis on EMF performance and field distribution with a close proximity to electromagnetic resonant coupling

To observe and investigate the electromagnetic field distributions and major performance indices, 3D finite-element method is used to undertake numerical computations to solve Maxwell equations (3.25) and field equations (3.30) to (3.42) in terms of magnetic flux density **B**, magnetic field strength **H**, electric current density **J** and energy stored in field. It is necessary to introduce and illustrate the main concepts in EMF as below.

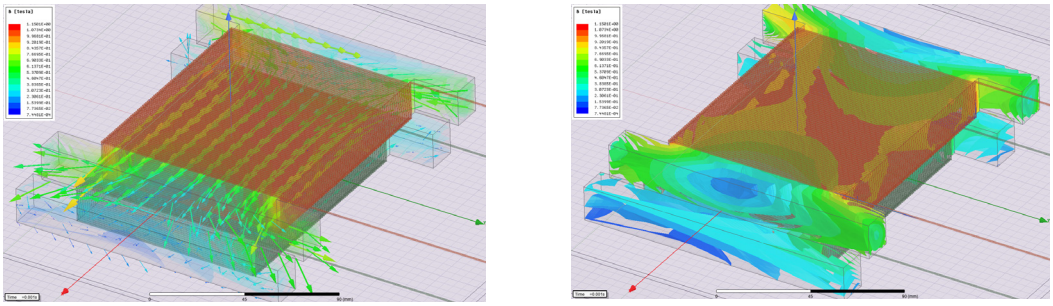

Figure 6.5: Illustration of magnetic flux density **B** in a field. (a) View of vectors. (b) Scalars.

As illustrated in Figure 6.5, the magnetic flux density **B** in tesla can be represented by vector arrows passing through both the lower and upper ferromagnetic cores in Figure 6.5(a) or can be depicted by scalar layers in Figure 6.5(b).

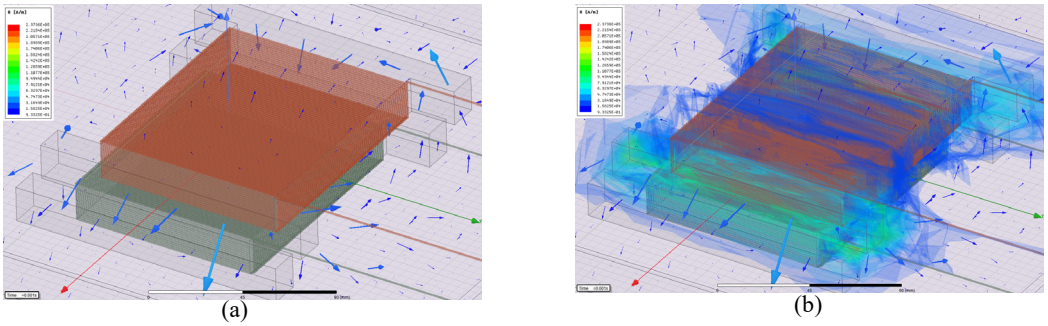

(a) (b)

Figure 6.6: Illustration of magnetic field strength **H** in a field. (a) View of vectors. (b) Scalars.

In Figure 6.6(a), the magnetic field strength **H** in ampere per meter is represented by vector arrows distributed at points in space excluding model cores and coupler materials. In Figure 6.6(b), scalars that appear to be like cloud layers can also be used to describe magnetic field strength. Both vectors and scalars of the **H** values are of help to analyse the magnetic field distribution in directions and performance in numerical values at specific points.

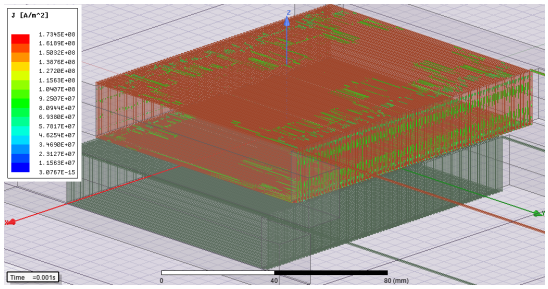

Figure 6.7: Illustration of electric current density **J** in a field.

From Figure 6.7, it can be noticed the electric current density only describes the density in windings, which accords with the electric field concepts applied to wire itself only and discussed within wire cross sections or surfaces.

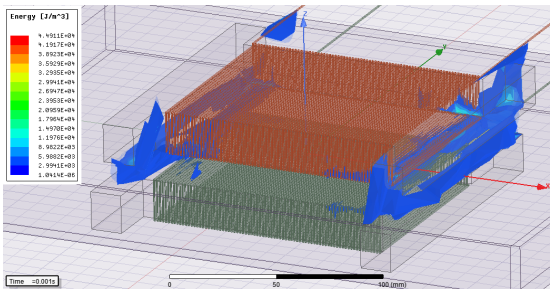

Figure 6.8: Illustration of energy stored in a field.

Energy stored in field can be seen in Figure 6.8, in which it can be noticed that energy storage as a metric in EMF is calculated and illustrated in air space only, meaning that a state of field energy is being stored in air region instead of solid model materials.

Regarding analysis and comparison, in the major part of this subsection below, the field performance of each lateral misalignment test at 1 millisecond is selectively observed as the system tends to reach a noticeable stabilization and optimal resonant coupling state with most EMF and power electronic outputs approaching maximums. Each of the three lateral tests are to be compared visibly and numerically according to the field distributions transiently captured and the RMS values of main field metrics computed in 3D Maxwell, which are presented in left, top and dimetric views in Figure 6.9 to Figure 6.11.

By observing the details of field distributions and comparing the maximum scalar values of four major indices in entire field from Figure 6.9 to Figure 6.11, there can be several significant findings required to be emphasized.

Firstly, the 10 mm misalignment in lateral direction may be a threshold point for this specific model since the maximum scalars of H field, B field, current density J can be seen to be increased from the 5 mm to 10 mm lateral misalignment tests while these scalars of the 15 mm test appear to drop below the values of 5 mm one. These phenomena about scalar variations of major field outputs could witness a critical point or ‘tipping point’ for this model to perform within a satisfactory range of lateral misalignment EMF behaviours.

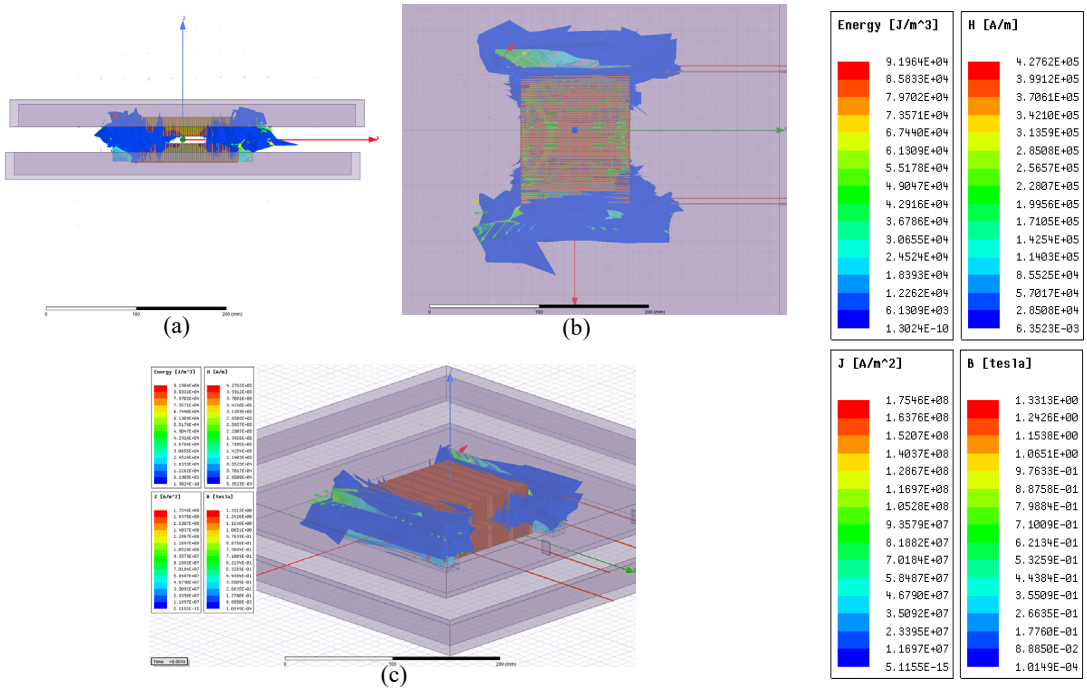


Figure 6.9: The 5 mm lateral misalignment test - Field distributions and illustrations of each metric of EMF performances at 8 kHz. (a) Left view. (b) Top view. (c) Dimetric view.

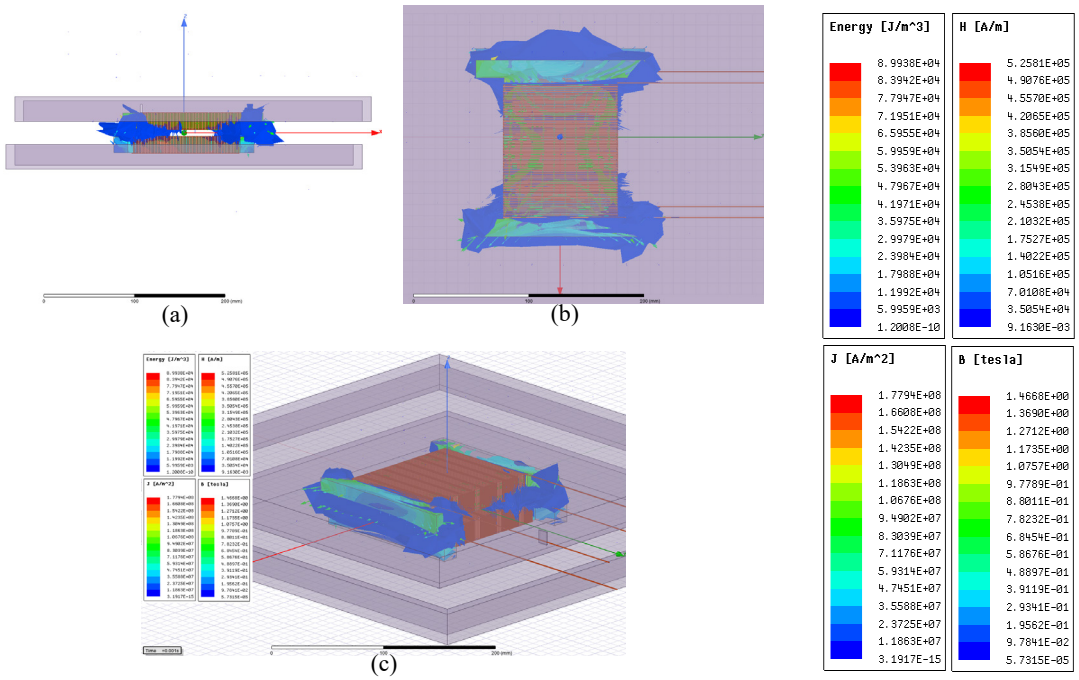


Figure 6.10: The 10 mm lateral misalignment test - Field distributions and illustrations of each metric of EMF performances at 8 kHz. (a) Left view. (b) Top view. (c) Dimetric view.

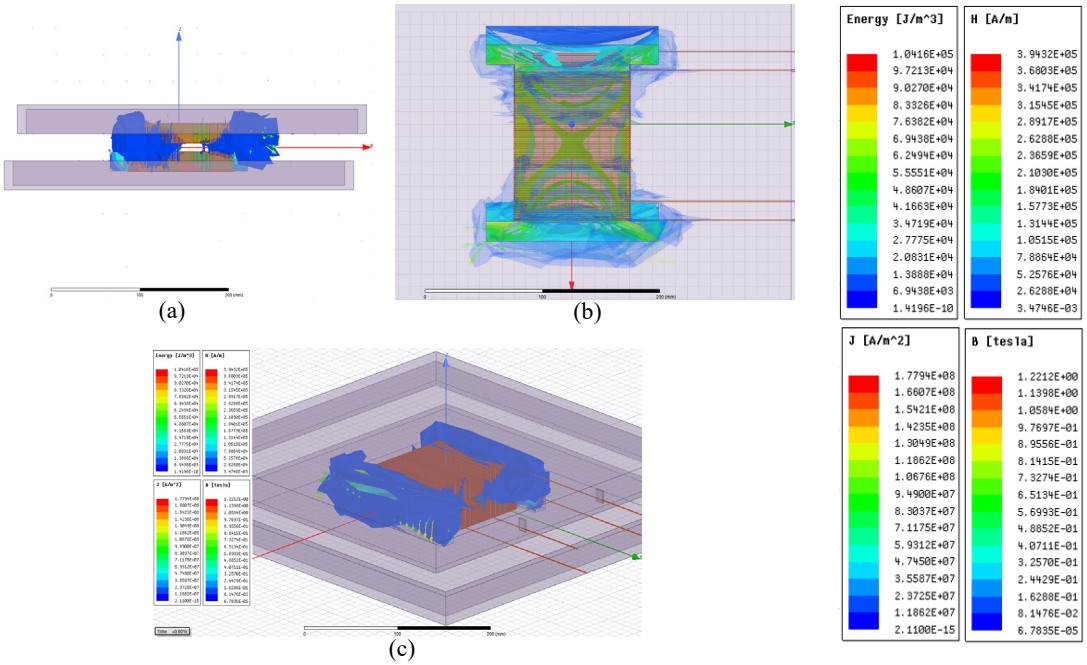


Figure 6.11: The 15 mm lateral misalignment test - Field distributions and illustrations of each metric of EMF performances at 8 kHz. (a) Left view. (b) Top view. (c) Dimetric view.

Secondly, an intuitively and visibly ‘stronger’ electromagnetic field may not definitely signify that this system would result in better RMS outputs from power electronics point of view. Along with numerical evidences over flux linkages, currents and RMS powers from curves in Figure 6.2 and Figure 6.3, it can be noticed that the primary flux linkage, primary coil power and primary currents tend to increase at 8000 Hz, which fairly accords with the increases of H value and B value from 5 mm to 10 mm lateral misalignments. Nonetheless, the most key system outputs such as the overall system efficiency, RMS power output are not seen to increase from 5 mm to 10 mm lateral misalignment fundamentally due to the actual angular phase deviations between the two sides leading to eventual differences on RMS results of the system.

Thirdly, the maximum scalar values need to be analysed along with actual tendencies of each EMF vectors at different coordinates in field and sometimes the directions of vector arrows play a more important and determinant role for a field distribution and a system power electronics performance of outputs. Based on Figure 6.9 to Figure 6.11, it can be found that the arrows of H vectors and B vectors at critical points like corners and external edges of the H-shape cores in the 5 mm lateral misalignment field appear to be significantly much stronger and more concentrated than the 10 mm and 15 mm ones,

especially for the vectors shown on the secondary side. This finding may explain the reason why the 5 mm lateral misalignment test produces better overall system performance than the 10 mm and 15 mm ones despite of sometimes lower satisfactory results about maximum EMF scalar values in figure legends.

## 6.4 Results and analyses for various longitudinal misalignments

In accordance with the analysis methods in Section 6.3, this Section 6.4 is to analyse the raw results and calculated results in terms of operating frequency and to describe the electromagnetic field distribution and performance at about magnetic resonant coupling conditions for a group of longitudinal misalignment models.

### 6.4.1 RMS Flux linkage and currents

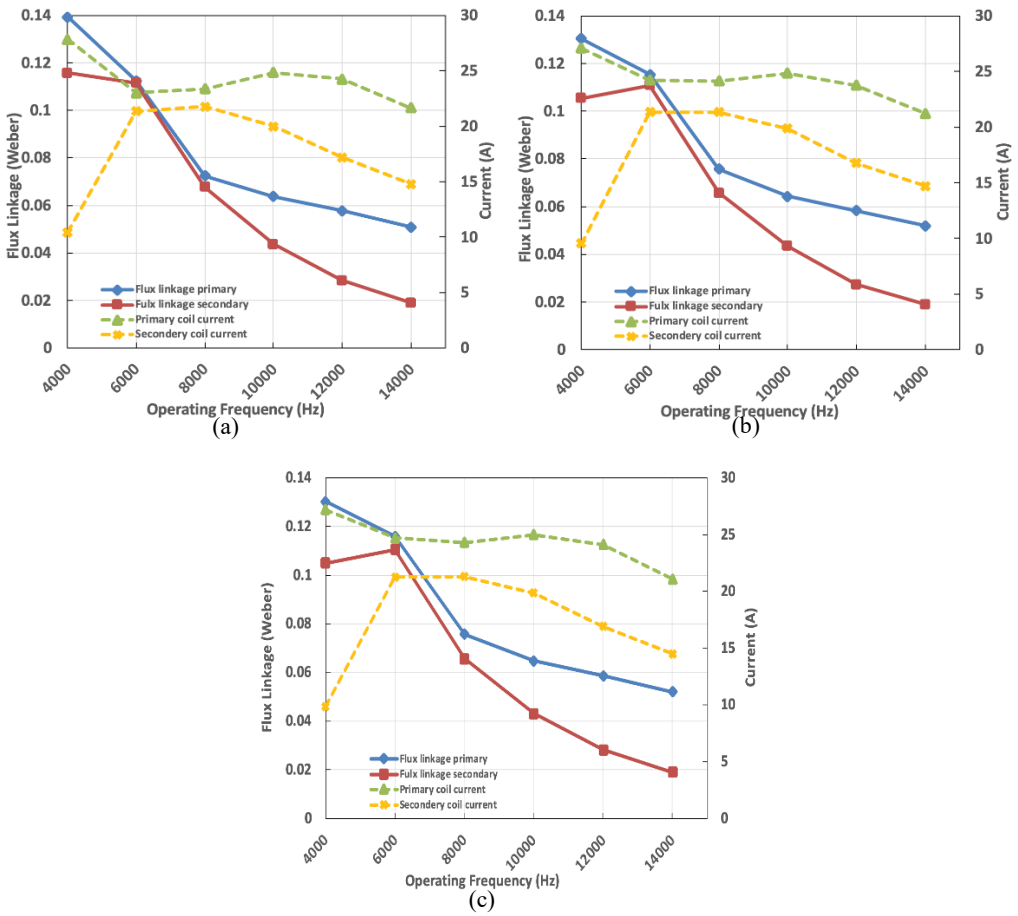


Figure 6.12: RMS flux linkages and currents versus operating frequencies for longitudinal misalignment tests. (a) 5 mm longitudinal misalignment. (b) 10 mm longitudinal misalignment. (c) 15 mm longitudinal misalignment.

The trends of flux linkages in longitudinal misalignment tests in terms of operating frequency in Figure 6.12 can be noticed to be different from flux linkages of lateral misalignment tests in Figure 6.2 before. From Figure 6.12(a) to (c), all the three graphs of primary RMS flux linkage show constantly decreasing trends versus operating frequency while the secondary flux linkages have an upward peak at 6000 Hz after which the curves start to drop. However, previously in Figure 6.2(a) and (c), both primary and secondary flux linkages appear to stabilize within a range of operating frequency of 6000 Hz to 8000 Hz. This difference between lateral and longitudinal tests may reflect a better tolerance of this coupler in a lateral direction than in longitudinal direction, which would lead to impacts on EMF characteristics and power outputs afterwards.

By comparing within these three longitudinal misalignment tests and with Figure 6.2 regarding tendencies of coil currents, it can be seen that almost all these trends about coil currents on both sides present to have fairly similarities in directions and in values with minor deviations. In Figure 6.12(a) to (c), all the three primary coil currents tend to show stable variations across the entire operating frequency range and reach the peaks at 10000 Hz with values of 24.8219 A, 24.8315 A and 24.9887 A, respectively. Regarding the secondary coil currents, the measured RMS peak values of each test are 21.7621 A, 21.3269 A and 21.2814 A, respectively, at about an approximate resonant frequency point of 8000 Hz, which accords with the theoretical relation of 'the larger misalignments, the smaller secondary induced currents produced'.

### 6.4.2 Efficiencies and RMS real powers

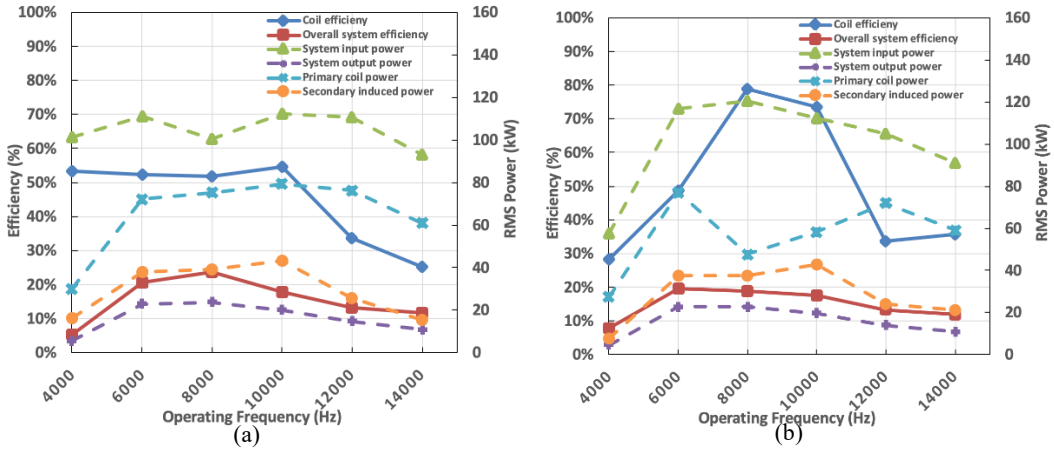

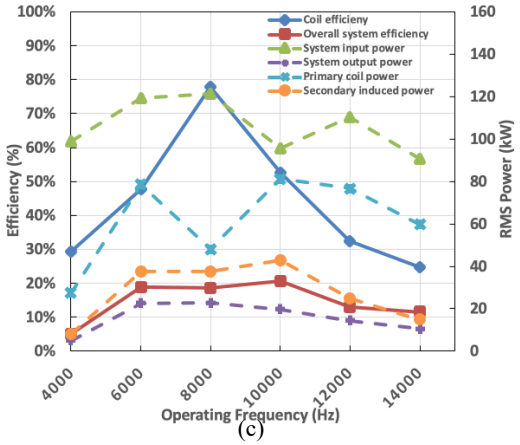


(c)

Figure 6.13: Efficiencies and RMS real powers versus operating frequencies for longitudinal misalignment tests. (a) 5 mm longitudinal misalignment. (b) 10 mm longitudinal misalignment. (c) 15 mm longitudinal misalignment.

After comparing coil efficiencies in Figure 6.13(a) to (c), it is apparent that the 5 mm longitudinal misalignment model shows a long and stable range of efficiency across 4000 Hz to 10000 Hz, which highlights a better tolerance in terms of operating frequency in longitudinal direction with an optimal value of 54.625% at 10000 Hz when compared with the 10 mm and 15 mm longitudinal displacement model tests. This finding may signify the acceptable tolerance in longitudinal direction is a maximum of 5 mm.

In terms of overall system efficiency rates, it can be found that the 5 mm test shows a peak at 8000 Hz with value of 23.572%, the 10 mm test shows a peak at 6000 Hz with value of 19.480% and the 15 mm test has a peak at 10000 Hz with value of 20.645%. The optimal operating frequency of peak of each misalignment test slightly increases in terms of the increase of longitudinal displacements from 5 mm to 15 mm.

As for RMS real powers, all the three longitudinal tests have peaks of secondary induced power at 10000 Hz with values of 43.345 kW, 42.823 kW and 42.632 kW, respectively. The trends of primary coil powers can be seen to vary especially after 6000 Hz operating frequency. Importantly, the maximums and trends of system output power of three longitudinal tests appear to be fairly similar to each other and tend to show relatively sustainable variations versus changes of operating frequency, despite significant variations of powers of other parts of the system. It can be found that the three longitudinal test models demonstrate the maximums of system output power on load at about operating frequency of 6000 Hz to 8000 Hz, with peak values of 23.679 kW, 22.732 kW and 22.645

kW, respectively. These particular trends are also similar with those in previously lateral misalignment tests, which reflects that both the lateral and longitudinal displacements when parking may lead to similar rates or extents of impacts onto the eventual RMS system output power in terms of operating frequency.

### 6.4.3 Calculated resonant frequency and calculated inductance

As introduced and discussed in previous Chapters 4 to 5 of the thesis, studying the variation trends of the calculated inductance and calculated resonant frequency can be of help in further knowing how delicately and subtly the minor changes of coupling status could impose influences on a CPT system from magnetic resonant coupling point of view.

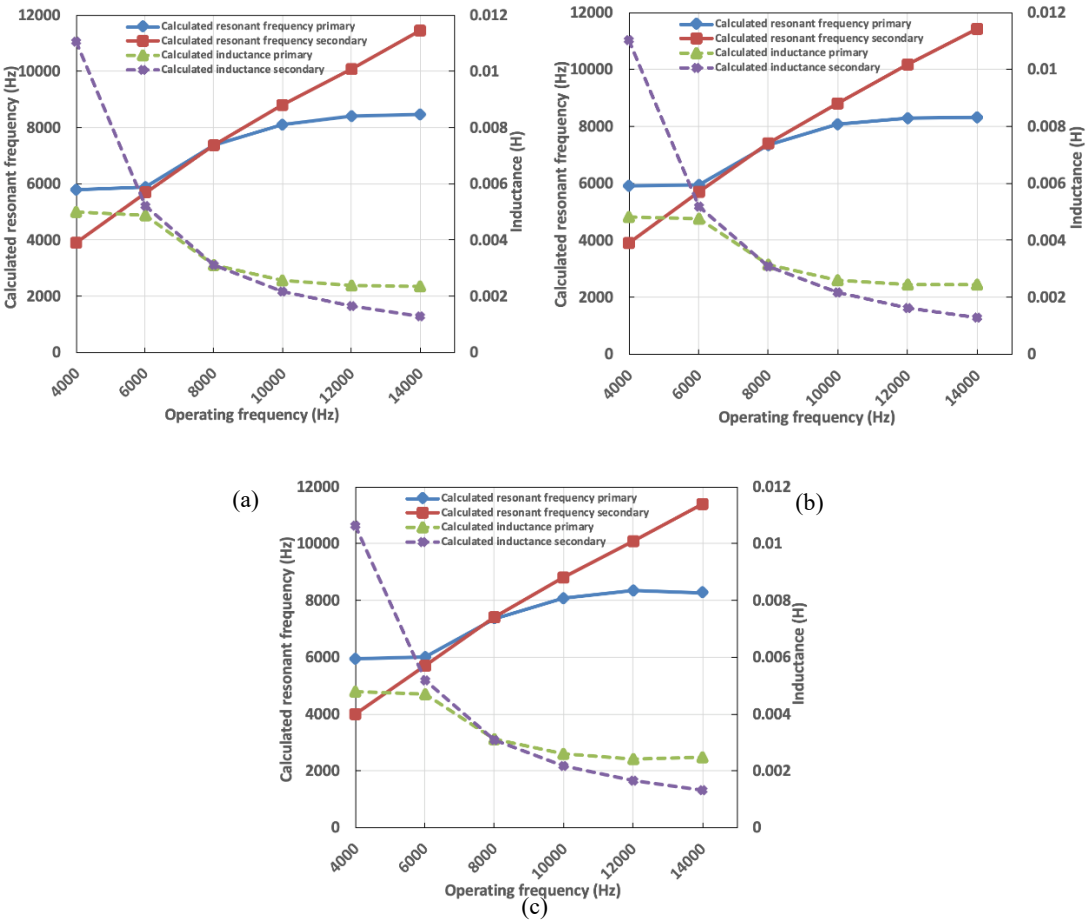


Figure 6.14: Calculated resonant frequencies, calculated inductances versus operating frequencies for longitudinal misalignment tests. (a) 5 mm longitudinal misalignment. (b) 10 mm longitudinal misalignment. (c) 15 mm longitudinal misalignment.

By tracking the calculated resonant frequency and regarding it as an optimal but changeable operation condition, the trends of actual inductance in values inductively

produced on coil windings can reflect how the misalignments impact on coupling and flux generation, which could indicate a regular pattern at some point or an approximate range of optimized resonant coupling status in terms of manoeuvring and providing the most appropriate operating frequency to make the system to resonate the most for both EMF and power electronic results.

Table 6.3: Calculated inductances and resonant frequencies versus operating frequency for longitudinal misalignments.

| Operating frequency (Hz) | ◆ *5 mm longitudinal misalignment* | | | |
|---|---|---|---|---|
| | Calculated inductance – primary (mH) | Calculated inductance – secondary (mH) | Calculated resonant freq. – primary (Hz) | Calculated resonant freq. – secondary (Hz) |
| 4000 | 5.0085 | 11.0725 | 5806.5814 | 3905.2732 |
| 6000 | 4.8836 | 5.2228 | 5880.3408 | 5686.2086 |
| 8000 | 3.1019 | 3.1109 | 7378.3361 | 7367.6768 |
| 10000 | 2.5703 | 2.1805 | 8105.5348 | 8800.2322 |
| 12000 | 2.3830 | 1.6578 | 8418.0446 | 10092.7370 |
| 14000 | 2.3455 | 1.2861 | 8485.0583 | 11458.9620 |
| | ◆ *10 mm longitudinal misalignment* | | | |
| | Calculated inductance – primary (mH) | Calculated inductance – secondary (mH) | Calculated resonant freq. – primary (Hz) | Calculated resonant freq. – secondary (Hz) |
| 4000 | 4.8120 | 11.0311 | 5923.9521 | 3912.5888 |
| 6000 | 4.7634 | 5.1963 | 5954.0980 | 5700.6809 |
| 8000 | 3.1339 | 3.0853 | 7340.6525 | 7398.1889 |
| 10000 | 2.5895 | 2.1834 | 8075.5199 | 8794.3987 |
| 12000 | 2.4550 | 1.6297 | 8293.6639 | 10179.2281 |
| 14000 | 2.4475 | 1.2908 | 8306.4624 | 11437.9621 |
| | ◆ *15 mm longitudinal misalignment* | | | |
| | Calculated inductance – primary (mH) | Calculated inductance – secondary (mH) | Calculated resonant freq. – primary (Hz) | Calculated resonant freq. – secondary (Hz) |
| 4000 | 4.7953 | 10.6387 | 5934.2781 | 3984.0944 |
| 6000 | 4.6898 | 5.1958 | 6000.6116 | 5700.9803 |
| 8000 | 3.1148 | 3.0825 | 7363.0744 | 7401.5500 |
| 10000 | 2.5892 | 2.1707 | 8075.9606 | 8820.0675 |
| 12000 | 2.4254 | 1.6607 | 8344.0888 | 10084.0055 |
| 14000 | 2.4659 | 1.3033 | 8275.2918 | 11383.0998 |

Based on both the graphic curves in Figure 6.14 and the numerical results with four digits after the decimal point in Table 6.3, there are several findings that can be noticed and stressed.

Firstly, the 5 mm longitudinal misalignment test produces relatively higher primary and secondary inductances than the 10 mm and 15 mm tests at the same operating frequency points despite the fairly similar trends of curves of inductances plotted in Figure 6.14(a) to (c). Secondly, for each test, it can be found that the primary coil inductance shows a stable trend before 6000 Hz in each graph but tends to gradually increase towards a relative stability with value at about 8000 Hz to 8500 Hz since operating frequency point of 8000 Hz. However, the secondary coil inductance continuously shows an approximately linear rise in terms of operating frequency rise, which means that the secondary side of the system may not be able to reach a stabilization of satisfactory magnetic resonance. Nonetheless, the performance of the primary coil along with power electronics outputs convincingly prove that the entire system can still achieve the optimized operation status with the primary coil side magnetically resonating at specific frequencies and coupler designs. Thirdly, comparing both the longitudinal and lateral groups of tests in Figure 6.4 and Figure 6.14 regarding calculated resonance frequency and calculated inductance, it can be found that the specific CPT system tends to reach a proximity of optimized magnetic resonance at about 8000 Hz to 8500 Hz with both the longitudinal and lateral misalignments. Misalignments of 5 mm in lateral and longitudinal directions may be the accepted limits or tolerance in terms of overall power outputs, system efficiency and EMF performance.

### 6.4.4 Analysis on EMF performance and field distribution with a close proximity to electromagnetic resonant coupling

When the CPT system tends to resonate at approximate magnetic resonant frequency, the electromagnetic field distribution parameters appear to be fairly strong, which can be observed by zooming in for analysing each parameter performance. The transient CPT coupling status at 1 ms when operating at AC stabilization with a close proximity to

electromagnetic magnetic resonance at 8 kHz has been selected for analysis and comparison over longitudinal misalignment behaviours below.

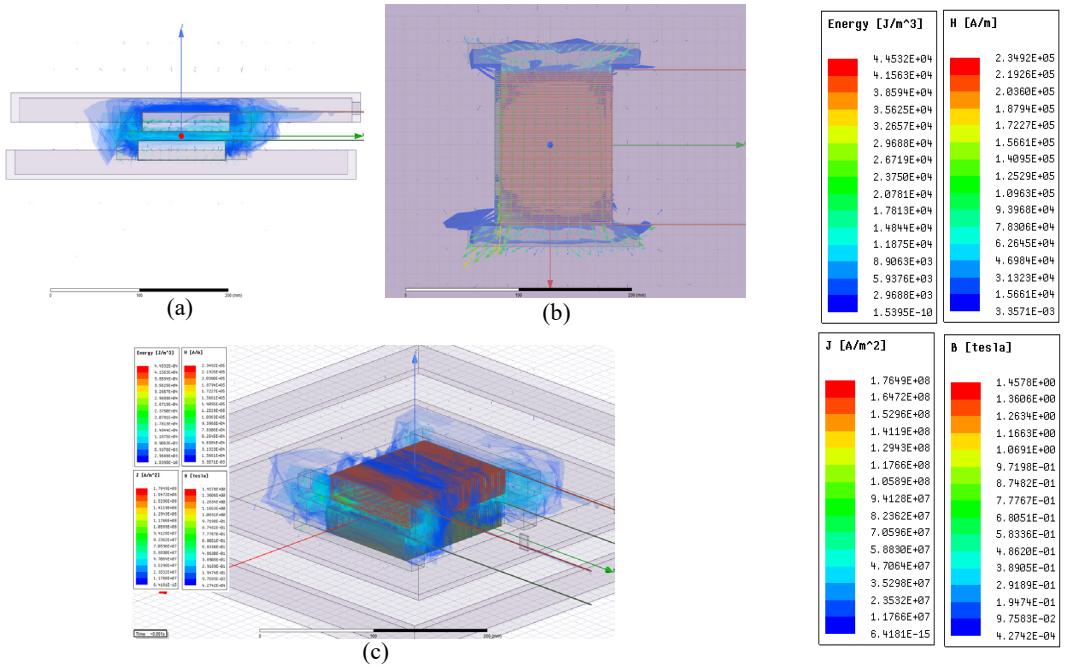


Figure 6.15: The 5 mm longitudinal misalignment test - Field distributions and illustrations of each metric of EMF performances at 8 kHz. (a) Left view. (b) Top view. (c) Dimetric view.

From Figure 6.15 of the 5 mm longitudinal misalignment EMF behaviours, it can be seen that the B field vectors especially those ‘thick and yellow’ arrows witness satisfactory and expected magnetic flux density vector paths and trajectories through the specifically designed H-shape cores, which reflects the effectiveness of the overall design of the coupler along with the scalar maximums of H field, B field and field energy shown in the figure legends.

Compared with the 5 mm longitudinal misalignment EMF behaviours in Figure 6.15, it is obvious that the B field scalar maximum drops from previous 1.4578 teslas to 1.1658 teslas of the 10 mm test in Figure 6.16, which is basically proportional to the misalignment rise and makes sense from magnetic flux density generation point of view.

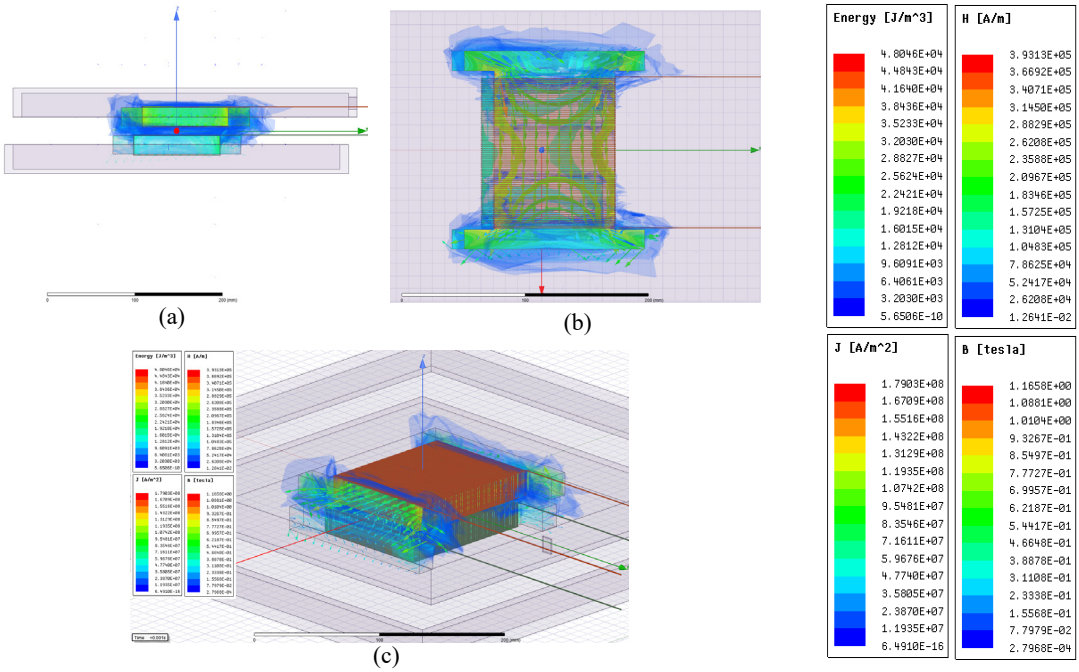


Figure 6.16: The 10 mm longitudinal misalignment test - Field distributions and illustrations of each metric of EMF performances at 8 kHz. (a) Left view. (b) Top view. (c) Dimetric view.

However, as depicted by all the views in Figure 6.16 regarding magnetic field strength H, it can be seen that the H field scalar maximum 3.93 x $10^5$ A/m of the 10 mm longitudinal test is significantly larger than that of the 5 mm one with scalar maximum 2.34 x $10^5$ A/m, which seems controversial and illogical but actually is reasonable since the vectors may not always have high scalar values at every coordinate of every trajectory and the scalar maximum may not always represent the actual effectiveness of vectors in effective directions in field, contributing to a high overall system performance by comprehensively affecting other parameters and a series of calculations when it comes to discussing active power results and reactive power results via finding out phase differences and power factor ratios.

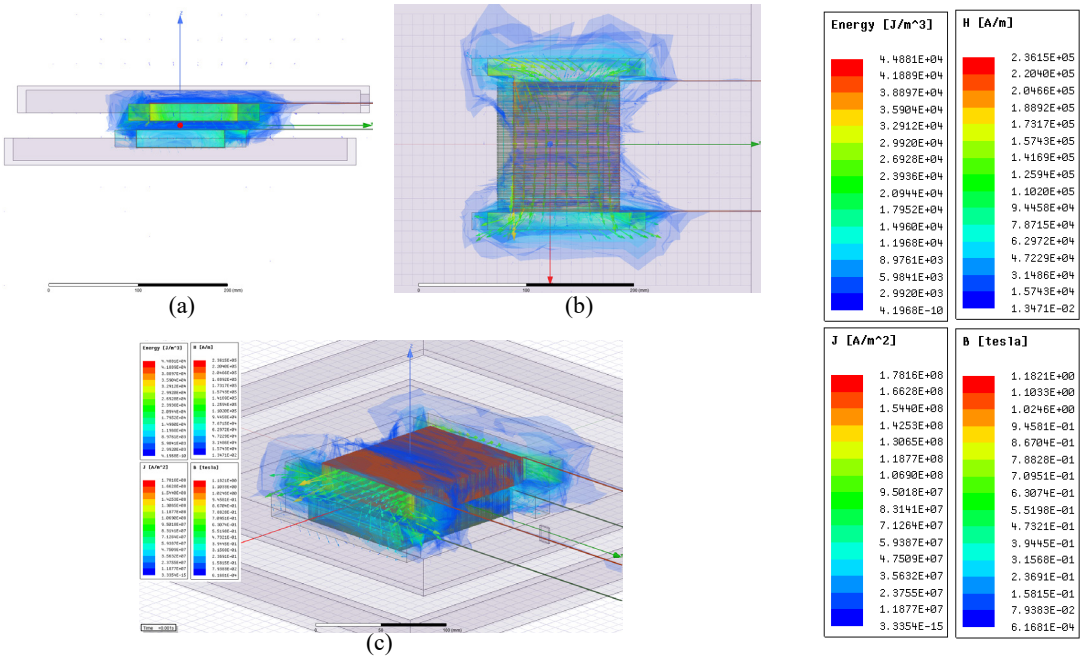


Figure 6.17: The 15 mm longitudinal misalignment test - Field distributions and illustrations of each metric of EMF performances at 8 kHz. (a) Left view. (b) Top view. (c) Dimetric view.

Based on each parameter of the electromagnetic field shown in legends of Figure 6.17 for the 15 mm longitudinal misalignment test, most of scalar maximums are similar with or slightly weaker than the 10 mm longitudinal misalignment test while the scalar layers of H field can be seen to have wider extension in space within the shielding shells than previous two test despite insignificant maximum point deviations in values.

Besides, a finding is that the upper receiving side of the coupler in Figure 6.17 and Figure 6.16 seem to have stronger B field and H field behaviours than the lower transmitting side at transient 1 ms. This phenomenon also seems more significant than the 5 mm tests in Figure 6.15. After the analysis according to graphs of powers and efficiency in Figure 6.13(b) and (c), it can be seen that the decline of primary power between about 6000 Hz to 12000 Hz is the major reason causing the coil efficiencies of the 10 mm and 15 mm tests appear to be higher than the 5 mm test, which also leads to a stronger EMF behaviour on the secondary side of the system.

Overall, from the perspective of electromagnetics, the strong EMF behaviour on the secondary receiving side may mean a high reactive power that is strongly established by inductive field energy to ensure a satisfactory magnetic-to-electric energy conversion. Therefore, at some transient time points of an alternatively stable coupling system, the

secondary side field behaviour would seem stronger than the primary side. Nonetheless, when it comes to overall power electronic outputs, the angular phase angles and active power RMS values must be taken into account so that the RMS real power in kW may be not that high and system efficiency may not be as high as the transient EMF behaviours presented to visibility and observation, which is apparently proved by numerical and graphic results in Sections 6.4. Further discussions in depth will be conducted in following Sections 6.5 and 6.6.

## 6.5 Analyses and comparisons on field performances with EMF results of lateral and longitudinal misalignment test variations

In order to study and analyse EMF results and field behaviours more comprehensively across a long range of testing frequency, the plotted numerical results of scalar maximums of both lateral and longitudinal misalignments over H field, B field, electric current density and energy of storage in field are gathered in this Section 6.5, in addition to the selected frequency and relatively optimal misalignment status for visually observable comparisons on electromagnetic field distributions in previous Sections 6.3 and 6.4.

There is unavoidably a limitation in Sections 6.3 and 6.4, which is that the figure views captured may not be able to profoundly reflect and comprehensively depict the entire field generation processes over time since only the whole 1 ms animations of each tests can indicate and stress the actual varying field characteristics with refined field vector arrows at critical positions such as some edges and corners in the geometric space. In the chapter, these transiently captured images of electromagnetic fields are mainly for basic demonstration purpose, as subsidiary presentations.

Therefore, in order for further delicate and overall investigations to be conducted, all series of RMS numerical results and power electronic outputs across all range of tested operating frequencies are plotted in this Section 6.5 for more ‘holistic’ analyses and comparisons on lateral and longitudinal misalignment behaviour variations.

### 6.5.1 Magnetic field strength - H field

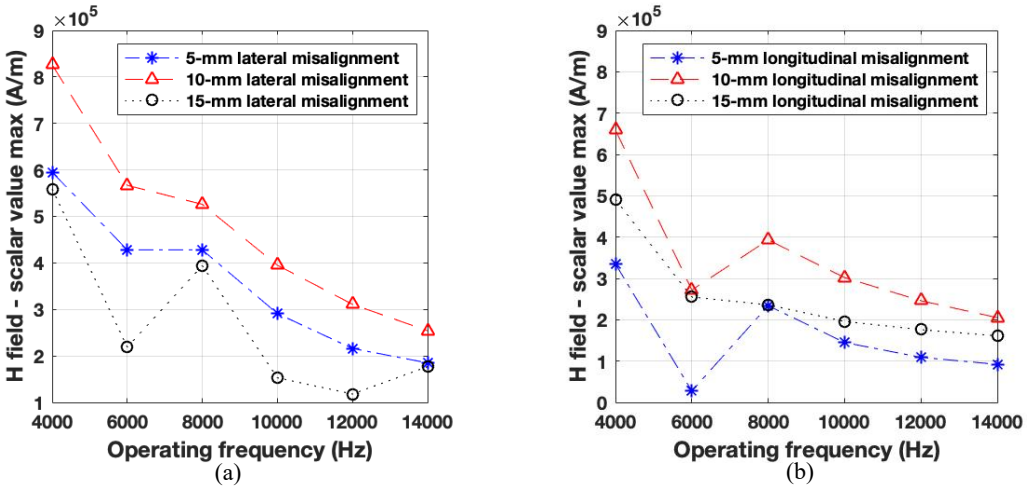


Figure 6.18: Magnetic field strength H maximum scalar values versus operating frequencies. (a) Lateral misalignment variations. (b) Longitudinal misalignment variations.

A noticeable finding is that both the 10 mm lateral and longitudinal displacements in Figure 6.18(a) and (b) tend to show interestingly better H field outcomes than the 5 mm displacements in both displacement directions, which may mirror that a more optimal magnetic field strength generation per se would be yielded with an slightly imperfect position-aligned coupling to some extent when discussing and studying the H field only, excluding considering other major determinant parameters to overall system outcomes.

Another finding based on all three misalignments of each direction is that the 10 mm misalignment distance may be the critical point of displacement tolerance for EMF behaviors on both X and Y axes, since both the 15 mm lateral and longitudinal misalignments present lower H field scalar maximums for the CPT coupling model.

Besides, by comparison on the 5 mm misalignments in Figure 6.18(a) and (b), it can be found that this designed CPT coupler may appear to have better tolerance of magnetic field strength H to lateral misalignments along X axis than longitudinal ones on Y axis when displacement is below 5 mm, since every H field scalar maximum in 5 mm lateral displacement behaviors can be seen higher than in 5 mm longitudinal displacement behaviors.

### 6.5.2 Magnetic flux density - B field

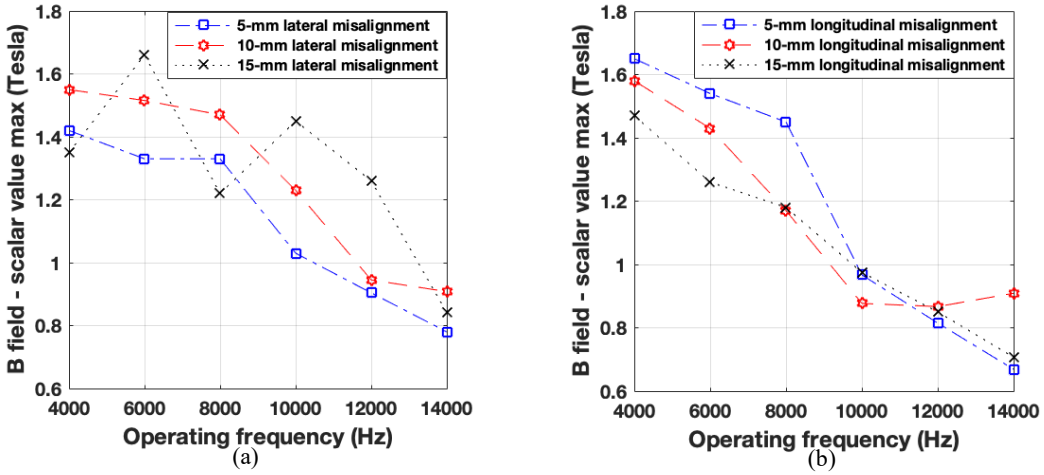


Figure 6.19: Magnetic flux density B maximum scalar values versus operating frequencies. (a) Lateral misalignment variations. (b) Longitudinal misalignment variations.

As is known, magnetic flux density B has relations with magnetic field strength H in magnetic field in saturable materials like ferromagnetic cores as described in equation (3.30d) and also in solenoid-type windings in terms of magnetic field energy storage and volume integral as described in equation (3.41) and Figure 3.14. Nevertheless, in a complicated nonlinear magnetic field system like the one designed and investigated in the thesis, the B field could show nonlinear and uncommon tendency against testing operating frequency, by which the magnetic relative permeability μ could be calculated but it is not quite necessary to discuss the nonlinearly varying μ in the thesis.

From Figure 6.19(a) and (b), it can be noticed that the B field scalar maximums of the 5 mm longitudinal misalignments show higher values than 10 mm and 15 mm ones, which seems reasonable and logical. However, the B field scalar maximums at most testing frequency present as the lowest in all the lateral misalignment tests, which means that the maximized magnetic flux density scalars may not definitely appear at every transient time intervals when the displacement on X axis is minimized and when the overall system power electronics RMS outputs are maximized. Along with the previous numerical results and studies, a finding here is that the maximum scalar of B field at some spatial coordinates may not absolutely signify the overall coupling system tends to present maximized magnetic flux density vectors and scalars at every single spatial points and edges all the times in the field including cores and air region.

### 6.5.3 Electric current density - J

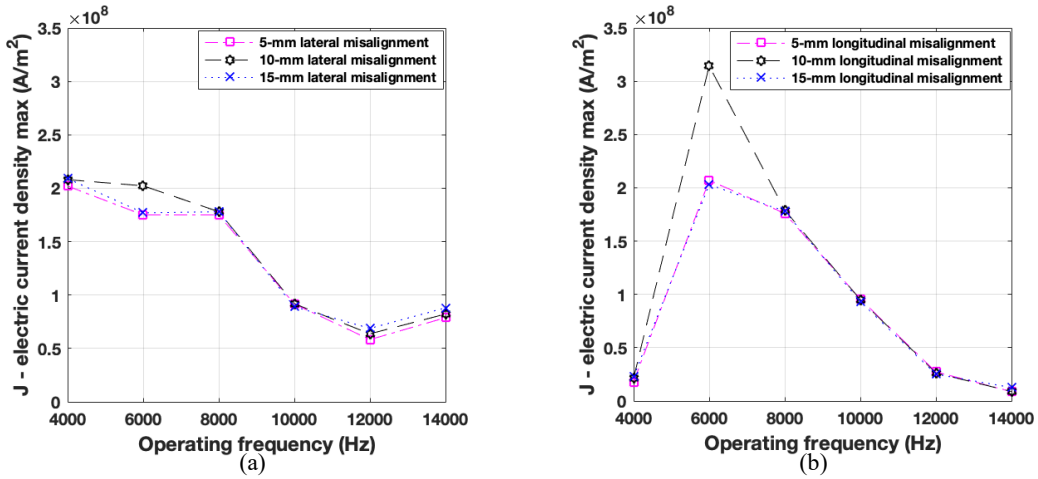


Figure 6.20: Electric current density J in field values versus operating frequencies. (a) Lateral misalignment variations. (b) Longitudinal misalignment variations.

As expressed in equations (3.30a) and (3.32), the electric current density J has relations with electric field strength E and magnetic field strength H but needs to be worked out by Maxwell equations established for the specific field. The electric current density in ANSYS Maxwell is only solved for conductive materials like the copper litz wires in the prototype of the thesis.

Since the maximum scalar or vector values cannot completely reflects the overall RMS real values of the system parameters, the electric current density maximums plotted in Figure 6.20 could not definitely witness the optimal electromagnetic resonance but could be observed to approximately estimate and compare the coupling states by induced currents per square meter.

As can be seen in Figure 6.20(b), the electric current density maximum of 10 mm longitudinal misalignment model tends to be much higher that other two test at 6000 Hz, which may mirror a strongly optimized magnetic resonant coupling status is achieved when compared with other displacements. By combined analysis with Figure 6.12(b) in Section 6.4(a), it can be noticed that the secondary induced current appears to reach a peak for the system with a 10 mm longitudinal displacement at 6000 Hz.

### 6.5.4 Energy stored in field

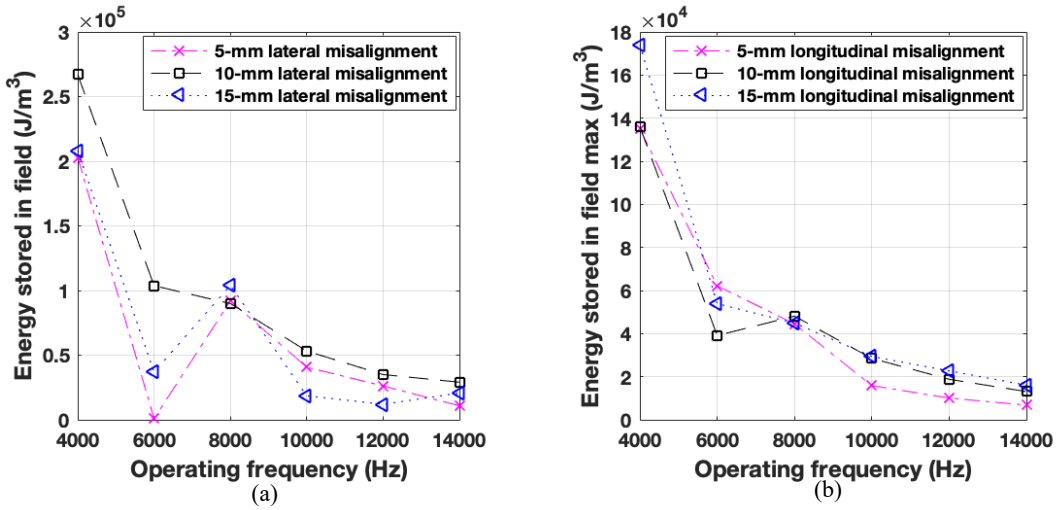


Figure 6.21: Energy versus operating frequencies. (a) Lateral misalignment variations. (b) Longitudinal misalignment variations.

Based on equation (3.41) regarding magnetic field energy storage, the transient nonlinear material-based energy stored in field can be computed by finite-element methods in ANSYS Maxwell and the accumulated total field energy storage when a coupling system stabilizes can also be calculated. Figure 6.21(a) and (b) depict the RMS total energy stored in field for variations of misalignments versus different testing operating frequency.

As can be seen from Figure 6.21(a) and (b), both the lateral and longitudinal misalignment behaviours appear to show upward maximum values at 8000 Hz, which corresponds to the closest states of coupling to the optimal magnetic resonance according to previous studies. After the 8000 Hz point, the curves of energy stored in field turn to drop, which accords with the RMS power outputs, induced currents and EMF parameter performances reasonably.

The upward peaks at the calculated resonant frequency point of 8000 Hz for this CPT model with nearly all the tested types of misalignment may also reflect the electric-magnetic energy conversion optimum states and the optimal electromagnetic resonant coupling conditions. According to theories of field establishment, reactive power and active power, the magnetic field behaviours could reach the relatively optimized resonant stabilization at 8000 Hz despite bearable misalignments and the CPT system efficiency could be determined more by higher satisfactory PF which facilitates the active power

from the primary side to be transferred to the load side with more satisfactory induced RMS real power.

In conclusion, therefore, a finding can be that the energy stored in field may be a relatively straightforward observable for rough analyses and tests on how and what an operating frequency could drive the CPT coupling system to a most approximate optimization of electromagnetic resonant coupling and to a most satisfactory power electronics outcomes, in spite of slight misalignments.

## 6.6 Discussions from waveform characteristics point of view

### 6.6.1 Sinusoidal flux linkage waveforms - Selected 8 kHz misalignments

For analysis and comparison on magnitudes and angular phase behaviours, the raw sinusoidal flux linkage waves of both lateral and longitudinal misalignments for coupler coils at 8 kHz as an optimal operating frequency condition have been acquired and shown in Figure 6.14 to Figure 6.16.

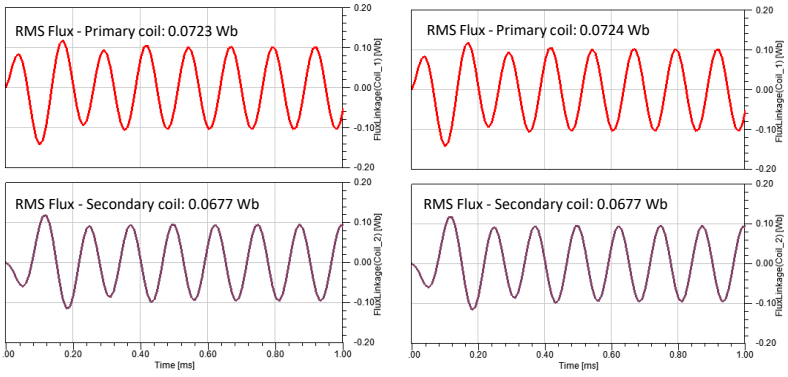


(a) (b)

Figure 6.22: 5 mm misalignment flux linkage waves at 8 kHz. (a) Lateral. (b) Longitudinal.

From Figure 6.22, the raw signal waves of flux linkages can witness very few differences between the 5 mm lateral and 5 mm longitudinal displacements from waveform characteristics point of view, which could mean that fairly slight misalignment below 5 mm on X and Y axes may not be a huge determinant to differences of flux linkage generations for a CPT coupling operation. Besides, the angular phases between the lateral and longitudinal tests here seem fairly similar.

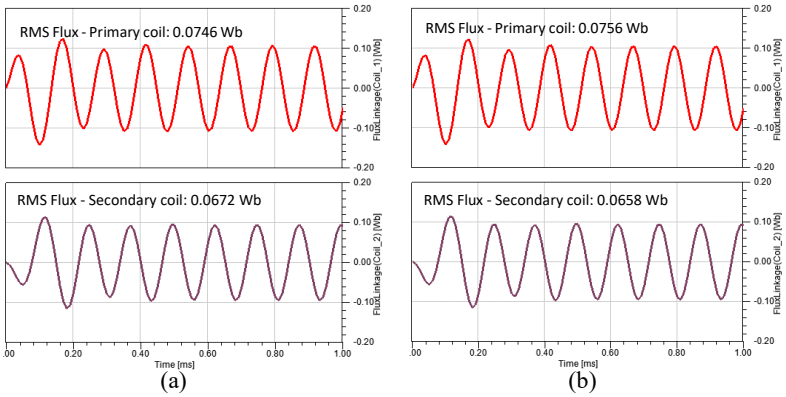


Figure 6.23: 10 mm misalignment flux linkage waves at 8 kHz. (a) Lateral. (b) Longitudinal.

Some visible and comparable differences can be seen in Figure 6.23, which is about the RMS flux linkage magnitudes between the lateral and longitudinal misalignment flux behaviours. The primary RMS flux linkage in the lateral misalignment model is 0.001 Wb smaller than that in the longitudinal one while the secondary RMS flux linkage of the lateral misalignment model is 0.0014 Wb higher than that in the longitudinal one. Difference about phases can be seen negligible between the lateral and longitudinal misalignment flux linkage signal behaviours.

A finding is that the secondary flux linkage performance can directly indicate the system power electronics outputs and overall efficiency, based on the relations in Figure 6.23 and results in Figure 6.3(b) and Figure 6.13(b) at 8000 Hz point. The secondary flux linkage of the 10 mm lateral misalignment test is relatively stronger than the longitudinal one, and the RMS system output power of the 10 mm lateral misalignment test is 23.287 kW while the 10 mm longitudinal model has 22.732 kW RMS output power. The system efficiencies are 22.453% and 19.480%, respectively, for this pair of comparison.

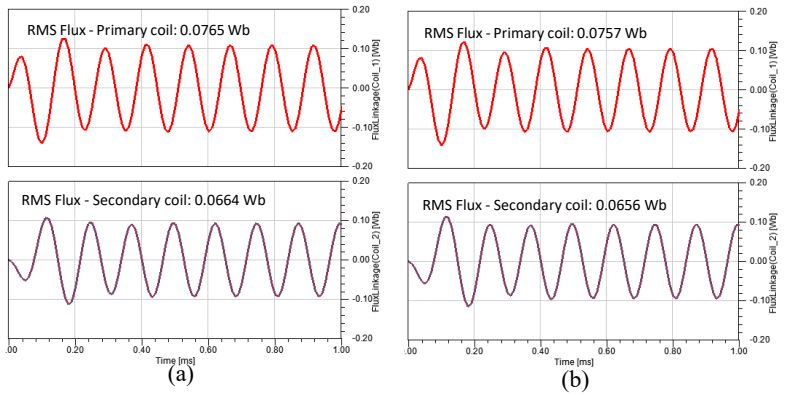


Figure 6.24: 15 mm misalignment flux linkage waves at 8 kHz. (a) Lateral. (b) Longitudinal.

Compared with the previous two groups of tests, both the 15 mm lateral and longitudinal misalignments show weaker RMS flux linkages on the secondary coil with 0.0664 Wb and 0.0656 Wb, respectively. However, the primary coil flux linkage presents the strongest magnitude with 0.0765 in all the three groups of tests, but this seems not to lead to higher satisfactory RMS power output and system efficiency rate according to previous analysis in Figure 6.3(c). On the other side, the secondary coil flux linkage of the 15 mm longitudinal misalignment model is expectedly the weakest within the 5 mm, 10 mm and 15 mm tests, which 'logically' corresponds to the least satisfactory power and efficiency performance of this model test based on results in Figure 6.13(c).

To summarize, a finding is that the misalignments in both X and Y axes would not have fundamental impacts on the angular phase performance of flux linkages, according to all the waveforms and phase characteristics in this section.

Another finding, comprehensively based on all the three pairs of tests and waves from Figure 6.22 to Figure 6.24, is that the secondary coil flux linkage performance could be more able to directly determine the overall effectiveness of the CPT system performance while the primary coil flux linkage waveform magnitude may not be able to reflect the actual coupling status and the eventually overall system outputs especially in imperfect-alignment scenarios like the studies in this Section 6.6.1.

### 6.6.2 Sinusoidal quantities of the circuit system outputs, angular phase differences and power factors

Major sinusoidal quantities such as currents and voltages fundamentally determine how the electrical power outputs of a circuit system would be produced. For the CPT systems, the calculations of RMS powers and system efficiency are essential for overall system performance evaluations and enhancement modifications. Thus, the actual behaviours of angular phases and power factors need to be accurately observed and computed for analysis and comparison on variations of systems in terms of variables such as misalignments in Chapter 6.

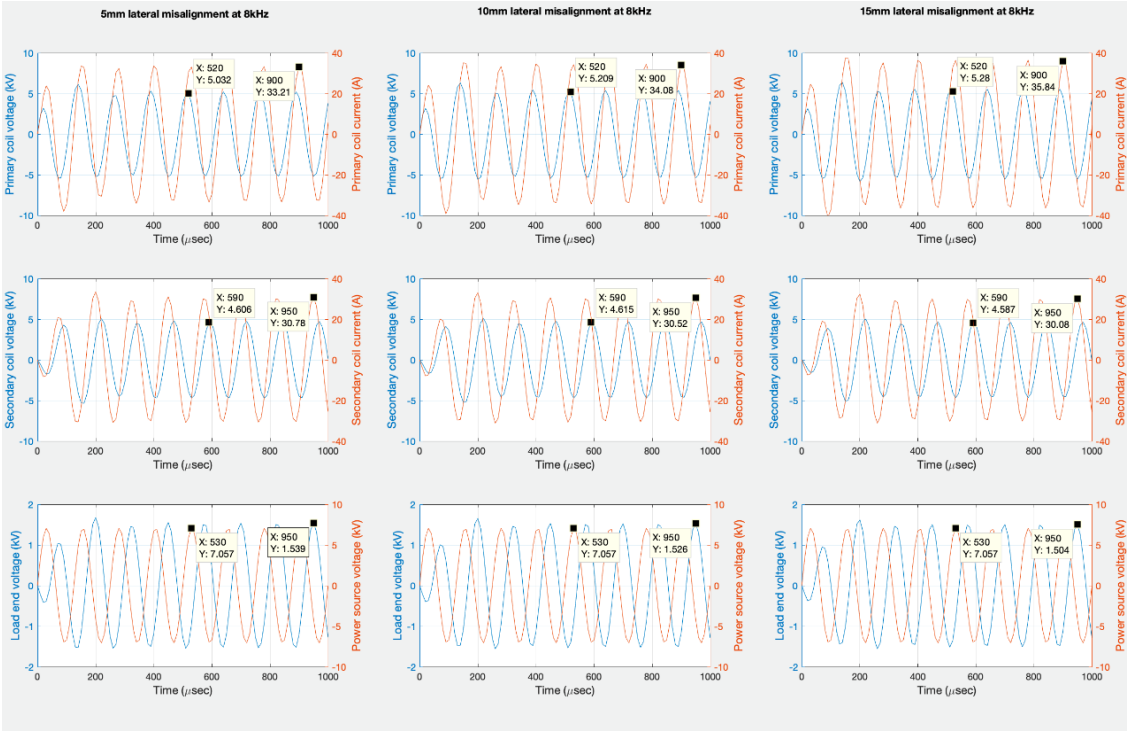


Figure 6.25: Waveforms of lateral misalignment tests at selectively 8 kHz with a close proximity to electromagnetic resonant coupling.

From Figure 6.25, it can be found, by selectively analysing the raw waveforms of voltages and currents of the CPT system at about magnetic resonant coupling condition of 8000 Hz, that the three lateral misalignment tests present exactly the same angular phases at 8000 Hz operating frequency, which correspond to a 28.8˚ phase angle difference on primary coil, a 57.6˚ phase angle difference on secondary coil and a 28.8˚ phase angle difference on the input power source.

In the result comparison of lateral misalignments, it can be noticed that the calculated primary coil RMS real power is proportional to the increase of lateral misalignment distance while the secondary coil RMS real power shows a reverse relation with the increase of X-axis displacement, which leads to a reverse proportion relation between coil efficiency and X-axis displacement for the CPT coupler. Besides, it can be seen that the system input RMS power slightly varies in terms of X-axis displacement in Figure 6.25, which does not affect and change the reverse relation between overall system efficiency and lateral misalignment according to previous Figure 6.3.

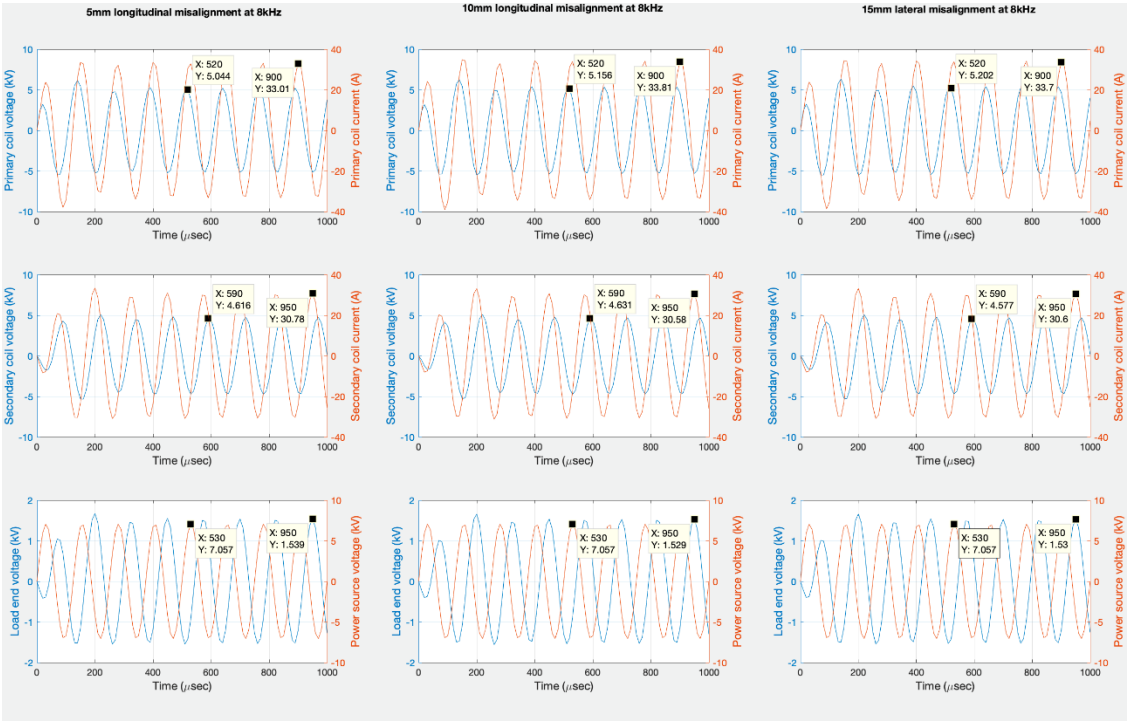


Figure 6.26: Waveforms of longitudinal misalignment tests at selectively 8 kHz with a close proximity to electromagnetic resonant coupling.

Regarding the longitudinal misalignment raw waveforms of main sinusoidal quantities depicted in Figure 6.26, the angular phase behaviours can be seen slightly impacted by Y-axis displacement variations.

The magnitudes of primary coil voltages and currents can be seen increased in terms of increase of Y-axis displacement, however, the RMS real power of primary coil tends to decrease due to slightly descending power factor caused by rise of phase difference on the primary side. For the secondary coil side, the current magnitude is seen decreases from 30.78 A to 30.60 A against increasing longitudinal misalignment from 5 mm to 15 mm according to Figure 6.26. Along with analysis on Figure 6.13 before, it can be found the coil efficiency per se for CPT systems with longitudinal misalignments is in proportion with Y-axis displacement, however, the overall system efficiency does not show the same relation and trend due to more imperfect coupling states and higher ohmic losses throughout the both sides of the CPT system.

Table 6.4 and Table 6.5 are built for investigating the relations between angular phase differences and operating frequencies for both lateral and longitudinal misalignment system behaviours.

Table 6.4: Angular phases and differences for lateral misalignment tests.

| Operating frequency | ◆ *5 mm lateral misalignment* | | | | | |
|---|---|---|---|---|---|---|
| | Primary coil phase angle difference | PF | Secondary coil phase angle difference | PF | Input system phase angle difference | PF |
| 4000 | 72 ˚ | 0.3090 | 86.4 ˚ | 0.0628 | 43.2 ˚ | 0.7289 |
| 6000 | 43.2 ˚ | 0.7289 | 43.2 ˚ | 0.7289 | 0 ˚ | 1 |
| 8000 | 28.8 ˚ | 0.8763 | 57.6 ˚ | 0.5358 | 28.8 ˚ | 0.8763 |
| 10000 | 36 ˚ | 0.8090 | 36 ˚ | 0.8090 | 0 ˚ | 1 |
| 12000 | 43.2 ˚ | 0.7289 | 43.2 ˚ | 0.7289 | 0 ˚ | 1 |
| 14000 | 50.4 ˚ | 0.6374 | 20.4 ˚ | 0.9373 | 0 ˚ | 1 |
| | ◆ *10 mm lateral misalignment* | | | | | |
| | Primary coil phase angle difference | PF | Secondary coil phase angle difference | PF | Input system phase angle difference | PF |
| 4000 | 72 ˚ | 0.3090 | 72 ˚ | 0.3090 | 43.2 ˚ | 0.7289 |
| 6000 | 43.2 ˚ | 0.7289 | 64.8 ˚ | 0.4258 | 21.6 ˚ | 0.9298 |
| 8000 | 28.8 ˚ | 0.8763 | 57.6 ˚ | 0.5358 | 28.8 ˚ | 0.8763 |
| 10000 | 36 ˚ | 0.8090 | 36 ˚ | 0.8090 | 0 ˚ | 1 |
| 12000 | 43.2 ˚ | 0.7289 | 43.2 ˚ | 0.7289 | 21.6 ˚ | 0.9298 |
| 14000 | 50.4 ˚ | 0.63742 | 50.4 ˚ | 0.63742 | 30.6 ˚ | 0.8607 |
| | ◆ *15 mm lateral misalignment* | | | | | |
| | Primary coil phase angle difference | PF | Secondary coil phase angle difference | PF | Input system phase angle difference | PF |
| 4000 | 72 ˚ | 0.3090 | 72 ˚ | 0.3090 | 57.6 ˚ | 0.5358 |
| 6000 | 43.2 ˚ | 0.7289 | 43.2 ˚ | 0.7289 | 0 ˚ | 1 |
| 8000 | 28.8 ˚ | 0.8763 | 57.6 ˚ | 0.5358 | 28.8 ˚ | 0.8763 |
| 10000 | 18 ˚ | 0.9511 | 36 ˚ | 0.8090 | 36 ˚ | 0.8090 |
| 12000 | 43.2 ˚ | 0.7289 | 43.2 ˚ | 0.7289 | 21.6 ˚ | 0.9298 |
| 14000 | 50.4 ˚ | 0.6374 | 50.4 ˚ | 0.6374 | 25.2 ˚ | 0.9048 |

With detailed and precise calculated results of phase angle performances in Table 6.4 for lateral misalignment tests, it can be found that the operating frequencies around 8000 Hz are relatively sensitive for the primary coil power factor (PF) performance and tolerant to slight misalignments such as 5 mm and 10 mm lateral displacements. However, the

secondary power factors appear to be fluctuating against testing operating frequency and variations of displacement.

There are a couple of findings from the lateral misalignment tests. The calculated natural resonant frequency of 8000 Hz seems applicable and effective for the primary side of 5 mm and 10 mm lateral misalignment systems as the both power factors tend to reach maximums of 0.8763. However, the 15 mm lateral misalignment system shows a maximum PF of 0.9511 at 10000 Hz instead of 8000 Hz anymore, which may prove that larger lateral misalignments would determine higher resonant frequency of primary side and mean that the CPT system would need to be adjusted and tuned up the operating frequency from the voltage power supply in order to fit a new real-time natural resonant frequency for a newly imperfect alignment after EV parking maneuverer. This viewpoint and discussion have been proposed once with insufficiently quantitative results in the limitation part, namely Section 4.25 before in the thesis. Another finding regarding the lateral misalignment tests is that the PF of input AC power supply tends to deviate from its optimal maximum of 1 when the misalignment is getting larger and when the coupling system tends to deviate from optimal magnetic resonance such as the numerical comparisons in Table 6.4.

Table 6.5: Angular phases and differences for longitudinal misalignment tests.

| Operating frequency | ◆ *5 mm longitudinal misalignment* | | | | | |
|---|---|---|---|---|---|---|
| | Primary coil phase angle difference | PF | Secondary coil phase angle difference | PF | Input system phase angle difference | PF |
| 4000 | 72 ˚ | 0.3090 | 57.6 ˚ | 0.5358 | 43.2 ˚ | 0.7289 |
| 6000 | 43.2 ˚ | 0.7289 | 64.8 ˚ | 0.4257 | 10.8 ˚ | 0.9822 |
| 8000 | 28.8 ˚ | 0.8763 | 57.6 ˚ | 0.5358 | 28.8 ˚ | 0.8763 |
| 10000 | 36 ˚ | 0.8090 | 36 ˚ | 0.8090 | 18 ˚ | 0.9510 |
| 12000 | 43.2 ˚ | 0.7289 | 43.2 ˚ | 0.7289 | 21.6 ˚ | 0.9297 |
| 14000 | 50.4 ˚ | 0.6374 | 50.4 ˚ | 0.6374 | 25.2 ˚ | 0.9048 |
| | ◆ *10 mm longitudinal misalignment* | | | | | |
| | Primary coil phase angle difference | PF | Secondary coil phase angle difference | PF | Input system phase angle difference | PF |
| 4000 | 72 ˚ | 0.3090 | 72 ˚ | 0.3090 | 64.8 ˚ | 0.4257 |
| 6000 | 43.2 ˚ | 0.7289 | 64.8 ˚ | 0.4257 | 11.0 ˚ | 0.9815 |

| | | | | | | |
|---|---|---|---|---|---|---|
| 8000 | 57.6 ˚ | 0.5358 | 57.6 ˚ | 0.5358 | 0 ˚ | 1 |
| 10000 | 54 ˚ | 0.5877 | 36 ˚ | 0.8090 | 18 ˚ | 0.9510 |
| 12000 | 43.2 ˚ | 0.7289 | 43.2 ˚ | 0.7289 | 21.6 ˚ | 0.9297 |
| 14000 | 50.4 ˚ | 0.6374 | 25.2 ˚ | 0.9048 | 25.2 ˚ | 0.9048 |
| | ◆ *15 mm longitudinal misalignment* | | | | | |
| | Primary coil phase angle difference | PF | Secondary coil phase angle difference | PF | Input system phase angle difference | PF |
| 4000 | 72 ˚ | 0.3090 | 72 ˚ | 0.3090 | 43.2 ˚ | 0.7289 |
| 6000 | 43.2 ˚ | 0.7289 | 64.8 ˚ | 0.4257 | 10.8 ˚ | 0.9822 |
| 8000 | 57.6 ˚ | 0.5358 | 57.6 ˚ | 0.5358 | 0 ˚ | 1 |
| 10000 | 36 ˚ | 0.8090 | 36 ˚ | 0.8090 | 36 ˚ | 0.8090 |
| 12000 | 43.2 ˚ | 0.7289 | 43.2 ˚ | 0.7289 | 21.6 ˚ | 0.9297 |
| 14000 | 50.4 ˚ | 0.6374 | 50.4 ˚ | 0.6374 | 25.2 ˚ | 0.9048 |

Some findings in terms of longitudinal misalignments can be extracted and understood based on PF results in Table 6.5. First, the peak PF of secondary side corresponds to the maximum of system efficiency and maximum of power transferred to load for all the longitudinal misalignment tests according to Figure 6.13 and Table 6.5. Second, it can be found that the longitudinal misalignment PF behaviour would be the same as the lateral misalignment when the displacements on both X and Y axes are the same, for instance, the PF results of the 5 mm longitudinal misalignment perform exactly the same as those of the 5 mm lateral misalignment tests versus operating frequency while the PF of larger longitudinal misalignments appear to differ from the 5 mm one further and further.

Overall, the primary side PF performance of both lateral and longitudinal misaligned CPT system plays a determinant role in the overall system behaviour. Mostly when the primary coil reaches its optimum of resonant coupling via a maximized PF at corresponding natural resonant frequency, the entire system will yield the most satisfactory power electronics outputs and produce the most optimistic electromagnetic field distributions with well-performed field parameters. The findings and viewpoints from analysis of angular phases and PF are mathematically anticipated and electromagnetically reasonable based on EMF energy transmission theories and efficiency equations in Chapter 3.

## 6.7 Chapter conclusions

Any degree or amount of misalignments in lateral and longitudinal directions will unavoidably determine a degraded electromagnetic induction and resonant coupling, which is one of the most challenging obstacles to reaching an optimal operation state of CPT coupling. Therefore, Chapter 6 accentuates the impacts from EV parking displacements in X and Y axes and emphasizes the CPT system misalignment behaviours based on results and analyses of groups of lateral and longitudinal misalignment tests using a previously prototyped CPT system with a 15 mm inner shielding shell-to-coil distance.

Optimizing the imperfectly aligned CPT system with proactively optimal frequency tracking method, along with the variations of misalignment towards proximities of resonant coupling optimum, has been adopted to investigate the system misalignment behaviours and the relative tolerances to directional displacements. By simulating models, raw data processing and analysing the results from perspectives of electromagnetics and power electronics, the groups of system performances have been quantitatively studied and a range of findings have been concluded in each section.

In addition to major system performance metrics such as RMS flux linkages, RMS currents, calculated resonant frequencies, calculated inductances, efficiencies and RMS powers against testing operating frequency and misalignment variations, this article also focuses on EMF result analyses such as H field scalar results, B field scalar results, electric current density results and field energy storage results, as well as on comparisons for the actual magnetic fields of the optimized CPT systems for EVs.

Moreover, a series of newly-concerned emphases on studying raw waveform characteristics of the flux linkage, the electric circuit outputs and the power factors with angular phases of main quantities have been implemented in Chapter 6 in order for the lateral and longitudinal misalignment system behaviours to be sophisticatedly investigated, in consideration of the lack of actual research focus in depth in the previous sections of the thesis over misalignment issues, and also in consideration of the obvious gaps between misalignment-related studies so far in the literature and contemporary industrialized small-sized wireless energy transmission applications.

# Chapter 7 Laboratory prototypes, experiments and model validations

Chapter 7 reports the characteristics and performances of a various CPT designs, which are axis-parallel coil coupler CPT with ferrite cores, planar circular coil based CPT coupler and H-shaped core CPT coupler. Data acquisition (DAQ) with Measurement Computing USB-1208-HS-2AO DAQ board, digital signal processing using FFT spectrum analysis with MATLAB are mainly used to analyse the root mean square results and overall system performance of each CPT model in the laboratory experiments of this chapter.

## 7.1 The context of this chapter

In practical EV charging apparatus, the conventional plug-in charging method could accidentally generate sparks causing electric shock and poor contact over time due to exposed plug-type conductors, which unavoidably and potentially produce safety hazard to EV users especially when it comes to relatively extreme weather conditions. Also, the current wire-contact charging approaches may not be sufficiently suitable for all EV charging circumstances such as outdoor airport shuttle vehicles and even further pursuit of dynamic EV charging. Therefore, contactless power transfer (CPT) charging is supposed to tackle the inherited drawbacks of plug-in charging and will broaden the prospects of wireless energy transmission applications.

Compared with currently popular wireless energy transfer modular design and output performance particularly in low-powered small device charging applications, a CPT system for EVs is much more high-power required and complex from either system performance or equipment installation point of view. Based on the previous system prototype design and simulation experiments and the same methodology proposed in Section 3.2, this chapter is to practically implement a couple of lab prototypes for analysis and comparison over the actual performance metrics and also for model validations corresponding to the similarly designed simulation models with Infolytica MagNet and ANSYS Maxwell throughout Chapters 4 to 6. All practical prototypes in the thesis are

small-sized lab-level versions and are proportionally scaled down for considerations on limitations of materials usage, feasible sine voltage supply, instrument budgets, etc.

## 7.2 Axis-parallel coil coupler with ferrite cores

### 7.2.1 Laboratory setup and prototype design

Considering the chassis layout and space of real-world EVs and the significance of geometric design of charging coils as accentuated throughout the thesis, a handcrafted small-sized axis-parallel coil coupler with rectangular ferrite cores is set up and utilized for the CPT experiments as shown in Figure 7.1.

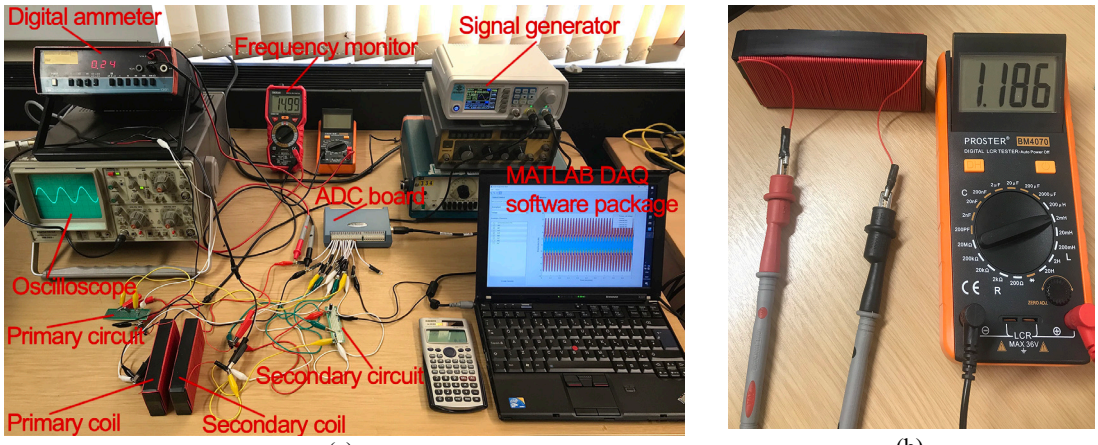


(a) (b)

Figure 7.1: A 15 mm air gap axis-parallel coil CPT prototype with rectangular ferrite cores. (a) A lab setup and signal outputs at 15 kHz. (b) The axis-parallel core with litz-wire winding measured with inductance of 1.186 mH.

The small-scaled axis-parallel CPT system has been built based on the performance and limitations of the DAQ board sampling rates, signal generator frequency limit and other measurement instruments. Details of the system is indicated in Table 7.1. According to the methodology in Section 3.2 and principle of resonant coupling, it is preliminary to calculate the anticipated approximate range of natural resonant frequency of the handcrafted coils by using a digital LCR tester first. Then tuning and approximating the operating frequency of the voltage power supply to approach the maximum currents of the two sides or one of the two sides can be implemented to narrow the targeted frequency range. In order to achieve the maximum of the entire system resonance or one side resonance, the inductance of the windings are tested as shown in Figure 7.1(b) and Table

7.1, which lead to two calculated theoretical natural resonant frequencies of this specific system with values of 20.668 kHz for closed-circuit status and 14.614 kHz for open-circuit status. This theoretically means that the electromagnetic resonant coupling may most likely occur during about 14 kHz to 21 kHz. Therefore, the experiments and results can be implemented and generated effectively for analysis and comparison in terms of optimal operating frequency and major performance metrics in the following subsection.

Table 7.1: Specifications of the axis-parallel rectangular core CPT lab prototype.

| Parameters | Values |
|---|---|
| Winding size | 120 mm x 58 mm x 23 mm |
| Core size | 125 mm x 55 mm x 20 mm |
| Primary winding number of turns | 93 turns |
| Secondary winding number of turns | 93 turns |
| Air gaps of the CPT charging system | 15 mm |
| Winding material | Litz wire |
| Relative permeability μ of core material | 1000 |
| Compensation topology adopted | Primary-Series to Secondary-Series (SS) |
| Compensation capacitors | 0.1 uF |
| Load resistance | 470 ohm resistor |
| Impedance matching resistors | 100 ohm |
| Voltage power supply | 11 V magnitude sine wave |
| Measured inductance of each winding (Open-circuit) | Around 1.186 mH |
| Range of operating frequency | 10 kHz to 45 kHz |
| Shielding | No shielding applied |
| Lateral misalignment | 0 mm |
| Longitudinal misalignment | 0 mm |

### 7.2.2 Results, analysis and frequency spectra of waveforms at optimal resonant coupling condition

According to natural resonant frequency equation and the actual inductance value measured by LCR tester in Figure 7.1(b) when open-circuited, the theoretical resonance condition of a single coil side can be found at about 14.614 kHz. Based on the methodology proposed in the thesis, proper observations on resonant currents and

voltages of the system in practical applications need to be implemented as an initial and preliminary step to approach the optimally anticipated operation status of the CPT system.

Therefore, by tuning, adjusting the operating frequency from about 10 kHz and by observing the real-time waveform and magnitudes of induced voltages and currents varying on oscilloscope display and multimeter illustrated in Figure 7.1(a) across a long range of operating frequency, the relative maximums of waveform magnitudes can be found and measured when the entire system or half side of the inductive coupling system is approximated to operate at around magnetic resonant coupling states, which can be called a tuning and tracking method as already proposed and deployed in previous chapters for investigating a specifically prototyped CPT system with performance optimization using electromagnetic resonant coupling phenomenon.

Accordingly, the main outputs and results of the system as performance assessment metrics are to be illustrated and analyzed in the following subsections. Besides, the waveform information of both sides of the system are obtained and the corresponding spectra are presented by data acquisition implementations and digital signal processing coded in MATLAB.

***(a) Main system outputs and performance results***

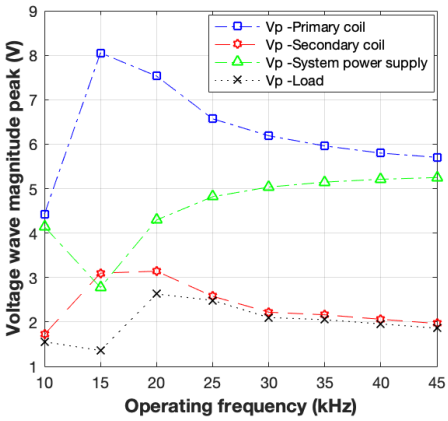


Figure 7.2: Voltages of the axis-parallel coil CPT system vs operating frequency.

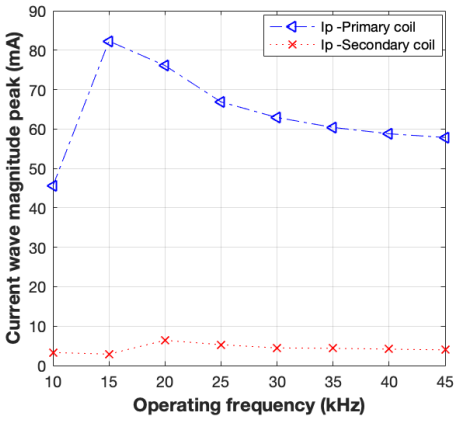


Figure 7.3: Currents of the axis-parallel coil CPT system vs operating frequency.

From Figure 7.2, it can be seen that the calculated resonant frequency of about 15 kHz literally determines the highest voltage on the primary coil with 8.054 V and the second highest for the secondary coil with 2.776 V, which both directly reflect the effects of

approximating an electromagnetic resonant coupling for a CPT system by operating at about calculated natural resonant frequency. Nevertheless, it is noticeable that the load voltage reaches its peak value of 2.629 V in an operating system at 20 kHz which is about 4.4 kHz higher than the 14.6 kHz resonant frequency calculated based on the LCR tester measured inductance value when open-circuited. This phenomenon accords with the finding and conclusion in Section 4.1 to Section 5.2 regarding coil resonance leading to maximum values for primary coil but not always for secondary coil side performance.

It can be found factual in Figure 7.3 that the maximum current on the secondary coil side occurs at 20 kHz corresponding to the maximum voltages of the secondary coil and of the load end whilst the primary current is as well highly satisfactory at 20 kHz with value of 76.1 mA in spite of the 82.3 mA peak value of the primary coil current occurring at 15 kHz which is rounded up from the previously calculated coil natural resonance frequency 14.614 kHz.

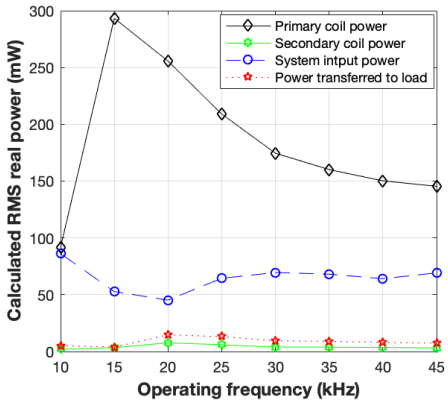


Figure 7.4: RMS powers of the axis-parallel coil CPT system vs operating frequency.

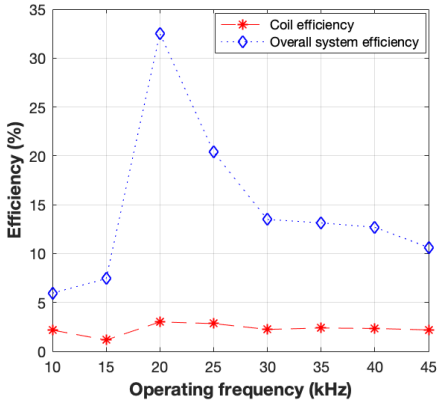


Figure 7.5: Efficiencies of the axis-parallel coil CPT system vs operating frequency.

Regarding the RMS real powers of the entire system, it can be known that the primary coil expectedly approaches the maximum power of 293.32 mW, after which the RMS value presents a downward trend until 45 kHz in Figure 7.4. The RMS power on the power supply input front end shows a lowest point at 20 kHz with 45.23 mW and tends slightly upward to be stable between 30 kHz to 45 kHz, which may indicate a potentially high energy transmission rate and an overall system efficiency to be determined. Importantly, both the load and secondary coil reach their maximums at 20 kHz with values of 7.69 mW and 14.71 mW, respectively.

This phenomenon over RMS powers indicates again that the calculated natural resonance frequency derived from individually tested inductance of coils may not lead to the optimal RMS power values on the load end and the secondary coil for specific CPT prototypes, which also suggests that the preliminary system characteristic tests are significantly necessary for CPT prototypes before applying to practical scenarios.

In terms of results of efficiency shown in Figure 7.5, it is apparent that both the system efficiency to load and coil energy transmission efficiency can reach maximums at 20 kHz with values of 32.523% and 3.006%, respectively. However, the coil efficiency decreases rapidly after 20 kHz to tend to stabilize after 30 kHz. In the meantime, the overall system efficiency seems relatively stable across almost entire range of operating frequency with values around 2%. These percentage results for the system may not be a significant advantage without a reference system in real-world applications and, for comparisons, a lab-level circular coil prototype system and an H-shaped coupler prototype system will be introduced and analysed in Section 7.3 and Section 7.4 for more comprehensive investigations over system performance in terms of different coupling modular designs.

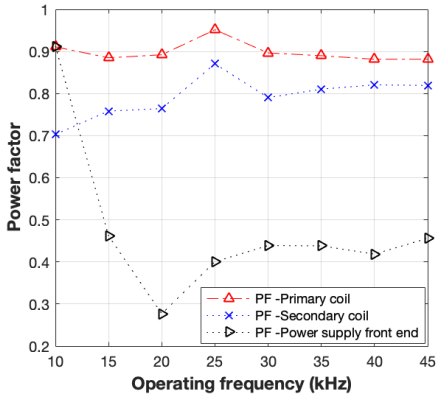


Figure 7.6: Calculated power factors of the axis-parallel coil CPT system vs operating frequency based on DSP and FFT.

By implementations of data acquisition (DAQ) and digital signal processing (DSP) with ADC board and FFT algorithm in MATLAB, angular phase information of each signal waveform can be acquired and analyzed in order to work out the power factors (PF) between alternating voltage and current waves. From Figure 7.6, it can be seen that both the power factors of two coil sides appear to show maximum points at operating frequency of 25 kHz with values of 0.9516 and 0.8707, respectively. It is noteworthy that the system does not present particular trend characteristics by values of primary and

secondary coil sides at 15 kHz and 20 kHz. However, the power supply front end appears to have a sharp downward minimum point at 20 kHz with value of 0.2768, which directly leads to the lowest power of system power supply input corresponding to the value of 45.23 mW in Figure 7.4 and indirectly indicates that a large amount of energy from the power supply front end, known as reactive power, may be deployed to establish the strongest and highly intensive electromagnetic field in terms of EMF metrics when the coil system tends to magnetically resonate at about 15 kHz. The reactive power in EMF is not any type of loss but an essentiality of building a magnetic field.

***(b) Waveform characteristics and spectral analysis***

Considering the following factual phenomena at operating frequency of 20 kHz from Figure 7.2 to Figure 7.6: the coil efficiency and system efficiency can reach the maximums; power on the load end and power on secondary coil tend to be maximized; almost all the voltages and currents of both sides especially the primary coil side could show nearly highest results, here in this subsection, frequency spectra of main waves at 20 kHz are selected and used to observe the signal behaviours and to derive out the angular phases in order to study the waveform characteristics a little further.

As the one of most significant parts of CPT systems, a coupling module, namely a magnetic coupler in the thesis, can most directly determine how the electromagnetic field actually operates in real-time scenarios in terms of H field and B field resulting in final power electronics outputs via performance of inductive coupling or intensive electromagnetic resonance, here the signal data of voltages and currents of the two coil sides have been acquired with Measurement Computing's analog-to-digital converter DAQ board and analysed in MATLAB.

For the primary coil, Figure 7.7 and Figure 7.8 depict the actual voltage and current waves over one second when the system has reached an AC stable status with a performance-based relatively optimal operating frequency of 20 kHz and the figures also present the signal waveforms with triangular window by default and with Hamming window for executions of FFT. The MATLAB codes for applying Hamming window, FFT and calculating power factors based on DAQ data can be seen in Appendix B of the thesis. The codes in Appendix B can be an example of processing the primary coil raw data and are also amended for secondary coil data DSP processing for the following subsections.

The fundamental purpose a Hamming window is introduced into the waveform analysis is to minimize and contain the spectral leakage or smearing across the spectrum. Data acquired from an ADC is prone to endpoint discontinuities due to a limited time block of signal and data amplitude not being shaped [224]. The discontinuity between the transient rectangular-windowed data end points needs a suitable windowing function in order to attenuate the values at the beginning and end of the recorded data for reduction of discontinuities and spectral leakage in the digital Fourier transform (DFT) spectrum [225].

◆ Primary coil - transmitting side

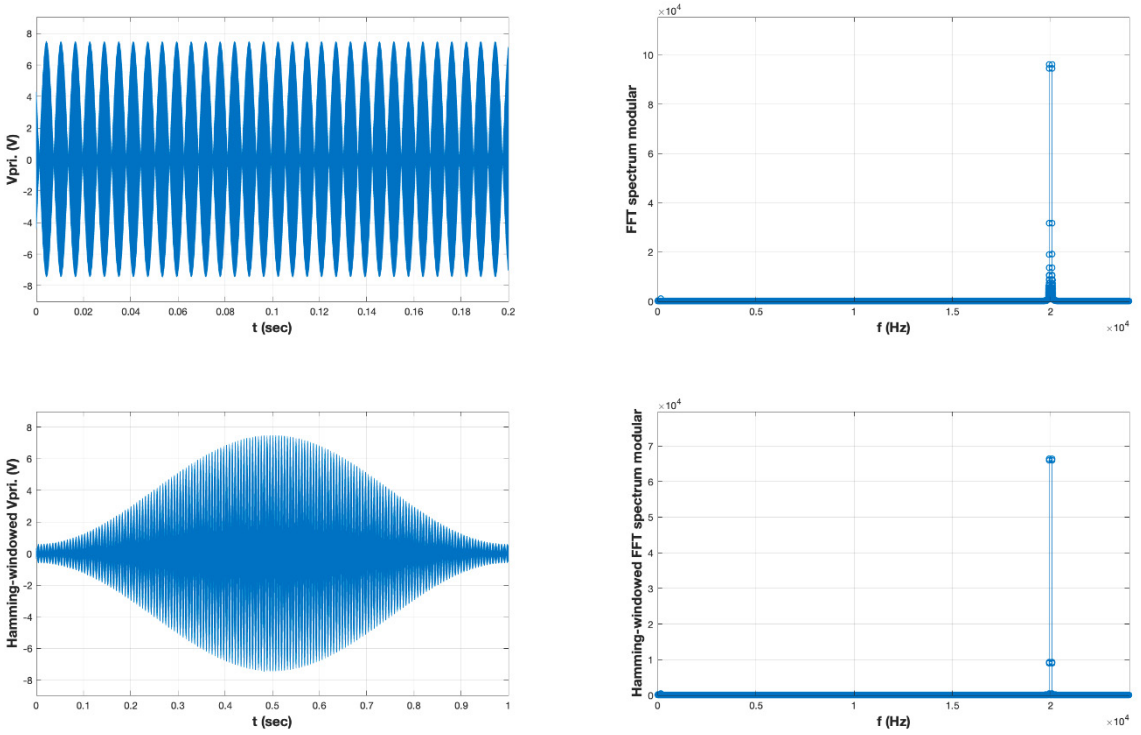


Figure 7.7: Primary coil voltage waveform by DAQ at 20 kHz and the spectrum with Hamming window and FFT for the axis−parallel coupler system.

The primary coil waveforms at the performance-based relatively optimal 20 kHz operating frequency have been presented in Figure 7.7 and Figure 7.8, along with corresponding frequency spectra before and after applying Hamming window for illustrative comparison and accuracy purpose. The effectiveness of adding a Hamming window can be seen: the side lobes in the originally rectangular windowed FFT spectrum have been reduced a lot when compared to the spectrum with Hamming window function in the right-hand side of both Figure 7.7 and Figure7.8; The center frequency can be seen more accurately accentuated in corresponding Hamming windowed spectra; eventually it

is more accurate for angular phases derivations with the effects of FFT after Hamming windowing on the primary voltage and current ADC-acquired waveforms.

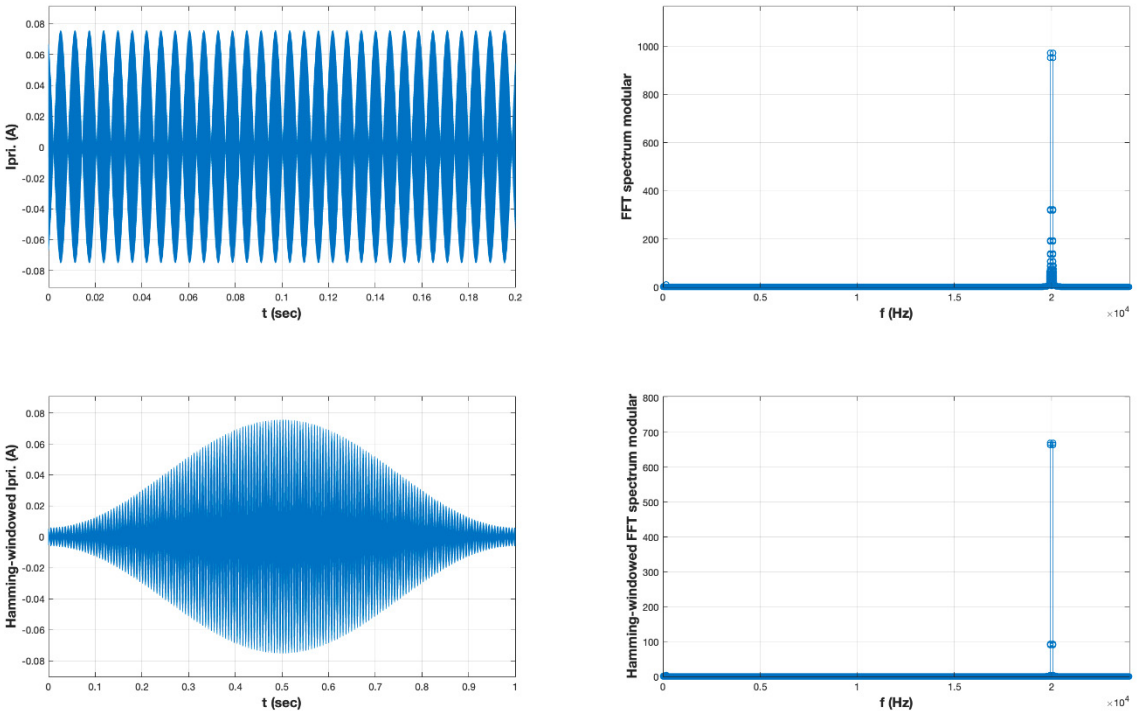


Figure 7.8: Primary coil current waveform by DAQ at 20 kHz and the spectrum with Hamming window and FFT for the axis−parallel coupler system.

The numerical magnitude values of the primary coil side voltage and current have been found to be 7.5317 V and 76.1 mA, respectively, from Figure 7.7 and Figure 7.8. After processes of DSP on the raw data sampled by Measurement Computing USB-1208-HS-2AO DAQ board, it can be found from the left-hand side waves of Figure 7.7 and Figure 7.8 that the phase of primary coil current lags the voltage by about 26.8617˚, which results in a power factor (PF) of 0.8921 for the RMS power calculation which is 255.66 mW on the primary transmitting coil.

◆ Secondary coil - receiving side

For the secondary coil voltage and current, Figure 7.9 and Figure 7.10 indicate the originally rectangular windowed waveforms, Hamming windowed waveforms and FFT spectra without and with Hamming window function.

The magnitudes of induced secondary coil voltage and current at 20 kHz can be seen to be 3.1421 V and 6.4 mA, respectively. By using Hamming windowed FFT algorithm, the

PF over the secondary coil is worked out with the value of 0.7644 and the voltage wave leads the current wave by about 40.1464˚, which results in an RMS power of 7.69 mW.

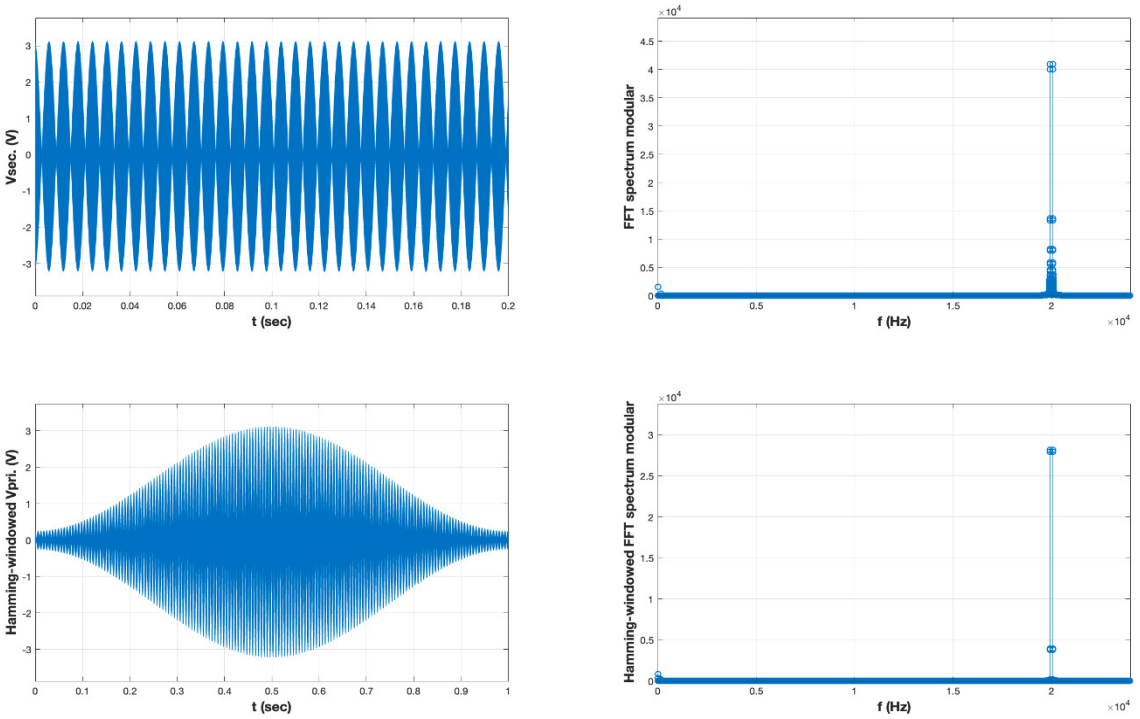


Figure 7.9: Secondary coil voltage waveform by DAQ at 20 kHz and the spectrum with Hamming window and FFT for the axis−parallel coupler system.

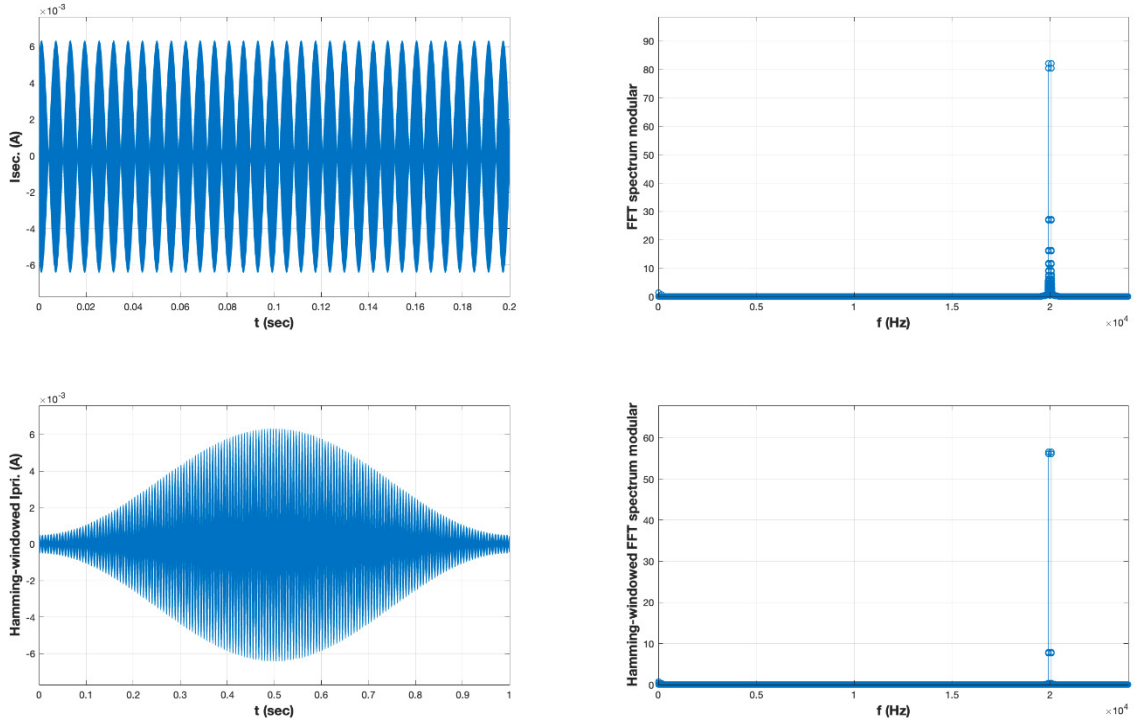


Figure 7.10: Secondary coil current waveform by DAQ at 20 kHz and the spectrum with Hamming window and FFT for the axis−parallel coupler system.

### 7.2.3 Summary

Section 7.2 presents a small-sized axis-parallel coil coupler CPT lab prototype with ferrite cores and reports the results in terms of voltages, currents, RMS powers, efficiencies and power factors of the system across a range of operating frequency. With focus on the preliminary measurement-based resonant frequency of coils, it can be found that the calculated natural resonant frequency of about 15 kHz (rounded up from 14.6 kHz) appears to produce highly satisfactory voltages and currents. But in fact, overall system efficiency, the coil efficiency, RMS real power transferred to the load and secondary coil RMS power are optimally maximized at 20 kHz with values of 32.523%, 3.006%, 4.69 mW and 14.71 mW, respectively.

Hamming window as a DSP technique has also been introduced into the method of investigating the waveform characteristics of the coils at its relatively optimal operating frequency of 20 kHz, in order to observe the actual angular phase performances and power factors that indirectly contributes to the RMS real powers via the magnetic field establishing and sustaining. This section also provides a method of testing a specifically designed CPT lab prototype for studies in the following sections.

## 7.3 Planar circular coil based CPT model

### 7.3.1 Laboratory setup and prototype design

In order to compare the overall performance between the conventional no-core circular coil-based CPT system and the ferromagnetic core-based axis-parallel rectangular coil CPT system, a planar circular coil-based lab prototype has been designed and the characteristics of this setup has been reported in this Section 7.3. The geometric space occupation of this circular coil system can be approximately equal to the axis-parallel core system of the previous section from coupler geometric size point of view. All practical prototypes in the thesis are scaled-down versions for limited materials-usage and feasible power supply and budget reasons as already mentioned and explained before.

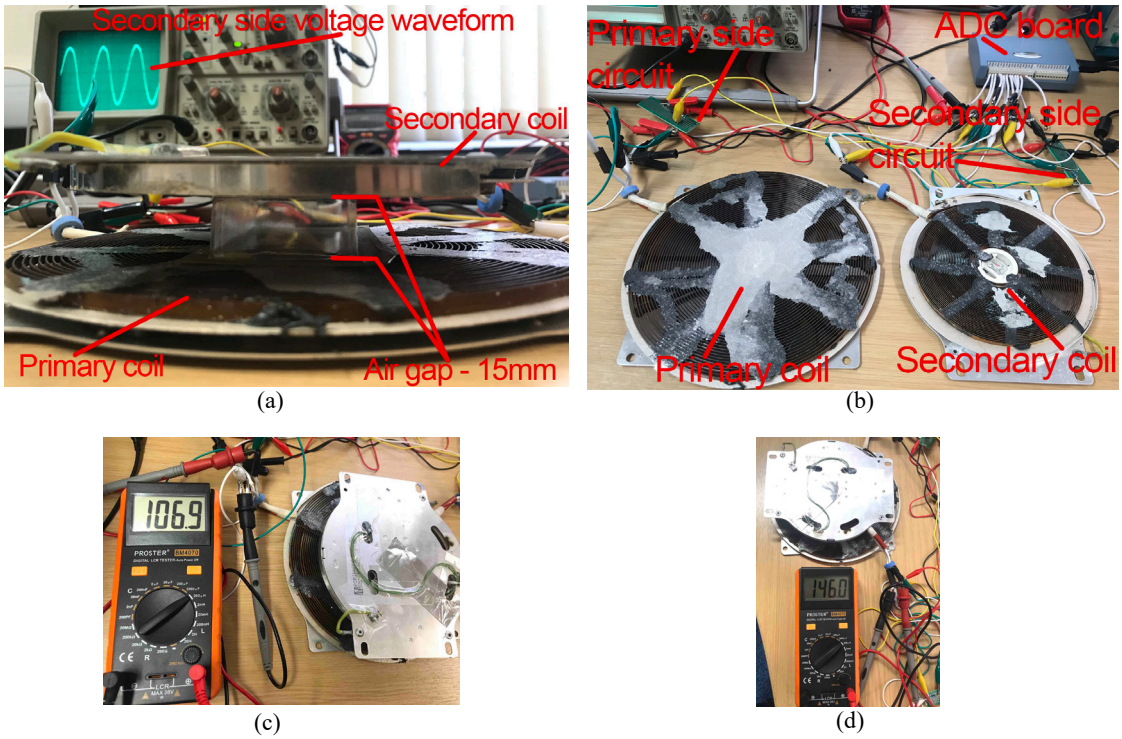


(a) (b)

(c) (d)

Figure 7.11: A 15 mm air gap circular coil coupler CPT lab setup. (a) An operating CPT prototype. (b) Geometric indication of primary and secondary circular copper coils with no ferromagnetic cores. (c) Inductance measured to be 106.9 uH for primary coil. (d) Inductance measured to be 146 uH for secondary coil.

Outwardly, a planar circular coupler seems more compact and convenient to be mounted under an EV chassis, but from overall system performance and EMF efficiency point of views, an alliance of a circular coil-based charging system and an EV chassis may not be an optimal design and option. Therefore, a 15 mm air gap planar circular coil-based CPT

system is built to be studied and tested from perspectives of power electronic outputs and main waveform spectra. The detailed systematic specifications are indicated in Table 7.2 and Figure 7.11.

Table 7.2: Specifications of the planar circular coil CPT lab prototype.

| Parameters | Values |
|---|---|
| Primary coil size | External radius 105 mm; Internal radius 20 mm |
| Secondary coil size | External radius 70 mm; Internal radius 20 mm |
| Primary coil number of turns | 40 turns |
| Secondary coil number of turns | 40 turns |
| Air gaps of the CPT charging system | 15 mm |
| Coil material | Copper wire |
| Relative permeability μ of core material | No cores applied |
| Compensation topology adopted | Primary-Series to Secondary-Series (SS) |
| Compensation capacitors | 0.1 uF |
| Load resistance | 470 ohm resistor |
| Impedance matching resistors | 100 ohm |
| Voltage power supply | 11 V magnitude sine wave |
| Measured inductance of primary coil (Open-circuit) | 106.9 uH |
| Measured inductance of secondary coil (Open-circuit) | 146 uH |
| Range of operating frequency | 30 kHz to 80 kHz |
| Shielding | No shielding applied |
| Lateral misalignment | 0 mm |
| Longitudinal misalignment | 0 mm |

### 7.3.2 Results, analysis and frequency spectra of waveforms

Based on the natural resonant frequency probe, test and tracking method as proposed in the methodology chapter and adopted in all experiments of the thesis, the primary and secondary coils of this no-core planar circular coil coupler CPT prototype have been measured with inductance values of 106.9 uH and 146 uH, respectively, using LCR tester as shown in Figure 7.11(c) and (d). The expected and calculated natural resonant coupling

frequency of the two coil sides of the system can be then worked out with values of around 48.7 kHz and 41.7 kHz.

It is necessary to mention that the testing frequency range for this specific system is set from 30 kHz to 80 kHz due to the sampling frequency maximum limit of 166 kHz of the DAQ board used in the thesis, which may unavoidably lead to lack of frequency coverage and missing results when some outcome information of the system tends to potentially appear at out-of-range high frequencies. This concern partially happens to the case of this circular coil system but could be neglected since the basic trends of most result curves have been estimated and also the power rating levels that yields in the system circuit can be observed with several-mW values. Nonetheless, the sustaining low-power level results over a long range of frequency as illustrated in Figure 7.12 to Figure 7.15 may sufficiently reflect the overall system performance to a large extent. Details about main performance outputs can be analyzed from the following part.

***(a) Main system outputs and performance results***

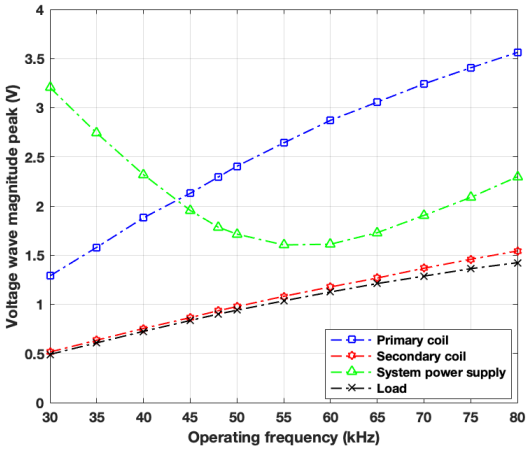


Figure 7.12: Voltages of the circular coil CPT system vs operating frequency.

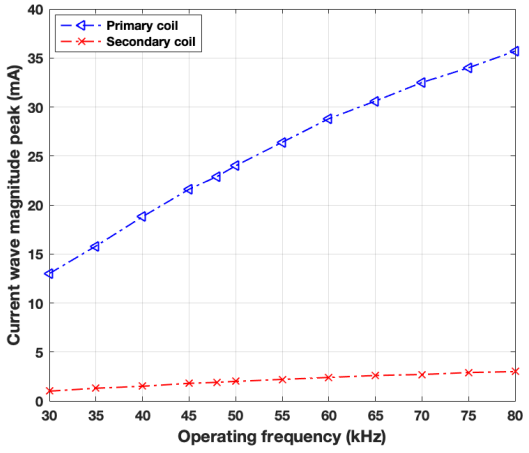


Figure 7.13: Currents of the axis-parallel coil CPT system vs operating frequency.

From Figure 7.12, it can be seen that the voltages of primary coil, secondary coil and load end show increasing trends against operating frequency, in which the secondary coil and the load present very similar gradients at each frequency point. It can be known from the curves that the primary coil voltage starts with 1.289 V at 30 kHz to rise until 3.562 V at 80 kHz, during which the primary coil voltage at 48 kHz (the rounded-up approximation of the calculated primary coil resonant frequency based on Figure 7.11) appears to be

2.295 V and it obviously does not evolve to be a maximum point with an anticipated resonant coupling phenomenon. This may represent a different characteristic of this no-core coupler system when it comes to estimating and expecting magnetic resonant coupling.

It also can be found from Figure 7.12 that both the secondary coil voltage and load end voltage increase from 0.515 V and 0.491 V to 1.543 V and 1.423 V, respectively, across the operating frequency of 30 kHz to 80 kHz. The gradients of the secondary coil voltage and load end voltage can be seen lower and lower in terms of operating frequency. Likewise, the voltages of secondary coil and load end do not appear to maximize at about 48 kHz, meaning the optimal resonant coupling does not occur within the testing frequency range. In the meantime, the system input end as the power supply presents a downward voltage curve in terms of frequency before 55 kHz and gradually increases until 80 kHz, during which the power supply end voltage shows a minimum value of 1.604 V at 55 kHz.

From Figure 7.13, it can be noticed that the current magnitudes of primary coil and secondary coil start from 13.0 mA and 1.0 mA to 35.7 mA and 3.0 mA, respectively, over the testing frequency range. Likewise, the maximum points of currents does not occur at about 48 kHz and 42 kHz, which again means the system tends to present fairly different resonance characteristics when compared with a core-based system like the axis-parallel core based CPT system in Section 7.2.

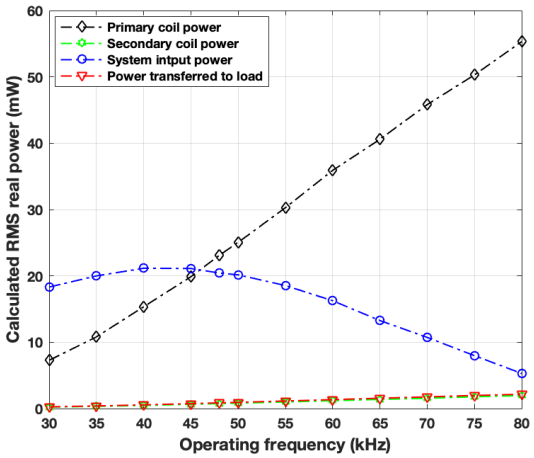


Figure 7.14: RMS powers of the axis-parallel coil CPT system vs operating frequency.

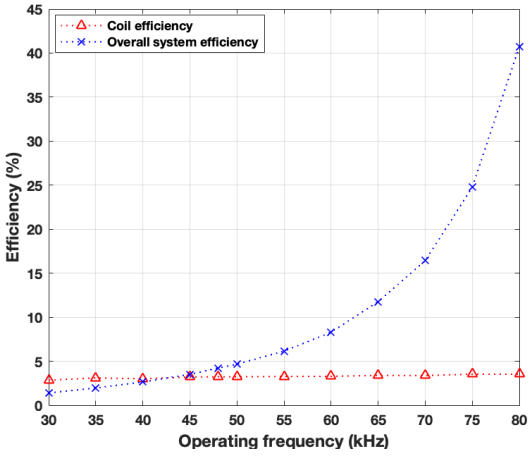


Figure 7.15: Efficiencies of the axis-parallel coil CPT system vs operating frequency.

In terms of RMS powers, from Figure 7.14, it can be found that the primary coil real power shows an increasing trend that starts from 7.27 mW at 30 kHz to 56.96 mW at 80 kHz, with 23.09 mW at 48 kHz. The RMS real power of secondary coil appears to increase, with an extremely low gradient, from 0.21 mW to 1.95 mW across frequency range of 30 kHz to 80 kHz, in which a real power of 0.75 mW is produced at 48 kHz. Likewise, the real power on the load end increases from 0.26 mW to 2.16 mW with 0.86 mW at 48 kHz. However, the system power supply front end presents a maximum value of 21.15 mW at 40 kHz, which is very close to 41.7 kHz, namely the calculated natural resonant frequency of secondary coil as measured and computed before. Nonetheless, the upward curve with an existence of peak point for the system input power supply RMS power in Figure 7.14 may reflect some characteristics in terms of calculated resonant frequencies of LCR-measured open-circuited inductance of coils. Moreover, when compared with the tens-of-mW power transferred to load end from the axis-parallel core-based CPT prototype in Section 7.2, the power rating level yielded on load end in this planar circular coil prototype seems fairly unsatisfactory with only about 2 mW. Once the prototypes are scaled up with all industrial scale components onto real-world applications, the comparisons and performance difference between an axis-parallel core-based system and a circular coil no-core system could be apparent.

According to Figure 7.15, the coil efficiency can be seen fairly stable at about 3.2% and has slightly increase from 2.853% at 30 kHz to 3.526% at 80 kHz. Meanwhile, the overall system efficiency keeps increasing versus operating frequency from 1.399% at 30 kHz to 40.738% at 80 kHz, which is fundamentally caused by the fast reducing RMS power rating of system input supply end rather than by any actual RMS power rise from the load end illustrated in Figure 7.14. On the other hand, the power transferred to load appears to be only several-mW level although the overall system efficiency keeps rising, which still indicates a pessimistic performance when it comes to charging EVs with satisfactory power for a pursuit of fast charging instead of energy saving only.

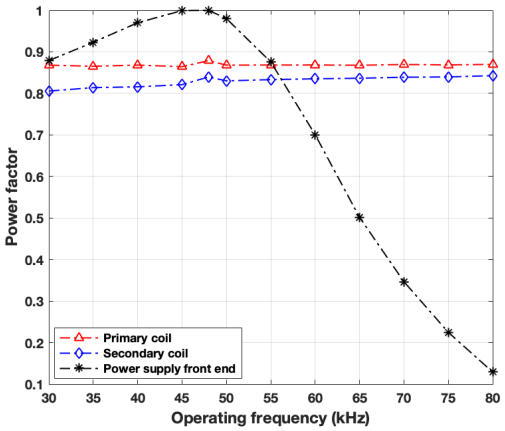


Figure 7.16: Calculated power factors of the circular coil CPT system vs operating frequency based on DSP and FFT.

Figure 7.16 illustrates relations of the three main power factors against variations of operating frequency based on FFT method for identifying angular phases. It can be seen that both the primary coil and secondary coil appear to show fairly slightly increase while the power supply front end tends to rise first and drop down in terms of operating frequency with a peak of 0.9999 at 48 kHz. The decreasing PF of power supply front end could be another reason that leads to the eventually increasingly high overall system efficiency in Figure 7.15. Two coils present relatively stable PFs versus testing frequency.

***(b) Waveform characteristics and spectral analysis***

- Primary coil - transmitting side

MATLAB codes used to undertake FFT and process all DAQ data for phase difference identifications of this section are adjusted based on Appendix B which was originally for Section 7.2. By calculating the angular phases of voltage and current waveforms with FFT in MATLAB, the 48 kHz waveforms have been selected to be analyzed from spectrum perspectives, as illustrated for of the primary coil side in Figure 7.17 and Figure 5.18. Side lobes are effectively reduced by applying Hamming windows. The power factor on the primary coil is calculated with a value of 0.8788 at 48 kHz. The magnitudes of primary coil voltage and current of this planar circular coil no-core system are about 2.29 V and 22.9 mA, respectively, which are found much smaller than results of the axis-parallel core system, 7.53 V and 76.1 mA in Section 7.2.

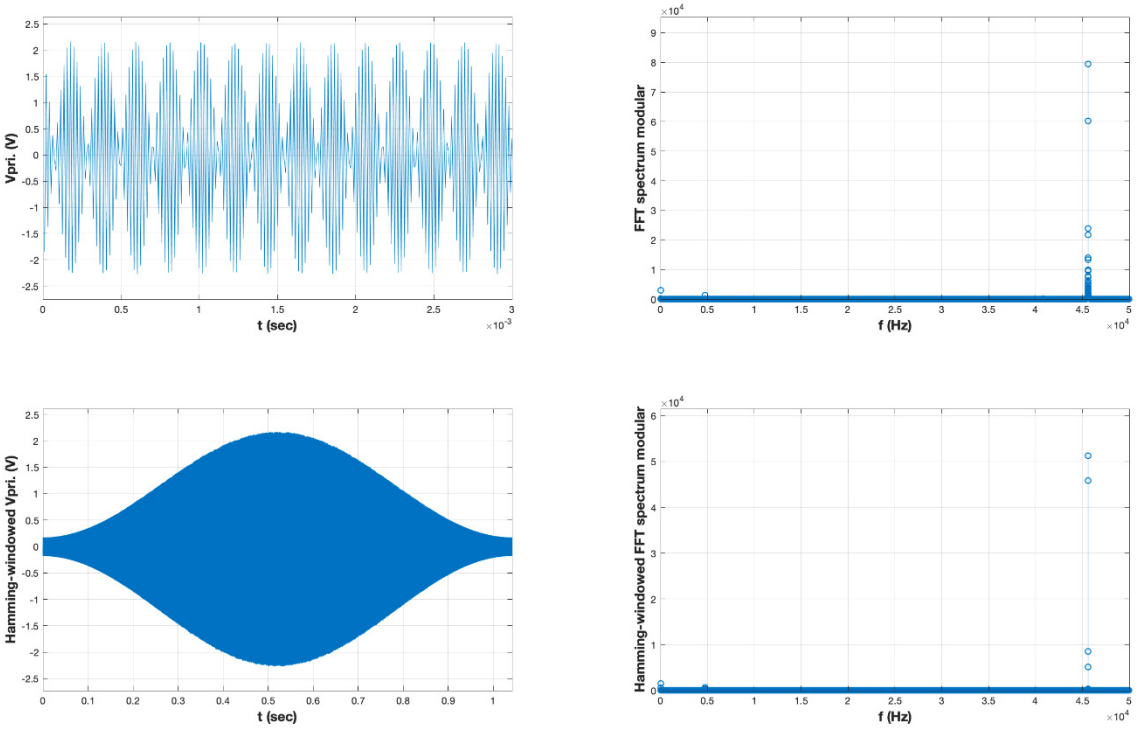


Figure 7.17: Primary coil voltage waveform by DAQ at 48 kHz and the spectrum with Hamming window and FFT for the circular coil coupler system.

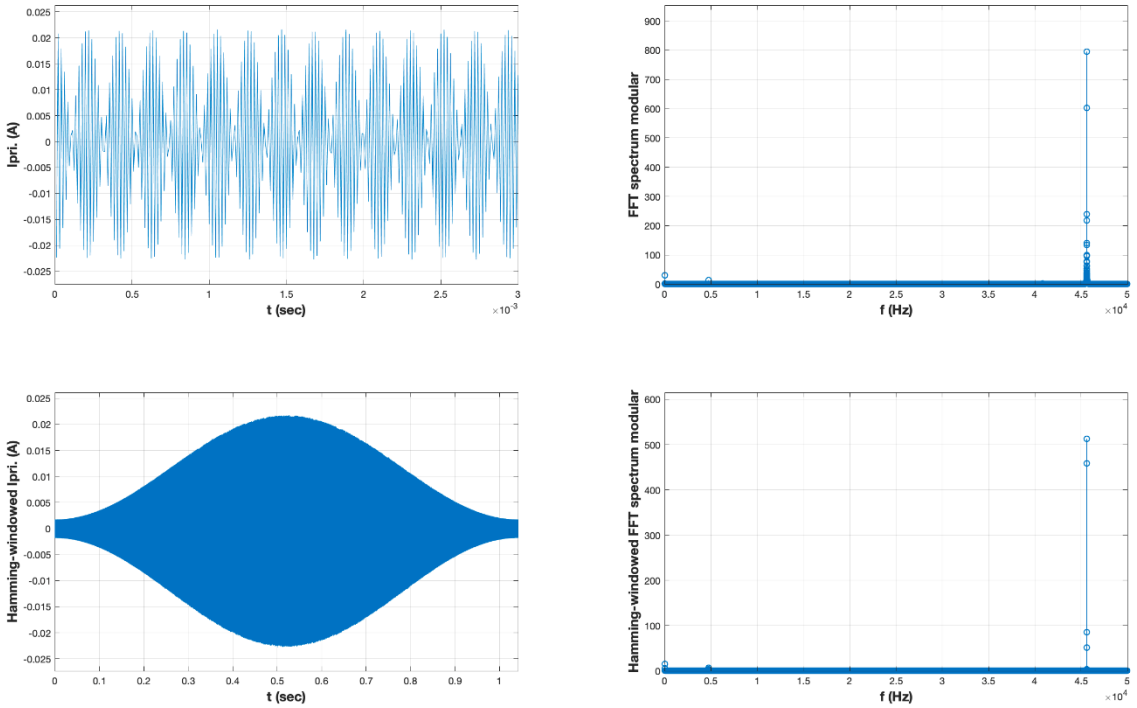


Figure 7.18: Primary coil current waveform by DAQ at 48 kHz and the spectrum with Hamming window and FFT for the circular coil coupler system.

The primary coil voltage wave can be found to lead the current wave by about 28.5021˚ at the 48 kHz operation status, which is slightly bigger than 26.8617˚ of the previous axis-parallel rectangular core-based prototype. Along with results shown in Figure 7.12 to Figure 7.15, it can be proved again that this circular coil no-core prototype does not appear to characteristically reach an approximation of magnetic resonance at about anticipated 48 kHz or 42 kHz, which seems different from the characteristics of core-based axis-parallel studied before.

◆ Secondary coil - receiving side

Based on waveforms in Figure 7.19 and Figure 7.20 with FFT analysis, the phase difference between the voltage and current waves of secondary coil can be derived out as 32.9126˚, corresponding to a PF of 0.8395 at 48 kHz. This secondary phase difference is smaller than that of the previous axis-parallel core system which is 40.1464˚ at its approximate resonant coupling state.

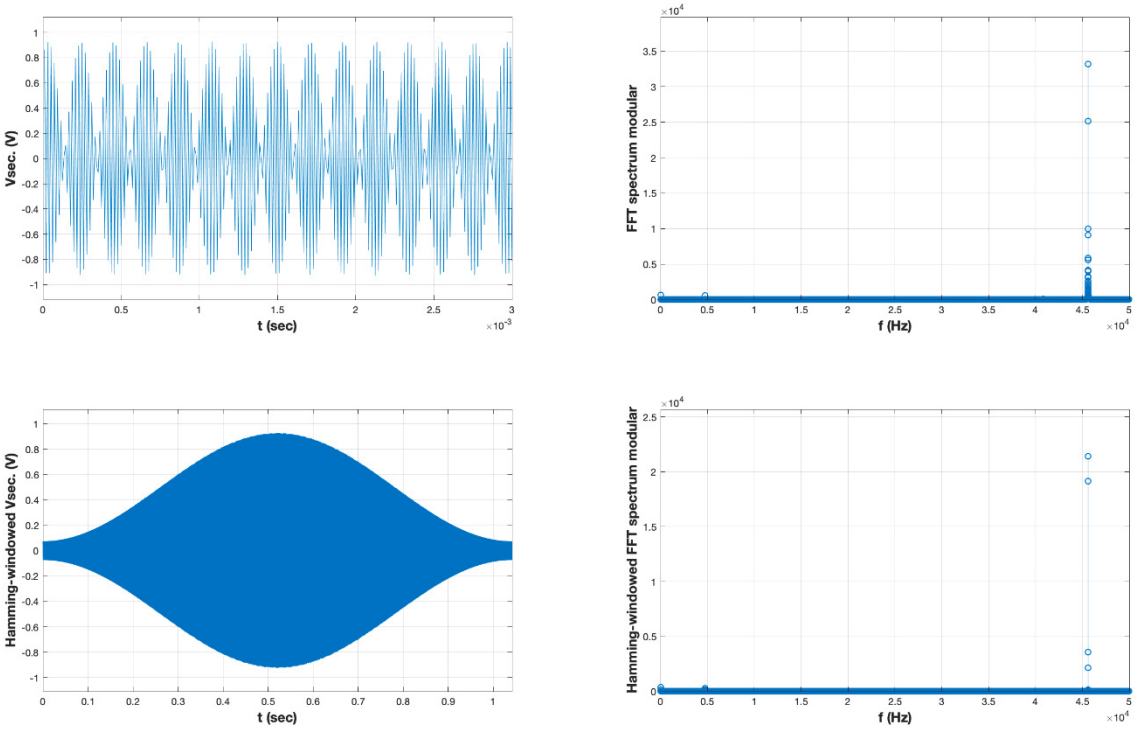


Figure 7.19: Secondary coil voltage waveform by DAQ at 48 kHz and the spectrum with Hamming window and FFT for the circular coil coupler system.

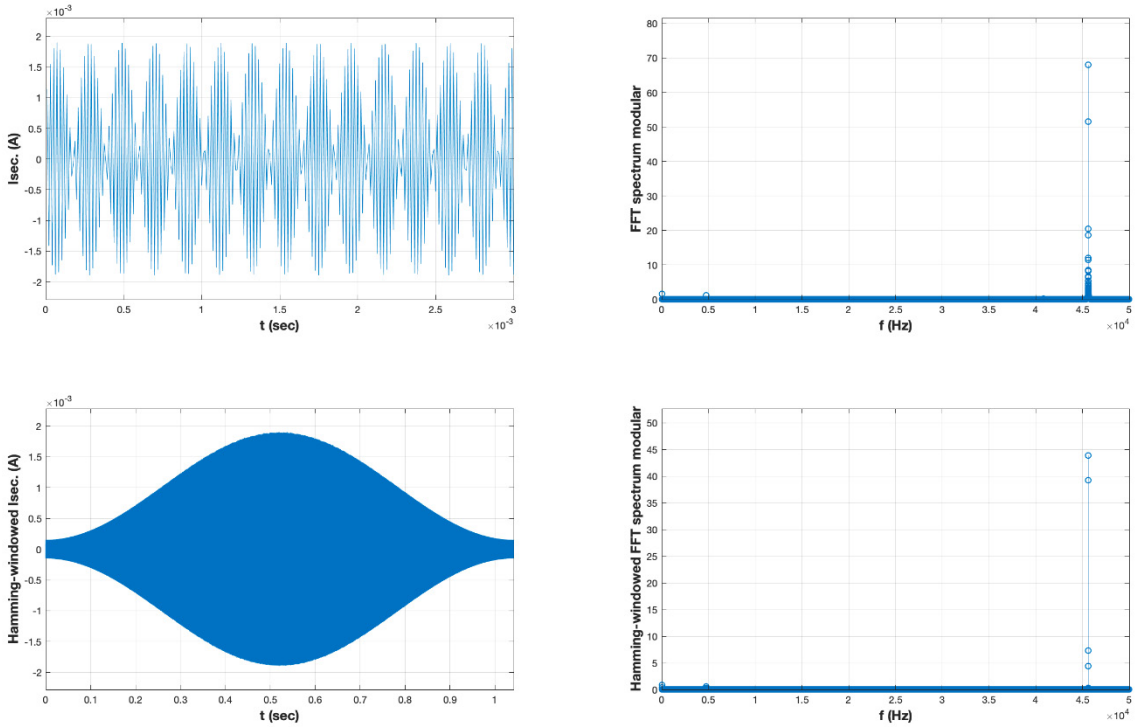


Figure 7.20: Secondary coil current waveform by DAQ at 48 kHz and the spectrum with Hamming window and FFT for the circular coil coupler system.

The magnitudes of secondary coil voltage and current of this planar circular coil no-core system are about 0.94 V and 1.9 mA, respectively. It can be found that the axis-parallel core-based system in Section 7.2 is able to present better secondary side performance with voltage and current peaks of 3.14 V and 6.4 mA, respectively, when it tends to achieve electromagnetic resonant coupling status at the calculated natural coil resonant frequency of about 20 kHz.

### 7.3.3 Summary

Overall, the laboratory experiments on the planar circular coil no-core CPT prototype not only individually reports the main system performance outputs in terms of operating frequencies, but also provides insights of searching for optimal coupling conditions despite much less obvious approaches to a satisfactory electromagnetic resonant coupling state by estimating, tuning and tracking with operating frequency. Moreover, the analysis and comparison between the previous axis-parallel core-based CPT prototype and the circular coil no-core CPT prototype have been implemented in this Section 7.3, from power electronics outputs and waveform characteristics perspectives.

A finding is that the planar circular coil CPT system without ferromagnetic cores could not reach an obvious resonant coupling state within available testing operating frequencies. Nevertheless, the coil efficiency of this system tends stabilize with a value of around 3.5% against operating frequency while the steadily-performed RMS power transferred to load can be only up to about 2 mW, which is much less acceptable than the power output performance of the axis-parallel rectangular core-based CPT system in previous section.

Apart from the quantitative output performance, another finding is that the planar circular coil no-core system would present completely different waveform performance characteristics, which may indicate different evaluation methods and optimization approaches when the CPT systems are to be categorized into with-core and without-core types. This could be further sub-topics for the future research in this area.

# 7.4 H-shaped core CPT models - Without and with aluminium shielding tests

## 7.4.1 Laboratory setup and prototype design

As a common experimental prototype with the coupler made of ferromagnetic cores and litz-wire windings, the high-power H-shaped coupler CPT model has been investigated from many aspects in the simulation-based Chapters 4 to 6 and has presented a series of advantages in relatively ideal operation environment. Section 7.4 reports implementations of a non-industrial level scaled-down H-shaped ferrite core based CPT prototype without and with passive shielding in terms of variations of operating frequency.

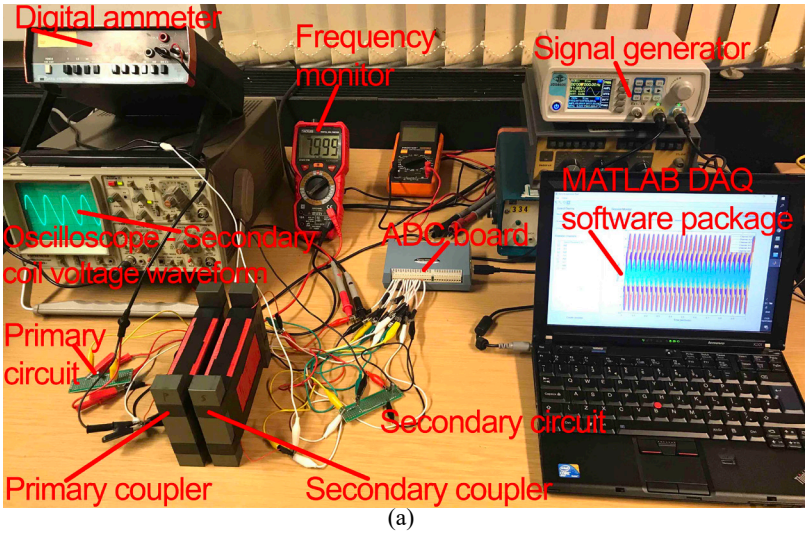


(a)

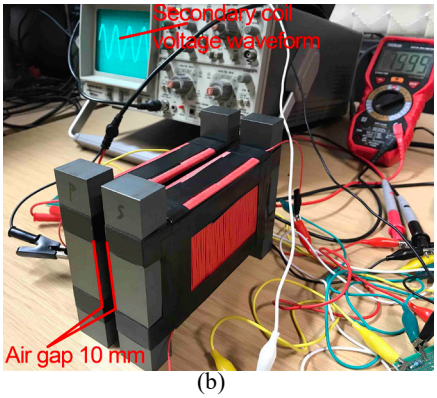


(b)

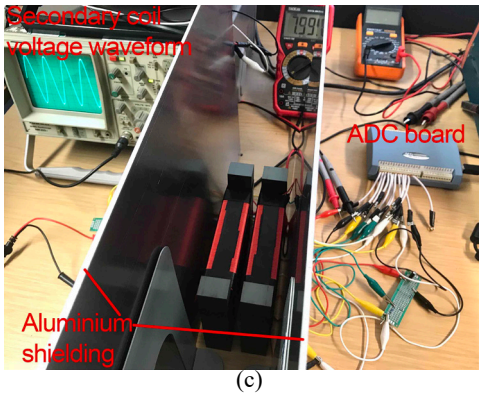


(c)

Figure 7.21: A 10 mm air gap H-shaped coupler CPT lab setup. (a) An operating CPT prototype. (b) Geometric design of the coupler windings, ferrite cores without shielding. (c) Coupling in operation with aluminium shielding.

In order to facilitate the actual overall performance of a CPT system and EMF characteristics generated in practical scenarios, the geometrically improved inductive coupling module, namely a handcrafted H-shaped couplers made of a couple of ferrite cores as illustrated in Figure 7.21 along with low core loss and high permeability of soft ferromagnetic materials as material advantages, can be beneficial to approaching an optimal flux line trajectories and magnetic field flux distributions especially when a CPT system approximates to states of electromagnetic resonant coupling. Notwithstanding, there exist some predicted limitations from imperfect setup, links of cores in the handmade production process and from calculation inaccuracies introduced by instruments when measuring for low-power application experiments, which may be negligible in this section's evaluations but could be regarded as subtopics for further discussions in the future studies.

Table 7.3: Specifications of the H-shaped core coupler CPT prototype, without and with aluminium shielding.

| Parameters | Values |
|---|---|
| Winding size | 125 mm x 80 mm x 28 mm |
| Core size | 125 mm x 75 mm x 28 mm |
| H-shaped core bar size of each side | 125 mm x 20 mm x 28 mm |
| Primary winding number of turns | 98 turns |
| Secondary winding number of turns | 98 turns |
| Air gaps of the CPT charging system | 10 mm |
| Inner shielding distance between coil and shell | 15 mm |
| Shielding thickness | 3 mm |
| Passive magnetic shielding materials | Alumimium |
| Winding material | Litz wire |
| Relative permeability μ of core material | 1000 |
| Relative permeability μ of shielding material | 1.000021 |
| Shielding aluminium material grade | RS 6082 |
| Compensation topology adopted | Primary-Series to Secondary-Series (SS) |
| Compensation capacitors | 0.1 uF |
| Load resistance | 470 ohm resistor |
| Impedance matching resistors | 100 ohm |
| Voltage power supply | 11 V magnitude sine wave |

| | |
|---|---|
| Measured inductance of primary coil (Open-circuit), with no shielding | 3.97 mH |
| Measured inductance of secondary coil (Open-circuit) , with no shielding | 3.90 mH |
| Measured inductance of primary coil (Open-circuit) , with shielding | 3.66 mH |
| Measured inductance of secondary coil (Open-circuit) , with shielding | 3.57 mH |
| Range of operating frequency | 4 kHz to 14 kHz |
| Lateral misalignment | Approximately 0 mm |
| Longitudinal misalignment | Approximately 0 mm |

The geometric specifications and major initial system setup parameters are set out in Table 7.3, in which the power electronic circuit design parameters are generically likewise the same as the axis-parallel core system in Section 7.2 and the planar circular coil no-core system and thus the main variables in Section 7.4 are derived from the overall coupling modular design. The methodology and initial step of investigating this specific prototype is the same as throughout Chapter 7.

### 7.4.2 Results, comparisons and analyses

To address the core-based H-shaped coupler system performances without and with presence of shielding effect, the major performance metrics such as induced voltages, currents, RMS powers, efficiencies, power factors are depicted in Figure 7.22 to Figure 7.26 for comparative analysis in terms of shielding effect and variations of tested operating frequency.

The methodology of undertaking the lab prototype tests and the preliminary natural resonant frequency probe and anticipation method have both been originally proposed since Chapter 3 and applied to experiments since Chapter 4. The results in Section 7.4.2 are again based on the same methodology of the thesis.

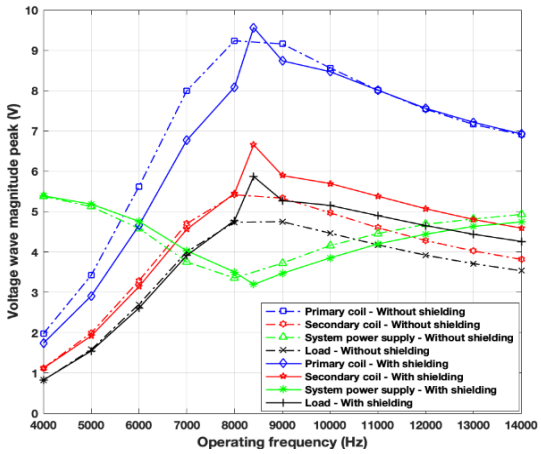


Figure 7.22: Voltages vs operating frequency for the H-shaped coupler CPT system with and without shielding.

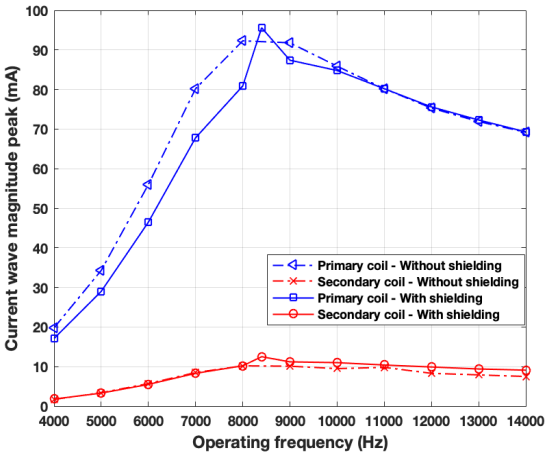


Figure 7.23: Currents vs operating frequency for the H-shaped coupler CPT system with and without shielding.

In Figure 7.22, it can be seen that the primary coil voltage Vp without shielding reaches its peak of 9.236 V at its preliminarily calculated natural resonant frequency of about 8 kHz, while the primary coil voltage Vp with shielding similarly shows a maximum of 9.563 V at its preliminarily calculated natural resonant frequency of about 8.4 kHz. Since 10 kHz onwards, voltage values of the two coils tend to be fairly close. As for the secondary coil voltage magnitudes without and with shielding, it can be found in Figure 7.22 that Vs without shielding reaches its maximum of 5.148 V at 8 kHz expectedly, and the Vs with shielding maximizes at 8.4 kHz with value of 6.655 V, after which Vs with shielding appears to perform better than Vs without shielding across the operating frequency range. Likewise, the load voltage shows a highly similar comparative trends in terms of shielding presence and operating frequency range, with peak values of 4.736 V and 5.869 V for Vload without and with shielding, respectively.

From Figure 7.23, the primary current and secondary induced current regarding presence of shielding effect are presented by result plots. For the primary coil side, Ip without shielding shows mostly higher magnitudes than Ip with shielding across frequency range, while the peak of Ip without shielding is 92.3 mA at 8 kHz and the peak of Ip without shielding is slightly higher with value of 95.6 mA. On the secondary coil side, it can be noticed that the Is without shielding presents less satisfactory results than the Is with shielding as the maximum of Is without shielding is 10.2 mA while the maximum of Is with shielding is 12.5 mA. The plots after resonant frequency points tend to reflect the

better induced current output with shielding than without shielding, which implies the stronger inductive coupling caused by presence of a shielding shell.

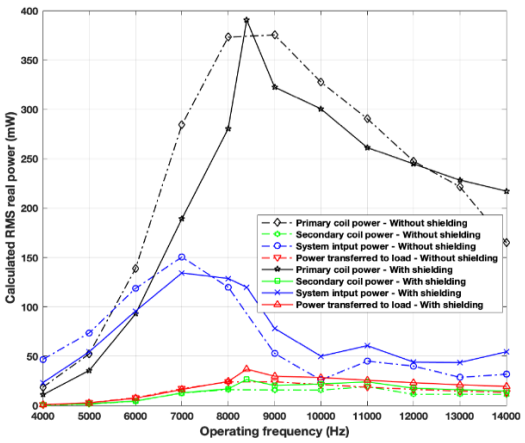


Figure 7.24: RMS powers vs operating frequency for the H-shaped coupler CPT system with and without shielding.

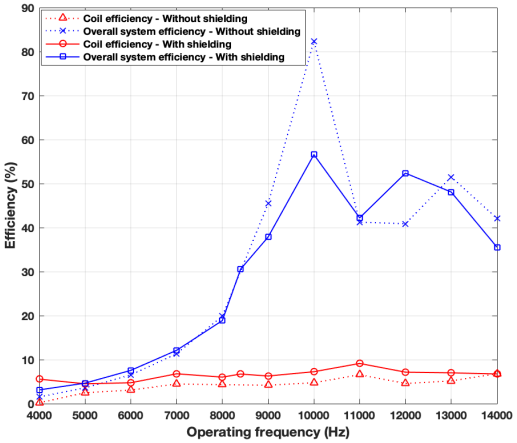


Figure 7.25: Efficiencies vs operating frequency for the H-shaped coupler CPT system with and without shielding.

In terms of RMS real powers in Figure 7.24, it can be seen that primary coil RMS powers without and with shielding reach maximums of 375.40 mW and 390.42 mW, respectively. On the other side, the secondary coil induced RMS powers without and with shielding appear to be maximized with 16.11 mW and 26.27 mW, respectively, at 8 kHz and 8.4 kHz. On the load end side, the Pload with shielding with peak of 36.65 mW can be found significantly higher than Pload without shielding with 23.86 mW. Besides, Pload with shielding performs apparently better than without shielding across the frequency range, which evidently reflects the effectiveness of deploying an aluminium shielding shell. Regarding the RMS system input power, by results in Figure 7.24, it can be known that the shielding deployment indirectly facilitates the results of the power supply front end, which leads to higher active power than results without shielding and contributes to overall system performance when undertaking calculations.

With regard to efficiency as one of the most important performance metrics, the system without and with shielding yields fairly comparative results as plotted in Figure 7.25. Evidently, it can be seen that the overall system efficiency with shielding presents two peaks of 56.588% at 10 kHz and 52.376% at 12 kHz. The overall system efficiency with shielding tends to show slightly better results compared to that without shielding across most of the frequency range, despite a sharp spike maximum of 82.374% of the overall

efficiency without shielding occurring at 10 kHz. Meanwhile, the coil efficiency with shielding obviously presents better results than without shielding over the entire test frequency range, with maximums of 9.138% and 6.585%, respectively.

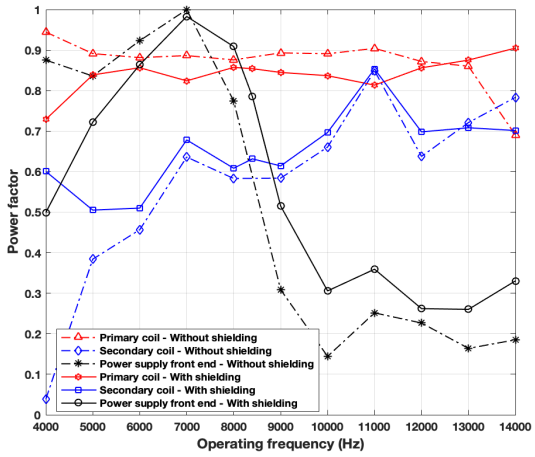


Figure 7.26: Power factors vs operating frequency for the H-shaped coupler CPT system with and without shielding.

Figure 7.26 illustrates all the power factors (PFs) of the specific CPT system operation without and with shielding. It can be know that the primary coil PF without shielding appears to be higher than with shielding by average of about 0.2. The secondary coil PF without shielding can be found lower than with shielding regardless similar curve trends with maximum values of 0.8488 and 0.8534, respectively. On the power supply front end, the PF without shielding in Figure 7.26 shows less satisfactory values than with shielding since 7 kHz, which corresponds to the calculated RMS powers of the front power input end in Figure 7.22.

Overall, almost all the results and trends of main performance metrics from Figure 7.22 to Figure 7.26 evidently reveal the significant effectiveness of using shielding for a ferrite core-based H-shaped coupler CPT system outcomes from power electronics output aspect. Detailed findings and conclusions from the results are to be addressed in the summary part of Section 7.4.

### 7.4.3 Spectral analysis of selected waveforms at optimal resonant coupling conditions

In order to make the CPT system approximate to operate at around magnetic resonant coupling status fast and accurately, a preliminary natural resonant frequency probe test as

proposed in the methodology and utilized throughout the thesis is needed to narrow the targeted operate frequency range for rapidly approaching optimizations of the formal system operation performance.

Without or with shielding effects fundamentally affects the EMF flux trajectories and final system performance via magnetic field distribution variations and different resonant coupling conditions when the studied system tends to reach an AC stabilization for executing contactless energy transmission in optimal ways. Selectively, the Section 7.4.3 is to analyse the waveform characteristics of main signals of the system at optimal resonant coupling conditions without and with aluminium shielding, and to observe the angular phase behaviours against shielding effects since the actual phase differences in real-time operation scenarios play a significant role when it comes to RMS real power and efficiency calculations as accentuated many times before in previous chapters.

On the other hand, the topic about phase differences as a determinant towards CPT system performance variations has not been addressed sufficiently in the literature. Thus, all the subsections regarding waveform phase analysis including this Subsection 7.4.3 can be regarded as another perspective of investigating CPT system behaviours facing external factors of influence. MATLAB codes used to undertake FFT and process all DAQ data for phase difference identifications of this section are again adjusted based on Appendix B which was originally for Section 7.2.

***(a) Electromagnetic resonant coupling at 8 kHz for the prototype without shielding***

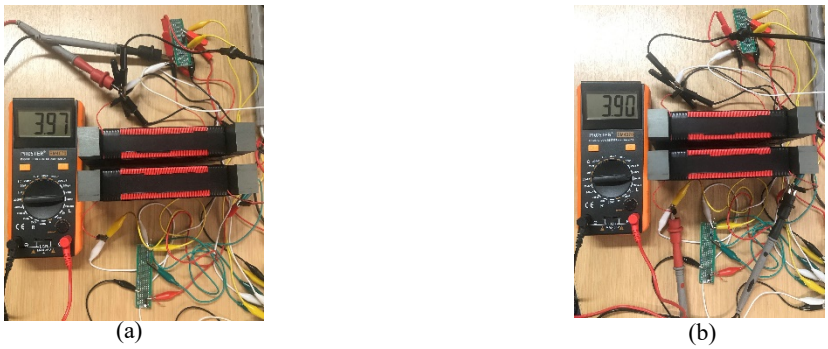


(a) (b)

Figure 7.27: H-shaper coupler inductance values measured by LCR tester when open-circuited, without shielding. (a) Primary winding, 3.97 mH. (b) Secondary winding, 3.90 mH.

Figure 7.27 illustrates the measured inductance values of the two coil windings before the sinusoidal voltage supply is formally fed to the system, by which the primary winding is

measured in milli-henry with value of 3.97 mH and the secondary winding is measured to be 3.90 mH, corresponding to 7987.7576 Hz and 8059.1238 Hz, respectively, based on natural resonant frequency equation in RLC circuit theory. For ease of operating frequency adjustment and orderly span considerations, the approximate resonant frequency based on calculations for this specific CPT system is rounded up at about 8 kHz. By analysing the results from Figure 7.22 to Figure 7.26, it is apparent that this system without shielding tends to produce relatively optimal overall system performance at the calculated fixed natural resonant frequency of 8 kHz, which indeed accords with the anticipation from preliminary inductance and frequency probes in Figure 7.27.

Hamming-windowed signals and spectra with FFT for both the primary and secondary coils without shielding are presented from Figure 7.28 to Figure 7.31 in order for waveform characteristics and angular phase information to be accurately computed and observably analysed.

- Primary coil - transmitting side

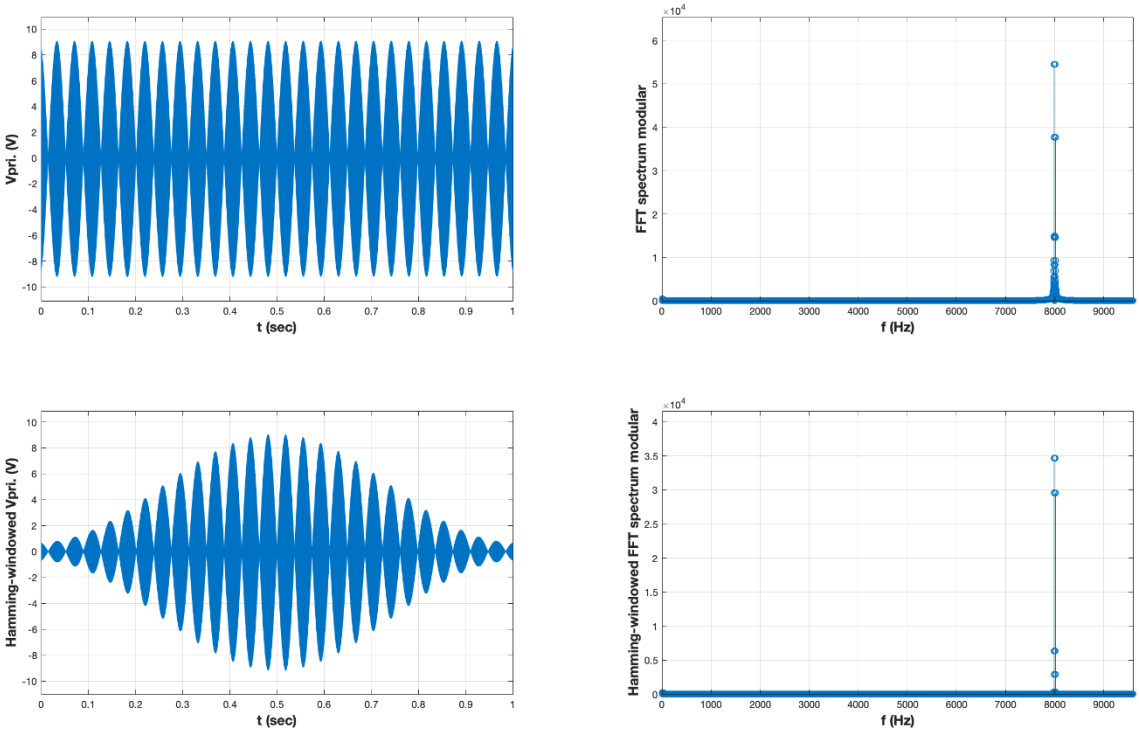


Figure 7.28: Primary coil voltage waveform by DAQ at 8 kHz and the spectrum with Hamming window and FFT for the H-shaped coupler system, without shielding.

For the primary coil, Figure 7.28 and Figure 7.29 along with phase angle difference computations and identifications by spectral analysis in MATLAB reveal that the primary coil voltage leads current by about 28.8721˚, corresponding to a power factor of 0.8757 on the primary coil. The peak values of primary coil voltage and current at 8 kHz are found to be 9.2358 V and 92.3 mA, respectively, resulting in a 373.25 mW RMS real power for the primary winding.

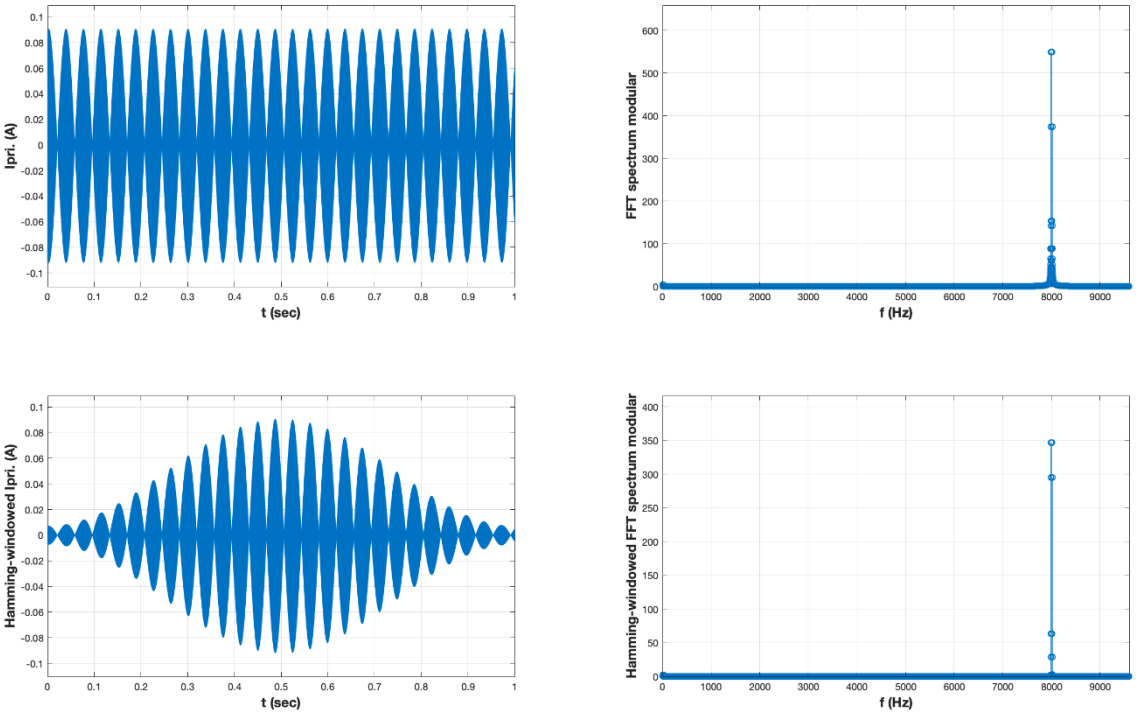


Figure 7.29: Primary coil current waveform by DAQ at 8 kHz and the spectrum with Hamming window and FFT for the H-shaped coupler system, without shielding.

◆ Secondary coil - receiving side

According to the raw rectangular waveforms and Hamming-windowed signals in Figure 7.30 and Figure 7.31, the secondary coil can be found to by spectral analysis have a power factor of 0.5831 and the current is found to lag the voltage wave by about 54.3311˚. The maximum magnitudes of the secondary winding voltage and current are 5.4175 V and 10.2 mA, respectively, resulting in a real power of 16.11 mW which is a peak RMS power result across the operating frequency and also represents an optimal system status at about the calculated resonant coupling frequency.

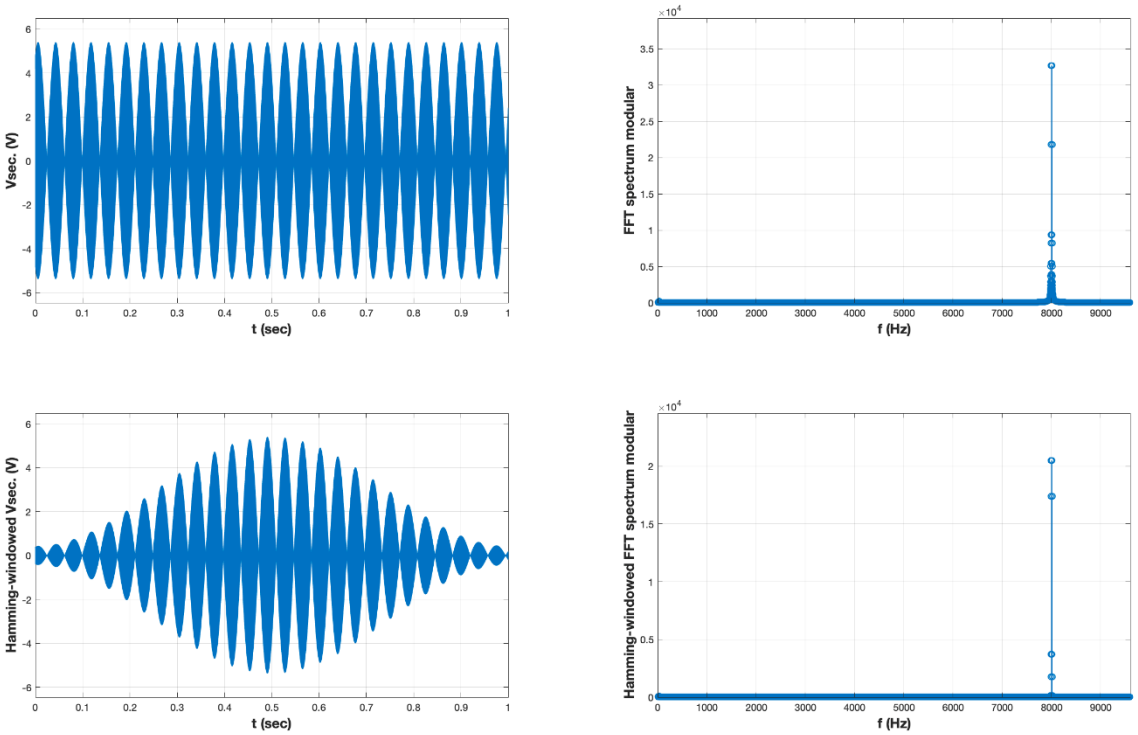


Figure 7.30: Secondary coil voltage waveform by DAQ at 8 kHz and the spectrum with Hamming window and FFT for the H-shaped coupler system, without shielding.

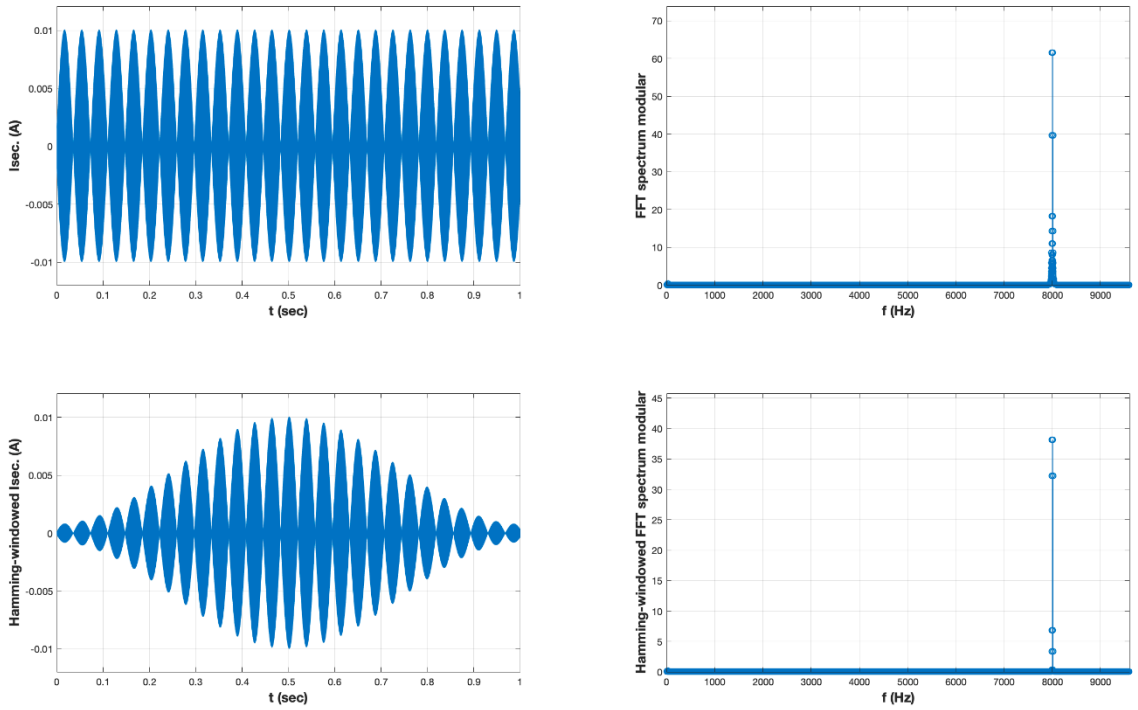


Figure 7.31: Secondary coil current waveform by DAQ at 8 kHz and the spectrum with Hamming window and FFT for the H-shaped coupler system, without shielding.

***(b) Electromagnetic resonant coupling at 8.4 kHz for the prototype with shielding***


(a) (b)

Figure 7.32: H-shaper coupler inductance values measured by LCR tester when open-circuited, with shielding. (a) Primary winding, 3.66 mH. (b) Secondary winding, 3.57 mH.

With effects from aluminium shielding, Figure 7.32 shows the preliminarily LCR-measured inductance values of the two windings differ from those in the system without shielding, which may evidently witness that the presence of shielding panels introduces impacts on the original windings with cores from inductance point of view. Based on the measured inductance values in Figure 7.32, the calculated natural resonant frequencies of the two coupling side can be found to be escalated to be 8319.1624 Hz and 8423.3728 Hz, respectively, which indicates a rise of about 400 Hz when compared with the system without shielding in Figure 7.27 before.

Again, the hamming-windowed signals and spectra with FFT for both the primary and secondary coils of the system with shielding are presented from Figure 7.33 to Figure 7.36 in order for waveform characteristics and angular phase information to be analysed.

◆ Primary coil - transmitting side

With regard to the primary winding, Figure 7.33 and Figure 7.44 describe the raw rectangular waveforms and Hamming-windowed waveforms of the voltage and current signals at 8.4 kHz. The power factor of the primary winding can be worked out by spectral analysis to be 0.8541. The voltage wave leads the current by about a phase angle difference of 31.3396˚, which is larger than the 28.8721˚ of the system without shielding, on the primary coil winding.

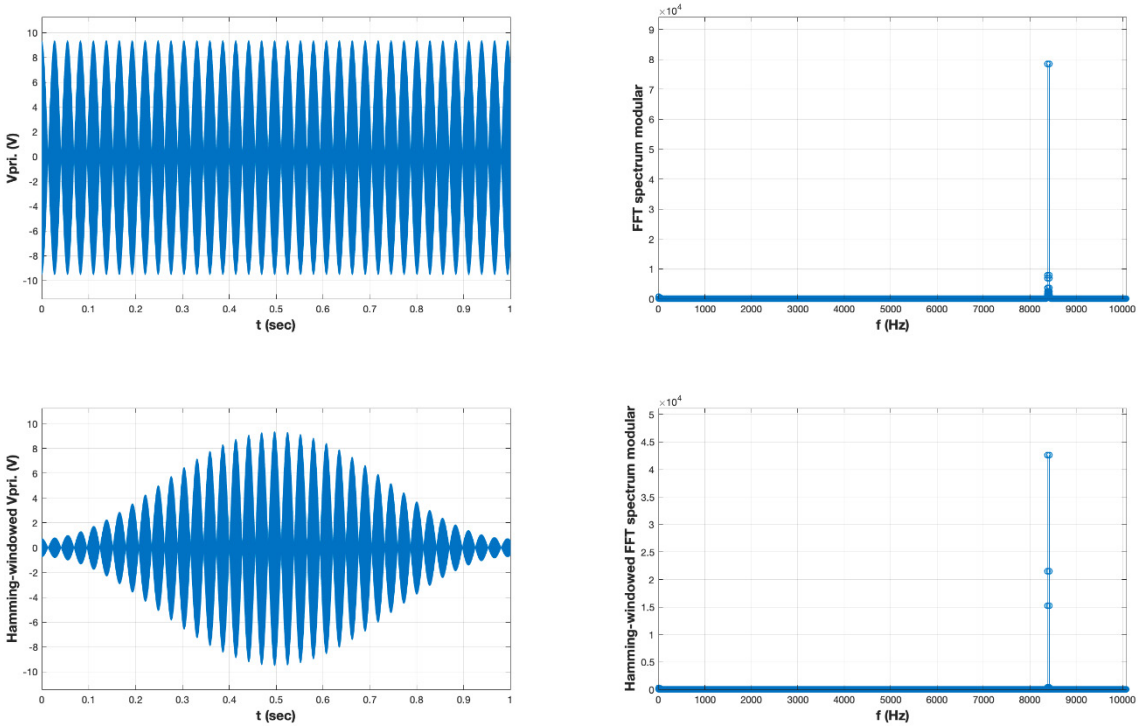


Figure 7.33: Primary coil voltage waveform by DAQ at 8.4 kHz and the spectrum with Hamming window and FFT for the H-shaped coupler system, with shielding.

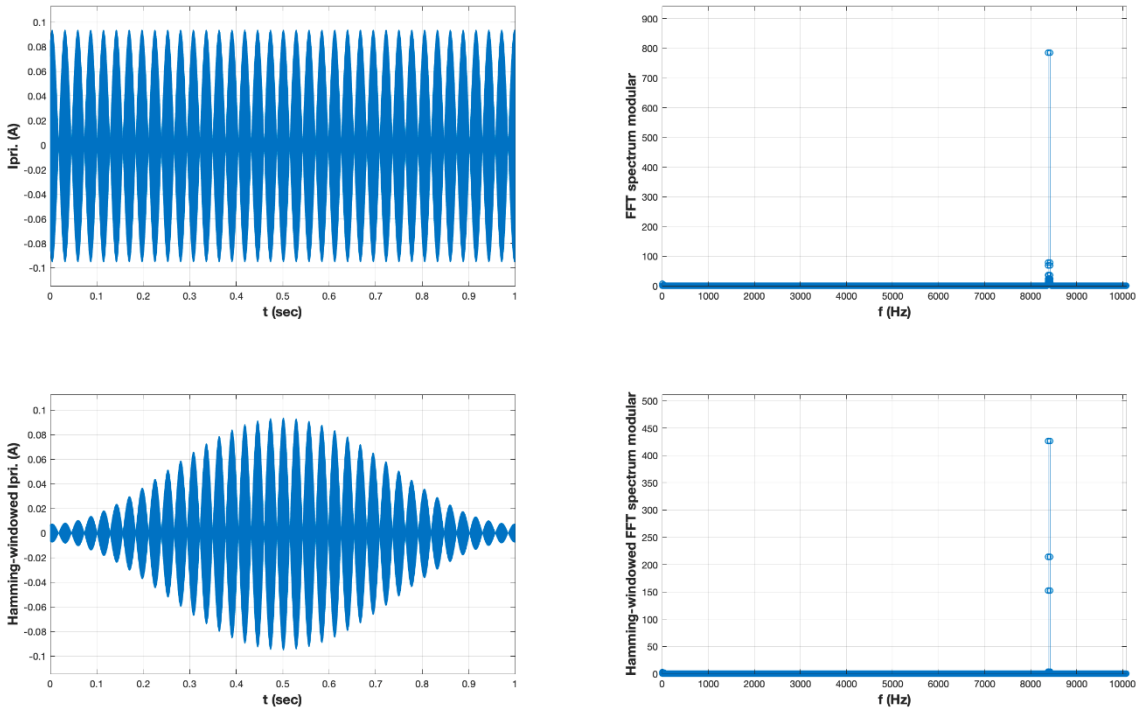


Figure 7.34: Primary coil current waveform by DAQ at 8.4 kHz and the spectrum with Hamming window and FFT for the H-shaped coupler system, with shielding.

The peak magnitude of primary voltage and current waves can be found to be 9.5630 V and 95.6 mA for the system with shielding, which both are higher than the voltage and

current of the system without shielding. These three metrics mean that at least the primary coil resonant coupling behaves better than the system without shielding when both systems operate at respective optimization status.

◆ Secondary coil - receiving side

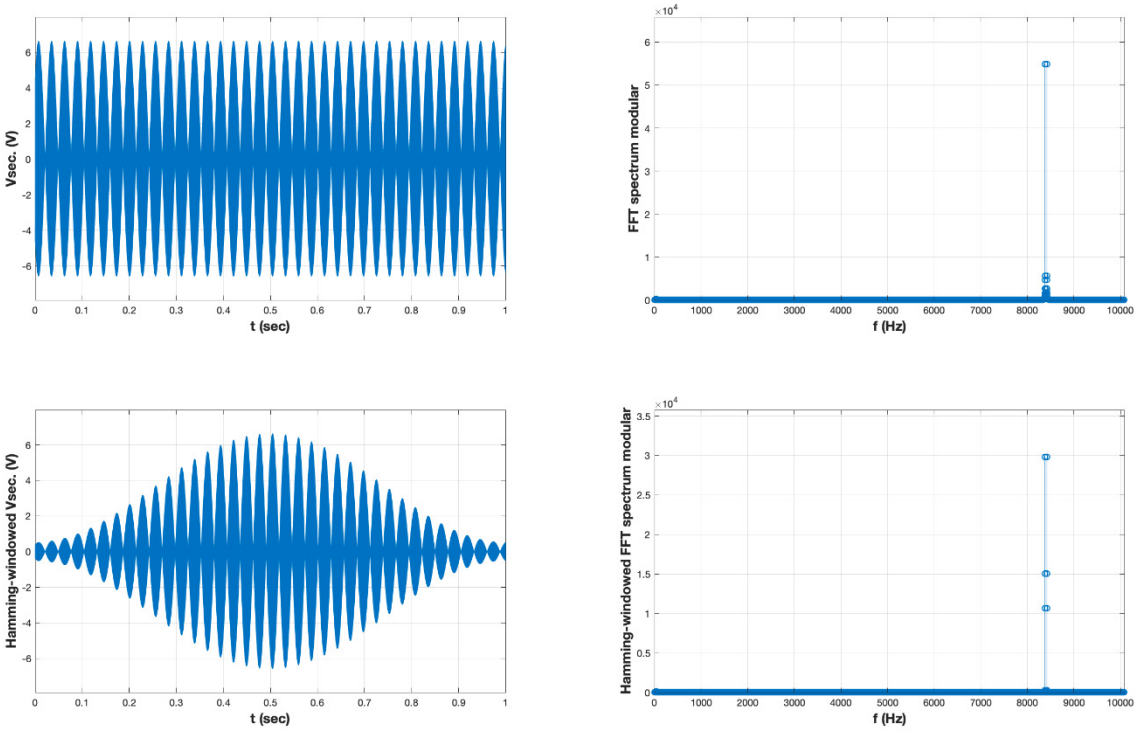


Figure 7.35: Secondary coil voltage waveform by DAQ at 8.4 kHz and the spectrum with Hamming window and FFT for the H-shaped coupler system, with shielding.

On the secondary winding at 8.4 kHz, after the CPT system tends to stabilize, the voltage and current signals are sampled by DAQ and plotted in Figure 7.35 and Figure 7.36, along with Hamming-windowed FFT spectra shown on the right hand side of the figures. By analysing and calculating based on spectral information, the secondary winding power factor can be found to be 0.6316 with the current wave lagging the voltage wave by 50.8317˚, which is smaller than 50.8317˚ of the secondary side of the system without shielding before.

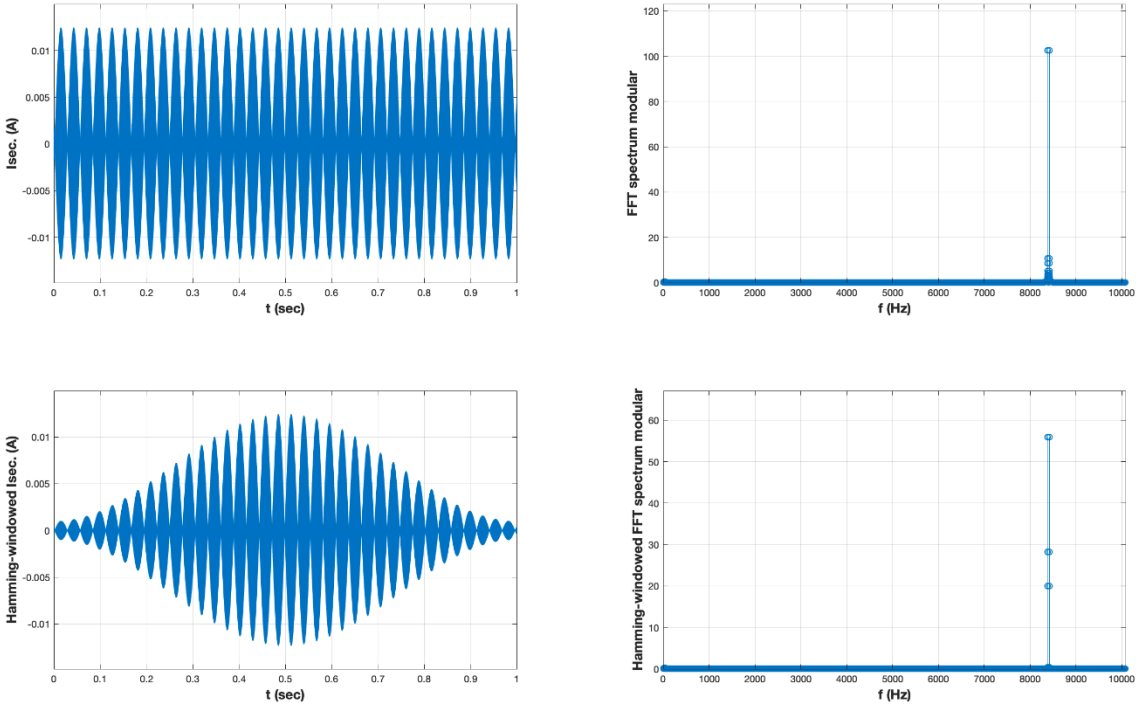


Figure 7.36: Secondary coil current waveform by DAQ at 8.4 kHz and the spectrum with Hamming window and FFT for the H-shaped coupler system, with shielding.

The magnitudes of the secondary voltage and current are found from the waveform data to be 6.6553 V and 12.5 mA, respectively, which are both higher than those results of the system without shielding by about 1.24 V and 2.3 mA, respectively. These improvements of magnitudes may indicate that the system with shielding effects appears to produce enhanced inductive coupling behaviours despite a slightly declined power factor compared with the previous system without shielding. Nonetheless, the results of power transferred to load for the system without shielding and with shielding are calculated to be 23.86 mW at 8 kHz and 36.65 mW at 8.4 kHz, respectively, which evidently reveals the output power enhancement when the CPT system tends to reach an optimal electromagnetic resonant coupling status with effectiveness of aluminium shielding.

### 7.4.3 Summary

To summarize, a scaled-down, small-sized and low-power H-shaped ferrite core-based CPT prototype has been tested in terms of presence of shielding effects in the system. With the enhancement effects of the specific geometric design and ferromagnetic core deployment, the groups of experiments without and with aluminium shielding panels have been implemented in Section 7.4. Results and comparisons have been analysed with

techniques of DSP, FFT transform and spectral analysis with Hamming windowing, from perspectives of power electronics outputs and optimal magnetic inductive coupling behaviours.

A couple of findings can be concluded for Section 7.4. Firstly, at calculated natural resonant frequency, namely 8 kHz and 8.4 kHz of the system without and with shielding, the powers transferred to load end achieve maximums, corresponding to optimized secondary currents, which proves the effectiveness of approximating electromagnetic resonant coupling states and validates the methodology of the thesis; Secondly, by comparisons, the optimal load power in the system with shielding can be seen at 8.4 kHz with value of 36.65 mW, which is more satisfactory than the system without shielding with maximum of 23.99 mW at 8 kHz and is also apparently much better than the axis-parallel core system in Section 7.2 with maximum of 14 mW; Thirdly, both the coil efficiency and overall system efficiency of the H-shaped core coupler system with shielding significantly show better results than the axis-parallel core system by at least 45% and 7%, respectively, which proves the efficacy of using H-shaped geometry design improvement and the effectiveness of adopting shielding shell as an enhancement to ensure better EMF inductive coupling; Fourthly, by gathering and comparing PFs, it can be found that the shielding effects indeed help facilitate the active powers, namely RMS powers of secondary coil, for instance, the secondary PF at 4 kHz without shielding is extremely low with value of 0.0382 while the value with shielding is drastically increased to 0.6006. These better PFs over all range of frequency on secondary coil indicates the positive effects by using aluminium shielding, which determines better coil energy transmission efficiency and then lead to higher inductive electric energy for load end. Fifthly, the optimal power transferred to load and the maximized system efficiency would not always be achieved at the same frequency point, which may reveal a trade-off between pursuing the optimizations of efficiency and RMS real power from the overall perspective for a CPT system. In real-world applications for EV charging, depending on the fast charging with higher power or on the energy economic-based consideration with higher system efficiency, EV users may need to make a compromise or compromises on pursuing optimizations of CPT system performance metrics.

In addition, the sampled data by DAQ board with Hamming window function in MATLAB at later stage of DSP process and spectral analysis can be found more accurate and solid for working out the angular phases than without Hamming window application. As mentioned before, data in these lab experiments is collected in fixed samples from ADC and is not a waveform after being illustrated, which needs applying a windowing function to attenuate and shape the values on the two sides of the originally transient data record in order to reduce the discontinuity for a better confined frequency spectrum with less side lobe distortion effect and more accurate performance.

As the actual PF values in real-time CPT applications contribute a lot to the RMS real power outputs, the appropriate windowing function such as Hamming window applied to raw data acquired by DAQ board in the range of FFT transforms of these experiments evidently provides more precise angular phase analysis results based on better frequency spectra with more sufficient side lobe suppression and less spectral leakages.

## 7.5 Evaluations and validations

In order to validate the typical models proposed and implemented in simulation environment in Chapter 7, the lab prototypes designed in Chapter 7 are tested despite a series of inevitable and foreseen limitations due to laboratory, material, instrument budgets, etc. A range of small-sized low-power CPT systems are practically evaluated in open-loop operation tests, producing relations between the specific prototype designs and major variables from Section 7.2 to Section 7.4, in spite of most results evaluated from aspects of power electronics outputs only. However, previously in Chapters 4 to 6, most simulation models are assessed and analysed from both perspectives of power electronics outputs and electromagnetics metrics, which are on the other hand the advantageous investigation methods of this thesis since few studies in the literature were conducted considering the factors and effects from EMF and actual coupling phenomenon aspects.

Chapter 7 reports four lab prototypes with result analyses and comparisons, in which three prototypes are supposed to correspond to the typical simulation models implemented in Chapters 4 to 6 for verification purpose. Although the power supply voltage sources between the corresponding simulation models and lab prototypes differ, the geometric sizes, air gaps, capacitance compensation topology methods, shielding material and inner shielding distances are basically the same for feasible validations on coil efficiency and overall system efficiency.

The axis-parallel core-based CPT lab prototype in Section 7.2 produces a 32.52% overall system efficiency and a 3.01% coil transmission efficiency at its optimal calculated natural resonant frequency for primary coil of 20 kHz. Meanwhile, for the axis-parallel core coupler CPT simulation model previously in Section 4.1, an overall system efficiency of 37.89% at calculated resonant frequency for primary coil of 1500 Hz is yielded despite a maximum spike of 85.13% at 750 Hz point; the coil efficiency is found to be 37.9% at 1500 Hz despite a peak of 85.89% at 930 Hz point. Therefore, an average of over 30% for overall system efficiency can be regarded as an acceptable verification from efficiency point of view for the axis-parallel type of coupler design, in spite of a difference between the coil efficiency curves of the simulation and lab model experiments.

In terms of the no-shielding H-shaped core coupler based CPT models, the simulation model in Section 4.2 produces an overall system efficiency of 57.4% at its calculated natural resonant frequency of 7 kHz despite a maximum of 59.5% at 11 kHz point. The corresponding lab prototype's experimental results in Section 7.4 show that the H-shaped coupler no-shielding system outputs a 19.92% system efficiency at its calculated natural resonant frequency of about 8 kHz, despite an upward sharp peak point of 82.37% at 10 kHz, and importantly, the curve shows a stability of system efficiency across a long operation frequency range with average of 40-50 percent. This may reflect the acceptable validation on the overall system efficiency for the no-shielding H-shaped coupler.

The third pair of simulation and lab models to be validated can be the H-shaped core coupler with 15 mm inner shielding distance and aluminium shielding. In Section 5.2, the simulation model yields a 36.3% system efficiency maximum at its calculated natural resonant frequency of 8 kHz, while the lab prototype produces a system efficiency of 30.59% at 8.4 kHz despite a maximum of 56.59% at 10 kHz. This is able to verify the system efficiency output performance of this type of CPT system design with close results at calculated natural resonant frequency of around 8 kHz and with magnetic resonance coupling effects such as maximized induced currents simultaneously taking place at this frequency point for both the simulation model and lab prototype tests.

Nonetheless, there still exist limitations and inaccuracies caused by predictable factors and unconfirmed uncertainties in this thesis as challenges for accomplishing more refined evaluations and verifications on many other performance metrics such optimal resonant frequency points, output PMS powers, coil transmission efficiency, misalignment behaviours, etc., which are required to be further investigated as subtopics in future research of this field.

## 7.6 Chapter conclusions

This chapter outlines and reports the overall designs and implementations of an axis-parallel core-based coupler CPT prototype, a planar circular coil no-core CPT prototype and an H-shaped ferrite-core based CPT prototype without and with aluminium shielding. Characteristics and actual performance of each prototype system have been analysed and compared from perspectives of power electronics outputs, electromagnetics and waveform characteristics with spectral analysis. Main CPT system performance metrics such as air gaps, optimal natural resonant frequency tracking, output RMS powers, coil efficiencies, overall system efficiencies have been considered throughout the sections of this chapter, despite some foreseen limitations and drawbacks from lab setup, instrument measurement to data processing as highlighted in Section 7.4.

Nevertheless, the designed variety of small-sized low-power CPT lab-level prototypes in Chapter 7 provide an overview of a number of inductive coupling-based system performance especially from a power electronics output point of view for real-world applications. Particularly, the H-shaped ferrite core coupler CPT prototype with aluminium shielding in Section 7.4 has been found to be an optimal model with a maximum system efficiency of 56.59% at 10 kHz, maximum coil efficiency of 9.14% at 11 kHz, RMS power to load of 36.65 mW at 8.4 kHz and relatively more stable performance outputs compared with other three prototype tests. Detailed findings based on this optimized prototype have been listed and concluded in Section 7.4.3, addressing the significant CPT design and analysis techniques such as coil coupler geometric design, core material utilization, shielding material deployment, inner shielding distance optimizations, DSP technique for accuracy, etc., from this specific model in order for ensuring the overall performance optimization and accordingly for verifying the methodology effectiveness based on both the simulation model experiments and lab prototype tests throughout Chapter 4 to Chapter 7.

# Chapter 8 Discussions

## 8.1 Methodology development

In order to establish a reliable, effective and feasible evaluation system for achieving optimal or comparatively satisfactory outcomes from a CPT system, the proposed methodology in Figure 3.1 of Section 3.2 has analytically depicted a wide range of aspects that are required to be taken into account to develop the methodology in details with not only generic performance metrics but also emphasized techniques.

For high-power magnetic resonant coupling based applications like EV charging in real world, the entire CPT system performance outputs are eventually expected to include promising output RMS powers and system efficiencies with characteristic system capacities like tolerance to all-directional displacements, optimum coil charging distances, optimal operating frequency range, under limited hardware conditions like CPT ground-side power source voltage levels, compensation capacitor availabilities, transmitting modular size, effectiveness of adopted coupling module ferromagnetic materials, passive shielding materials, thermal materials, etc.

In the concise methodological architecture in Figure 3.1 of Chapter 3, a contributively specific technique is originally proposed for this thesis, which is called the preliminary natural resonant frequency probe and anticipation method for effective tracking and tuning purposes towards reaching an optimal electromagnetic resonant coupling state of the system. It is noteworthy to mention that, the development of this technique was not put forward at once in the beginning of this research work but raised, revised and improved time and again during these years, based on the findings and observations throughout the thesis over the relation between the stability of calculated resonant frequency variation and the suitability of operating frequency that is fed to the system. As a preliminary frequency probe test for a parameters-configured CPT model using RLC circuit resonance, this technique has been proved throughout these chapters as a fast way to narrow the frequency range and then anticipate the optimally suitable operating frequency points, which is called the calculated natural resonant frequencies for each specific case in the thesis, before practically implementing, tuning and approximating the

front supply end frequency towards a holistic system performance optimization realization with necessary minor adjustments on other system conditions and factors.

Besides, the geometric structure designs and optimizations of coil coupler module are also a contributed strategy in the methodology as the actual electromagnetic field characteristics in each CPT scenario crucially play fundamental roles in determining EMF results and power electronic outputs, which has been accentuated in each chapter. By focusing on coupler designs and selections according to comparisons of system performance results, findings have been concluded based on each group of both simulation and lab experiments in the thesis.

Furthermore, EMF analysis can be also considered as another methodological technique for this thesis. By analysing electromagnetic metrics of each control group of models, some advantages based on behaviours of EMF performance like magnetic flux density, magnetic field strength, electric field strength, magnetic vector potential can be worked out using 3D FEM on Maxwell equations to be able to indicate the complex relation between electromagnetic field distributions and electronic outcomes for more comprehensive considerations when pursuing design optimizations of CPT systems.

Moreover, a waveform characteristic analysis and a frequency spectral characteristic analysis method based on ADC-acquired output signals from DSP point of view have been used in the investigations to derive out the angular phase relations for accurately identifying PFs and calculating RMS real powers, with assistance of Hamming windowing functions and FFT in MATLAB.

With these techniques adopted and methods proposed in the methodology, the 3D FEM based simulation models and lab-level small-scaled prototypes are designed, tested and analysed in the thesis. Findings and contributions arising from each group of experiments are summarized in the end of each section.

## 8.2 Limitations

CPT technologies have been believed to become a feasible alternative to deliver power for battery charging ranging from small low-powered devices to high-powered

applications over the past decades due to the foreseen reliance and many other advantages as described in previous chapters. However, some issues and challenges of current CPT prototypes have not yet been adequately addressed and comprehensively resolved from theoretical levels to practical applications despite some immature contactless energy transmission techniques that have been applied to small devices nowadays.

There always exist emerging obstacles and challenges during developing a technology towards a mature status in commercialization and industrialization. Likewise, the CPT technologies investigated in this thesis have witnessed and will encounter more technical difficulties and practical challenges. This subsection summarizes and briefly discusses the major challenges that have been stressed throughout the previous chapters from a global view of the technology improvement.

Numerical complication and computational intensity in solving 3D FEM-based simulations in Infolytica MagNet and ANSYS Maxwell inevitably would cause inaccuracies of results, which can be dependent of characteristics of adopted materials, mesh element size, polynomial order and boundary condition setting. Particularly, the boundary condition settings of about 15 times the coupling module size have been built to be considered as an equivalent to real-world magnetic coupling scenarios rather than an hundred percent open boundary in this thesis, which could be a limitation to a perfect flux traces' meshing and simulation especially for those flux lines that are generically escaping from the field into space by nature. This imperfection leads to inaccuracies on computed results and more or less impacts analysis over each subtopic of CPT technology development.

Regarding challenges from losses, the models in the thesis have been considered with copper losses while core losses have been neglected and not been taken into account when solving the 3D FEM simulations. Nonetheless, core losses consist of hysteresis loss, eddy current loss, which are proportional to frequency and square of frequency, respectively. In HF applications like the industrial scaled-up prototypes of those from this thesis in the future, thereby the core losses need to be carefully considered and calculated in terms of increasingly high operating frequencies for high power transfer purposes in more sophisticated future studies. On the other hand, copper losses generally include circuit wire loss and winding loss. Whilst winding loss comprises skin effect loss and proximity

effect loss, which are caused by alternating currents concentrating in the surface layer of conductors and introduced by eddy currents in adjacent multi-layer conductors, respectively, especially at high frequencies. Thus, further discussions over all aspects of losses in the future are required to address core losses at very high frequencies. Copper losses from the circuit and winding as the main energy loss in the entire CPT system are also required to be profoundly disintegrated and considered as a trade-off criterion when the maximum RMS power transferred to the load is required as a priority for a rapid charging option from customer end in the real-world high-frequency oscillation and high-power EV CPT applications.

In terms of ferromagnetic materials and permeability, the air region employed in the simulation models has a relative permeability of 1.0000004 H/m. The ferrite core material is a steel1010 type with a nonlinear relative permeability of about 1000 to 18000 H/m in its B-H curve. The main losses as mentioned above are also contributed by the winding Litz wires with a copper relative permeability of 0.999991 H/m. The higher permeability of core materials, the higher B field could be induced as the magnetic field density **B** is dependent of permeability μ when the exciting magnetic field strength **H** is constant. By generating more satisfactory magnetic field density on primary coil side, most EMF performance parameters in the field and on the secondary coil side are induced and enabled based on field equations for overall better system outputs from both perspectives of power electronics and electromagnetics. The limitations on selections of ferromagnetic materials for cores and even shielding shells are subject to development of material science in the future considerations.

When it comes to safety concerns, the foreign matters and interfering media issues in between the electromagnetic coupling space include foreign metallic objects and live objects, which may lead to critical flaming hazard, explosive risk, dangers of death to animals and may also reduce CPT efficiency outputs by eddy current effects on objects and overheating. Within the high flux density electromagnetic field, high AC flux can induce different levels of eddy currents circulating in any unintended components, thereby internal temperature of theses interfered objects by conduction losses would increase and some circuit damages may be caused to lead to entire system faults or failure if the temperature growth considerably exceeds a safety concern level. Thus foreign

objects and thermal detection technologies will be necessary for real-world applications in the future.

From modelling point of view, the model sizes in the simulations and lab tests are not sufficiently large to be equivalent to a real-world application for an EV chassis since unavoidable computational complexity and inaccuracy in the selected 3D FEM environment have to be minimized in the studies. Hopefully, industrial scaled-up and completely geometry-equivalent simulation models and lab prototypes would be built for more accurate and convincing analysis in more powerful simulation environment and more advanced laboratory if possible.

The inner shielding distances, namely the gap in between windings and inner shielding surfaces, in the prototype of Section 7.2 might be too small and inadequate to reflect an optimization design in terms of this variable and system performance. This limitation and insufficient variable-driven testing groups probably have caused distribution of the ultimately optimal magnetic field flux to be restricted and optimum flux linkage scalar values at space points to be achieved. To fill the gap of this subtopic, future tests and implementations against this variable are supposed to be enlarged and scaled up to tens of centimetre levels to simulate real-world space underneath EV chassis in order to empirically identify the optimum inner shielding distances accordingly for varying CPT charging rear ends due to types of vehicles and receiving module protocols. On the other hand, in practical lab tests of the thesis, B field and H field were not practically tested in the real-time real-world electromagnetic field in each test due to limits of lab measurement instrument budgets that could not afford a suitable AC Gauss tester, which was an obstacle to EMF result analysis for lab prototypes tests and model validations to some extent.

Axial misalignments in lateral and longitudinal directions have been considered in limited ranges by Chapter 6, in spite of angular displacement and complex blended misalignment scenarios having not been tested more comprehensively. In real-world applications, depending on how the vehicle users park and align the cars over the CPT charging dock every time, the actual angular, lateral and longitudinal displacement degrees would significantly affect the inductive coupling performance due to more imperfect

electromagnetic field generations. This limitation needs to be addressed in the future investigations.

Extended mileage goal, as a mid-to-long term challenge for any battery-based EVs, will have been the main subtopic to be covered in the future, which will continue introducing more research trends in advancement of material science, in development of high energy-density battery and in emerging dynamic charging research as a further derivative long-term objective and solution for an ultimate EV driving range.

Conventional transportations and power cord-based plug-in EVs in many industrial sectors are believed and expected to be replaced by CPT technologies-based EVs in the next half a century despite technical challenges as discussed above, policy-related difficulties, commercial recognitions and integral feasibilities.

## 8.3 Contributions and discussions with key findings

The overall system performance objectives, as accentuated in the methodology and the thesis contents, mainly consist of maximizing system efficiency, RMS power transfer rating, optimizing air gap of coupling coils and tolerance to misalignments, etc. Whereas a range of emphasized technical performance metrics, according to the observations and findings throughout the experiments of the thesis, have been considered as key determinants or indirect factors, which are operating frequency for electromagnetic resonant coupling, ferromagnetic coupler core material, shielding material, inner shielding distance, EMF flux distribution, RMS flux linkage, actual inductance in field, magnetic flux density, magnetic field strength, field energy, power factors of system outputs, output waveform characteristics, etc.

Key contributions and findings from the thesis are to be discussed as follows in spite of detailed contributions and evaluations corresponding to each result analysis and section summary of Chapter 3 to Chapter 7.

◆ ***Inductance values of coils towards magnetic resonant coupling status.*** Inductance value of primary coil could not be influenced noticeably in terms of varying operating frequency whereas the inductance value of secondary coil (vehicle chassis receiving side)

can be significantly altered by change of power source operating frequency. Accordingly, the natural resonant frequency of primary coil is able to tend to be relatively stable in terms of operating frequency for achieving magnetic resonance, however the calculated natural resonant frequency of secondary coil is most likely not to be considered as constant, meaning unlikely resonance status to be reached for secondary side of CPT systems. This finding has been observed based on 3D FEM simulations in both Infolytica MagNet and ANSYS Maxwell through Chapter 4 to Chapter 6, which is also contributing to further studies on optimization designs using electromagnetic resonant coupling.

- ***Higher natural resonant frequency in terms of CPT performance outputs.*** It has been found that setting a higher natural resonant frequency by adequately changing compensation capacitors for a magnetic resonant coupling CPT system could be beneficial to induce higher magnitudes of currents and voltages, and could lead to a higher system efficiency when the operating frequency is properly tuned and approximated to the new natural resonant frequency point of primary coil side. This finding verifies the theoretical magnetic resonance advantages for inductive coupling with higher resonant frequency resulting in more satisfactory electric energy transmission behaviours despite some limitations over compensation capacitors from material point of view in real-world system configurations.

- ***Lateral misalignments in terms of pursuing satisfactory resonance.*** In terms of lateral misalignments, comparing the primary and secondary calculated resonant frequency curves, a significant finding is that the primary calculated resonant frequency of each test seems able to reach a relatively constant stability after about 10 kHz, which means the CPT system can show a satisfactory tolerance to lateral misalignment effects as a long range of frequency supply can be utilized to resonate the secondary-side energy eventually to the load. However, the secondary side shows a more linear relation when re-tuning and tracking its natural resonant frequency, which may reflect a difficulty in pursuing a satisfactory resonant state for secondary coil to enhance wireless energy transmission performance by front coupling side tuning maneuverers.

- ***5 mm lateral and longitudinal misalignments as general maximum tolerance in terms of EMF performance.*** Comparing both the longitudinal and lateral groups of tests regarding calculated resonance frequency and calculated inductance, it can be found that

the specific H-shaped coupler CPT system with shielding tends to reach a proximity of optimized magnetic resonance at about 8000 Hz to 8500 Hz with both the longitudinal and lateral misalignments. Therefore, a misalignments of 5 mm in lateral and longitudinal directions may be considered as the accepted limits or general maximum tolerance in terms of overall power outputs, system efficiency and EMF performance. From the H field performance perspectives only, it is interestingly found that a more optimal magnetic field strength, namely H field generation per se, would be yielded with a slightly imperfect position-aligned coupling.

◆ ***Angular phases behaviors and PFs in terms of flux linkages and system outputs***. As for phase angle differences and optimization of PFs, it is empirically found from the waveform analyses of the thesis that mostly when the primary coil reaches its optimum of resonant coupling via a maximized PF at corresponding natural resonant frequency, the entire system will yield the most satisfactory power electronics outputs and produce the most optimistic electromagnetic field distributions with well-performed field parameters. Besides, the maximum PF of secondary side can normally correspond to the maximum of system efficiency and maximum of power transferred to load for all the longitudinal misalignment tests. Another finding is that a larger lateral displacement would determine higher resonant frequency of primary side of the system. However, for angular phases, the misalignments in both X and Y axes would not have fundamental impacts on the angular phase performance of flux linkages, according to all the waveforms and phase characteristics in Section 6.6. By flux linkage waveforms of Chapter 6, it is found that the secondary flux linkage performance can directly indicate and can be more able to determine the overall effectiveness of system performance including power electronics outputs and efficiency rates.

◆ ***Optimized 'threshold' inner shielding distance and air gap exist, instead of a minimized inner shielding shell-to-coil gap and coupler air gap absolutely leading to maximized system performance.*** Regarding optimizing the air gap, namely the charging distance, it has been found that a smaller air gap generally leads to relatively better system efficiency and RMS power transferred to load. Nonetheless, a finding from the experiments of the thesis is that there exist optimal threshold points for charging distance and for inner shielding distance to reach a holistic CPT performance optimization for

specific models, which could be explained from EMF point of view that an existence of optimal closed-loop flux line paths and flux linkage distributions within a limited field in between shielding shell and couplers may determine an optimum air gap of a magnetic resonant coupling CPT system. This optimum air gap for each system in real-world EV charging applications is required to be practically measured and tested for an accurate identification under conditions of any other variables and factors remaining unchanged. Likewise, the inner shielding distance also needs to be assessed and evaluated by an adequate amount of empirically practical tests for any newly designed model towards an optimal lateral, longitudinal or angular misalignment tolerance as required in actuality.

- ***Operating at exact natural resonant frequency point may not always lead to an overall system performance optimization, while setting the system in close proximity to an edge of anticipated natural frequency would achieve optimizations of most required performance metrics.*** Through the investigations and experiments, a finding is that the output RMS power and system efficiency of any specific CPT system markedly hinge upon the actual real-time magnetically inductive coupling performance via how the actual operating frequency supply is adopted based on anticipated resonance status and calculations. In practical cases, it has been found that approaching the approximated resonant frequency of primary coil may not always determine a maximum of RMS power on load or system efficiency or even both maximizations at the same time subject to many internal and external factors. In some cases, the most adequate and suitable operating frequency point or points particularly need to be set tens of kilohertz away from the exactly central anticipated natural resonant frequency point or be in close proximity to an edge of resonant frequency range in order to achieve an overall system satisfaction considering most performance metrics optimizations such as RMS power rating, efficiency, total loss, EMF intensity, air gap, etc. Thus, these relatively complicated coupling cases based on reality-parking manoeuvres need to be measured, calculated and tested more empirically rather than idealistic simulations and insufficient amount of lab-based experiments.

- ***Satisfactory sustainability and capacity of operating at optimized status across long frequency range can be reliable and important for real-world EV charging in addition to major performance metrics maximizations.*** Nonetheless, several designed CPT

models in the thesis also indicate that, within some particular frequency ranges, different models tend to appear to be sustainably and stably capable of producing relatively highly satisfactory overall system efficiency as well as RMS power onto load in spite of peaks of the two key performance criteria not necessarily taking place at the same operating frequency, which can also reflect how the holistic compatibility, usability, reliability, suitability of the designed CPT model would be when the microscopic magnetic coupling cases vary due to change of EMF situations caused by different vehicle parking manoeuvres from EV user end.

◆ ***The preliminary natural resonant frequency probe and anticipation method.*** For effective tracking and tuning purposes towards reaching an optimal electromagnetic resonant coupling state of the system fast and effectively, the methodological flowchart in Figure 3.1 of the beginning of Chapter 3 has depicted major constructive elements, factors and considerations for a high-performance CPT system. All the focuses from pre-design to post-evaluation are included in this uniquely developed methodological structure for this thesis, in which the power electronics, EMF metrics and overall targeted outputs are addressed in order to achieve an optimized CPT system design. Furthermore, this methodological system can be more specific and derived towards further improved CPT system realizations.

◆ ***Trade-off considerations between maximizing system efficiency and RMS power transfer in practical CPT implementations for EV charging.*** A critical finding is that an inevitable trade-off may need to be carefully considered between pursuits of RMS power transfer maximization and optimized overall system efficiency, even when using the proposed optimal CPT model in Chapter 6. According to the experiments in the thesis, an optimization of overall system efficiency is definitely meaningful from energy saving point of view for EV development but may not simultaneously occur with high-power output on load as required especially for real-world demand of fast EV charging, and vice versa. This compromise is subject to differently adopted CPT system characteristics and also depend on how the aimed preferences would be among all the CPT objectives from the EV user end. In other words, varied technical or user experience demands such as preference or acceptance on the charging gap optimization range, the fastest time of charging and the most energy-saving option would lead to and correspond to different

optimum operating frequency supply determinations according to a pre-evaluated empirical performance characteristics for the specific CPT coupler module mounted on the specific EV chassis. On the other hand, an optimal CPT coupling modular design with an optimal schematic from power supply front end to load rear end may not be the ultimate solution towards CPT charging optimizations for EVs and, in contrast, sufficiently empirical and practical test-based CPT systems are required for considering and covering most CPT coupling scenarios in order for a holistic CPT charging optimization solution to be achieved in the near future.

# Chapter 9 Concluding remarks and future work

## 9.1 Conclusions

By analytically designing and implementing various CPT simulation models and laboratory prototypes based on the particularly proposed research methodology, this thesis investigates the output characteristics of the proposed CPT systems towards holistic system performance optimizations and maximizations from analysis perspectives of power electronics results and electromagnetic field behaviours.

The geometric design improvements of coil coupler with effectiveness of using H-shaped ferromagnetic cores have been accomplished, which can be found to play a significant role in enhancing CPT system performance by forming flux line trajectories as expected and strengthening magnetic flux density of the targeted magnetically inductive coupling field, through the computer simulations in Infolytica MagNet and ANSYS Maxwell in the thesis.

An axis-to-axis (coaxial) rectangular coupler CPT model, an axis-parallel (non-coaxial) rectangular coupler CPT model and a C-type coupler CPT model have been established, analysed and compared according to the power electronics outputs and electromagnetic behaviours, by which it can be evidently found that the C-type coupler CPT system with a 10 kV RMS voltage supply is able to result in more satisfactory overall performance than the former three, with a peak coil efficiency of 74.23%, a maximized overall system efficiency of 74.3% and a maximized output RMS power of 46.23 kW at its calculated natural resonant frequency of 800 Hz.

A novel small-sized CPT prototype based on a further geometrically improved H-shaped magnetic coupler with a 5 kV RMS voltage supply using SS compensation topology and electromagnetic resonant coupling has been modelled and investigated. This specific prototype is found to be an optimal CPT system design solution after evaluating overall system performance towards major objectives, with a maximized coil efficiency of 83.8%

at 10 kHz, a maximized system efficiency of 59.5% at 11 kHz and a maximized 42.8 kW RMS power to load at 8 kHz. This particular H-shaped ferromagnetic core based coupler considered as a coupling module optimization has been then applied to most of the model variations for further investigations.

In terms of shielding design for CPT systems with better tolerance to misalignments, the groups of system designs using different shielding materials in ANSYS Maxwell have been carried out, which have witnessed that the specifically prototyped semi-enclosed passive shielding using aluminium material with an optimized inner shielding distance of 15 mm can result in a maximized overall system efficiency of 36.3% at 8 kHz, a maximized coil efficiency of 57.5% at 10 kHz and a peak RMS output power of 22.63 kW at 6 kHz. This specifically prototyped semi-enclosed passive shielding CPT model is found to be able to deliver a relatively optimal overall system performance including tolerance to lateral and longitudinal misalignments, EMF characteristics, efficiency and RMS power to load, etc., when compared with other tested designs.

Different shielding materials tests, various inner shielding distance tests and misalignments tests have been implemented for investigations, by which results in terms of each significant determinant and emphasis from perspectives of power electronics and electromagnetics have been quantitatively analysed for exploring optimization approaches with improved methodology for CPT technologies applied on EV charging. Misalignment tests could witness that different specifications and directional misalignments of laboratory CPT prototypes may have variable critical threshold points of displacement in terms of performing a satisfactory series of outputs with acceptable EMF behaviours. Lateral misalignment tolerance of a system could be more satisfactory than longitudinal one when evaluating both electromagnetic field metrics and electronics results.

An axis-parallel coil coupler model with ferrite cores, a planar circular coil CPT model without ferrite cores and an H-shaped core coupler CPT model (with and without shielding) have been tested in laboratory. Main system outputs, performance results, waveform characteristics including spectra analysis have been compared and evaluated, which evidently proves and validates that the advantageous outcomes and holistic performance of the scaled-down low-power H-shaped core CPT model setup with 15 mm

inner-distance aluminium shielding indeed stand out of all the three tested laboratory-based prototypes using electromagnetic resonant coupling, with system efficiencies of 56.6% at 10 kHz and 30.6% at its calculated natural resonant frequency of 8.4 kHz.

Electromagnetic resonant coupling CPT technologies based on this thesis and the studies until present are promising for real-world implementations with highly optimized performance in the next decades. In order to reach more general optimizations for wider applicable CPT scenarios including high-power charging for EVs, the design of magnetic coupler as an emphasis to perform longer energy transfer distance and to deliver optimized high-power transfer at higher frequencies with reduced system losses against unavoidable external limits and conditions still needs to be further innovatively developed and effectively improved.

## 9.2 Further scope of research

In real-world CPT applications, some unverified patterns and possible influences on induced currents, voltages, power factors of coils via alternating EMF flux linkages, along with other external uncertainties, might also determine the overall CPT system output characteristics, which requires further analytical model studies and quantitative experiment-based investigations in order to draw more comprehensively empirical conclusions for CPT optimization solutions in the future research.

In addition to CPT system performance optimizations addressing the main objectives and challenges that have been investigated in this thesis, it is undoubted that the evolution of CPT technologies for EVs will have been tending to be developed towards safe, light-weighted, geometric-compact for installation, low manufacturing and maintenance cost, low cost of long-term use, in-motion charging, eco-friendly use of materials, etc. The future work in the wider CPT domain will also tend to be extended onto more advanced biomedical implants, smart electronic devices, unmanned aerial vehicles (UAVs), automated guided vehicles (AGVs) for complex logistics warehouse, underwater instruments and robots, etc.

# Publications and award during PhD research

(1) J. Duan and W. Wang, "Electromagnetic Coupling Optimization by Coil Design Improvements for Contactless Power Transfer of Electric Vehicles," in Proceedings of the Future Technologies Conference (FTC) Vancouver, Canada 2018. *Advances in Intelligent Systems and Computing, vol 881, pp 944-958.* Springer, Cham, Switzerland, ISSN: 2194-5357, ISBN: 978-3-030-02682-0. DOI: https://doi.org/10.1007/978-3-030-02683-7_69.

(2) J. Duan and W. Wang, "A Novel Coupler Design and Analysis with Shielding Material Tests for a CPT System of Electric Vehicles Based on Electromagnetic Resonant Coupling," *IOP Conf. Ser.: Materials Science Engineering*, vol. 647, p. 012005, Oct. 2019, DOI: https://doi.org/10.1088/1757-899X/647/1/012005.

(3) J. Duan and W. Wang, "Design and analysis of a novel CPT system with soft ferromagnetic material cores and electromagnetic resonant coupling for EVs," *Juniper Online Journal Material Science*, vol. 5, no. 4, pp. 1–12, Aug. 2019, DOI: https://doi.org/10.19080/JOJMS.2019.05.555668.

(4) J. Duan and W. Wang, "An Optimal Design of Contactless Power Transfer System Applied for Electric Vehicles Using Electromagnetic Resonant Coupling," in Proceedings of the Future Technologies Conference (FTC) San Francisco, USA 2019. *Advances in Intelligent Systems and Computing, vol 1069, pp 919-933.* Springer, Cham, Switzerland, ISSN: 2194-5357, ISBN: 978-3-030-32519-0, DOI: https://doi.org/10.1007/978-3-030-32520-6_66.

(5) J. Duan and W. Wang, "Review on Stationary CPT Technologies and Coil Designs for EVs", *Juniper Online Journal Material Science*, vol. 5, no. 5, pp. 1–8, Jan. 2020, DOI: https://doi.org/10.19080/JOJMS.2020.05.555675.

(6) J. Duan and W. Wang, "Investigations with Various Inner Shielding Distance Tests for a Novel Coupler-based CPT System Applied for Electric Vehicles Using Electromagnetic Resonant Coupling and Aluminium Shielding Material", *IOP Conf. Ser.:*

*Materials Science Engineering*, vol. 812, p. 012004, May 2020, DOI: https://doi.org/10.1088/1757-899X/812/1/012004.

**Award:**

*Best Student Paper Award* for the paper titled “An Optimal Design of Contactless Power Transfer System Applied for Electric Vehicles Using Electromagnetic Resonant Coupling” at FTC2019, San Francisco, USA, 25 Oct 2019, which was granted by the SAI organization committee and the conference chair Prof Pascal Lorenz.

# References

[1] N. Tesla, “Apparatus for transmitting electrical energy,” US1119732A, Dec. 01, 1914.

[2] N. Tesla, “System of transmission of electrical energy,” US645576A, Mar. 20, 1900.

[3] V. Rizzoli, A. Costanzo, D. Masotti, and F. Donzelli, “Integration of numerical and field-theoretical techniques in the design of single- and multi-band rectennas for micro-power generation,” *Int. J. Microw. Wirel. Technol.*, vol. 2, no. 3–4, pp. 293–303, Aug. 2010, doi: 10.1017/S1759078710000553.

[4] M. Reinhard, C. Spindler, T. Schuer, V. Birk, and J. Denk, “New approaches for contactless power transmission systems integrated in PM motor drives transferring electrical energy to rotating loads,” in *Proceedings of the 2011 14th European Conference on Power Electronics and Applications*, Aug. 2011, pp. 1–10.

[5] J. A. Russer, M. Dionigi, M. Mongiardo, and P. Russer, “A moving field inductive power transfer system for electric vehicles,” in *2013 European Microwave Conference*, Oct. 2013, pp. 519–522, doi: 10.23919/EuMC.2013.6686706.

[6] T. Ohira, “Via-wheel power transfer to vehicles in motion,” in *2013 IEEE Wireless Power Transfer (WPT)*, May 2013, pp. 242–246, doi: 10.1109/WPT.2013.6556928.

[7] Chwei-Sen Wang, O. H. Stielau, and G. A. Covic, “Design considerations for a contactless electric vehicle battery charger,” *IEEE Trans. Ind. Electron.*, vol. 52, no. 5, pp. 1308–1314, Oct. 2005, doi: 10.1109/TIE.2005.855672.

[8] M. Eghtesadi, “Inductive power transfer to an electric vehicle-analytical model,” in *40th IEEE Conference on Vehicular Technology*, May 1990, pp. 100–104, doi: 10.1109/VETEC.1990.110303.

[9] J. Huh, S. W. Lee, W. Y. Lee, G. H. Cho, and C. T. Rim, “Narrow-Width Inductive Power Transfer System for Online Electrical Vehicles,” *IEEE Trans. Power Electron.*, vol. 26, no. 12, pp. 3666–3679, Dec. 2011, doi: 10.1109/TPEL.2011.2160972.

[10] K. D. Papastergiou and D. E. Macpherson, “An Airborne Radar Power Supply With Contactless Transfer of Energy—Part I: Rotating Transformer,” *IEEE Trans. Ind. Electron.*, vol. 54, no. 5, pp. 2874–2884, Oct. 2007, doi: 10.1109/TIE.2007.902044.

[11] K. D. Papastergiou, D. E. Macpherson, and F. Fisher, “A 1kW Phase-Shifted Full Bridge Converter incorporating Contact-less Transfer of Energy,” in *2005 IEEE 36th Power Electronics Specialists Conference*, Jun. 2005, pp. 83–89, doi: 10.1109/PESC.2005.1581606.

[12] A. Costanzo, A. Romani, D. Masotti, N. Arbizzani, and V. Rizzoli, “RF/baseband co-design of switching receivers for multiband microwave energy harvesting,” *Sens. Actuators Phys.*, vol. 179, pp. 158–168, Jun. 2012, doi: 10.1016/j.sna.2012.02.005.

[13] K. Eom *et al.*, “A wireless power transmission system for implantable devices in freely moving rodents,” *Med. Biol. Eng. Comput. Heidelb.*, vol. 52, no. 8, pp. 639–51, Aug. 2014, doi: http://dx.doi.org/10.1007/s11517-014-1169-3.

[14] M. A. Hannan, S. M. Abbas, S. A. Samad, and A. Hussain, “Modulation Techniques for Biomedical Implanted Devices and Their Challenges,” *Sensors*, vol. 12, no. 1, pp. 297–319, Jan. 2012, doi: 10.3390/s120100297.

[15] A. Kawamura, K. Ishioka, and J. Hirai, “Wireless transmission of power and information through one high-frequency resonant AC link inverter for robot manipulator applications,” *IEEE Trans. Ind. Appl.*, vol. 32, no. 3, pp. 503–508, May 1996, doi: 10.1109/28.502160.

[16] A. J. Moradewicz and M. P. Kazmierkowski, “Contactless Energy Transfer System With FPGA-Controlled Resonant Converter,” *IEEE Trans. Ind. Electron.*, vol. 57, no. 9, pp. 3181–3190, Sep. 2010, doi: 10.1109/TIE.2010.2051395.

[17] A. P. Hu, Y. W. You, F.-Y. B. Chen, D. McCormick, and D. M. Budgett, “Wireless Power Supply for ICP Devices With Hybrid Supercapacitor and Battery Storage,” *IEEE J. Emerg. Sel. Top. Power Electron.*, vol. 4, no. 1, pp. 273–279, Mar. 2016, doi: 10.1109/JESTPE.2015.2489226.

[18] R. W. Porto, V. J. Brusamarello, I. Müller, F. L. Cabrera Riaño, and F. Rangel De Sousa, “Wireless power transfer for contactless instrumentation and measurement,” *IEEE Instrum. Meas. Mag.*, vol. 20, no. 4, pp. 49–54, Aug. 2017, doi: 10.1109/MIM.2017.8006394.

[19] Y. Hamnerius, “Measurements of human exposure from emerging wireless technologies,” *The Environmentalist*, vol. 29, no. 2, pp. 118–123, Jun. 2009, doi: 10.1007/s10669-009-9220-x.

[20] M. Jufer, “Electric drive system for automatic guided vehicles using contact-free energy transmission,” in *2008 13th International Power Electronics and Motion Control Conference*, Sep. 2008, pp. 1–6, doi: 10.1109/EPEPEMC.2008.4635238.

[21] R. Trevisan and A. Costanzo, “A 1-kW Contactless Energy Transfer System Based on a Rotary Transformer for Sealing Rollers,” *IEEE Trans. Ind. Electron.*, vol. 61, no. 11, pp. 6337–6345, Nov. 2014, doi: 10.1109/TIE.2014.2311395.

[22] D. A. G. Pedder, A. D. Brown, and J. A. Skinner, “A contactless electrical energy transmission system,” *IEEE Trans. Ind. Electron.*, vol. 46, no. 1, pp. 23–30, Feb. 1999, doi: 10.1109/41.744372.

[23] A. P. Sample, B. H. Waters, S. T. Wisdom, and J. R. Smith, “Enabling Seamless Wireless Power Delivery in Dynamic Environments,” *Proc. IEEE*, vol. 101, no. 6, pp. 1343–1358, Jun. 2013, doi: 10.1109/JPROC.2013.2252453.

[24] A. Hoseinpour, M. Mardaneh, and A. Rahideh, “Investigation of the Effects of Different Magnetization Patterns on the Performance of Series Hybrid Excitation

Synchronous Machines," in *Progress in electromagnetics research M.*, 2018, vol. 64, pp. 109–121, doi: 10.2528/PIERM17102006.

[25] J. Hirai, Tae-Woong Kim, and A. Kawamura, "Wireless transmission of power and information and information for cableless linear motor drive," *IEEE Trans. Power Electron.*, vol. 15, no. 1, pp. 21–27, Jan. 2000, doi: 10.1109/63.817358.

[26] S. Chopra, V. Prasanth, B. E. Mansouri, and P. Bauer, "A contactless power transfer — Supercapacitor based system for EV application," in *IECON 2012 - 38th Annual Conference on IEEE Industrial Electronics Society*, Oct. 2012, pp. 2860–2865, doi: 10.1109/IECON.2012.6389441.

[27] J. P. C. Smeets, D. C. J. Krop, J. W. Jansen, and E. A. Lomonova, "Contactless power transfer to a rotating disk," in *2010 IEEE International Symposium on Industrial Electronics*, Jul. 2010, pp. 748–753, doi: 10.1109/ISIE.2010.5637414.

[28] D. Thenathayalan and J.-H. Park, "Wide-Air-Gap Transformer Model for the Design-Oriented Analysis of Contactless Power Converters," *IEEE Trans. Ind. Electron.*, vol. 62, no. 10, pp. 6345–6359, Oct. 2015, doi: 10.1109/TIE.2015.2423662.

[29] Xu Chen and Y. C. Liang, "Contactless power delivery for mobile device charging applications," in *2013 IEEE 14th Workshop on Control and Modeling for Power Electronics (COMPEL)*, Jun. 2013, pp. 1–4, doi: 10.1109/COMPEL.2013.6626455.

[30] T. Hiramatsu, X. Huang, M. Kato, T. Imura, and Y. Hori, "Wireless charging power control for HESS through receiver side voltage control," in *2015 IEEE Applied Power Electronics Conference and Exposition (APEC)*, Charlotte, NC, USA, Mar. 2015, pp. 1614–1619, doi: 10.1109/APEC.2015.7104563.

[31] S. Ahson and M. Ilyas, Eds., *RFID handbook: applications, technology, security, and privacy*. Boca Raton: CRC Press, 2008.

[32] W. C. Brown, "The History of Power Transmission by Radio Waves," *IEEE Trans. Microw. Theory Tech.*, vol. 32, no. 9, pp. 1230–1242, Sep. 1984, doi: 10.1109/TMTT.1984.1132833.

[33] M. Salazar-Palma, T. K. Sarkar, and D. Sengupta, "The father of radio: A brief chronology of the origin and developments of wireless communication and supporting electronics," in *2010 Second Region 8 IEEE Conference on the History of Communications*, Madrid, Spain, Nov. 2010, pp. 1–8, doi: 10.1109/HISTELCON.2010.5735325.

[34] F. F. A. van der Pijl, M. Castilla, and P. Bauer, "Adaptive Sliding-Mode Control for a Multiple-User Inductive Power Transfer System Without Need for Communication," *IEEE Trans. Ind. Electron.*, vol. 60, no. 1, pp. 271–279, Jan. 2013, doi: 10.1109/TIE.2012.2200209.

[35] M. Kiani and M. Ghovanloo, "A Figure-of-Merit for Designing High-Performance Inductive Power Transmission Links," *IEEE Trans. Ind. Electron.*, vol. 60, no. 11, pp. 5292–5305, Nov. 2013, doi: 10.1109/TIE.2012.2227914.

[36] S. Valtchev, B. Borges, K. Brandisky, and J. B. Klaassens, “Resonant Contactless Energy Transfer With Improved Efficiency,” *IEEE Trans. Power Electron.*, vol. 24, no. 3, pp. 685–699, Mar. 2009, doi: 10.1109/TPEL.2008.2003188.

[37] F. Musavi, M. Edington, and W. Eberle, “Wireless power transfer: A survey of EV battery charging technologies,” in *2012 IEEE Energy Conversion Congress and Exposition (ECCE)*, Sep. 2012, pp. 1804–1810, doi: 10.1109/ECCE.2012.6342593.

[38] E. Waffenschmidt and T. Staring, “Limitation of inductive power transfer for consumer applications,” in *2009 13th European Conference on Power Electronics and Applications*, Sep. 2009, pp. 1–10.

[39] J. Wang, S. L. Ho, W. N. Fu, and M. Sun, “Analytical Design Study of a Novel Witricity Charger With Lateral and Angular Misalignments for Efficient Wireless Energy Transmission,” *IEEE Trans. Magn.*, vol. 47, no. 10, pp. 2616–2619, Oct. 2011, doi: 10.1109/TMAG.2011.2151253.

[40] S. F. Tie and C. W. Tan, “A review of energy sources and energy management system in electric vehicles,” *Renew. Sustain. Energy Rev.*, vol. 20, pp. 82–102, Apr. 2013, doi: 10.1016/j.rser.2012.11.077.

[41] K. T. Chau, Y. S. Wong, and C. C. Chan, “An overview of energy sources for electric vehicles,” *Energy Convers. Manag.*, vol. 40, no. 10, pp. 1021–1039, Jul. 1999, doi: 10.1016/S0196-8904(99)00021-7.

[42] C. C. Chan, “The State of the Art of Electric, Hybrid, and Fuel Cell Vehicles,” *Proc. IEEE*, vol. 95, no. 4, pp. 704–718, Apr. 2007, doi: 10.1109/JPROC.2007.892489.

[43] A. M. Foley, I. J. Winning, and B. P. Ó. Ó Gallachóir, “State-of-the-art in electric vehicle charging infrastructure,” in *2010 IEEE Vehicle Power and Propulsion Conference*, Sep. 2010, pp. 1–6, doi: 10.1109/VPPC.2010.5729014.

[44] “Tesla V3 Supercharger: We Put the Latest Fast Charger to the Test,” *Motor Trend*, Jul. 22, 2019. https://www.motortrend.com/news/teslas-v3-supercharger-tested/ (accessed Dec. 12, 2019).

[45] “WestTrans Electric Vehicle Charging leaflets,” *Current WestTrans Projects*. http://www.westtrans.org/wla/wt2.nsf/pages/WT-223 (accessed Dec. 11, 2019).

[46] N. A. Keeling, G. A. Covic, and J. T. Boys, “A Unity-Power-Factor IPT Pickup for High-Power Applications,” *IEEE Trans. Ind. Electron.*, vol. 57, no. 2, pp. 744–751, Feb. 2010, doi: 10.1109/TIE.2009.2027255.

[47] M. Budhia, J. T. Boys, G. A. Covic, and C.-Y. Huang, “Development of a Single-Sided Flux Magnetic Coupler for Electric Vehicle IPT Charging Systems,” *IEEE Trans. Ind. Electron.*, vol. 60, no. 1, pp. 318–328, Jan. 2013, doi: 10.1109/TIE.2011.2179274.

[48] H. H. Wu, J. T. Boys, and G. A. Covic, “An AC Processing Pickup for IPT Systems,” *IEEE Trans. Power Electron.*, vol. 25, no. 5, pp. 1275–1284, May 2010, doi: 10.1109/TPEL.2009.2037002.

[49] Z. Li, C. Zhu, J. Jiang, K. Song, and G. Wei, “A 3-kW Wireless Power Transfer System for Sightseeing Car Supercapacitor Charge,” *IEEE Trans. Power Electron.*, vol. 32, no. 5, pp. 3301–3316, May 2017, doi: 10.1109/TPEL.2016.2584701.

[50] W.-S. Lee, W.-I. Son, K.-S. Oh, and J.-W. Yu, “Contactless Energy Transfer Systems Using Antiparallel Resonant Loops,” *IEEE Trans. Ind. Electron.*, vol. 60, no. 1, pp. 350–359, Jan. 2013, doi: 10.1109/TIE.2011.2177611.

[51] J. Huh and C.-T. Rim, “KAIST Wireless Electric Vehicles - OLEV,” SAE International, Warrendale, PA, SAE Technical Paper 2011-39–7263, May 2011. Accessed: Dec. 12, 2019. [Online]. Available: https://www.sae.org/publications/technical-papers/content/2011-39-7263/.

[52] H. H. Wu, A. Gilchrist, K. Sealy, P. Israelsen, and J. Muhs, “A review on inductive charging for electric vehicles,” in *2011 IEEE International Electric Machines & Drives Conference (IEMDC)*, Niagara Falls, ON, Canada, May 2011, pp. 143–147, doi: 10.1109/IEMDC.2011.5994820.

[53] N. R. Chawla and S. Tosunoglu, “State of the Art in Inductive Charging for Electronic Appliances and its Future in Transportation,” 2012.

[54] “Hyundai Motor Group Unveils Innovative Electric Vehicle Charging and Automated Parking Systems Concept,” *Hyundai Media Newsroom*, Jan. 01, 2019. https://www.hyundai.news/eu/brand/hyundai-motor-group-unveils-innovative-electric-vehicle-charging-and-automated-parking-systems-concept/ (accessed Dec. 13, 2019).

[55] F. Chen, N. Taylor, and N. Kringos, “Electrification of roads: Opportunities and challenges,” *Appl. Energy*, vol. 150, pp. 109–119, Jul. 2015, doi: 10.1016/j.apenergy.2015.03.067.

[56] S. Kitazawa, K. Kondo, and T. Kashiwagi, “Power Flow Control of a Power Conversion Circuit for Contactless Power Transformer Systems with Coil Misalignment,” *Electr. Eng. Jpn.*, vol. 193, no. 1, pp. 55–64, 2015, doi: 10.1002/eej.22609.

[57] R. Miskiewicz and A. Moradewicz, “Contactless power interface for plug-in electric vehicles in V2G systems,” *Bull. Pol. Acad. Sci. Tech. Sci.*, vol. 59, no. 4, pp. 561–568, Dec. 2011, doi: 10.2478/v10175-011-0069-z.

[58] M. Budhia, G. A. Covic, and J. T. Boys, “Design and Optimization of Circular Magnetic Structures for Lumped Inductive Power Transfer Systems,” *IEEE Trans. Power Electron.*, vol. 26, no. 11, pp. 3096–3108, Nov. 2011, doi: 10.1109/TPEL.2011.2143730.

[59] B. G. Pollet, I. Staffell, and J. L. Shang, “Current status of hybrid, battery and fuel cell electric vehicles: From electrochemistry to market prospects,” *Electrochimica Acta*, vol. 84, pp. 235–249, Dec. 2012, doi: 10.1016/j.electacta.2012.03.172.

[60] S. Eaves and J. Eaves, “A cost comparison of fuel-cell and battery electric vehicles,” *J. Power Sources*, vol. 130, no. 1, pp. 208–212, May 2004, doi: 10.1016/j.jpowsour.2003.12.016.

[61] M. McDonough, “Integration of Inductively Coupled Power Transfer and Hybrid Energy Storage System: A Multiport Power Electronics Interface for Battery-Powered Electric Vehicles,” *IEEE Trans. Power Electron.*, vol. 30, no. 11, pp. 6423–6433, Nov. 2015, doi: 10.1109/TPEL.2015.2422300.

[62] M. M. Jovanovic and Y. Jang, “State-of-the-art, single-phase, active power-factor-correction techniques for high-power applications - an overview,” *IEEE Trans. Ind. Electron.*, vol. 52, no. 3, pp. 701–708, Jun. 2005, doi: 10.1109/TIE.2005.843964.

[63] D. M. Vilathgamuwa and J. P. K. Sampath, “Wireless Power Transfer (WPT) for Electric Vehicles (EVs)—Present and Future Trends,” in *Plug In Electric Vehicles in Smart Grids*, S. Rajakaruna, F. Shahnia, and A. Ghosh, Eds. Singapore: Springer Singapore, 2015, pp. 33–60.

[64] T. Imura, H. Okabe, and Y. Hori, “Basic experimental study on helical antennas of wireless power transfer for Electric Vehicles by using magnetic resonant couplings,” in *2009 IEEE Vehicle Power and Propulsion Conference*, Dearborn, MI, Sep. 2009, pp. 936–940, doi: 10.1109/VPPC.2009.5289747.

[65] H. Kim *et al.*, “Coil Design and Measurements of Automotive Magnetic Resonant Wireless Charging System for High-Efficiency and Low Magnetic Field Leakage,” *IEEE Trans. Microw. Theory Tech.*, pp. 1–18, 2016, doi: 10.1109/TMTT.2015.2513394.

[66] Chwei-Sen Wang, G. A. Covic, and O. H. Stielau, “Power transfer capability and bifurcation phenomena of loosely coupled inductive power transfer systems,” *IEEE Trans. Ind. Electron.*, vol. 51, no. 1, pp. 148–157, Feb. 2004, doi: 10.1109/TIE.2003.822038.

[67] N. Jamal, S. Saat, and A. Z. Shukor, “A study on performances of different compensation topologies for loosely coupled inductive power transfer system,” in *2013 IEEE International Conference on Control System, Computing and Engineering*, Penang, Malaysia, Nov. 2013, pp. 173–178, doi: 10.1109/ICCSCE.2013.6719954.

[68] Z. N. Low, J. J. Casanova, and J. Lin, “A Loosely Coupled Planar Wireless Power Transfer System Supporting Multiple Receivers,” *Advances in Power Electronics*, 2010. https://www.hindawi.com/journals/ape/2010/546529/ (accessed Nov. 17, 2019).

[69] J. J. Casanova, Z. N. Low, and J. Lin, “A Loosely Coupled Planar Wireless Power System for Multiple Receivers,” *IEEE Trans. Ind. Electron.*, vol. 56, no. 8, pp. 3060–3068, Aug. 2009, doi: 10.1109/TIE.2009.2023633.

[70] Y. D. Chung, C. Y. Lee, H. C. Jo, Y. G. Park, and S. W. Yim, “Operating characteristics of contactless power transfer for electric vehicle from HTS antenna to normal conducting receiver,” *Phys. C Supercond. Its Appl.*, vol. 504, pp. 115–119, Sep. 2014, doi: 10.1016/j.physc.2014.03.007.

[71] A. Esser and A. Nagel, “Contactless high speed signal transmission integrated in a compact rotatable power transformer,” in *1993 Fifth European Conference on Power Electronics and Applications*, Sep. 1993, pp. 409–414 vol.4.

[72] S. Ojika, Y. Miura, and T. Ise, “Evaluation of Inductive Contactless Power Transfer Outlet with Coaxial Coreless Transformer,” *Electr. Eng. Jpn.*, vol. 195, no. 2, pp. 57–67, 2016, doi: 10.1002/eej.22819.

[73] T. C. Beh, T. Imura, M. Kato, and Y. Hori, “Wireless Power Transfer System via Magnetic Resonant Coupling at Restricted Frequency Range,” p. 4.

[74] C. Zheng *et al.*, “High-Efficiency Contactless Power Transfer System for Electric Vehicle Battery Charging Application,” *IEEE J. Emerg. Sel. Top. Power Electron.*, vol. 3, no. 1, pp. 65–74, Mar. 2015, doi: 10.1109/JESTPE.2014.2339279.

[75] J. Duan and W. Wang, “Electromagnetic Coupling Optimization by Coil Design Improvements for Contactless Power Transfer of Electric Vehicles,” in *Proceedings of the Future Technologies Conference (FTC) 2018*, Cham, 2019, pp. 944–958, doi: 10.1007/978-3-030-02683-7_69.

[76] P. Li and R. Bashirullah, “A Wireless Power Interface for Rechargeable Battery Operated Medical Implants,” *IEEE Trans. Circuits Syst. II Express Briefs*, vol. 54, no. 10, pp. 912–916, Oct. 2007, doi: 10.1109/TCSII.2007.901613.

[77] S. Y. R. Hui and W. C. Ho, “A new generation of universal contactless battery charging platform for portable consumer electronic equipment,” in *2004 IEEE 35th Annual Power Electronics Specialists Conference (IEEE Cat. No.04CH37551)*, Jun. 2004, vol. 1, pp. 638-644 Vol.1, doi: 10.1109/PESC.2004.1355823.

[78] D. Robertson, A. Chu, A. Sabitov, and G. A. Covic, “High power IPT stage lighting controller,” in *2011 IEEE International Symposium on Industrial Electronics*, Jun. 2011, pp. 1974–1979, doi: 10.1109/ISIE.2011.5984461.

[79] M. Budhia, V. Vyatkin, and G. A. Covic, “Powering flexible manufacturing systems with intelligent contact-less power transfer,” in *2008 6th IEEE International Conference on Industrial Informatics*, Jul. 2008, pp. 1160–1165, doi: 10.1109/INDIN.2008.4618278.

[80] A. Radecki *et al.*, “6W/25mm2 inductive power transfer for non-contact wafer-level testing,” in *2011 IEEE International Solid-State Circuits Conference*, Feb. 2011, pp. 230–232, doi: 10.1109/ISSCC.2011.5746297.

[81] G. Buja, M. Bertoluzzo, and H. K. Dashora, “Lumped Track Layout Design for Dynamic Wireless Charging of Electric Vehicles,” *IEEE Trans. Ind. Electron.*, vol. 63, no. 10, pp. 6631–6640, Oct. 2016, doi: 10.1109/TIE.2016.2538738.

[82] A. P. S. Hasanzadeh and P. S. Vaez-Zadeh, “A Review of Contactless Electrical Power Transfer: Applications, Challenges and Future Trends,” *Automatika*, vol. 56, no. 3, pp. 367–378, Jan. 2015, doi: 10.7305/automatika.2015.12.727.

[83] Guoxing Wang, Wentai Liu, M. Sivaprakasam, and G. A. Kendir, “Design and analysis of an adaptive transcutaneous power telemetry for biomedical implants,” *IEEE Trans. Circuits Syst. Regul. Pap.*, vol. 52, no. 10, pp. 2109–2117, Oct. 2005, doi: 10.1109/TCSI.2005.852923.

[84] S. Arai, H. Miura, F. Sato, H. Matsuki, and T. Sato, “Examination of circuit parameters for stable high efficiency TETS for artificial hearts,” *IEEE Trans. Magn.*, vol. 41, no. 10, pp. 4170–4172, Oct. 2005, doi: 10.1109/TMAG.2005.854860.

[85] H. Matsuki, Y. Yamakata, N. Chubachi, S.-I. Nitta, and H. Hashimoto, “Transcutaneous DC-DC converter for totally implantable artificial heart using synchronous rectifier,” *IEEE Trans. Magn.*, vol. 32, no. 5, pp. 5118–5120, Sep. 1996, doi: 10.1109/20.539509.

[86] G. Iddan, G. Meron, A. Glukhovsky, and P. Swain, “Wireless capsule endoscopy,” *Nature*, vol. 405, no. 6785, pp. 417–417, May 2000, doi: 10.1038/35013140.

[87] X. Li, C.-Y. Tsui, and W.-H. Ki, “A 13.56 MHz Wireless Power Transfer System With Reconfigurable Resonant Regulating Rectifier and Wireless Power Control for Implantable Medical Devices,” *IEEE J. Solid-State Circuits*, vol. 50, no. 4, pp. 978–989, Apr. 2015, doi: 10.1109/JSSC.2014.2387832.

[88] Richard H. Englemann, *Static and rotating electromagnetic devices*. New York: Dekker, 1982.

[89] “HUAWEI Wireless Charger, Qi standard, universal wireless charger I HUAWEI UK.” https://consumer.huawei.com/uk/accessories/wireless-charger/ (accessed Dec. 19, 2019).

[90] D. W. Baarman, “Inductively powered lamp assembly,” EP1502479A2, Feb. 02, 2005.

[91] J. Kim, H. Son, D. Kim, and Y. Park, “Optimal design of a wireless power transfer system with multiple self-resonators for an LED TV,” *IEEE Trans. Consum. Electron.*, vol. 58, no. 3, pp. 775–780, Aug. 2012, doi: 10.1109/TCE.2012.6311317.

[92] “Lisbon Tram No.28,” *LisbonLisboaPortugal.com*. https://lisbonlisboaportugal.com/lisbon-transport/lisbon-tram-28.html (accessed Apr. 02, 2021).

[93] “Charging electric buses quickly and efficiently: bus stops fitted with modular components make ‘Charge & Go’ simple to implement - Conductix-Wampfler.” https://www.conductix.us/en/news/2013-05-29/charging-electric-buses-quickly-and-efficiently-bus-stops-fitted-modular-components-make-charge-go (accessed Dec. 29, 2019).

[94] M. Jufer, V. Bourquin, and M. Sawley, “Global Modelisation of the Swissmetro Maglev Using a Numerical Platform,” presented at the MAGLEV’2006: The 19th International Conference on Magnetically Levitated Systems and Linear Drives, Dresden, Sep. 2006, Accessed: Dec. 20, 2019. [Online]. Available: https://trid.trb.org/view/795571.

[95] J. Sallan, J. L. Villa, A. Llombart, and J. F. Sanz, “Optimal Design of ICPT Systems Applied to Electric Vehicle Battery Charge,” *IEEE Trans. Ind. Electron.*, vol. 56, no. 6, pp. 2140–2149, Jun. 2009, doi: 10.1109/TIE.2009.2015359.

[96] A. Esser, “Contactless charging and communication for electric vehicles,” *IEEE Ind. Appl. Mag.*, vol. 1, no. 6, pp. 4–11, Nov. 1995, doi: 10.1109/2943.469997.

[97] U. K. Madawala and D. J. Thrimawithana, “A Bidirectional Inductive Power Interface for Electric Vehicles in V2G Systems,” *IEEE Trans. Ind. Electron.*, vol. 58, no. 10, pp. 4789–4796, Oct. 2011, doi: 10.1109/TIE.2011.2114312.

[98] O. C. Onar, J. M. Miller, S. L. Campbell, C. Coomer, Cliff. P. White, and L. E. Seiber, “A novel wireless power transfer for in-motion EV/PHEV charging,” in *2013 Twenty-Eighth Annual IEEE Applied Power Electronics Conference and Exposition (APEC)*, Mar. 2013, pp. 3073–3080, doi: 10.1109/APEC.2013.6520738.

[99] “California Partners for Advanced Transportation Technology.” https://path.berkeley.edu/node/74 (accessed Dec. 22, 2019).

[100] O. H. Stielau and G. A. Covic, “Design of loosely coupled inductive power transfer systems,” in *PowerCon 2000. 2000 International Conference on Power System Technology. Proceedings (Cat. No.00EX409)*, Dec. 2000, vol. 1, pp. 85–90 vol.1, doi: 10.1109/ICPST.2000.900036.

[101] G. A. Covic and J. T. Boys, “Inductive Power Transfer,” *Proc. IEEE*, vol. 101, no. 6, pp. 1276–1289, Jun. 2013, doi: 10.1109/JPROC.2013.2244536.

[102] Yungtaek Jang and M. M. Jovanovic, “A contactless electrical energy transmission system for portable-telephone battery chargers,” in *IN$^{TEL}$EC. Twenty-Second International Telecommunications Energy Conference (Cat. No.00CH37131)*, Sep. 2000, pp. 726–732, doi: 10.1109/INTLEC.2000.884329.

[103] J. B. Turner and G. W. Roth, “Regulator for inductively coupled power distribution system,” US4914539A, Apr. 03, 1990.

[104] J. T. Boys and A. W. Green, “Inductive power distribution system,” US5293308A, Mar. 08, 1994.

[105] A. W. Green and J. T. Boys, “10 kHz inductively coupled power transfer-concept and control,” in *1994 Fifth International Conference on Power Electronics and Variable-Speed Drives*, Oct. 1994, pp. 694–699, doi: 10.1049/cp:19941049.

[106] J. T. Boys, G. A. Covic, and A. W. Green, “Stability and control of inductively coupled power transfer systems,” *IEE Proc. - Electr. Power Appl.*, vol. 147, no. 1, pp. 37–43, Jan. 2000, doi: 10.1049/ip-epa:20000017.

[107] O. C. Onar, J. M. Miller, S. L. Campbell, C. Coomer, Cliff. P. White, and L. E. Seiber, “Oak Ridge National Laboratory Wireless Power Transfer Development for Sustainable Campus Initiative,” in *2013 IEEE Transportation Electrification Conference and Expo (ITEC)*, Jun. 2013, pp. 1–8, doi: 10.1109/ITEC.2013.6574506.

[108] J. M. Miller, C. P. White, O. C. Onar, and P. M. Ryan, “Grid side regulation of wireless power charging of plug-in electric vehicles,” in *2012 IEEE Energy Conversion Congress and Exposition (ECCE)*, Raleigh, NC, USA, Sep. 2012, pp. 261–268, doi: 10.1109/ECCE.2012.6342814.

[109] H. H. Wu, A. Gilchrist, K. D. Sealy, and D. Bronson, “A High Efficiency 5 kW Inductive Charger for EVs Using Dual Side Control,” *IEEE Trans. Ind. Inform.*, vol. 8, no. 3, pp. 585–595, Aug. 2012, doi: 10.1109/TII.2012.2192283.

[110] W. Li, “High efficiency wireless power transmission at low frequency using permanent magnet coupling,” University of British Columbia, 2009.

[111] T. Horiuchi and K. Kawashima, “Study on Planar Antennas for Wireless Power Transmission of Electric Vehicles,” *IJTIA*, vol. 130, no. 12, pp. 1371–1377, 2010, doi: 10.1541/ieejias.130.1371.

[112] Teck Chuan Beh, Takehiro Imura, Masaki Kato, and Yoichi Hori, “Basic study of improving efficiency of wireless power transfer via magnetic resonance coupling based on impedance matching,” in *2010 IEEE International Symposium on Industrial Electronics*, Bari, Italy, Jul. 2010, pp. 2011–2016, doi: 10.1109/ISIE.2010.5637484.

[113] T. Imura, H. Okabe, T. Uchida, and Y. Hori, “Wireless Power Transfer during Displacement Using Electromagnetic Coupling in Resonance,” *IEEJ Trans. Ind. Appl.*, vol. 130, no. 1, pp. 76–83, 2010, doi: 10.1541/ieejias.130.76.

[114] T. Zelder and B. Geck, “Contactless Scattering Parameter Measurements,” *IEEE Microw. Wirel. Compon. Lett.*, vol. 21, no. 9, pp. 504–506, Sep. 2011, doi: 10.1109/LMWC.2011.2162619.

[115] T. Imura and Y. Hori, “Maximizing Air Gap and Efficiency of Magnetic Resonant Coupling for Wireless Power Transfer Using Equivalent Circuit and Neumann Formula,” *IEEE Trans. Ind. Electron.*, vol. 58, no. 10, pp. 4746–4752, Oct. 2011, doi: 10.1109/TIE.2011.2112317.

[116] T. Imura, T. Yasuda, K. Oshima, T. Nayuki, M. Sato, and A. Oshima, “Wireless power transfer for electric vehicle at the kilohertz band: WIRELESS POWER TRANSFER FOR ELECTRIC VEHICLE,” *IEEJ Trans. Electr. Electron. Eng.*, vol. 11, pp. S91–S99, Dec. 2016, doi: 10.1002/tee.22340.

[117] T. Imura and Y. Hori, “Unified Theory of Electromagnetic Induction and Magnetic Resonant Coupling,” *Electr. Eng. Jpn.*, vol. 199, no. 2, pp. 58–80, Apr. 2017, doi: 10.1002/eej.22953.

[118] M. P. Kesler, “Highly Resonant Wireless Power Transfer: Safe, Efficient, and over Distance,” 2013.

[119] A. Karalis, J. D. Joannopoulos, and M. Soljačić, “Efficient wireless non-radiative mid-range energy transfer,” *Ann. Phys.*, vol. 323, no. 1, pp. 34–48, Jan. 2008, doi: 10.1016/j.aop.2007.04.017.

[120] A. Kurs, A. Karalis, R. Moffatt, J. D. Joannopoulos, P. Fisher, and M. Soljačić, “Wireless Power Transfer via Strongly Coupled Magnetic Resonances,” *Science*, vol. 317, no. 5834, pp. 83–86, 2007.

[121] A. Karalis, A. B. Kurs, R. Moffatt, J. D. Joannopoulos, P. H. Fisher, and M. Soljacic, “Wireless energy transfer,” US7825543B2, Nov. 02, 2010.

[122] “Bombardier’s PRIMOVE E-buses Pass 500,000 km Milestone,” *Bombardier Transportation*. https://localhost:4503/en/newsroom/press-releases.html/bombardier/news/2017/bt_20170118_bombardiers-primove-e-buses-pass-500-000-km-mileston/en (accessed Jan. 02, 2020).

[123] “HEVO: Wireless Charging for Electric Vehicles.” https://hevopower.com/ (accessed Jan. 02, 2020).

[124] G. A. Covic, “Fact Sheet Series : No . 1 – Basic Concepts,” 2013.

[125] R. Bosshard, U. Iruretagoyena, and J. W. Kolar, “Comprehensive Evaluation of Rectangular and Double-D Coil Geometry for 50 kW/85 kHz IPT System,” *IEEE J. Emerg. Sel. Top. Power Electron.*, vol. 4, no. 4, pp. 1406–1415, Dec. 2016, doi: 10.1109/JESTPE.2016.2600162.

[126] “Inductive Power Transfer IPT-Charge, Conductix-Wampfler.” https://www.conductix.us/en/products/inductive-power-transfer-iptr/inductive-power-transfer-iptr-charge?parent_id=5798 (accessed Dec. 29, 2019).

[127] R. Laouamer, M. Brunello, J. P. Ferrieux, O. Normand, and N. Buchheit, “A multi-resonant converter for non-contact charging with electromagnetic coupling,” in *Proceedings of the IECON’97 23rd International Conference on Industrial Electronics, Control, and Instrumentation (Cat. No.97CH36066)*, Nov. 1997, vol. 2, pp. 792–797 vol.2, doi: 10.1109/IECON.1997.671998.

[128] H. Sakamoto, K. Harada, S. Washimiya, K. Takehara, Y. Matsuo, and F. Nakao, “Large air-gap coupler for inductive charger [for electric vehicles],” *IEEE Trans. Magn.*, vol. 35, no. 5, pp. 3526–3528, Sep. 1999, doi: 10.1109/20.800578.

[129] J. Hirai, Tae-Woong Kim, and A. Kawamura, “Study on intelligent battery charging using inductive transmission of power and information,” *IEEE Trans. Power Electron.*, vol. 15, no. 2, pp. 335–345, Mar. 2000, doi: 10.1109/63.838106.

[130] X. Liu and S. Y. Hui, “Optimal Design of a Hybrid Winding Structure for Planar Contactless Battery Charging Platform,” *IEEE Trans. Power Electron.*, vol. 23, no. 1, pp. 455–463, Jan. 2008, doi: 10.1109/TPEL.2007.911844.

[131] S. Judek and K. Karwowski, “Supply of electric vehicles via magnetically coupled air coils,” in *2008 13th International Power Electronics and Motion Control Conference*, Sep. 2008, pp. 1497–1504, doi: 10.1109/EPEPEMC.2008.4635479.

[132] J. L. Villa, J. Sallán, A. Llombart, and J. F. Sanz, “Design of a high frequency Inductively Coupled Power Transfer system for electric vehicle battery charge,” *Appl. Energy*, vol. 86, no. 3, pp. 355–363, Mar. 2009, doi: 10.1016/j.apenergy.2008.05.009.

[133] Y. Shi-chun, S. Sheng-zhuang, C. Yao-guang, G. Wen-zhuang, and J. Fen-zhu, “Research on Efficiency of High Power Resonant Electric Vehicle Contactless Power Transfer Charger,” *Adv. Mech. Eng.*, vol. 6, p. 940890, Jan. 2014, doi: 10.1155/2014/940890.

[134] J. Duan and W. Wang, “Design and analysis of a novel CPT system with soft ferromagnetic material cores and electromagnetic resonant coupling for EVs,” *Juniper Online J. Mater. Sci.*, vol. 5, no. 4, pp. 1–12, Aug. 2019, doi: 10.19080/JOJMS.2019.05.555668.

[135] J. Wang, M. Hu, C. Cai, Z. Lin, L. Li, and Z. Fang, “Optimization design of wireless charging system for autonomous robots based on magnetic resonance coupling,” *AIP Adv.*, vol. 8, no. 5, p. 055004, May 2018, doi: 10.1063/1.5030445.

[136] F. W. Grover, *Inductance Calculations: Working Formulas and Tables*. Dover, 1962.

[137] J. T. Boys and G. A. Covic, “The Inductive Power Transfer Story at the University of Auckland,” *IEEE Circuits Syst. Mag.*, vol. 15, no. 2, pp. 6–27, Secondquarter 2015, doi: 10.1109/MCAS.2015.2418972.

[138] A. Zaheer, H. Hao, G. A. Covic, and D. Kacprzak, “Investigation of Multiple Decoupled Coil Primary Pad Topologies in Lumped IPT Systems for Interoperable Electric Vehicle Charging,” *IEEE Trans. Power Electron.*, vol. 30, no. 4, pp. 1937–1955, Apr. 2015, doi: 10.1109/TPEL.2014.2329693.

[139] S. Y. Choi, J. Huh, W. Y. Lee, and C. T. Rim, “Asymmetric Coil Sets for Wireless Stationary EV Chargers With Large Lateral Tolerance by Dominant Field Analysis,” *IEEE Trans. Power Electron.*, vol. 29, no. 12, pp. 6406–6420, Dec. 2014, doi: 10.1109/TPEL.2014.2305172.

[140] T. Hosotani and I. Awai, “A novel analysis of ZVS wireless power transfer system using coupled resonators,” in *2012 IEEE MTT-S International Microwave Workshop Series on Innovative Wireless Power Transmission: Technologies, Systems, and Applications*, May 2012, pp. 235–238, doi: 10.1109/IMWS.2012.6215801.

[141] A. N. Laskovski and M. R. Yuce, “Class-E oscillators as wireless power transmitters for biomedical implants,” in *2010 3rd International Symposium on*

*Applied Sciences in Biomedical and Communication Technologies (ISABEL 2010)*, Nov. 2010, pp. 1–5, doi: 10.1109/ISABEL.2010.5702913.

[142] S. T. Kim, T. Song, J. Choi, F. Bien, K. Lim, and J. Laskar, "Semi-active high-efficient CMOS rectifier for wireless power transmission," in *2010 IEEE Radio Frequency Integrated Circuits Symposium*, May 2010, pp. 97–100, doi: 10.1109/RFIC.2010.5477403.

[143] Q. Deng *et al.*, "Edge Position Detection of On-line Charged Vehicles With Segmental Wireless Power Supply," *IEEE Trans. Veh. Technol.*, vol. 66, no. 5, pp. 3610–3621, May 2017, doi: 10.1109/TVT.2016.2598183.

[144] M. Hutin and M. Leblang, "Transformer system for electric railways," US527857A, Oct. 23, 1894.

[145] Y. J. Jang and Y. D. Ko, "System architecture and mathematical model of public transportation system utilizing wireless charging electric vehicles," in *2012 15th International IEEE Conference on Intelligent Transportation Systems*, Anchorage, AK, USA, Sep. 2012, pp. 1055–1060, doi: 10.1109/ITSC.2012.6338821.

[146] C. Rim, "The development and deployment of On-Line Electric Vehicles (OLEV)," *IEEE ECCE 2013*, 2013, Accessed: Nov. 08, 2019. [Online]. Available: http://koasas.kaist.ac.kr/handle/10203/192077.

[147] F. Sato, J. Morita, T. Takura, T. Sato, and H. Matsuki, "Research on Highly Efficient Contactless Power Station System using Meander Coil for Moving Electric Vehicle Model," *J. Magn. Soc. Jpn.*, vol. 36, no. 3, pp. 249–252, 2012, doi: 10.3379/msjmag.1205R014.

[148] P. Foy, "Utah to deploy electric bus that needs no plug," *msnbc.com*, Nov. 25, 2011. http://www.nbcnews.com/id/45438112/ns/technology_and_science-innovation/t/utah-deploy-electric-bus-needs-no-plug/ (accessed Jan. 16, 2020).

[149] X. Zhang, Z. Yuan, Q. Yang, Y. Li, J. Zhu, and Y. Li, "Coil Design and Efficiency Analysis for Dynamic Wireless Charging System for Electric Vehicles," *IEEE Trans. Magn.*, vol. 52, no. 7, pp. 1–4, Jul. 2016, doi: 10.1109/TMAG.2016.2529682.

[150] I. S. Grant, *Electromagnetism*, 2nd ed.. Chichester: Wiley, 1990.

[151] W. J. Duffin, *Electricity and magnetism*, 4th ed.. London ; New York: McGraw-Hill, 1990.

[152] J. K. Watson, *Applications of Magnetism*. Wiley, 1980.

[153] J. A. Stratton, *Electromagnetic Theory*. McGraw-Hill, 1941.

[154] Abraham I. Pressman, *Switching power supply design*, 3rd ed.. New York ; London: McGraw-Hill, 2009.

[155] J. Duncan Glover author, *Power system analysis and design.*, Fifth edition, SI edition / J. Duncan Glover, Mulukutla S. Sarma, Thomas J. Overbye.. Stamford, Conn: Cengage Learning, 2012.

[156] Ned. Mohan, *Power electronics: converters, applications and design*, 2nd ed.. New York: Wiley, 1995.

[157] B. Mulgrew, *Digital signal processing: concepts and applications*, 2nd ed.. Basingstoke: Palgrave Macmillan, 2003.

[158] Philip Denbigh author, *System analysis and signal processing: with emphasis on the use of MATLAB*. Harlow: Addison-Wesley, 1998.

[159] E. P. Wohlfarth and K. H. J. Buschow, *Ferromagnetic materials: a handbook on the properties of magnetically ordered substances*. Amsterdam: North-Holland, 1988.

[160] T. Beh, M. Kato, T. Imura, and Y. Hori, "Wireless Power Transfer System via Magnetic Resonant Coupling at Fixed Resonance Frequency-Power Transfer System Based on Impedance Matching-," *World Electr. Veh. J.*, vol. 4, no. 4, pp. 744–753, Dec. 2010, doi: 10.3390/wevj4040744.

[161] I.-S. Jeong, Y.-K. Lee, and H.-S. Choi, "Improvement of Transmission Distance by Using Ferrite in Superconductive Wireless Power Transfer," *J. Supercond. Nov. Magn.*, vol. 30, no. 10, pp. 2971–2975, Oct. 2017, doi: 10.1007/s10948-016-3951-y.

[162] K. E. Koh, T. C. Beh, T. Imura, and Y. Hori, "Impedance Matching and Power Division Using Impedance Inverter for Wireless Power Transfer via Magnetic Resonant Coupling," *IEEE Trans. Ind. Appl.*, vol. 50, no. 3, pp. 2061–2070, May 2014, doi: 10.1109/TIA.2013.2287310.

[163] A. P. Sample, D. T. Meyer, and J. R. Smith, "Analysis, Experimental Results, and Range Adaptation of Magnetically Coupled Resonators for Wireless Power Transfer," *IEEE Trans. Ind. Electron.*, vol. 58, no. 2, pp. 544–554, Feb. 2011, doi: 10.1109/TIE.2010.2046002.

[164] Anthony John. Pointon, *AC and DC network theory*. London: Chapman & Hall, 1991.

[165] J. Duan and W. Wang, "A Novel Coupler Design and Analysis with Shielding Material Tests for a CPT System of Electric Vehicles Based on Electromagnetic Resonant Coupling," *IOP Conf. Ser. Mater. Sci. Eng.*, vol. 647, p. 012005, Oct. 2019, doi: 10.1088/1757-899X/647/1/012005.

[166] J. Duan and W. Wang, "An Optimal Design of Contactless Power Transfer System Applied for Electric Vehicles Using Electromagnetic Resonant Coupling," in *Proceedings of the Future Technologies Conference (FTC) 2019*, Cham, 2020, pp. 919–933, doi: 10.1007/978-3-030-32520-6_66.

[167] S. Chopra and P. Bauer, "Analysis and design considerations for a contactless power transfer system," in *2011 IEEE 33rd International Telecommunications*

*Energy Conference (INTELEC)*, Oct. 2011, pp. 1–6, doi: 10.1109/INTLEC.2011.6099774.

[168] Jia Hou, Qianhong Chen, Siu-Chung Wong, C. K. Tse, and Xinbo Ruan, "Analysis and Control of Series/Series-Parallel Compensated Resonant Converter for Contactless Power Transfer," *IEEE J. Emerg. Sel. Top. Power Electron.*, vol. 3, no. 1, pp. 124–136, Mar. 2015, doi: 10.1109/JESTPE.2014.2336811.

[169] W. Zhang, S.-C. Wong, C. K. Tse, and Q. Chen, "Analysis and Comparison of Secondary Series- and Parallel-Compensated Inductive Power Transfer Systems Operating for Optimal Efficiency and Load-Independent Voltage-Transfer Ratio," *IEEE Trans. Power Electron.*, vol. 29, no. 6, pp. 2979–2990, Jun. 2014, doi: 10.1109/TPEL.2013.2273364.

[170] J. L. Villa, J. Sallan, J. F. Sanz Osorio, and A. Llombart, "High-Misalignment Tolerant Compensation Topology For ICPT Systems," *IEEE Trans. Ind. Electron.*, vol. 59, no. 2, pp. 945–951, Feb. 2012, doi: 10.1109/TIE.2011.2161055.

[171] M. P. Kazmierkowski and A. J. Moradewicz, "Unplugged But Connected: Review of Contactless Energy Transfer Systems," *IEEE Ind. Electron. Mag.*, vol. 6, no. 4, pp. 47–55, Dec. 2012, doi: 10.1109/MIE.2012.2220869.

[172] W. Zhang, S.-C. Wong, C. K. Tse, and Q. Chen, "Load-independent current output of inductive power transfer converters with optimized efficiency," in *2014 International Power Electronics Conference (IPEC-Hiroshima 2014 - ECCE ASIA)*, May 2014, pp. 1425–1429, doi: 10.1109/IPEC.2014.6869772.

[173] K. Aditya and S. S. Williamson, "Comparative study of Series-Series and Series-Parallel compensation topologies for electric vehicle charging," in *2014 IEEE 23rd International Symposium on Industrial Electronics (ISIE)*, Jun. 2014, pp. 426–430, doi: 10.1109/ISIE.2014.6864651.

[174] Gyu Bum Joun and B. H. Cho, "An energy transmission system for an artificial heart using leakage inductance compensation of transcutaneous transformer," *IEEE Trans. Power Electron.*, vol. 13, no. 6, pp. 1013–1022, Nov. 1998, doi: 10.1109/63.728328.

[175] H. Abe, H. Sakamoto, and K. Harada, "A noncontact charger using a resonant converter with parallel capacitor of the secondary coil," *IEEE Trans. Ind. Appl.*, vol. 36, no. 2, pp. 444–451, Apr. 2000, doi: 10.1109/28.833760.

[176] M. Pinuela, D. C. Yates, S. Lucyszyn, and P. D. Mitcheson, "Maximizing DC-to-Load Efficiency for Inductive Power Transfer," *IEEE Trans. Power Electron.*, vol. 28, no. 5, pp. 2437–2447, May 2013, doi: 10.1109/TPEL.2012.2215887.

[177] Zhen Ning Low, R. A. Chinga, R. Tseng, and Jenshan Lin, "Design and Test of a High-Power High-Efficiency Loosely Coupled Planar Wireless Power Transfer System," *IEEE Trans. Ind. Electron.*, vol. 56, no. 5, pp. 1801–1812, May 2009, doi: 10.1109/TIE.2008.2010110.

[178] R. Trevisan and A. Costanzo, “State-of-the-art of contactless energy transfer (CET) systems: design rules and applications,” *Wirel. Power Transf.*, vol. 1, no. 1, pp. 10–20, Mar. 2014, doi: 10.1017/wpt.2014.2.

[179] Z. Pantic and S. M. Lukic, “Framework and Topology for Active Tuning of Parallel Compensated Receivers in Power Transfer Systems,” *IEEE Trans. Power Electron.*, vol. 27, no. 11, pp. 4503–4513, Nov. 2012, doi: 10.1109/TPEL.2012.2196055.

[180] G. A. J. Elliott, G. A. Covic, D. Kacprzak, and J. T. Boys, “A New Concept: Asymmetrical Pick-Ups for Inductively Coupled Power Transfer Monorail Systems,” *IEEE Trans. Magn.*, vol. 42, no. 10, pp. 3389–3391, Oct. 2006, doi: 10.1109/TMAG.2006.879619.

[181] G. A. Covic, G. Elliott, O. H. Stielau, R. M. Green, and J. T. Boys, “The design of a contact-less energy transfer system for a people mover system,” in *PowerCon 2000. 2000 International Conference on Power System Technology. Proceedings (Cat. No.00EX409)*, Dec. 2000, vol. 1, pp. 79–84 vol.1, doi: 10.1109/ICPST.2000.900035.

[182] G. A. Covic, J. T. Boys, M. L. G. Kissin, and H. G. Lu, “A Three-Phase Inductive Power Transfer System for Roadway-Powered Vehicles,” *IEEE Trans. Ind. Electron.*, vol. 54, no. 6, pp. 3370–3378, Dec. 2007, doi: 10.1109/TIE.2007.904025.

[183] C. Fernandez, O. Garcia, R. Prieto, J. A. Cobos, S. Gabriels, and G. Van Der Borght, “Design issues of a core-less transformer for a contact-less application,” in *APEC. Seventeenth Annual IEEE Applied Power Electronics Conference and Exposition (Cat. No.02CH37335)*, Mar. 2002, vol. 1, pp. 339–345 vol.1, doi: 10.1109/APEC.2002.989268.

[184] W. G. Hurley and M. C. Duffy, “Calculation of self and mutual impedances in planar magnetic structures,” *IEEE Trans. Magn.*, vol. 31, no. 4, pp. 2416–2422, Jul. 1995, doi: 10.1109/20.390151.

[185] I. Awai, S. Iwamura, H. Kubo, and A. Sanada, “Separation of coupling coefficient between resonators into electric and magnetic contributions,” *Electron. Commun. Jpn. Part II Electron.*, vol. 89, no. 8, pp. 27–33, 2006, doi: 10.1002/ecjb.20251.

[186] Matthew N. O. Sadiku, *Numerical techniques in electromagnetics*. Boca Raton: CRC P, 1992.

[187] David J. Griffiths, *Introduction to electrodynamics*, 3rd ed. [International edition].. Upper Saddle River, N.J.: Prentice Hall, 2003.

[188] H. A. Haus and J. R. Melcher, *Electromagnetic fields and energy*. Englewood Cliffs, N.J: Prentice Hall, 1989.

[189] P. L. Penfield and H. A. Haus, “Electrodynamics of Moving Media,” Research Laboratory of Electronics (RLE) at the Massachusetts Institute of Technology (MIT),

Technical Report, Apr. 1966. Accessed: Nov. 25, 2019. [Online]. Available: https://dspace.mit.edu/handle/1721.1/55447.

[190] David Keun. Cheng, *Fundamentals of engineering electromagnetics*. Reading, Mass.: Addison-Wesley, 1993.

[191] K. F. Riley, *Mathematical methods for physics and engineering*, Third edition.. Cambridge ; New York: Cambridge University Press, 2013.

[192] "IEEE Recommended Practice for Measurements and Computations of Radio Frequency Electromagnetic Fields With Respect to Human Exposure to Such Fields,100 kHz-300 GHz," *IEEE Std C953-2002 Revis. IEEE Std C953-1991*, pp. i–126, 2002, doi: 10.1109/IEEESTD.2002.94226.

[193] A. Chiba, K. Isaka, Y. Yokoi, M. Nagata, M. Kitagawa, and T. Matsuo, "Application of Finite Element Method to Analysis of Induced Current Densities Inside Human Model Exposed to 60-Hz Electric Field," *IEEE Power Eng. Rev.*, vol. PER-4, no. 7, pp. 66–67, Jul. 1984, doi: 10.1109/MPER.1984.5525912.

[194] D. R. Lynch, K. D. Paulsen, and J. W. Strohbehn, "Finite element solution of Maxwell's equations for hyperthermia treatment planning," *J. Comput. Phys.*, vol. 58, no. 2, pp. 246–269, Apr. 1985, doi: 10.1016/0021-9991(85)90179-2.

[195] M. A. Morgan, "Finite Element Calculation of Microwave Absorption by the Cranial Structure," *IEEE Trans. Biomed. Eng.*, vol. BME-28, no. 10, pp. 687–695, Oct. 1981, doi: 10.1109/TBME.1981.324662.

[196] Y. Yamashita and T. Takahashi, "Use of the Finite Element Method to Determine Epicardial from Body Surface Potentials Under a Realistic Torso Model," *IEEE Trans. Biomed. Eng.*, vol. BME-31, no. 9, pp. 611–621, Sep. 1984, doi: 10.1109/TBME.1984.325305.

[197] P. P. Silvester, *Finite elements for electrical engineers*, Third edition.. Cambridge: University Press, 1996.

[198] Charles W. Steele, *Numerical computation of electric and magnetic fields*. New York: Van Nostrand Reinhold, 1987.

[199] S. Vajda, "Symposium on Monte Carlo Methods. Edited by H. A. Meyer pp. 382. 1956. 60s. (Wiley, New York; Chapman and Hall)," *Math. Gaz.*, vol. 41, no. 338, pp. 318–318, Dec. 1957, doi: 10.2307/3610170.

[200] J. D. Jackson and L. B. Okun, "Historical roots of gauge invariance," *Rev. Mod. Phys.*, vol. 73, no. 3, pp. 663–680, Sep. 2001, doi: 10.1103/RevModPhys.73.663.

[201] V. J. Kumar, V. G. K. Murti, and P. Sankaran, "Inductance Measurement," in *Wiley Encyclopedia of Electrical and Electronics Engineering*, American Cancer Society, 1999.

[202] M. Gyimesi and D. Ostergaard, “Inductance computation by incremental finite element analysis,” *IEEE Trans. Magn.*, vol. 35, no. 3, pp. 1119–1122, May 1999, doi: 10.1109/20.767144.

[203] Michael P. Perry, *Low frequency electromagnetic design*. New York: Dekker, 1985.

[204] M. H. Rashid, *Power electronics: circuits, devices, and applications*, 2nd ed.. Englewood Cliffs: Prentice Hall, 1993.

[205] Leonard J. Tung, *Circuit analysis*. River Edge, N.J.: World Scientific, 2001.

[206] M. Budhia, G. A. Covic, and J. T. Boys, “Design and optimisation of magnetic structures for lumped Inductive Power Transfer systems,” in *2009 IEEE Energy Conversion Congress and Exposition*, Sep. 2009, pp. 2081–2088, doi: 10.1109/ECCE.2009.5316197.

[207] S. Lee, J. Huh, C. Park, N.-S. Choi, G.-H. Cho, and C.-T. Rim, “On-Line Electric Vehicle using inductive power transfer system,” in *2010 IEEE Energy Conversion Congress and Exposition*, Sep. 2010, pp. 1598–1601, doi: 10.1109/ECCE.2010.5618092.

[208] C. Zheng, H. Ma, J.-S. Lai, and L. Zhang, “Design Considerations to Reduce Gap Variation and Misalignment Effects for the Inductive Power Transfer System,” *IEEE Trans. Power Electron.*, vol. 30, no. 11, pp. 6108–6119, Nov. 2015, doi: 10.1109/TPEL.2015.2424893.

[209] M. Chigira, Y. Nagatsuka, Y. Kaneko, S. Abe, T. Yasuda, and A. Suzuki, “Novel Core Structure and Iron-Loss Modeling for Contactless Power Transfer System of Electric Vehicle,” *Electr. Eng. Jpn.*, vol. 184, no. 2, pp. 61–70, Jul. 2013, doi: 10.1002/eej.22377.

[210] M. Chigira, Y. Nagatsuka, Y. Kaneko, S. Abe, T. Yasuda, and A. Suzuki, “Small-size light-weight transformer with new core structure for contactless electric vehicle power transfer system,” in *2011 IEEE Energy Conversion Congress and Exposition*, Sep. 2011, pp. 260–266, doi: 10.1109/ECCE.2011.6063778.

[211] G. Ombach, D. Kurschner, S. Mathar, and W. Chlebosz, “Optimum magnetic solution for interoperable system for stationary wireless EV charging,” in *2015 Tenth International Conference on Ecological Vehicles and Renewable Energies (EVER)*, Mar. 2015, pp. 1–8, doi: 10.1109/EVER.2015.7112996.

[212] Y. H. Sohn, B. H. Choi, E. S. Lee, G. C. Lim, G.-H. Cho, and C. T. Rim, “General Unified Analyses of Two-Capacitor Inductive Power Transfer Systems: Equivalence of Current-Source SS and SP Compensations,” *IEEE Trans. Power Electron.*, vol. 30, no. 11, pp. 6030–6045, Nov. 2015, doi: 10.1109/TPEL.2015.2409734.

[213] M. Kissin, Chang-Yu Huang, G. A. Covic, and J. T. Boys, “Detection of the Tuned Point of a Fixed-Frequency *LCL* Resonant Power Supply,” *IEEE Trans. Power*

*Electron.*, vol. 24, no. 4, pp. 1140–1143, Apr. 2009, doi: 10.1109/TPEL.2008.2011641.

[214] G. A. Covic, J. T. Boys, A. M. W. Tam, and J. C.-H. Peng, "Self tuning pick-ups for inductive power transfer," in *2008 IEEE Power Electronics Specialists Conference*, Rhodes, Greece, Jun. 2008, pp. 3489–3494, doi: 10.1109/PESC.2008.4592495.

[215] S. Raju, R. Wu, M. Chan, and C. P. Yue, "Modeling of Mutual Coupling Between Planar Inductors in Wireless Power Applications," *IEEE Trans. Power Electron.*, vol. 29, no. 1, pp. 481–490, Jan. 2014, doi: 10.1109/TPEL.2013.2253334.

[216] Yang Sun, Chang-jin Jeong, Seok-kyun Han, and Sang-gug Lee, "A high speed comparator based active rectifier for wireless power transfer systems," in *2011 IEEE MTT-S International Microwave Workshop Series on Intelligent Radio for Future Personal Terminals*, Aug. 2011, pp. 1–2, doi: 10.1109/IMWS2.2011.6027216.

[217] "Introduction to Electromagnetic Compatibility, 2nd Edition | Wiley," *Wiley.com*. https://www.wiley.com/en-us/Introduction+to+Electromagnetic+Compatibility%2C+2nd+Edition-p-9780471755005 (accessed Apr. 25, 2020).

[218] UK Power Networks, "UK Power Networks-Transmitting electricity," 2014. http://powerup.ukpowernetworks.co.uk/powerup/en/over-11/electric-journey/transmitting-electricity/ (accessed Apr. 29, 2020).

[219] HSE.gov.uk, "Description of processes/plants or systems Power Distribution Systems," Jul. 22, 2019. https://www.hse.gov.uk/comah/bpgrange/append/power.htm (accessed Apr. 29, 2020).

[220] University of Strathclyde, "Introduction to Integrating Renewable Technologies," May 2002. http://www.esru.strath.ac.uk/EandE/Web_sites/01-02/RE_info/integration.htm (accessed Apr. 29, 2020).

[221] J. Duan and W. Wang, "Investigations with Various Inner Shielding Distance Tests for a Novel Coupler-based CPT System Applied for Electric Vehicles Using Electromagnetic Resonant Coupling and Aluminium Shielding Material," *IOP Conf. Ser. Mater. Sci. Eng.*, vol. 812, p. 012004, May 2020, doi: 10.1088/1757-899X/812/1/012004.

[222] D. K. Biswas, N. T. Tasneem, and I. Mahbub, "Effects of Coaxial-Lateral and Coaxial-Angular Displacements on Link Efficiency of a Wirelessly Powered Optogenetic Implant: Design, Modeling, and Experimental Validation," *IEEE J. Electromagn. RF Microw. Med. Biol.*, vol. 3, no. 4, pp. 269–275, Dec. 2019, doi: 10.1109/JERM.2019.2909391.

[223] S. Aldhaher, P. C.-K. Luk, and J. F. Whidborne, "Electronic Tuning of Misaligned Coils in Wireless Power Transfer Systems," *IEEE Trans. Power Electron.*, vol. 29, no. 11, pp. 5975–5982, Nov. 2014, doi: 10.1109/TPEL.2014.2297993.

[224] E. W. Kamen and B. S. Heck, *Fundamentals of Signals and Systems Using the Web and MATLAB*. Pearson Prentice Hall, 2007.

[225] F. J. Harris, “On the use of windows for harmonic analysis with the discrete Fourier transform,” *Proc. IEEE*, vol. 66, no. 1, pp. 51–83, Jan. 1978, doi: 10.1109/PROC.1978.10837.

# Appendix A

$\nabla = \mathbf{i}\frac{\partial}{\partial x} + \mathbf{j}\frac{\partial}{\partial y} + \mathbf{k}\frac{\partial}{\partial z}$ is the operator called 'del' which is a vector differential operator.

The divergence $\nabla \cdot$ of a vector field:

Div $\mathbf{F}$ or $\nabla \cdot \mathbf{F}$ is defined as the divergence of $\mathbf{F}$ in the vector field $\mathbf{F}(\mathrm{x},\mathrm{y},\mathrm{z}) = F_1\boldsymbol{i} + F_2\boldsymbol{j} + F_3\boldsymbol{k}$, and $\nabla \cdot \mathbf{F} \equiv \frac{\partial F_1}{\partial_x} + \frac{\partial F_2}{\partial_y} + \frac{\partial F_3}{\partial_z}$ is a scalar depending on position in field. Alternatively, the divergence of $\mathbf{F}$ can be written as a full result with $\nabla$ and $\mathbf{F}$ in components: $\nabla \cdot \mathbf{F} = (\boldsymbol{i}\frac{\partial}{\partial_x} + \boldsymbol{j}\frac{\partial}{\partial_y} + \boldsymbol{k}\frac{\partial}{\partial_z}) \cdot (F_1\boldsymbol{i} + F_2\mathbf{J} + F_3\mathbf{k})$ where $\boldsymbol{i} \cdot \boldsymbol{i} = 1, \mathbf{i} \cdot \mathbf{j} = 0$.

The geometric meaning of the divergence is:

Consider a point $\mathbf{r}$ and consider a small closed surface surrounding that point, if the divergence div $\mathbf{F}$ is positive at $\mathbf{r}$, then on average the vector field $\mathbf{F}$ is point 'away' from the point and out of the surface; if the divergence is negative, then on balance the vector field $\mathbf{F}$ is pointing towards the point and into the surface.

The curl $\nabla \times$ of a vector field:

$\nabla \times \mathbf{F} = \left(\frac{\partial F_3}{\partial_y} - \frac{\partial F_2}{\partial_z}\right)\boldsymbol{i} + \left(\frac{\partial F_1}{\partial_z} - \frac{\partial F_3}{\partial_x}\right)\boldsymbol{j} + \left(\frac{\partial F_2}{\partial_x} - \frac{\partial F_1}{\partial_y}\right)\mathbf{k}$ is defined as the curl of a vector field $\mathbf{F}$, in which curl $\mathbf{F}$ or $\nabla \times \mathbf{F}$ is vector depending on position in field. With writing out the determinant in full, the original definition can also be equivalent to $\nabla \times \mathbf{F} = \begin{vmatrix} \boldsymbol{i} & \boldsymbol{j} & \boldsymbol{k} \\ \frac{\partial}{\partial_x} & \frac{\partial}{\partial_y} & \frac{\partial}{\partial_z} \\ F_1 & F_2 & F_3 \end{vmatrix}$.

The geometric meaning of the curl is:

If at some point in space the component of the curl in the **n** direction is positive, it means that in the vicinity of the point and in a plane normal to **n**, the vector field tends to go round in an anti-clockwise direction if one looks along vector **n**; if the component of the curl is negative, it would mean that the vector field tends to go round in a clockwise direction.

# Appendix B

```
clear all; close all;
load 15mm_20kHz_11VPk_Air_Gap_AxisParallel_20200717.mat

[N,M]=size(data);
T=N/40000;
dT=1/40000;
t=dT:dT:T;


figure(20200806);
x=data(:,2);

subplot(2,2,1);
plot(t,x);
axis([ 0 T/5  1.2*min(x) 1.2*max(x)]);
xlabel('t (sec)','fontsize',14,'fontweight','bold');
ylabel('Vpri. (V)','fontsize',14,'fontweight','bold');
grid on;
set(gcf,'color','w')

subplot(2,2,2);
X=fft(x);
f=1:N;f=f/T;
stem(f,abs(X));
xlabel('f (Hz)','fontsize',14,'fontweight','bold');
axis([0 N/2*1.2 0 max(abs(X))*1.2]);

ylabel('FFT spectrum modular','fontsize',14,'fontweight','bold');
grid on;
set(gcf,'color','w')

subplot(2,2,3);
```

```
for n=1:N
w(n)=0.54+0.46*cos((2*n-N+1)*pi/N);
end;
x1=x'.*w;

plot(t,x1);
axis([ 0 T  1.2*min(x1) 1.2*max(x1)]);
xlabel('t (sec)','fontsize',14,'fontweight','bold');
ylabel('Hamming-windowed Vpri. (V)','fontsize',14,'fontweight','bold');
grid on;

subplot(2,2,4);
X1=fft(x1);
stem(f,abs(X1));
xlabel('f (Hz)','fontsize',14,'fontweight','bold');
ylabel('Hamming-windowed FFT spectrum modular','fontsize',14,'fontweight','bold');
axis([0 N/2*1.2 0 max(abs(X1))*1.2]);
grid on;
set(gcf,'color','w')


figure(202008061);
y=data(:,3)/100;

subplot(2,2,1);
plot(t,y);
axis([ 0 T/5  1.2*min(y) 1.2*max(y)]);
xlabel('t (sec)','fontsize',14,'fontweight','bold');
ylabel('Ipri. (A)','fontsize',14,'fontweight','bold');
grid on;
set(gcf,'color','w')

subplot(2,2,2);
Y=fft(y);
f=1:N;f=f/T;
stem(f,abs(Y));
xlabel('f (Hz)','fontsize',14,'fontweight','bold');
axis([0 N/2*1.2 0 max(abs(Y))*1.2]);

ylabel('FFT spectrum modular','fontsize',14,'fontweight','bold');
grid on;
set(gcf,'color','w')

subplot(2,2,3);
for n=1:N
w(n)=0.54+0.46*cos((2*n-N+1)*pi/N);
end;
y1=y'.*w;

plot(t,y1);
axis([ 0 T  1.2*min(y1) 1.2*max(y1)]);
xlabel('t (sec)','fontsize',14,'fontweight','bold');
ylabel('Hamming-windowed Ipri. (A)','fontsize',14,'fontweight','bold');
grid on;

subplot(2,2,4);
Y1=fft(y1);
stem(f,abs(Y1));
xlabel('f (Hz)','fontsize',14,'fontweight','bold');
ylabel('Hamming-windowed FFT spectrum modular','fontsize',14,'fontweight','bold');
axis([0 N/2*1.2 0 max(abs(Y1))*1.2]);
grid on;
set(gcf,'color','w')


phi1=atan2(imag(X1(19919)),real(X1(19919)));
phi2=atan2(imag(Y1(19919)),real(Y1(19919)));
d_phi=phi1-phi2;
cos(d_phi)
```